

VERSLAGEN EN VERHANDELINGEN

REPORTS AND TRANSACTIONS

NATIONAAL LUCHTVAARTLABORATORIUM

NATIONAL AERONAUTICAL RESEARCH INSTITUTE

AMSTERDAM

XVIII — 1953

Preface

This Volume of "Verslagen en Verhandelingen" contains a selection of reports published by the NLL.

To give a better survey of the scientific work, carried out at the NLL, and of its organization, it is decided to include a shortened version of the Annual Report into the Volume, which will be issued in a yearly edition from now on.

In section A a survey is given of the organization of the NLL and the constitution of the Board, in section B a description is given of the scientific work of the various sections, when possible accompanied by the number of the report, in which the results are published. A list of non-printed technical reports and other miscellaneous publications published during 1953 concludes this section.

C. ZWIKKER,
Director.

July 1954.

Contents

Preface	I
Thirty-fourth Annual Report.....	III
List of publications	X

Report	Author(s)	Title	
A. 1205	Meyer Drees, J. and Hendal, W. P.	The field of flow through a helicopter rotor obtained from windtunnel smoke tests.	p. A. 17—A. 20
A. 1263	Wijker, H.	Experiments on the two-dimensional flow over a NACA 0018 profile at high angles of attack.	p. A. 1—A. 14
F. 118	IJff, J.	Influence of compressibility on the calculated flexure-torsion flutter speed of a family of rectangular cantilever wings.	p. F. 7—F. 16
F. 122	Bergh, H. and IJff, J.	Application of experimental aerodynamic coefficients to flutter calculation.	p. F. 1—F. 6
F. 129	Van de Vooren, A. I.	An approach to lifting surface theory.	p. F. 17—F. 30
M. 1857	Hartman, A. and Duyn, G. C.	A comparative investigation on the fatigue strength at fluctuating tension of several types of riveted lap joints, a series of bolted and some series of glued lap joints of 24 ST Alclad.	p. M. 1—M. 26
S. 416	Rondeel, J. H., Kruithof, R. and Plantema, F. J.	Comparative fatigue tests with 24 ST alclad riveted and bonded stiffened panels.	p. S. 1—S. 14
S. 421	Besseling, J. F. and Floor, W. K. G.	Torsional strength and stiffness tests of wing leading edges.	p. S. 25—S. 42
S. 426	Bentham, J. P.	Note on the general stress-strain relations of some ideal bodies showing the phenomena of creep and of relaxation.	p. S. 15—S. 24
V. 1535	Meyer Drees, J., Lucassen, L. R. and Hendal, W. P.	Airflow through helicopter-rotors in vertical flight.	p. V. 13—V. 20
V. 1648	Kalkman, C. M. and Buhrman, J.	The effect of the compressibility of the air on the dynamic longitudinal stability of an aeroplane in gliding flight.	p. V. 1—V. 12

Thirty-fourth Annual Report

of the

National Aeronautical Research Institute

N.L.L.

1953

A. Board and organization.

In 1918 the Ministry of War established the "Studie-afdeling van de luchtvaartdienst", which soon changed its name to "Rijksstudiedienst voor de Luchtvaart" (R. S. L.).

By Royal Decree of 16 February 1920, no 67 the RSL has been incorporated into the Ministry of "Waterstaat" and regulations were given as to its task and duties, being aeronautical research in the broadest sense of the word.

In 1937 the "Rijksstudiedienst voor de Luchtvaart" has been transformed into the Institution "Nationaal Luchtvaartlaboratorium" by the Government in co-operation with the Association of Dutch Aircraft Manufacturers, the Royal Dutch Airlines (KLM) and the Royal Dutch Aeronautical Association. Members of the Board of the Institution were appointed by the participating governmental and private bodies. All members serve as such without compensation.

On 31 December 1953 the Board consisted of the following members:

for the Ministry of Education, Arts and Sciences	Prof. Dr Ir H. J. van der Maas Technical University, Delft President
for the Ministry of Transport and "Waterstaat"	J. W. F. Backer Dir. Gen. Department of Civil Aviation Vice-President L. Neher Postmaster General Prof. Dr D. Dresden President National Council for Industrial Research TNO
for the Ministry of War	Maj. Gen. J. A. Bach Dir. of Ordnance and Supplies, Royal Dutch Air Force
for the Ministry of the Navy	Commander J. Lugtenburg Dir. Air Materiel Division, Royal Dutch Navy
for the Ministry of Overseas Territories	Dr J. W. de Stoppelaar Head Department of Economic Affairs
for the Ministry of Economic Affairs	Drs H. P. Jongsma Dir. for Financial Participations
for the Royal Dutch Airlines, KLM	C. Wijdooge KLM Head Techn. Sales Department
for the Royal Dutch Aeronautical Association	Prof. Dr W. J. D. van Dijk Scient. Advisor Royal Dutch Shell
and as observer for the Ministry of Finance	Mr O. W. Vos
Director of the Laboratory,	Prof. Dr C. Zwikker
Secretary-treasurer of the Institution,	Mr G. C. Klapwijk.

Under the Act of Incorporation, the Board is assisted by an Advisory Scientific Committee appointed by the Minister of Transport. The present members are:

Chairman to be appointed,	
Prof. Ir D. Dresden	Vice Chairman
National Council for Industrial Research TNO	
Prof. Dr J. M. Burgers	
Technical University, Delft	
Prof. Dr Ir W. F. Brandsma	
Technical University, Delft	
Prof. Dr W. Bleeker	
Royal Dutch Meteorological Institute	
Prof. Dr Ir W. T. Koiter	
Technical University, Delft	
Maj. Gen. Prof. Dr Ir G. Otten	
Air Materiel Command, Royal Dutch Air Force	
Dr J. H. Greidanus	
Royal Dutch Aircraft Factories Fokker	
Secretary, Ir J. van Buuren.	

During the year the organization of the Laboratory, has been changed in such a way that the scientific activities have been divided into 7 scientific sections:

- Aerodynamics (A)
- Combustion (C)
- Flutter and theoretical Aerodynamics (F)
- Helicopters (H)
- Materials and Structures (M and S)
- Flying Models (O)
- Flight Testing (V)

and 7 scientific services:

- Electronic Laboratory
- Windtunnel Equipment
- Model Construction
- Analogues
- Computing Office
- Library and Documentation
- Catalogue of Aerodynamic Measurements.

In the middle of May 1953 the Government approved the proposals of the Board for continuing the extension of the windtunnel equipment of the laboratory. In the second half of the year the Board was able to contract the completement of the Pilottunnel (small high-speed tunnel) and the power station.

The President of the Board and the Director of the Laboratory were appointed National Delegates to AGARD by the Minister of War and attended the meetings of the AGARD Windtunnel-panel in USA, the General Assembly in London and of the Combustion Panel in Cambridge (Engl.).

B. The Laboratory.

1 General.

The laboratory was staffed by 42 scientists (engineers, mathematicians and physicists), 33 graduates of Technical Colleges, 87 technicians, 32 administrative officers and 20 other employees, 214 in total. 15 members of the staff, among whom 8 engineers, were in military service.

Research contracts were given by the Netherlands Aircraft Development Board (NIV), the Air Materiel Command of the Royal Dutch Air Force and Navy, the Royal Dutch Airlines and the Department of Civil Aviation.

A number of small orders from the industry, including testing and calibration of apparatus and wind-tunnel measurements on ship-models etc. has moreover been carried out.

The planning and design for the new windtunnels monopolized the attention of a number of engineers. The cooperation within the Advisory Group for Aeronautical Research and Development was of great value for these and other problems in the laboratory.

The projects for the high-speed windtunnel, the pilottunnel and the supersonic windtunnel are being adapted to the new developments. The pilottunnel will be in service in 1954, giving the

NLL the disposal of a windtunnel with a working-section of $0.42 \times 0.55 \text{ m}^2$ for high subsonic speed (to $\text{Ma} = 0.95$). The large high-speed windtunnel, which was originally planned for high subsonic speed, has been redesigned as a transsonic tunnel for Mach numbers up to 1.3 with a working section of $2.00 \times 1.60 \text{ m}^2$. The design of the supersonic tunnel has also been revised in view of the newest developments.

New methods of model-construction were studied including copying-lathe machining. A high-altitude, low-temperature instrument-testing cabinet and a Siemens apparatus for ultrasonic research of materials have been put into use.

Research has been started on the use of strain-gauge balances, on measuring aerodynamic and flight characteristics of wings and complete aircraft by means of free-flying models, on the applicability of analogue computers and on combustion problems in ramjets.

2 Aerodynamics Section.

Besides model measurements for the development of various aircraft designs, investigations have been made on the following subjects:

Model of Siebel-laboratory aeroplane.

Measurements have been made on the influencing of the wing-fuselage interference by splits in the wing alongside the fuselage-wall or by a fairing (Report A.1310).

Results of model tests with the Siebel aeroplane and G6vier sailplane have been summarized and compared with flight tests (Report A.1292 (Siebel) and Report A.1322 (G6vier)).

The influence of working propellers and flaps on the indication of an angle-of-attack and slip-indicator before the fuselage-nose has been investigated (Report A.1324).

Swept wings.

The influence of a flat plate in the plane of symmetry on the flow along a symmetrical swept wing has been investigated in view of the application of wall-mounted half-models (Report A.1328).

The flow and pressure distribution over swept wings have been investigated, particularly the influence of the variation of camber along the span (Report A.1332).

3 Flutter and theoretical aerodynamics section.

Boundary layer theory.

TIMMAN's one parameter method for the calculation of laminar boundary layers (F.35) was extended to compressible flow. Since there exists an interaction between the velocity and the temperature profiles in compressible flow, at first a separate investigation towards the temperature boundary layer in incompressible flow has been performed (Report F.127, F.130). Report F.141 contains the description of this method for flows with arbitrary pressure gradient, PRANDTL and MACH numbers and for the cases without and with heat transfer at the wall. The method can be applied for two-dimensional and for rotationally-symmetric flows.

A semi-empiric method for the calculation of turbulent boundary layers in compressible flow was developed. (Report F.132).

The investigation of the laminar part of the boundary layer of a swept wing was continued. The general method of calculation has been described in Report F.66. The swept-wing has been schematized by a flat ellipsoid. The potential flow about this ellipsoid at zero incidence has been calculated in Report F.74.

Load distribution of swept wings in steady flow.

A generalization of PRANDTL's equation was derived for the calculation of the load distribution on swept wings of large aspect ratio. (Reports F.95, F.121). For wings of arbitrary aspect ratio a lifting surface theory, which uses a series expansion for the chordwise vorticity distribution, was developed (Report F.129). If this chordwise vorticity distribution agrees with that of an infinite flat plate, the method becomes identical with WEISSINGER's method.

Theory of transsonic and supersonic flow.

A study was made of the theory of supersonic conical flow (Report F.152). By aid of this theory stability derivatives for rolling motion have been calculated for a certain swept wing in the MACH number range from a little over 1 to 1.5.

An investigation is being made about GULLSTRAND's method for the calculation of the flow about a profile in steady transsonic flow.

Oscillating aerofoils.

The calculation of aerodynamic coefficients for an oscillating wing-flap system in two-dimensional subsonic flow was continued. It was shown in report F.142 that the solution of the exact theory (TIMMAN's thesis, F.54) satisfied the POSSIO equation. For a number of values of reduced

frequency, Mach number and ratio between flap and wing chord, exact numerical results are available. These results have been interpolated toward the reduced frequency with an interval of 0.02 in the range 0 to 1 (Report F.151). Results will also be interpolated toward the chord ratio.

A strip theory was developed for the calculation of the aerodynamic forces on an oscillating swept wing of large aspect ratio (Report F.146). These forces depend only on sectional quantities and contain corrections due to the angle of sweep compared with the forces given by strip theory for a straight wing. Aerodynamic forces have been measured for a wing-flap system at low speeds. In order to compare experimental and theoretical results the influence of tunnel wall corrections has been investigated (Reports F.69, F.140).

Flutter.

The influence of compressibility on the flutter speed of a family of rectangular wings was investigated. Report F.118 contains result for a wing without flap, while in report F.147 results for a wing with flap are given.

The influence of a gust alleviator, producing flap deflection due to wing bending, on the flutter speed was investigated for a certain configuration.

Experimental supersonic flow.

Some measurements of the pressure distribution around a rotationally symmetric halfmodel in the 3×3 cm² supersonic windtunnel at increased stagnation pressure were made (Report F.133) and compared with the results obtained abroad in larger tunnels.

4. Materials and structures section.

Theoretical structures work.

The theoretical work of the department was mainly concerned with continuations of studies initiated in 1952 on the stress and deflection analysis of swept wings, plastic buckling theories on flat plates, as well as a comparison with experimental results, and the calculation of design charts for diagonal tension field webs, supplementing previously published charts.

The design charts for incomplete diagonal tension fields give the effective stresses according to HUBER's yield criterion and thus enable the determination of the range of validity of the previous charts, concerning average stresses and strains in the elastic range (Report S.427).

The work on swept wings led to an inclusion of the principal diagonal of the deflection matrix between fairly narrow limits (Report S.417). Further improvement of the computed stresses in the reinforced skin will be attempted. As a result of the literature search on plastic buckling a programme for tests with flat plates and square tubes was set up (Report S.423).

Static testing of structural components.

Shear tests were carried out on a second series of webs with lightening holes. Reports on the first test series and on torsion tests of wing leading edges, carried out in 1952, were published (Report S.413, S.421). Likewise, a report on tests to determine the effective width of 24 S-T flat plates in the plastic range was completed and a second test series on this subject was carried out. The test results led to simple design rules for determining the effective width and the load-carrying capacity (Report S.414).

A report was completed, containing the results of a qualitative study and some tests on the effective radius of aircraft tyres (Report S.428).

Fatigue.

Various fatigue investigations continued to form an important part of the research programme. Among the tests on structural components may be mentioned:

repeated load tests in tension on lugs and on riveted joints in 24 S-T alclad sheets to investigate the effect of a variation of some important design parameters (Report M.1932, M.1943);

repeated load tests in tension to investigate the effect of the fit (positive and negative clearances) of pin-hole joints on their fatigue strength;

repeated load tests in compression or three-point bending with various types of glued built-up spar booms of simple or more complicated shapes (Report M.1936).

A more investigation was concerned with the verification of the cumulative-damage hypothesis for riveted joints (Report M.1923) and simple notched and unnotched 24 S-T alclad strips.

The international collaboration on fatigue between various European laboratories, which was started in 1951, was continued, the most important event being a conference at the Aeronautical Research Institute of Sweden in Stockholm.

Rapid-loading tests.

Rapid-loading tests representative of gust or landing loads on aircraft were carried out on riveted and bolted joints in tension, strips of various weldable materials in tension (Report S.415)

and simple U-sections of the same materials in 3-point bending (Report S.430). The riveted joints showed ultimate strengths up to 15% less than the static strength; the U-sections showed a significant increase in strength compared with a static test.

Adhesives and plastics.

Apart from the tests on bonded spar booms, mentioned under "Fatigue", and a number of ad-hoc tests on bonded stiffened panels, the second part of a systematic investigation concerning the Aero Research peeling test was carried out (Report M.1940).

After the completion of a literature search on glassfiber and similar laminates a series of tests to determine the mechanical properties of glassfiberpolyester laminates was started (Report M.1917).

5 *Flight testing section.*

Stability and control.

Besides flight tests and calculations concerning several prototype and commercial aircraft, measurements have been made of the longitudinal stability and control of the Siebel laboratory-aircraft in gliding flight with feathered propellers for comparison with windtunnel measurements (Report V.1698).

The influence of the compressibility (unto a Machnumber of about 0.8) on the dynamic longitudinal stability has been studied (Report V.1648).

An investigation has been made into the cause of tightening and its connection with stability characteristics (Report V.1725).

Various.

Some model-tests on the problem of lightening hazard have been carried out. An apparatus for determining the drag of pneumatic ducts and a Machmeter calibration stand have been constructed.

Some memoranda have been drafted for AGARD on special flight-testing methods and apparatus.

The Siebel Laboratory aeroplane assisted in the droppings of food and materials during the floods in February 1953.

6 *Helicopters section.*

Assistance has been given for the drafting of airworthiness requirements for helicopters. In cooperation with the SOBEH an electrical analogue is under construction for the investigation of vibrations.

7 *Documentation and Publications.*

Central Documentation of Aeronautical Literature (C.C.L.).

Through the activities of the AGARD-Documentation Committee a cooperation has been started between the C.C.L. and the Index Aeronauticus, the Instituté of Aeronautical Sciences and the Service de Documentation et d'Information Technique Aéronautique.

With some representatives of the ASLIB Aeronautical Group the improvement of the aeronautical chapters of U.D.C. has been discussed with the object of attaining an internationally usable code. Moreover proposals have been made under auspices of the AGARD-Documentation Committee for revision of the NACA classification with the aid of the C.C.L.-classification.

Catalogue of Aerodynamic Measurements (CAM).

The interest which AGARD took in the CAM, resulted in a joint meeting of the ASLIB-Aeronautical Group and some AGARD-representatives in Cranfield, during which meeting the N.L.L. initiative was encouraged. At the following AGARD-meeting in September in London all country-members were recommended to subscribe to the catalogue. The definite manufacture of the cards was started and at the end of the year it was possible to send 400 cards to each of the 28 institutes, which had entered a subscription to the CAM at that time.

Publications.

In the September-meeting of the AGARD-Documentation Committee some recommendations were made on standardization of size and format of reports and on including catalogue cards in reports, which caused some alterations in the publishing of the N.L.L. reports.

(6) In 1953 152 reports were completed, of which the following were published:

a) *Multigraphed and ozalided reports:*

- F. 92 Bosschaart, A. C. A. Survey of some theories on lift distribution of wings with large aspect ratio. (In Dutch).
 Van de Vooren, A. I.
- F. 115 Van de Vooren, A. I. Aerodynamic coefficients of an oscillating aerofoil with a pressure-seal balanced aileron.
 IJff, J.
- F. 121 Van de Vooren, A. I. The generalization of PRANDTL's equation for yawed and swept wings.
- F. 125a De Kock, A. C. The N.L.L. card system catalogue of aerodynamic measurements.
 Van de Vooren, A. I.
- F. 127 Zaat, J. A. A one-parameter method for the calculation of the temperature-profile of laminar incompressible boundary layer flow with a pressure gradient.
- F. 129 Van de Vooren, A. I. An approach to lifting surface theory.
- F. 133 Arthur, P. D. Discussion of some hypersonic wind tunnel problems and condensation of water vapor in wind tunnels.
- F. 134 Meijer, A. W. Test at high reservoir pressure of a rotationally symmetric half model mounted on the wall of a supersonic wind tunnel.
 Arthur, P. D.
- M. 1893 Hartman, A. The peeling tests of Redux-bonded light alloy sheet. I. (In Dutch).
- M. 1917 Hartman, A. Literature search on asbestos and glass-fiber laminates. (In Dutch).
- S. 405 Benthien, J. P. On the stress analysis of swept wings. (In Dutch).
- S. 407 Besseling, J. F. On the buckling of rods and plates in the plastic region. I. Theory. (In Dutch).
- S. 409 Floor, W. K. G. Additional investigation on the failure of flat stiffened plates in diagonal tension under shear loads. (In Dutch).
- S. 411 Rondeel, J. H. Comparative fatigue tests with 24 ST Alclad riveted and bonded stiffened panels.
 Kruithof, R.
 Plantema, J. F.
- S. 413 Floor, W. K. G. Shear tests on 24 ST unstiffened and stiffened webs with flanged holes. Part I.
- S. 414 Besseling, J. F. The experimental determination of the effective width of flat plates in the elastic and the plastic range. (In Dutch).
- S. 419 Rondeel, J. H. A semi-automatrical impact testing-machine for structural components. (In Dutch).
- V. 1587 Lucassen, L. R. Take-off tests with a Tiger Moth towing a Gövier sailplane. (In Dutch).
- V. 1704 Scherpenhuijsen Literature search on all-weather approach lighting.
 Rom, G.

b) *Miscellaneous Publications:*

- MP. 75 Van de Vooren, A. I. Aerodynamic coefficients of an oscillating airfoil with control surface in two-dimensional subsonic flow. *Journal Aero. Sci.* March 1953, Vol. 20, No. 3, p. 153--159.
- MP. 78 — Reports of the N.L.L. on the collapsing stresses of thin walled cylinders and round tubes. (1941--1948).
- MP. 80 Rondeel, J. H. A solid-guide fixture for determining the compressive properties of thin-sheet materials: *Polyt. Tijdschr.* Vol. 8, No. 43/44, 27-X-1953, p. 785a. (In Dutch).
- MP. 81 Bartelink, J. A. A strain gauge leakage tester. (In Dutch). *Polyt. Tijdschr.* Vol. 8, Nr. 25/26, 13-VI-1953, p. 465a.

- MP. 82 Rondeel, J. H. Some particulars on measuring methods used in structural testing at the N.L.L. (In Dutch). *De Ingenieur*, Vol. 65, Nr. 10, 6-III-1953, p. L. 1.
- MP. 83 Plantema, F. J. Some experiences in calibrating and testing measuring instruments. (In Dutch). Lectures for the Symposium on experimental stress- and vibration analysis, Delft, 10—12 Sept. 1952.
- MP. 85 Schering, D. C. Experience with acceleration pick-ups with remote indication. (In Dutch). Lectures for the Symposium on experimental stress- and vibration analysis, Delft, 10—12 Sept. 1952.
- MP. 86 Timman, R. General principles of boundary layer theory. (In Dutch). *De Ingenieur*, Vol. 64, Nr. 13 (28-III-52), p. L 6.
- MP. 87 Rondeel, J. H. A simple method of measuring angular deformations by means of the Moré-effect. (In Dutch). Lectures for the Symposium on experimental stress- and vibration analysis, Delft, 10—12 Sept. 1952.
- MP. 88 Rondeel, J. H. An apparatus for determining the compressive stress-strain curve of thin-sheet materials. (In Dutch). Lectures for the Symposium on experimental stress- and vibration analysis, Delft, 10—12 Sept. 1952.
- MP. 89 Scherpenhuijsen Rom, G. The practice of a general abstracting service compared with some practice of special documentation. (Lecture Cranfield, 1953).
- MP. 90 Scherpenhuijsen Rom, G. General and special documentation problems in aeronautics. *T.N.O.-Nieuws*, Vol. 8, nr. 7, p. 231, June 1953. (In Dutch).
- MP. 91 De Jager, E. M. Van Spiegel, E. Bemerkung zur Lösung von Integralgleichungen aus der Tragflügeltheorie.
- MP. 92 Hengeveld, J. F. Summary of test program for M. S. Kungsholm by the N.L.L. (In Dutch). *Schip en Werf*.
- MP. 101 Marx, A. J. Dynamic stability research and testing in the U.S.A.; artificially stabilised flight. (In Dutch). *De Ingenieur*, Vol. 65, Nr. 49 (4-XII-1953), p. L 35.
- MP. 102 Pool, A. Schedule for determining airspeed, altitude and ambient air temperature. (In Dutch). *De Ingenieur*, Vol. 65, Nr. 49 (4-XII, 1953), p. L 41.

REPORT A. 1263.

Experiments on the Two-Dimensional Flow over a N.A.C.A. 0018 Profile at High Angles of Attack

by

H. WIJCKER.

Summary.

Pressure distributions over the surface of a model with N.A.C.A. 0018 profile in two-dimensional flow were measured at a Reynolds number of about 2.7×10^6 . Transition points were found by the liquid film method and separation phenomena were studied mainly with the aid of tufts.

The lift coefficients at high angles of attack were calculated for a model with aspect ratio 6.

The influence of the tunnel walls on the pressure distribution over the suction side was determined theoretically.

Contents.

- 1 Introduction.
- 2 Lift measurements.
- 3 The transition point.
- 4 Turbulent separation and stalling.
- 5 Comparison of theory and experiment.
- 6 References.

Appendix I. Calculation of the lift at high angles of attack for an aspect ratio $\Lambda = 6$.

Appendix II. Influence of tunnel walls on the pressure distribution.

3 tables.

14 figures.

1 Introduction.

In order to check ZAAT's method for the calculation of the separation point of a turbulent boundary layer (ref. 1), some experiments were carried out on a cylindrical model with N.A.C.A. 0018 profile at high angles of attack and at a REYNOLDS number of about 2.7×10^6 . The model had a chord of 0.6 m and a height of about 2 m. It extended from the floor to the ceiling of the test section of tunnel 3 of the N.L.L., the vertical walls of which are 3 m apart. The intensity of the turbulence at the test section of the empty tunnel is about $3\frac{1}{2}\%$.

The lift was calculated from the measured pressure distribution over the surface of the model,

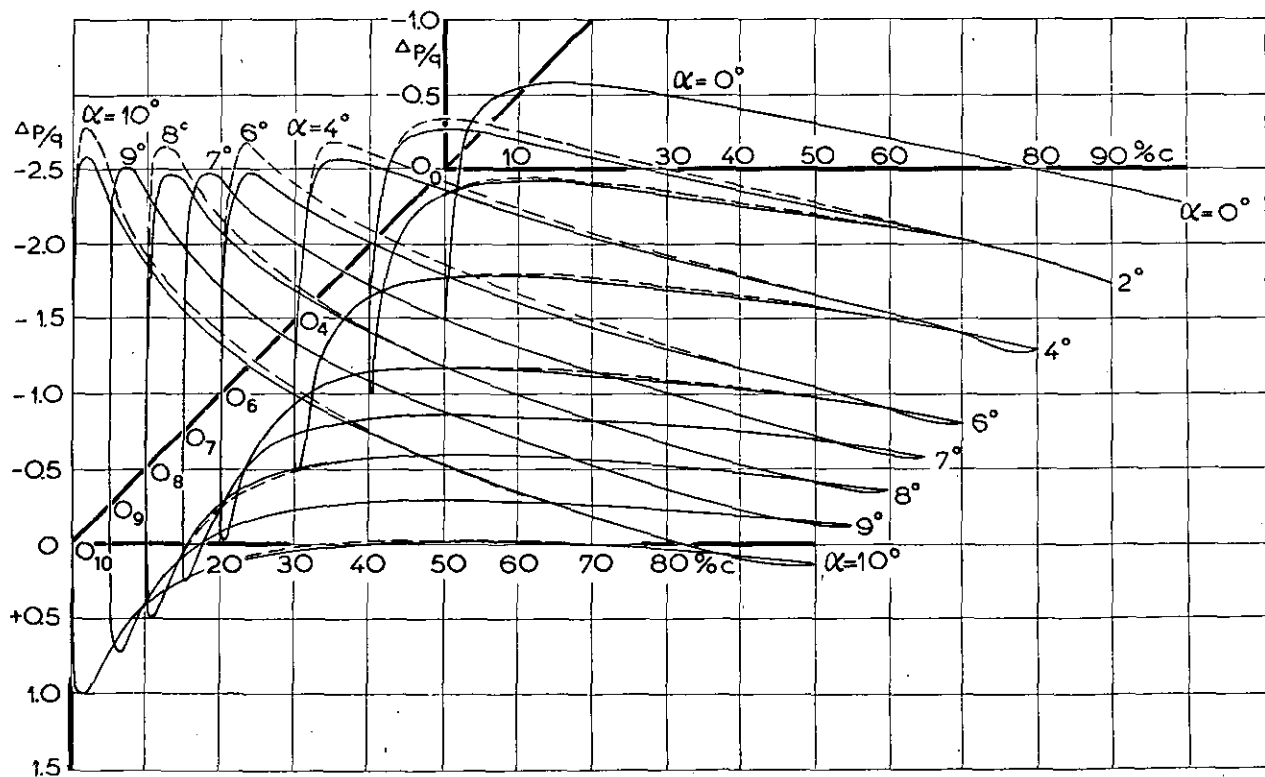


Fig. 1a

Pressure distribution along the chord of a N.A.C.A. 0018 profile at $Re = 2.7 \times 10^6$.
(For legend p. t. o.)

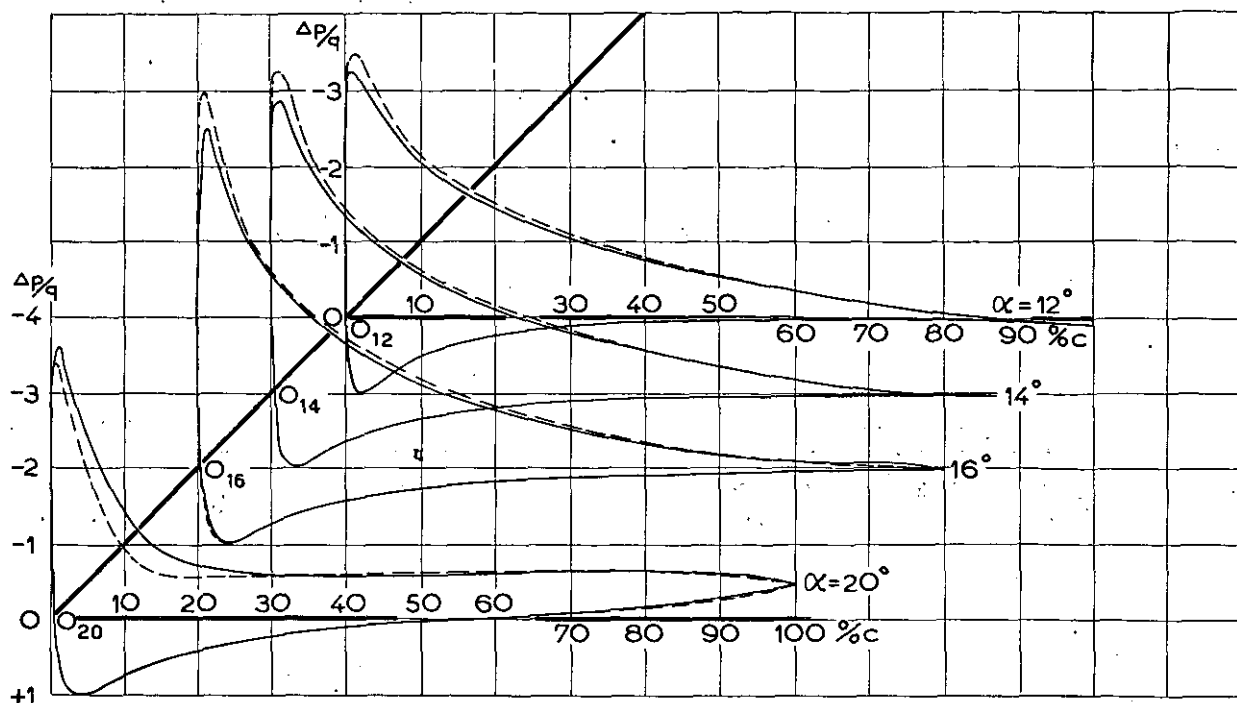


Fig. 1b

Pressure distribution along the chord of a N.A.C.A. 0018 profile at $Re = 2.7 \times 10^6$.

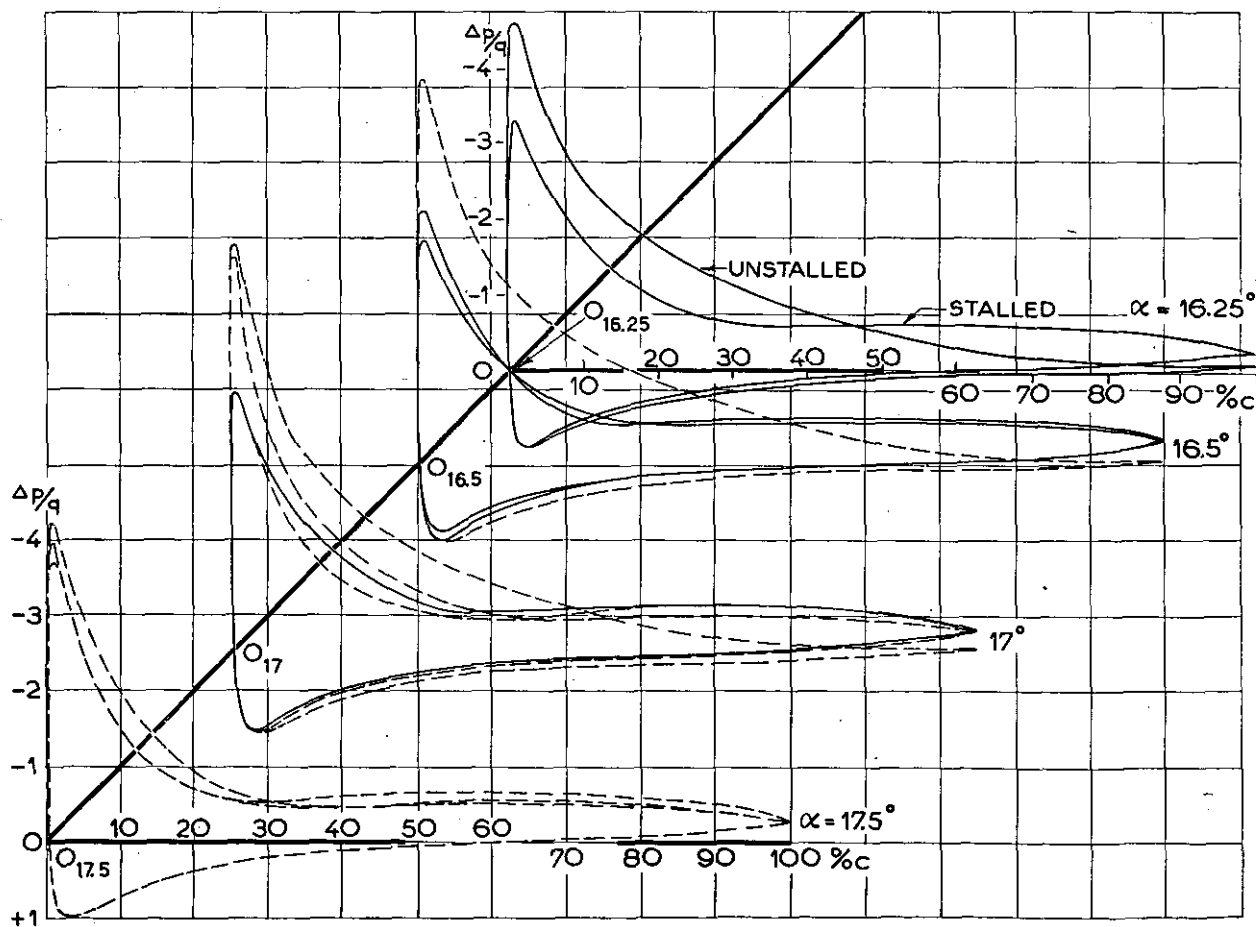


Fig. 1c

Pressure distribution along the chord of a N.A.C.A. 0018 profile at $Re = 2.7 \times 10^6$.

Legend:

— The left side of the model is suction side

- - - The right side of the model is suction side

h = total head; p = static pressure; $p(\infty)$ = static pressure at infinity

q = dynamic pressure at infinity; $\Delta p = p - p(\infty) = p - h + q$

O_α = origin of the coordinates at α° angle of incidence

the transition point was determined by the liquid film method (ref. 2) and separation phenomenae were studied mainly with the aid of tufts.

The experiments were performed on behalf of the "Nederlands Instituut voor Vliegtuigontwikkeling" (Netherlands Aircraft Development Board).

2 Lift measurements.

The lift was calculated from the measured pressure distribution along the chord 90 cm from the tunnel floor (fig. 1). Though the tunnel floor and ceiling introduced strong secondary flows over the surface of the model (fig. 3a), it may be assumed, that the pressure distribution in the middle part of the model is hardly influenced by them (ref. 3).

The lift coefficients C_L are given in fig. 2. In order to get a better approximation to the free flow value, α , the angle of attack in the tunnel, is usually corrected (ref. 3, vol. III, p. 301). In the case on hand, however, these corrections were smaller than 0.1° for the whole range of measured lift coefficients and have therefore been omitted. Some asymmetry in the model and the tunnel flow caused differences between the lift coefficients at corresponding positive and negative angles of incidence.

In the stalled flow condition C_L fluctuates with time; only a few instantaneous values are given.

$C_{L, \max}$, the maximum value of C_L , and the corresponding angle of incidence α_m , are compared with those, found in several N.A.C.A. reports (table 1).

All N.A.C.A. measurements; however, were carried out with a model with an aspect ratio $\Lambda = 6$. From this, α was corrected with the aid of the formula given on p. 10 of ref. 5, leaving C_L constant, in order to get values for infinite aspect

ratio. This formula only holds for a linear C_L - α relation and therefore the values of $C_{L, \max}$ and α_m for infinite aspect ratio, given in the N.A.C.A. reports, referred to in table 1, have to be rejected.

In order to be able to make a comparison, the C_L - α relation for $\Lambda = 6$ has been calculated from the measurements for $\Lambda = \infty$ using MULTHOPP's

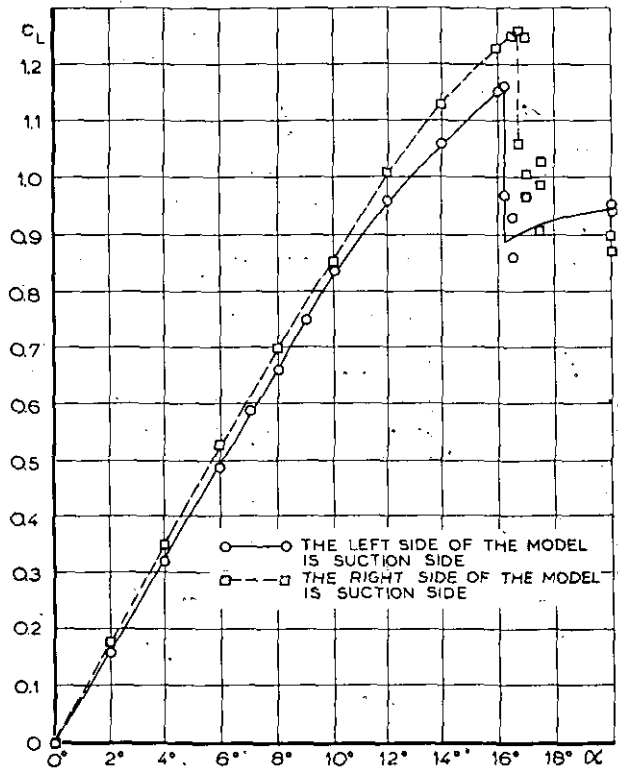


Fig. 2

C_L as a function of α for a two-dimensional model with N.A.C.A. 0018 profile at $Re = 2.7 \times 10^6$.

TABLE 1.

Maximum lift coefficient $C_{L, \max}$ and stalling angle α_m for a cylindrical aerofoil with N.A.C.A. 0018 profile.

Source	Aspect Ratio Λ	$10^{-6} Re$	$C_{L, \max}$	α_m	Tunnel
N.A.C.A. Rep. 460 fig. 8	6	3.15	1.5	23°	V.D.T. = Variable
	$(6 \rightarrow) \infty^*)$		1.5	17.5°	Density Tunnel
N.A.C.A. Rep. 586 fig. 5	$(6 \rightarrow) \infty$	2.97	1.43	17°	V.D.T.
		2.36	1.43	17°	
		1.25	1.33	16.5°	
		0.65	1.28	15.5°	
N.A.C.A. Rep. 647 fig. 9	6	3.4	1.30	18.5°	Full Scale Tunnel
N.A.C.A. Rep. 669 fig. 34	6	3.33	1.34	21°	V.D.T.
		7.84	1.43	21.5°	
N.L.L. Rep. A. 1263 fig. 2	∞	2.7	1.26	16.8°	N.L.L. Tunnel No. 3
			1.16	16.3°	
	$(\infty \rightarrow) 6$		1.05	17.9°	

*) $(6 \rightarrow) \infty$ means, that the value for infinite aspect ratio is derived from the measured one at $\Lambda = 6$.

method (ref. 6), the experimental stalling contours given in ref. 7 and the flow characteristics of fig. 3b (see appendix I). The result is line III of fig. 6 on page A.7. The values of $C_{L, \max}$ and α_m from this line are inserted in table 1. Though the shape of line III of fig. 6 resembles that of line IV closely, (line IV gives experimental results of N.A.C.A. measurements (ref. 7)), the differences in $C_{L, \max}$ and α_m are evident. These differences can not be explained as being due to the influence of the tunnel walls on the pressure distribution; on the contrary, calculations, carried out in appendix II, show, that this influence consists of a flattening of the pressure curve over the suction side, so that separation is delayed. That means, one may expect somewhat higher values of $C_{L, \max}$ and α_m in the tunnel than in free flow. However, in the cases under consideration the flattening effect of the tunnel walls on the pressure distribution appears to be extremely small (fig. 10 gives the differences $\Pi_s - \Pi_{s,z}$ of the calculated static pressure coefficients in free flow and in tunnel flow (additional suffix z) as well as the differences of their gradients along the chord). It may be pointed out that the difference in $C_{L, \max}$ or α_m between the lines III and IV, of fig. 6 does not deviate much from the difference in $C_{L, \max}$ or α_m between the lines I and II. So, if the C_L - α -line for $\Lambda = 6$ would have been calculated from line II, the resulting line might have been in close agreement with line IV.

3 The transition point.

Transition points, as obtained by the liquid film method (ref. 2), are given in fig. 3b. At high angles of attack transition may be preceded by laminar separation, in which case the liquid film method indicates the point, where the main flow, turbulent now, rejoins the surface.

4 Turbulent separation and stalling.

Originally an attempt was made to get some information about regions of separated flow from the speed of evaporation of a liquid rubbed onto the surface. Following ref. 8 the movement of the lines, separating wet and dried parts of the surface, may give the required information in a number of cases. The experiments, however, failed, probably because the variation of drying time with place in the explored regions is small compared with the variations introduced by inequality of the thickness of the liquid layer over the surface.

Therefore we passed over to the usual technique with tufts, neglecting the influence of the tufts on the flow.

The following observation were made:—

For those cases, in which the turbulent boundary layer separates from the surface at $\alpha < \alpha_m$ (α_m is the angle of attack at which C_L is a maximum), the separation point does not fluctuate appreciably with time, nor does the pressure at any point whatsoever. So C_L is constant with time.

For $\alpha > \alpha_m$ stalling occurs. The separation point moves irregularly to and fro along a region of the

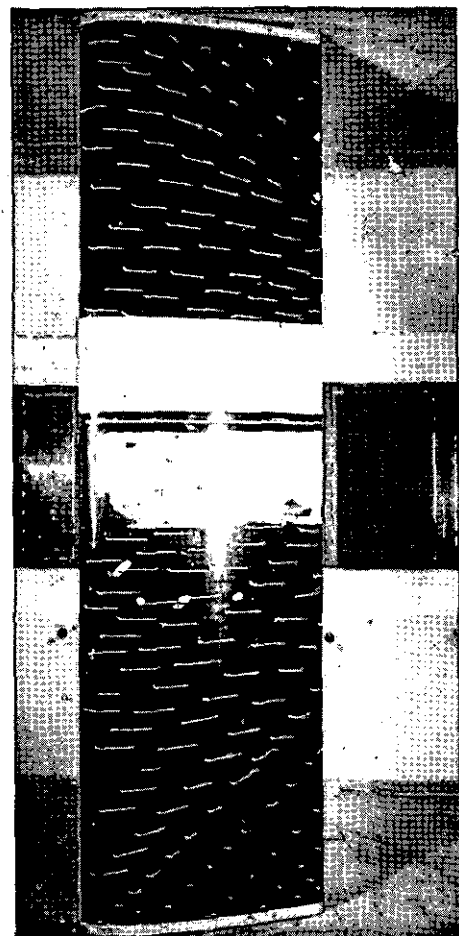
chord, that will be called the "swept over region"; the changes with time in the pressure distribution may be considerable and the changes in C_L as well. From the movements of the tufts an estimation has been made of the place and extent of the swept over region, the outer points of which could be defined only to the nearest 5 % chord (fig. 3b). The results for the case, where the left side of the model (fig. 3a) is the suction side, are given in fig. 3b. It is questionable, whether the position of the separation point on the middle part of the model will be the same with and without strong secondary flows on the upper and the lower part.

For very small positive values of $\alpha - \alpha_m$ separation took place at the back of the swept over region nearly continually, only now and then the separation point moved forward. For higher values of $\alpha - \alpha_m$, the separation mostly took place in the front region of the swept over region; occasionally it moved back.

A vortex indicator (ref. 9) was placed at a distance z from the plane through the chord and the trailing edge at the suction side of the model.

Fig. 3

Flow characteristics on a two-dimensional model with N.A.C.A. 0018 profile at $Re = 2.7 \times 10^5$ in a tunnel with about $3\frac{1}{2}\%$ turbulence intensity.



Direction of flow.

Fig. 3a

Left hand side of the model. $\alpha = 12^\circ$.

The projection of the indicator on this plane lay about 20 cm behind the trailing edge.

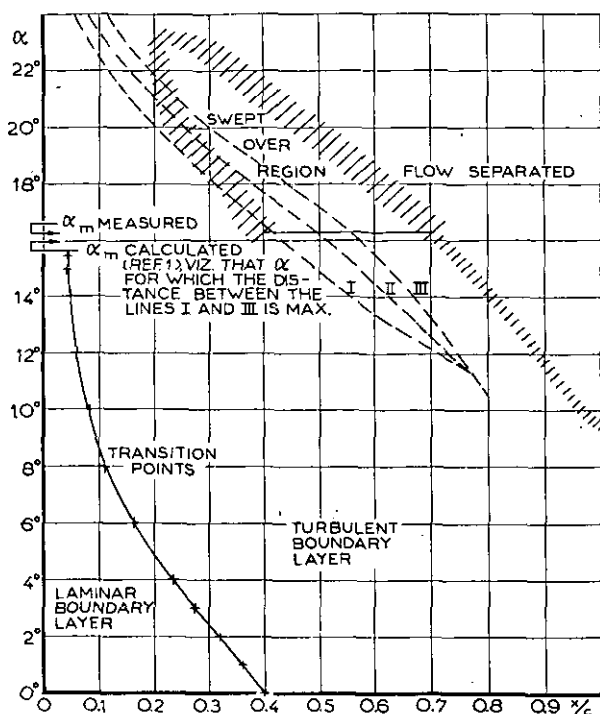


Fig. 3b

The left hand side of the model is suction side.

- I points, where $dH/d(s/c)$ has a maximum following ref. 1.
- II points, where $dH/d(s/c)$ has a minimum following ref. 1.
- III points, where $dH/d(s/c)$ becomes very large following ref. 1.
- α_m is the value of α for which $C_L = C_{L,max}$

For small positive values of $\alpha - \alpha_m$ the following behaviour of the indicator was observed:—

- 1st for small values of z the blade wheel of the indicator turned round continually;
- 2nd for high values of z it did not move at all;
- 3rd for intermediate values of z it started and stopped alternately.

Correlation between either rotation or non rotation of the blade wheel and the position of the separation point was not very marked. Only for those cases in which the time interval, during which the separation point stayed at one of the outer points of the swept over region of the chord, was rather long, the following correlation seemed to occur:—

When the separation point stayed as close as possible either to the leading edge or to the trailing edge, the blade wheel respectively moved and was stationary during the greater part of the time interval.

5 Comparison of theory and experiment.

ZAAT has obtained a number of theoretical results (ref. 1), which may be compared with the results of the measurements given in this report. As for the pressure distributions, ZAAT himself has already compared the calculated ones with those given in fig. 1. The agreement is reasonable.

Furthermore ZAAT found, that for α greater than some value between 10° and 12° the gradient

$dH/d(s/c)$ along the surface (H = ratio of displacement thickness to momentum thickness, s the distance from the leading edge of the point considered, measured along the surface) first increases with increasing s , then decreases and finally increases rapidly to very great values (ref. 1, fig. 6). The value of s , at which the line $dH/d(s/c)$ versus s has a vertical asymptote, is the abscissa of the separation point. For $\alpha = 10^\circ$ the maximum and minimum were missing, but a vertical asymptote existed already.

Lines I, II and III of fig. 3b give the points of the maximum, minimum and vertical asymptote, obtained by ZAAT, versus α (the coordinates of ref. 1 are reduced to x/c).

It appears, that the calculated values of the separation points (line III) lay about 15 % nearer to the leading edge than the measured values; the gradients of the lines, however, are very much the same.

Line I, the line of the maxima, coincides with the forward boundary of the swept over region at $\alpha = \alpha_m$. Though the directions of the two lines are somewhat different, the deviations are unimportant.

The agreement of calculated and measured values is surprisingly good, considering the inaccuracies involved both in measurements and theoretical method.

ZAAT reasoned that the distance between the maximum and the asymptote is maximum for the stalling angle α_m (the distance between maximum and minimum appeared to be greatest for $\alpha = \alpha_m$ as well). From this he found that $\alpha_m = 16^\circ$. The measured value was $16\frac{1}{4}^\circ$ if the left side and $16\frac{3}{4}^\circ$ if the right side of the model was the suction side. A very good agreement again between theory and experiment.

The fluctuations of the separation point may be explained as follows:—

During the formation of a vortex behind the dead region (ref. 1) the separation point moves forward. If the vortex is carried away, the blade wheel of the vortex indicator, placed at an intermediate value of z (z = distance from the plane through leading and trailing edge), will turn round. If the separation point stays in its forward position for a longer time, it is believed, that a series of strong vortices is formed behind the dead region and carried along with the flow, so that the blade wheel turns round continuously. As long as the separation point is in its rear position, however, the flow does not carry along such strong vortices and the wake is smaller, so that the blade wheel of the vortex indicator in its intermediate- z -position is not hit by vortices and does not revolve.

So the behaviour of the indicator, described in § 4, though not being extremely expressive, supports ZAAT's explanation of the fluctuations of the separation point reasonably well.

6 References.

1. ZAAT, J. A. The Calculation of the Point of Turbulent-Boundary-Layer Separation on a N.A.C.A. 0018 Profile and the Determination of the Optimum Angle of Incidence. N.L.L. report F.89.

2. GRAY, W. E. A Simple Visual Method of Recording Boundary Layer Transition (Liquid Film). A.R.C. Techn. Note Aero 1816 (1946).
3. MENDELSON, R. A. and POLHAMUS, J. E. Effect of the Tunnel-Wall Boundary Layer on Test Results of a Wing Protruding from a Tunnel Wall. N.A.C.A. Techn. Note 1244.
4. DURAND, W. F. Aerodynamic Theory; Springer 1935.
5. JACOBS, E. N. and ABBOTT, I. A. The N.A.C.A. Variable-Density Wind Tunnel. N.A.C.A. Rep. 416.
6. MULTHOFF, H. Die Berechnung der Auftriebsverteilung von Tragflügeln. Luftfahrt Forschung 1938, S. 153.
7. GOETT, H. J. and BULLIVANT, W. K. Tests of N.A.C.A. 0009, 0012 and 0018 Airfoils in the Full-Scale Tunnel. N.A.C.A. Rep. 647.
8. WEIKER, H. Survey of Transition Point Measurements at the N.L.L., Mainly for Two-Dimensional Flow over a N.A.C.A. 0018 Profile. N.L.L. Rep. A. 1269.
9. ZWAANEVELD, J. About a vortex-indicator and the possible development of a vortex-intensity gauge (in Dutch). N.L.L. Report A. 1231.
10. GLAUERT, H. The Elements of Aerofoil and Airscrew Theory, Cambridge Univ. Press 1947.
11. KNOFF, K. Theorie und Anwendung der unendlichen Reihen. Springer 1931.
12. ABBOTT, I. H., VON DOENHOFF, A. E. and STIVERS, L. S. Summary of Airfoil Data. N.A.C.A. Rep. 824.

APPENDIX I.

Calculation of the lift at high angles of attack for an aspect ratio $\Lambda = 6$.

The lift L of an aerofoil can be calculated from the formula

$$L = \rho V \int_{-\frac{1}{2}s}^{+\frac{1}{2}s} \Gamma dy \quad (I-1)$$

in which s = span, Γ = circulation per unit of length, y = coordinate in the direction of the span, V = velocity, ρ = density.

As $c_L = L/\frac{1}{2} \rho V^2 c s$ (we shall write c_L for the lift-coefficient of an aerofoil with finite aspect ratio $\Lambda = s/c$, C_L for the two-dimensional lift coefficient ($\Lambda = \infty$)), we find for a symmetrical aerofoil with constant chord c

$$c_L = \Lambda \int_{-1}^1 \gamma d\eta \quad (I-2)$$

in which $\gamma = \Gamma/Vs$ and $\eta = y/\frac{1}{2}s$ ($-1 \leq \eta \leq 1$).

Once C_L versus α is known, the calculation of γ for the case when the span is normal to the velocity, may be based on the following formulae (ref. 10, p. 137)

$$\gamma = \frac{1}{2\Lambda} C_L(\alpha_{\text{eff}}.)$$

$$\alpha_{\text{eff.}} = \alpha - \alpha_{\text{ind.}}$$

$$\alpha_{\text{ind.}} = w/V =$$

$$= \frac{1}{4\pi V} \int_{-\frac{1}{2}s}^{+\frac{1}{2}s} \frac{(d\Gamma/dy') dy'}{y - y'} = \quad (I-3)$$

$$= \frac{1}{2\pi} \int_{-1}^1 \frac{(d\gamma/d\eta') d\eta'}{\eta - \eta'}$$

Here eff. = effective, ind. = induced, w = induced velocity (negative in the direction of the lift), $C_L(\alpha_{\text{eff.}})$ means C_L as a function of $\alpha_{\text{eff.}}$.

MULTHOFF (ref. 6) has worked out a method of calculation, which may be used also for the case, when C_L is not proportional to $\alpha_{\text{eff.}}$. However, one element of the method is the intersection of a line PQ with the C_L - α -line (fig. 4) and this

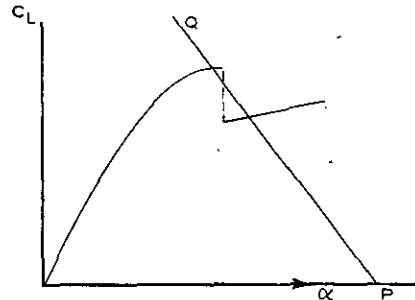


Fig. 4

may lead to more than one solution. Indeed, for a number of α 's it appeared possible to get consistent solutions following MULTHOFF's method with an arbitrary choice of y^* in a certain region along the span. Herein y^* is the value of y for that cross section, which separates the stalled flow from the unstalled one. It must be pointed out, that of the mutual influences of the flow in a neighbouring cross section only the influence due to the induced velocity has been taken into account; the other influences have been neglected, so that velocity components in the direction of the span have not been considered.

In order to be able to carry out calculations for an aerofoil with $\Lambda = 6$, we used values of y^* , derived from experiments in the following way:—

Fig. 13 of ref. 7 gives stalling contours of an aerofoil with N.A.C.A. 0018 profile and $\Lambda = 6$ at $Re = 3.10^6$. This REYNOLDS-number is nearly the same as that at which our measurements were carried out (viz. 2.7×10^6). From fig. 3 of this report we conclude, that $\alpha > \alpha_m$ for those cross sections, for which the separated flow extends to more than 30 % chord from the trailing edge. So drawing lines parallel to the trailing edge at a distance of 30 % in fig. 13 of ref. 7 (fig. 5b), one finds the value of y^* from the intersection of this line with the given stalling contours. Fig. 5b gives $\eta^* = y^*/\frac{1}{2}s$ versus α .

The values of γ are given in table 2 on page A 8. In order to be able to draw graphs γ vs η (fig. 5a), the following considerations have to be taken into account:—

1st γ must be a continuous function of η . A discontinuity would mean, that a concentrated vortex leaves the surface. This vortex would induce velocities, which tend to infinity in the neighbourhood of the vortex. So from physical point of view a discontinuity of γ has to be excluded.

2nd $d\gamma/d\eta$ must be a continuous function of η . Assuming a discontinuity for $\eta = \eta_a$, $d\gamma/d\eta$ can be considered as the sum of two functions,

a continuous function $(d\gamma/d\eta)_1$ and a discontinuous function $(d\gamma/d\eta)_2$ which will be as-

Fig. 5a. Distribution of the dimensionless circulation $\gamma = \Gamma/sV$ along the span for an aerofoil with N.A.C.A. 0018 profile and aspect ratio $= 6$ calculated from the drawn C_L vs α -line of fig. 2.

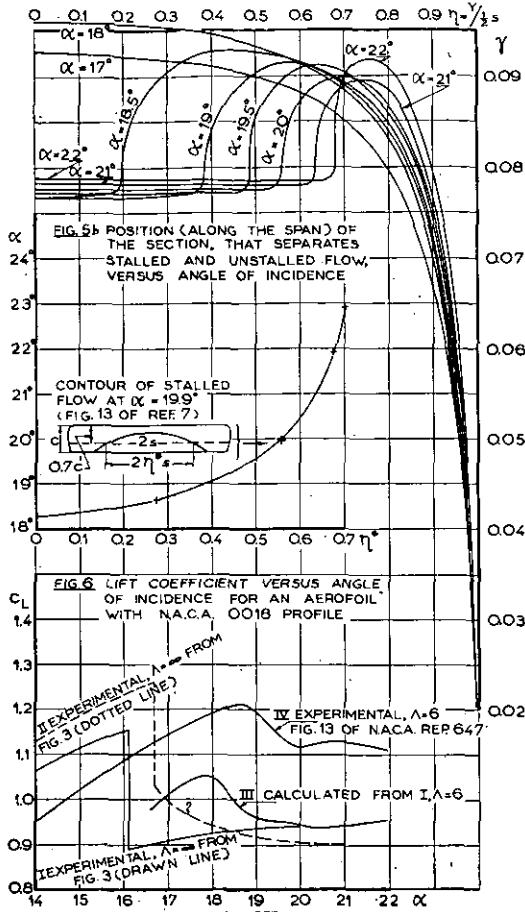


Fig. 5 and 6

sumed to be zero for $\eta > \eta_d$ and $\eta < -\eta_d$ and to have a constant value c for $-\eta_d < \eta < \eta_d$.

Then $\alpha_{ind.} = \frac{1}{2\pi} \int_{-1}^1 \frac{(d\gamma/d\eta') d\eta'}{\eta - \eta'}$ will contain

the term $\frac{c}{2\pi} \ln \frac{\eta + \eta_d}{\eta - \eta_d}$, which tends to infinity if η approaches either η_d or $-\eta_d$. So from physical point of view a discontinuity of $d\gamma/d\eta$ is impossible.

3rd $\alpha_{eff.}$ shows a discontinuity, if the C_L - α -graph shows a discontinuity. For, assuming that there is no discontinuity, $\alpha_{eff.}$ would decrease continuously from $\alpha_{eff.} > \alpha_m$ to $\alpha_{eff.} < \alpha_m$ for increasing $|\eta|$. So the C_L - η -graph would show a discontinuity and, as $\gamma = C_L/2\Lambda$, the γ - η -graph as well. This is in contradiction with the 1st point.

4th The γ - η -graph has a point of inflexion with vertical tangent where $\alpha_{eff.}$ shows a discontinuity. $\alpha_{eff.}$, and as a consequence w have discontinuities for $\eta = \eta^*$ and $\eta = -\eta^*$, in which

$$\frac{w(\eta^* - 0) - w(\eta^* + 0)}{V} = \frac{w(-\eta^* + 0) - w(-\eta^* - 0)}{V} = a, \text{ say.} \quad (\text{I-4})$$

We separate both w and $d\gamma/d\eta$ into two parts:

$$\left. \begin{aligned} w &= w_1 + w_2 \\ d\gamma/d\eta &= d\gamma_1/d\eta + d\gamma_2/d\eta \end{aligned} \right\} \quad (\text{I-5})$$

in such a way, that

$$w_i/V = \frac{1}{2\pi} \int_{-1}^1 \frac{(d\gamma_i/d\eta) d\eta'}{\eta - \eta'} \quad (i=1, 2) \quad (\text{I-6})$$

and

$$\begin{aligned} w_2 &= -bV & \text{for } -1 \leq \eta < -\eta^* \text{ and for } \eta^* < \eta \leq 1 \\ w_2 &= -bV + aV & \text{for } -\eta^* < \eta < \eta^* \end{aligned} \quad (\text{I-7})$$

The constant b will be chosen later.

By choosing w_2 following (I-7), w_1 will be a continuous function of η .

Now we introduce the new coordinate ϑ where

$$\eta = -\cos \vartheta. \quad (\text{I-8})$$

Then formula (I-6) becomes

$$w_i(\vartheta)/V = \frac{1}{2\pi} \int_0^\pi \frac{(d\gamma_i/d \cos \vartheta') \sin \vartheta' d\vartheta'}{\cos \vartheta' - \cos \vartheta} \quad (i=1, 2). \quad (\text{I-9})$$

Expansion of $w_2(\vartheta)/V$ in FOURIER series with period π gives

$$w_2(\vartheta)/V = \sum_{n=1}^{\infty} -\frac{2a}{n\pi} \sin 2n\vartheta^* \cos 2n\vartheta. \quad (\text{I-10})$$

Here the constant term for $n=0$ has been chosen zero, which is the case for

$$b = (1 - 2\vartheta^*/\pi)a.$$

From (I-9) and (I-10) it follows that

$$\begin{aligned} d\gamma_2/d \cos \vartheta' &= \sum_{n=1}^{\infty} \frac{4a}{n\pi} \sin 2n\vartheta^* \sin 2n\vartheta' = \\ &= \sum_{n=1}^{\infty} \frac{2a}{n\pi} \{ \cos 2n(\vartheta' - \vartheta^*) - \cos 2n(\vartheta' + \vartheta^*) \} \end{aligned} \quad (\text{I-11})$$

which may be easily verified with the aid of the definite integral

$$\int_0^\pi \frac{\cos n\vartheta' d\vartheta'}{\cos \vartheta' - \cos \vartheta} = \pi \frac{\sin n\vartheta}{\sin \vartheta} \quad (\text{ref. 10, p. 93})$$

Using the formula

$$\sum_{n=1}^{\infty} \frac{\cos nx}{n} = -\ln \left(2 \sin \frac{x}{2} \right) \quad (\text{e.g. ref. 11, p. 390})$$

and omitting the dash of ϑ , formula (I-11) leads to

$$d\gamma_2/d \cos \vartheta = \frac{2a}{\pi} \ln \frac{\sin(\vartheta + \vartheta^*)}{\sin(\vartheta - \vartheta^*)} \quad (\text{I-12})$$

From (I-12) it follows, that $d\gamma_2/d \cos \vartheta$ becomes arbitrarily large if ϑ approximates either ϑ^* or $\pi - \vartheta^*$.

TABLE 2.

Circulation coefficient $\gamma = \Gamma/Vs$ versus $\eta = y/(1/2 s)$ and α for an aerofoil with N.A.C.A. 0018 profile and aspect ratio 6
(Centre line of the model : $\eta = 0$).

$\alpha \backslash \eta$	0.9952	0.9808	0.9569	0.9239	0.8819	0.8315	0.7730	0.7071	0.6344	0.5556	0.4714	0.3827	0.2903	0.1951	0.0980	0
17°	—	0.0361	—	0.0615	—	0.0769	—	0.0849	—	0.0892	—	0.0913	—	0.0924	—	0.0928
18°	—	0.0378	—	0.0647	—	0.0806	—	0.0886	—	0.0925	—	0.0948	—	0.0958	—	0.0958
18.5°	0.0203	0.0384	0.0536	0.0658	0.0749	0.0815	0.0859	0.0889	0.0909	0.0923	0.0928	0.0928	0.0900	0.0783	0.0768	0.0767
19°	0.0208	0.0392	0.0545	0.0667	0.0759	0.0823	0.0867	0.0893	0.0909	0.0917	0.0894	0.0783	0.0768	0.0767	0.0766	0.0767
19.5°	0.0213	0.0400	0.0558	0.0682	0.0773	0.0837	0.0878	0.0902	0.0914	0.0894	0.0784	0.0773	0.0773	0.0771	0.0772	0.0772
20°	0.0216	0.0406	0.0565	0.0690	0.0781	0.0843	0.0883	0.0900	0.0886	0.0784	0.0775	0.0775	0.0775	0.0775	0.0775	0.0775
21°	0.0224	0.0420	0.0584	0.0709	0.0801	0.0860	0.0895	0.0888	0.0789	0.0782	0.0783	0.0783	0.0783	0.0783	0.0783	0.0783
22°	0.0233	0.0437	0.0608	0.0740	0.0832	0.0886	0.0918	0.0908	0.0792	0.0785	0.0787	0.0787	0.0788	0.0787	0.0788	0.0788

The double line separates the stalled part (below at the right) from the unstalled one, following fig. 5 b.

TABLE 3.

Pressure distributions and their gradients over the suction side of a N.A.C.A. 0018 profile in tunnel flow (suffix z) and free flow (no suffix) at angles of attack $\alpha = 10^\circ$ and $\alpha = 16^\circ$. (Π = dynamic pressure coefficient, Π_s = static pressure coefficient).

% chord from leading edge	Π_z from fig. 1		Π calculated from (II-23)		$\Pi_s - \Pi_{s,z}$		% chord from leading edge	$d\Pi_{s,z}/d(x/c)$		$d\Pi_s/d(x/c)$		$\frac{d\Pi_s}{d(x/c)}$	
	$\alpha = 10^\circ$	$\alpha = 16^\circ$	$\alpha = 10^\circ$	$\alpha = 16^\circ$	$\alpha = 10^\circ$	$\alpha = 16^\circ$		$\alpha = 10^\circ$	$\alpha = 16^\circ$	$\alpha = 10^\circ$	$\alpha = 16^\circ$	$\alpha = 10^\circ$	$\alpha = 16^\circ$
0	0.60	2.00	0.5988	1.9982	0.0012	0.0018							
5	3.29	4.39	3.2890	4.3904	0.0010	0.0004	7.5	9.2	17.2	9.198	17.210	-0.002	0.010
10	2.83	3.53	2.8291	3.5299	0.0009	0.0001	15	4.9	9.0	4.903	9.011	0.003	0.011
20	2.34	2.63	2.3388	2.6288	0.0012	0.0012	25	3.4	5.2	3.404	5.209	0.004	0.009
30	2.00	2.11	1.9984	2.1079	0.0016	0.0021	35	2.5	3.3	2.503	3.306	0.003	0.006
40	1.75	1.78	1.7481	1.7773	0.0019	0.0027	45	2.2	2.6	2.203	2.606	0.003	0.006
50	1.53	1.52	1.5278	1.5167	0.0022	0.0033	55	1.8	2.0	1.802	2.003	0.002	0.003
60	1.35	1.32	1.3476	1.3164	0.0024	0.0036	65	1.6	1.4	1.601	1.403	0.001	0.003
70	1.19	1.18	1.1875	1.1761	0.0025	0.0039	75	1.6	0.9	1.601	0.903	0.001	0.003
80	1.03	1.09	1.0274	1.0858	0.0026	0.0042	85	1.2	0.2	1.201	0.204	0.001	0.004
90	0.91	1.07	0.9075	1.0654	0.0025	0.0046	95	0.6	0.9	0.601	0.901	0.001	0.001
100	0.85	0.98	0.8474	0.9753	0.0026	0.0047							

APPENDIX II.

Influence of tunnel walls on the pressure distribution.

The influence of the tunnel walls is a curvature of the flow in which the model is placed. In order to calculate this influence, the z -plane of the tunnel flow is transformed to the ζ -plane, in which this curvature is reduced to zero. The dynamic pressure ratio of corresponding points of z - and ζ -plane is calculated. Then the dynamic pressure over the contour in the ζ -plane is known from the dynamic pressure, measured in the tunnel. The profile in the ζ -plane, however, is cambered. The camber is calculated as well as the contribution of this camber to the dynamic pressure. By subtracting the latter from the dynamic pressure in the ζ -plane, the dynamic pressure over the contour of the profile in free flow is obtained.

The following nomenclature will be used:

A_1, A_2	constants (see II-3).
B	tunnel-width (3 m).
c	chord of the model in the tunnel (0.6 m).
c^*	chord of the transformed profile (in ζ -plane).
C	$=4HU \cos \alpha$.
C_L	lift coefficient.
f, f_1, f_{P_1}, f_{P_2}	coefficients (see II-5).
H	constant (see II-9a).
i	$\sqrt{-1}$.
$\Delta P_z, \Delta P_\zeta$	dynamic pressure in z - and ζ -plane.
U	velocity at infinity.
\bar{u}, \bar{v}	see definition of w .
u, v	components of $V \rightarrow U$ for flow over a flat plate.
\bar{u}, \bar{v}	components of $V \rightarrow U$ for flow over a cambered plate.
V	velocity over surface of a profile in infinite parallel flow.
\bar{V}, \bar{V}	V for a flat plate and a cambered plate.
V_z	velocity over the surface of a model in the tunnel.
V_ζ	velocity over the contour of the profile in the ζ -plane.
w	$=u + iv$, complex velocity in the z -plane.
w^*	$=u - iv$.
x, y	coordinates in z -plane.
x^*, y^*	coordinates in ζ -plane following fig. 11.
X, Y	$=\pi x/B$ and $\pi y/B$.
z	$=x + iy$ (z -plane).
α	angle of incidence in z -plane.
$\Delta \alpha$	difference of angles of incidence in ζ - and z -plane.
β	angle between chord and tangent of the mean line.
γ	$=\Gamma/4BU$ (Mind that γ is not a vorticity/area).
$\bar{\gamma}, \bar{\gamma}$	vorticity per unit length and width of a flat plate and a cambered plate.
Γ	circulation per unit length of span.
δ	$=\pi z/2B$.
ζ	$=\xi + i\eta$, complex coordinate in ζ -plane.

ζ^*	$=\xi - i\eta$.
η	see ζ .
ϑ	defined by $x^* = -\frac{1}{2}c^* \cos \vartheta$.
λ	$=10 (\mu - 0.05)$.
μ	length along chord from axis of model, divided by B (see fig. 8, p. A 10).
ξ	see ζ .
Π	dynamic pressure coefficient.
Π_s	static pressure coefficient.
φ	angle (see fig. 8, p. A 10).

In order to find the influence of tunnel walls on the pressure distribution, we shall transform the z -plane ($z = x + iy$) of the tunnel into the ζ -plane ($\zeta = \xi + i\eta$), so that the velocity V_z in the tunnel (see below) is transformed into a parallel flow with $V_\zeta = U$, in which U is the velocity of the flow in the tunnel without model. Using the methods of images (ref. 4, Vol. III, p. 300), one finds, that the model seems to be placed in a flow with curved stream lines. The curvature is caused by the images of the vortex, which may represent the model in a first approximation.

So

$$V_z = U + w,$$

in which $w = u + iv$ and u and v are the velocity components (fig. 7) due to the row of images.

The conjugate complex velocity $w^* = u - iv$ has been calculated:

$$w^* = i\Gamma \left\{ \frac{1}{2\pi z} - \frac{1}{2B \cdot \text{sh}(\pi z/B)} \right\}^1.$$

Here Γ is the circulation per unit of length.

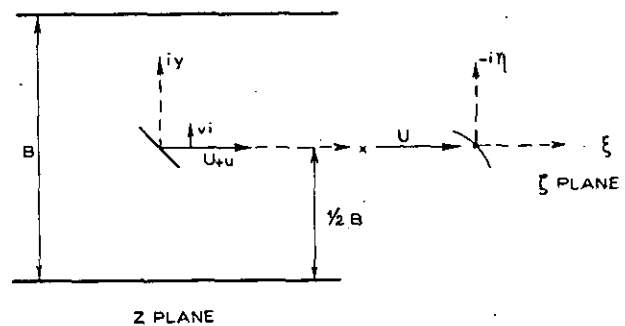


Fig. 7

The transformation is given by

$$\frac{dz}{d\zeta} = \frac{U}{U + w}; \quad d\zeta = \left(1 + \frac{w}{U}\right) dz.$$

ζ^* , the conjugate function of ζ , may be calculated:

$$\frac{d\zeta^*}{dz} = 1 + \frac{w^*}{U} = 1 + i\gamma \left\{ \frac{1}{\delta} - \frac{2}{\text{sh } 2\delta} \right\},$$

in which $\delta = \pi z/2B$ and $\gamma = \Gamma/4BU$.

¹⁾ This formula may be derived from the formula (4.2) of ref. 4, Vol. III, p. 300 by subtracting the central vortex $-\frac{i\Gamma}{2\pi z}$, and after putting $k=B$ and $k_1=\frac{1}{2}B$, using the relation

$$\coth \delta - \coth \left(\delta + \frac{1}{2} \pi i \right) = \coth \delta - \frac{1}{\coth \delta} = \frac{2}{\text{sh } 2\delta}$$

Integration gives

$$\zeta^* = \frac{2B}{\pi} \{ \delta + i\gamma \ln \delta - i\gamma \ln \operatorname{th} \delta \}.$$

The integration constant has the arbitrarily chosen value zero.

As $\gamma = \frac{1}{8} C_L c/B$, which may be derived from formula (I-1) ($c = \text{chord}$), and $\zeta^* = \xi - i\eta$, we find

$$\left. \begin{aligned} \xi &= x - \frac{C_L}{4\pi} c \operatorname{bg} \operatorname{tg} \frac{y}{x} + \frac{C_L}{4\pi} c \operatorname{bg} \operatorname{tg} \frac{\sin \frac{\pi}{B} y}{\operatorname{sh} \frac{\pi}{B} x} \\ -\eta &= y + \frac{C_L}{8\pi} c \ln \left[\frac{1}{4} \frac{\pi^2}{B^2} (x^2 + y^2) \right] - \frac{C_L}{8\pi} c \ln \left[\frac{\operatorname{sh}^2 \frac{\pi}{B} x + \sin^2 \frac{\pi}{B} y}{\left(\operatorname{ch} \frac{\pi}{B} x + \cos \frac{\pi}{B} y \right)^2} \right] \end{aligned} \right\} \quad (\text{II-1})$$

The dynamic pressure ratio in corresponding points of the z - and ζ -plane is

$$\Delta P_z / \Delta P_\zeta = \left| 1 + \frac{w}{U} \right|^2 = \left(1 + \frac{w}{U} \right) \left(1 + \frac{w^*}{U} \right)$$

which leads to

$$\Delta P_z / \Delta P_\zeta = 1 + C_L \frac{c}{B} A_1 + \frac{1}{4} C_L^2 \frac{c^2}{B^2} (A_1^2 + A_2^2) = \left(1 + \frac{1}{2} C_L \frac{c}{B} A_1 \right)^2 + \left(\frac{1}{2} C_L \frac{c}{B} A_2 \right)^2 \quad (\text{II-2})$$

in which

$$\left. \begin{aligned} 2A_1 &= - \frac{\operatorname{ch}(\pi x/B) \sin(\pi y/B)}{\operatorname{sh}^2(\pi x/B) + \sin^2(\pi y/B)} + \frac{By}{\pi(x^2 + y^2)} \\ 2A_2 &= \frac{\operatorname{sh}(\pi x/B) \cos(\pi y/B)}{\operatorname{sh}^2(\pi x/B) + \sin^2(\pi y/B)} - \frac{Bx}{\pi(x^2 + y^2)} \end{aligned} \right\} \quad (\text{II-3})$$

For the points of a line l (fig. 8), which makes an angle φ with the axis of the tunnel,

$$\left. \begin{aligned} x &= \mu B \cos \varphi \\ y &= -\mu B \sin \varphi \end{aligned} \right\} \quad (\text{II-4})$$

in which μ is the distance of a point of l from the origin expressed in B as unit of length.

With these values of x and y our formulae change into:

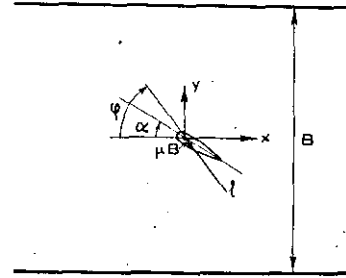


Fig. 8

$$\left. \begin{aligned} (\xi - x)/B &= f_\xi(\mu, \varphi) \cdot \frac{c}{B} C_L(\alpha) \text{ or } (\xi - x)/c = f_\xi(\mu, \varphi) \cdot C_L(\alpha) \\ (-\eta - y)/B &= f_\eta(\mu, \varphi) \cdot \frac{c}{B} C_L(\alpha) \text{ or } (-\eta - y)/c = f_\eta(\mu, \varphi) \cdot C_L(\alpha) \\ (P_z - P_\zeta)/\Delta P_\zeta &= f_{P_1}(\mu, \varphi) \cdot \frac{c}{B} C_L(\alpha) + f_{P_2}(\mu, \varphi) \left\{ \frac{c}{B} C_L(\alpha) \right\}^2, \end{aligned} \right\} \quad (\text{II-5})$$

in which

$$\left. \begin{aligned} f_\xi(\mu, \varphi) &= \frac{1}{4\pi} \left\{ \varphi - \operatorname{bg} \operatorname{tg} \frac{\sin(\pi\mu \sin \varphi)}{\operatorname{sh}(\pi\mu \cos \varphi)} \right\} \quad (\text{angles in radians}) \\ f_\eta(\mu, \varphi) &= \frac{1}{4\pi} \left\{ \frac{1}{2} \ln \left(\frac{1}{2} \pi \mu \right)^2 - \frac{1}{2} \ln \frac{\operatorname{sh}^2(\pi\mu \cos \varphi) + \sin^2(\pi\mu \sin \varphi)}{\left\{ \operatorname{ch}(\pi\mu \cos \varphi) + \cos(\pi\mu \sin \varphi) \right\}^2} \right\} \\ f_{P_1}(\mu, \varphi) &= A_1 \text{ and } f_{P_2}(\mu, \varphi) = \frac{1}{4} (A_1^2 + A_2^2) \\ \text{with } \left\{ \begin{aligned} 2A_1 &= + \frac{\operatorname{ch}(\pi\mu \cos \varphi) \cdot \sin(\pi\mu \sin \varphi)}{\operatorname{sh}^2(\pi\mu \cos \varphi) + \sin^2(\pi\mu \sin \varphi)} - \frac{\sin \varphi}{\pi\mu} \\ 2A_2 &= \frac{\operatorname{sh}(\pi\mu \cos \varphi) \cdot \cos(\pi\mu \sin \varphi)}{\operatorname{sh}^2(\pi\mu \cos \varphi) + \sin^2(\pi\mu \sin \varphi)} - \frac{\cos \varphi}{\pi\mu} \end{aligned} \right. \end{aligned} \right\} \quad (\text{II-6})$$

For small values of $\pi x/B = X$, and $\pi y/B = Y$, say, expansion in series may be useful:

$$\left. \begin{aligned} f_{\xi} &= -\frac{1}{24\pi} XY \left\{ 1 - \frac{7}{60} (X^2 - Y^2) + \dots \right\} \\ f_{\eta} &= \frac{1}{48\pi} \left\{ (X^2 - Y^2) - \frac{7}{120} (X^4 - 6X^2Y^2 + Y^4) + \dots \right\} \\ f_{P_1} = A_1 &= -\frac{1}{12} Y \left\{ 1 + \frac{7}{60} (Y^2 - 3X^2) + \frac{31}{2520} (5X^4 - 10X^2Y^2 + Y^4) + \dots \right\} \\ A_2 &= -\frac{1}{12} X \left\{ 1 - \frac{7}{60} (X^2 - 3Y^2) + \dots \right\} \\ f_{P_2} &= \frac{1}{576} (X^2 + Y^2) \left\{ 1 - \frac{7}{30} (X^2 - Y^2) + \dots \right\} \end{aligned} \right\} \quad (\text{II-7})$$

and with $x = \mu B \cos \varphi$ and $y = -\mu B \sin \varphi$, so that $X = \pi \mu \cos \varphi$ and $Y = -\pi \mu \sin \varphi$

$$\left. \begin{aligned} f_{\xi} &= \frac{1}{48} \pi \mu^2 \sin 2\varphi \left\{ 1 - \frac{7}{60} \pi^2 \mu^2 \cos 2\varphi + \dots \right\} \\ f_{\eta} &= \frac{1}{48} \pi \mu^2 \left\{ \cos 2\varphi - \frac{7}{120} \pi^2 \mu^2 \cos 4\varphi + \dots \right\} \\ f_{P_1} = A_1 &= \frac{1}{12} \pi \mu \sin \varphi \left\{ 1 - \frac{7}{60} \pi^2 \mu^2 (1 + 2 \cos 2\varphi) + \right. \\ &\quad \left. + \frac{31}{2520} \pi^4 \mu^4 (1 + 2 \cos 2\varphi + 2 \cos 4\varphi) + \dots \right\} \\ A_2 &= -\frac{1}{12} \pi \mu \cos \varphi \left\{ 1 + \frac{7}{60} \pi^2 \mu^2 (1 - 2 \cos 2\varphi) + \dots \right\} \\ f_{P_2} &= \frac{1}{576} \pi^2 \mu^2 \left\{ 1 - \frac{7}{30} \pi^2 \mu^2 \cos 2\varphi + \dots \right\} \end{aligned} \right\} \quad (\text{II-8})$$

With the aid of these formulae $\Delta P_z/\Delta P_{\xi}$ has been calculated for points on the suction side of the N.A.C.A. 0018 profile, chord 0.6 m, placed in a tunnel with $B = 3$ m at $\alpha = 10^\circ$ ($C_L(10^\circ) = 0.832$) and at $\alpha = 16^\circ$ ($C_L(16^\circ) = 1.150$) (fig. 9). From a comparison with the values of $\Delta P_z/\Delta P_{\xi}$, following the formulae for points on the chord (fig. 9), it appears that it is not permissible, to use the latter values as an approximation to the former ones. Division of the values ΔP_z , measured in the tunnel, by ΔP_{ξ} gives the dynamic pressures ΔP_{ξ} on the contour of the model, obtained by transforming the points on the contour of the N.A.C.A. 0018 profile in the z -plane to the ξ -plane. Instead of carrying out this cumbersome calculation, it seems reasonable to use an approximated contour in the ξ -plane, viz. a contour with the same thickness-distribution as the N.A.C.A. 0018 profile and with the line into which the chord of the profile in the z -plane is transformed, as mean line.

As the values of μ of the points on the chord in the z -plane are rather small in our case ($-0.05 \leq \mu \leq 0.15$) the coordinates ξ and η of the mean line in the ξ -plane may be calculated with an accuracy of a few percent with the aid of the following formulae:

$$\frac{\xi - x}{c} = C_L \frac{\pi}{48} \mu^2 \sin 2\alpha$$

$$\frac{-\eta - y}{c} = C_L \frac{\pi}{48} \mu^2 \cos 2\alpha$$

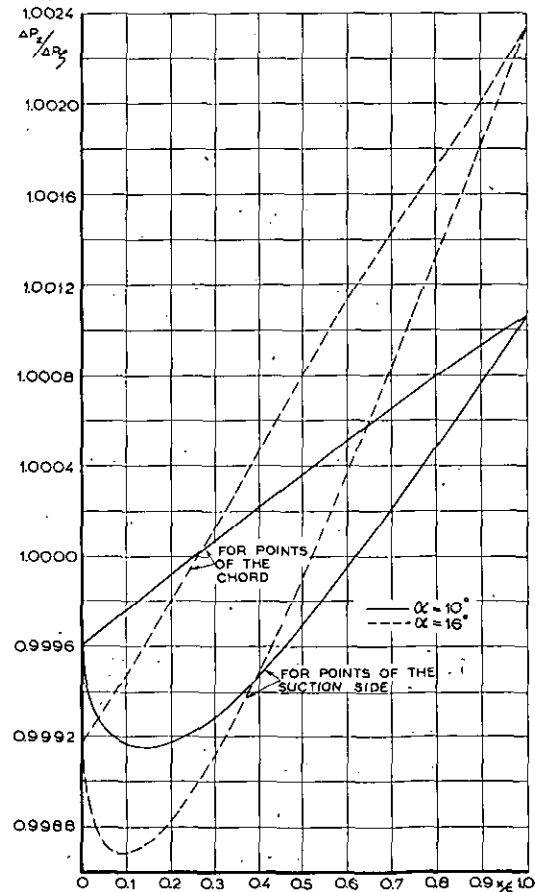


Fig. 9

Ratio of the dynamic pressures in z - and ξ -plane for the suction side of the N.A.C.A. 0018 profile and for a flat plate (points of the chord).

Elimination of either μ or α gives either

$$\frac{-\eta - y}{\xi - x} = \cot 2\alpha$$

or

$$r = c C_L \cdot \frac{\pi}{48} \mu^2 \text{ with } r^2 = (\xi - x)^2 + (-\eta - y)^2.$$

The meaning of these formulae is illustrated in fig. 10 in which P' in the ξ -plane is the transform of P in the z -plane.

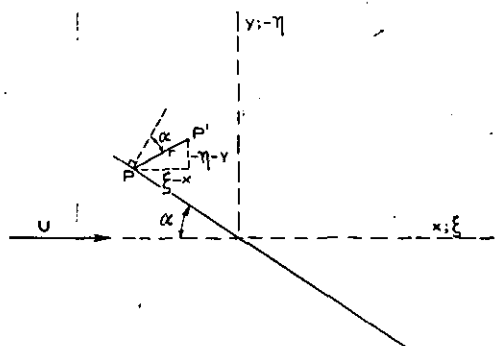


Fig. 10

The equation of the mean line on the coordinates x^* and y^* (fig. 11) is

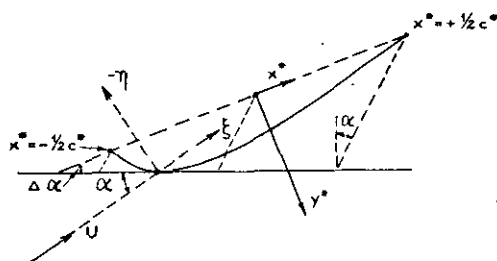


Fig. 11

$$\left. \begin{aligned} y^*/c^* &= H(1 - \lambda^2) \\ x^*/c^* &= \frac{1}{2}\lambda - J(1 - \lambda^2) \\ c^* &= Mc. \end{aligned} \right\} \quad (\text{II-9})$$

Here

$$\left. \begin{aligned} \lambda &= 10(\mu - 0.05); \\ H &= \frac{2K}{M} \cos(\alpha + \Delta\alpha); J = \frac{2K}{M} \sin(\alpha + \Delta\alpha); \\ K &= \frac{\pi}{19200} C_L; M^2 = 1 + 16K^2 + 16K \sin \alpha; \\ \sin \Delta\alpha &= \frac{4K}{M} \cos \alpha. \end{aligned} \right\} \quad (\text{II-9a})$$

As $-0.05 \leq \mu \leq 0.15$ it follows that $-1 \leq \lambda \leq +1$. For $\alpha = 10^\circ$ calculation gives $\Delta\alpha = 0.03^\circ$ and

$$\left. \begin{aligned} y^*/c^* &= 0.00027(1 - \lambda^2) \\ x^*/c^* &= \frac{1}{2}\lambda - 0.00047(1 - \lambda^2) \\ c^* &= 1.0002c \end{aligned} \right\} \quad (\text{II-10})$$

and for $\alpha = 16^\circ$ we find $\Delta\alpha = 0.04^\circ$ and

$$\left. \begin{aligned} y^*/c^* &= 0.00036(1 - \lambda^2) \\ x^*/c^* &= \frac{1}{2}\lambda - 0.000104(1 - \lambda^2) \\ c^* &= 1.0004c. \end{aligned} \right\} \quad (\text{II-11})$$

In these cases the line

$$\frac{y^*}{c^*} = H \left\{ 1 - 4 \left(\frac{x^*}{c^*} \right)^2 \right\} \quad (\text{II-12})$$

approximates the line, given by (II-9) for $-1 \leq \lambda \leq 1$ within 0.4% .

The dynamic pressure ΔP_ξ over the contour of a cambered profile with the mean line (II-12) and the same thickness distribution as the N.A.C.A. 0018 profile may be written (ref. 12, p. 11)

$$\Delta P_\xi / \frac{1}{2} \rho U^2 = \left(\frac{V}{U} + \frac{V_c}{U} \right)^2 \quad (\text{II-13})$$

in which ρ = density, V = velocity of the potential flow over the surface of a N.A.C.A. 0018 profile, placed at an angle of attack α° in a parallel flow with velocity U , V_c = contribution to the velocity in potential flow introduced by the camber of the profile. ΔP_ξ , equaling the quotient of the dynamic pressure measured in the tunnel and the factor $\Delta P_z / \Delta P_\xi$ (fig. 9), is known.

In order to find $\Delta P = \frac{1}{2} \rho V^2$, an approximate value of V_c/U will be calculated theoretically.

Consider two plates, a flat one and a cambered one, both with the same chord, placed in a parallel flow, velocity U , with an angle of attack α (fig. 12).

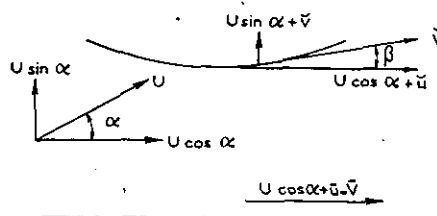


Fig. 12

The difference of the velocities at corresponding points may be $\check{V} - \bar{V}$ (the sign $\check{}$ above a character indicates, that it refers to the cambered model, the sign $\bar{}$ is connected with the model without camber). It is supposed, that $\check{V} - \bar{V}$ is the same for two models, the mean lines of which are those of fig. 12, provided that those two models both have the same thickness distribution. In other words, $\check{V} - \bar{V}$ is independent of the thickness distribution. As for the plates of fig. 12 \check{V} has to be tangent to the mean line, it follows that

$$\left. \begin{aligned} \frac{U \sin \alpha + \check{v}}{U \cos \alpha + \check{u}} &= \tan \beta \\ U \sin \alpha + \bar{v} &= 0. \end{aligned} \right\} \quad (\text{II-14})$$

and

$$U \sin \alpha + \bar{v} = 0.$$

Now the mean lines will be covered with vortices, the intensities per unit of length $\check{\gamma}$ and $\bar{\gamma}$ of which will be determined in such a way, that the obtained velocities fulfil the conditions (II-14). However, the following simplifications will be made for the cambered model:

- a) the vortices will be placed on the chord line instead of on the mean line;
 b) the conditions (II-14) will be fulfilled at points on the chord line.

These simplifications are allowed if the camber is small compared with the chord, which is the case here.

We chose the origin at the mid point of the chord and the positive x -axis along the chord in the direction of the trailing edge.

The velocity components at the point $(x; +0)$, due to the vortex sheet, are (ref. 4, vol. II, p. 34)

$$\left. \begin{aligned} u &= +\frac{1}{2}\gamma \\ v &= \int_{-\frac{1}{2}c}^{+\frac{1}{2}c} \frac{\gamma(x')}{2\pi(x'-x)} dx' \end{aligned} \right\} \quad (\text{II-15})$$

As $u \ll U \cos \alpha$, the conditions (II-14) may be written

$$U \sin \alpha + \int_{-\frac{1}{2}c}^{+\frac{1}{2}c} \frac{\gamma(x')}{2\pi(x'-x)} dx' = U \cos \alpha \cdot \operatorname{tg} \beta(x) \quad (\text{II-16a})$$

$$U \sin \alpha + \int_{-\frac{1}{2}c}^{+\frac{1}{2}c} \frac{\gamma(x')}{2\pi(x'-x)} dx' = 0 \quad (\text{II-16b})$$

From (II-12) it follows (the asterisks are omitted)

$$\operatorname{tg} \beta(x) = \frac{dy}{dx} = -8H \frac{x}{c}. \quad (\text{II-17})$$

Now introducing $x = -\frac{1}{2}c \cos \vartheta$ and subtracting (II-16b) from (II-16a), we find

$$\frac{1}{2\pi} \int_0^\pi \frac{\{\check{\gamma}(\vartheta') - \bar{\gamma}(\vartheta')\} \sin \vartheta' d\vartheta'}{\cos \vartheta - \cos \vartheta'} = 4HU \cos \alpha \cos \vartheta \quad (\text{II-18})$$

This is an integral equation for $\check{\gamma}(\vartheta') - \bar{\gamma}(\vartheta')$ of the same type as (I-9).

The solution is

$$\check{\gamma}(\vartheta) - \bar{\gamma}(\vartheta) = 8HU \cos \alpha \sin \vartheta. \quad (\text{II-19})$$

Further

$$\begin{aligned} V_c &= \check{V} - \bar{V} = \frac{U \cos \alpha + \check{u}}{\cos \beta} - \\ &= (U \cos \alpha + \check{u}) \approx (U \cos \alpha + \check{u})(1 + \frac{1}{2}\beta^2) - \\ &= (U \cos \alpha + \check{u}) = \check{u} - \bar{u} + \frac{1}{2}\beta^2 (U \cos \alpha + \check{u}) \approx \\ &\approx \check{u} - \bar{u} + \frac{1}{2}\beta^2 V = \frac{1}{2}(\check{\gamma} - \bar{\gamma}) + \frac{1}{2}\beta^2 V = \\ &= 4HU \cos \alpha \sin \vartheta + \frac{1}{2}\beta^2 V = \\ &= 4HU \cos \alpha \cdot \sqrt{1 - (x/c)^2} + \frac{1}{2}\beta^2 V. \end{aligned}$$

The term $\frac{1}{2}\beta^2 V$ may be neglected, as will be shown below.

As β is a small angle, $\beta \approx \operatorname{tg} \beta = -8H(x/c)$. So

$$\frac{\frac{1}{2}\beta^2 V}{4HU \cos \alpha \cdot \sqrt{1 - (x/c)^2}} \approx \frac{8H(x/c)^2}{\cos \alpha \cdot \sqrt{1 - (x/c)^2}} \frac{V}{U}$$

As H is very small, (e. g. $H = 0.00036$ for $\alpha = 16^\circ$) and $-0.5 \leq x/c \leq 0.5$ (fig. 11), this ratio is negligible compared with 1. So we can use the formula

$$\left. \begin{aligned} V_c/U &= C \sqrt{1 - x^2/c^2} \\ C &= 4H \cos \alpha. \end{aligned} \right\} \quad (\text{II-20})$$

This formula is in accordance with the formula given in ref. 4, vol. II, p. 49, but for the factor $\cos \alpha$.

So the differences of the velocities at corresponding points of a cambered and a flat plate at α° angle of incidence may be derived from the differences at 0° by multiplying the latter by $\cos \alpha$, a factor, which only equals one for small values of α .

For $\alpha = 10^\circ$

$$V_c/U = 0.00106 \sqrt{1 - (x/c)^2} \quad (\text{II-21})$$

and for $\alpha = 16^\circ$

$$V_c/U = 0.00138 \sqrt{1 - (x/c)^2}. \quad (\text{II-22})$$

The dynamic pressure coefficient for the N.A.C.A. 0018 profile in parallel flow is

$$\frac{\Delta P}{\frac{1}{2}\rho U^2} = \frac{V^2}{U^2} = \Pi, \text{ say} \quad (\text{II-23})$$

From (II-13) it follows, that

$$\Pi_\xi^{1/2} - V_c/U = V/U = \Pi^{1/2}$$

As

$$\Pi_\xi = \Pi_z (\Delta P_z / \Delta P_\xi)^{-1} \text{ and } V_c/U = C \sqrt{1 - (x/c)^2}$$

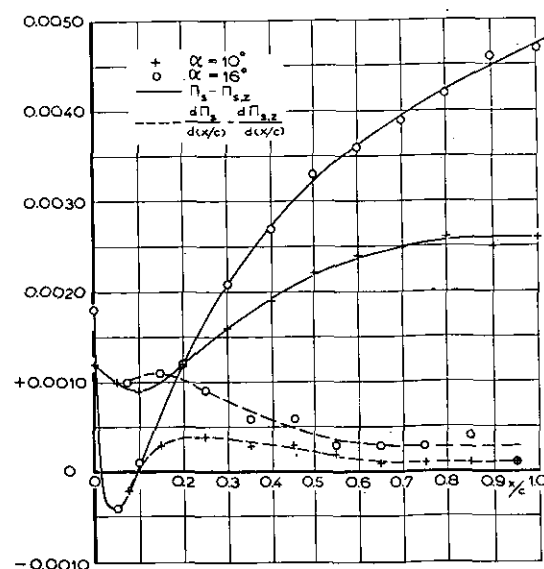


Fig. 13

Difference of static pressure coefficients without and with tunnel walls ($\Pi_z - \Pi_{g,z}$) and its gradient versus position on chord.

it is

$$\Pi = \left\{ \Pi_z^{1/2} (\Delta P_z / \Delta P_z)^{-1/2} - C \sqrt{1 - (x/c)^2} \right\}^2. \quad (\text{II-24})$$

Table 3 gives Π_z from fig. 1, Π is calculated following (II-24) with the aid of fig. 9, the gradients of the static pressure coefficients $d\Pi_{s,z}/d(x/c)$, $d\Pi_s/d(x/c)$ and their differences (fig. 13) for

$\alpha = 10^\circ$ and $\alpha = 16^\circ$. (The gradient of the static pressure coefficient is the opposite of the gradient of the dynamic pressure coefficient).

It appears, that the gradient in free flow is greater than in tunnel flow. So the tunnel walls flatten the pressure distribution line, so that separation is delayed and α_m , the angle of maximum lift, is increased. The influence, however, is extremely small for the cases under consideration.

REPORT A. 1205

The field of flow through a helicopter rotor obtained from wind tunnel smoke tests

by

J. MEIJER DREES and W. P. HENDAL.

Summary.

In this report results are given of wind tunnel smoke tests carried out on a simplified helicopter rotor in the open-jet wind tunnel of the N.L.L.. For these tests a new method of smoke generation was developed.

Contents.

- 1 Introduction.
- 2 Apparatus and test-method.
 - 2.1 Apparatus.
 - 2.1.1 The hot wire smoke generator.
 - 2.1.2 The rotor
 - 2.1.3 Light sources and camera mounting.
 - 2.2 Test method.
- 3 The field of flow.
 - 3.1 General remarks.
 - 3.2 The flow pattern for various rates of climb and forward speeds.
 - 3.3 Horizontal flights and climb at various forward speeds.
 - 3.4 Descending flight at various forward speeds.
- 4 Conclusions.
- 5 References.
- Appendix.
- Fig. 1—16.

1 Introduction.

For the calculation of the flow through a helicopter rotor many methods are available, in all of which more or less simplifying assumptions have been made. This is due to the complicated character of the rotor-flow, and to the absence of sufficient experimental data.

For this reason a windtunnel investigation of the field of flow through and in the neighbourhood of a simplified see-saw hinged helicopter-rotor was undertaken with the object to get as complete as possible a picture of the flow pattern for the primary working conditions.

The flow was made visible by means of a number of hot-wire smoke generators.

2 Apparatus and test-method.

2.1 Apparatus.

2.1.1 The hot wire smoke generator.

The working principle of the hot wire smoke generator is based on the evaporation of oil by

heating. A schematic drawing of the apparatus is shown in fig. 1. Common lubricating oil is led through a plastic tube from a reservoir, in which the pressure is slightly more than atmospheric, to the smoke generators. These consist of the metal parts (a) and (b) separated by the insulating layer (c) and kept together by insulated wires. To the lower half (b) of the smoke head a piece of copper tubing (d) is soldered through which an insulated wire (e) is led to the upper part.

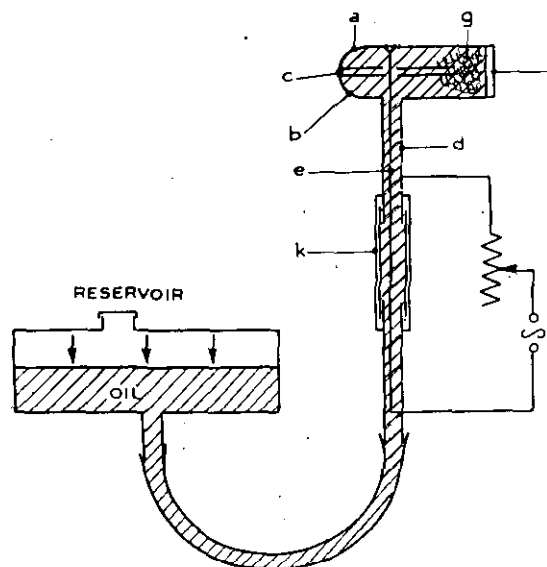


Fig. 1. Hot wire smoke generator.

These parts form a circuit by which an electric current can be introduced into a platinum wire (f) ($\varnothing \approx 0.1$ mm) soldered across the mouth of the smoke head.

In order to distribute the oil evenly over the wire and to prevent a rapid loss of pressure in the oil reservoir, the mouth of the smoke head is filled up with cotton (g). At some distance from the smoke head a flexible joint (k) enables the smoke head to be placed parallel to the direction

of the flow. The wires are heated with A.C. current obtained from a low tension transformer fed via a variac, thus enabling a simple regulation of the amount of smoke generated.

The advantages of this method of smoke production are:

- the velocity introduced into the field of flow under observance is negligible,
- smoke can be produced or cut off instantaneously,
- a non-corrosive smoke is obtained,
- the easy regulation of the amount of smoke enables the observer to perform preliminary observations with very thin smoke, thus preventing a filling up with smoke of the tunnel-circuit,
- the amount of smoke can be controlled from any point the observer chooses.

2.1.2 The rotor.

For the investigation a small two bladed rotor, with constant pitch and see-saw hinge, of about 0.3 m diameter was made. A schematic drawing of the experimental set-up is given in fig. 2. The

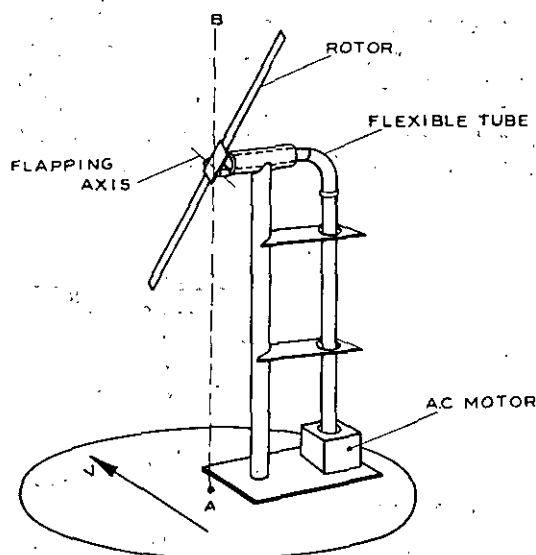


Fig. 2. Experimental set up of model rotor.

rotor was driven by a small single phase AC-motor, the number of revolutions of which could be regulated with a variac. By turning the foot-plate around AB and varying the rotor tip-speed, all possible working conditions could be imitated.

2.1.3 Light sources and camera mounting.

As light sources two Philips H/P 300-highpressure mercury vapour lamps were mounted downstream of the rotor model. Due to the fact that light from these lamps is emitted from a line source it has been possible, by adjusting the distance between the lamp and a lens positioned in front of the lamp to obtain a horizontal plane of light coinciding with the plane of the smoke threads. In this way a sharp contrast between the dark background and the smoke was obtained. The camera was mounted in the line A—B.

2.2 Test method.

During the tests the windtunnel speed was — except for the hovering condition — kept constant at a velocity of about 2 m sec⁻¹. The smoke generators, four of which were used, were placed in various points of the horizontal plane through the rotor axis.

3 The field of flow.

3.1 General remarks.

The obtained pictures of the flow pattern are given in fig. 4 to fig. 15. The object of this investigation was in the first place to get an impression about the possibilities of this method of visualizing the flow pattern. Therefore, the wind velocity, the number of revolutions of the rotor and the thrust of the rotor were not measured.

To get at least some idea of the flight conditions corresponding with the given flow patterns, the parameters κ/μ and λ/μ *) were roughly determined from the angle between the direction of the flow in front of the rotor and the rotor axis and from that one between the direction of the slipstream at some distance behind the rotor and the rotor axis. The relations between these angles and the parameters mentioned above are given in ref. 1. These parameters define the working condition of the rotor; they can be plotted in a diagram like fig. 3, from which the working condition can be read easily.

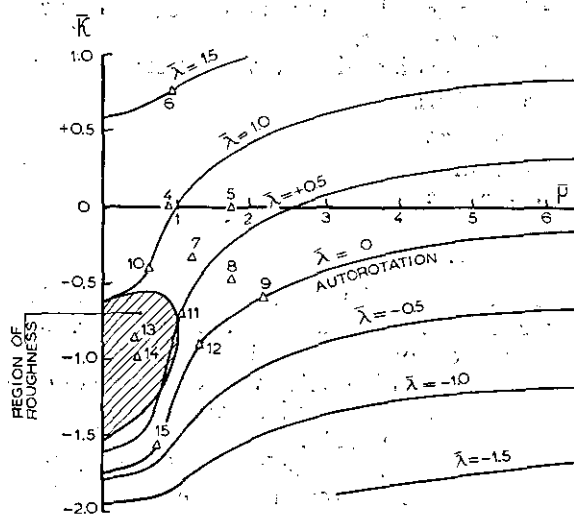


Fig. 3. Relationship between dimensionless rotor coefficients.

Points 4—15 refer to figs. 4—15.

*) κ = rate of climb coefficient.

μ = forward velocity coefficient.

λ = axial flow coefficient.

The rate of climb is measured perpendicular to the rotordisc, the forward velocity parallel with the disc.

These coefficients are equal to the corresponding velocity, divided by the theoretical induced velocity through the hovering disc.

3.2 The flow pattern for various rates of climb and forward speeds.

The pictures obtained for these conditions are shown in fig. 4 to 15. The corresponding values of $\frac{\bar{\kappa}}{\mu}$ and $\frac{\bar{\lambda}}{\mu}$ are given in the subscripts. The flow pattern shows no deviations which are in contradiction to the assumptions generally made with regard to the induced flow through the rotor disc. The increase in axial velocity when moving in downstream direction along the rotor axis, is clearly visible from the change of the direction of the flow under the rotor disc.

3.3 Horizontal flights and climb at various forward speeds.

The flow patterns for these conditions are shown in figs. 4 to 6 and do not show any new points of view. In horizontal flight the upflow in front of and through part of the rotor disc is shown clearly for the various working conditions. Fig. 6 presents a climb at low forward speed.

3.4 Descending flight at various forward speeds.

The vortex ringstate and the so-called region of roughness being the less known flight conditions, the flow patterns occurring in this region were tested more elaborately than those already discussed.

The results of these tests are shown in fig. 7 to 15, from which some interesting results can be obtained. In the first place it became definitely clear that the rough behaviour of the rotor as already mentioned in ref. 3 and 2, is due to the fact that in this working condition the flow has an unstable character.

A continuous changing of the flow pattern with a constant periodicity can be observed. This marked periodicity occurs especially at very low forward speeds and may explain the change in the rate of descent of a helicopter in the region of roughness as observed during flights tests (see ref. 3).

That the periodical shedding of vortices in pure vertical descent does not show the pronounced regularity which occurs when descending at a low forward speed may be due to the fact that in the last case the flow parallel to the rotordisc creates a direction of preference while in vertical descending flight disturbances in any direction may occur.

Herefrom may be concluded that the possibility of a pure vertical descent will be utterly questionable. The mechanism of the flow in this condition is not quite clear, at the time of writing of this report but more information may come available from cinematographic pictures which are being taken (see appendix of this report).

The second point of interest lies in the observation that at higher forward speeds the instability of the flow pattern disappears completely; this means that the region of roughness, when characterised as a flow with an unstable character

is limited to a rather sharply bounded region of flight conditions as shown by the shaded area of fig. 3.

4 Conclusion.

1. The region of roughness is shown to be characterised by a periodical changing of the flow pattern. From this unstable flow the observed changing of the rate of descent in this region may be explained.
2. The region of roughness occurring in descending flight does not extend into the whole range of flight conditions, but is shown to be limited to a rather sharply bound region at low forward speeds.

5 References.

1. MEYER DREES, J. A Theory of Airflow through Rotors and its Application to some Helicopter Problems. J. Helicopter Ass. Great Britain, Vol. 3 no 2, 1949, p. 79.
2. LUCASSEN, L. R., MEYER DREES, J., HENDAL, W. P. Airflow through Helicopter Rotors in Vertical Flight. N.L.L.-Report V. 1535, Dec. 1949.
3. BROTHERHOOD, P. Flow through Helicopter Rotor in Vertical Descent. RAE-report Aero 2272, 1948.

APPENDIX.

The flow pattern in the region of roughness and vertical descending flight.

Although the pictures shown in the preceding report, give a clear view of the flow pattern in stationary conditions, for the non-stationary conditions the results are not completely satisfactory, especially with regard to the region downstream of the rotor.

Thanks to an order received from the "Dutch Helicopter Foundation" the making of a film of the various flow patterns became possible. From this film a series of pictures showing a complete cycle of the flow in the region of roughness when descending at low forward speed, are given in figs. 16.1 to 16.47 incl. They illustrate quite clearly the conclusions drawn from the observations already obtained.

In figs: 17.1 to 17.5 incl. some pictures are shown taken with a normal type camera, illustrating the typical flow patterns of the helicopter rotor in vertical descent.

These pictures show that the flow patterns as constructed by Brotherhood from flight tests are probably incorrect, due to the fact that during these tests only part of the field of flow was observed.

Completed: Febr. 1950.

Fig. 4

$$\begin{aligned}\bar{\kappa} &\approx 0 \\ \bar{\mu} &\approx 0.9 \\ \bar{\lambda} &\approx 1.95\end{aligned}$$

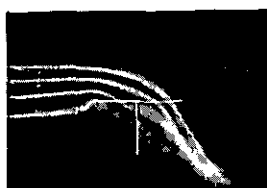


Fig. 5

$$\begin{aligned}\bar{\kappa} &\approx 0 \\ \bar{\mu} &\approx 1.7 \\ \bar{\lambda} &\approx 0.7\end{aligned}$$

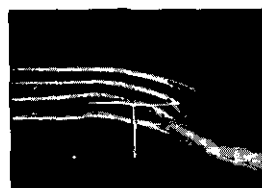


Fig. 6

$$\begin{aligned}\bar{\kappa} &\approx 0.75 \\ \bar{\mu} &\approx 0.9 \\ \bar{\lambda} &\approx 1.5\end{aligned}$$

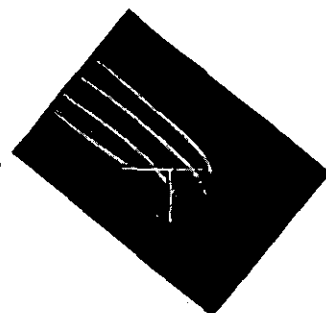


Fig. 7

$$\begin{aligned}\bar{\kappa} &\approx -0.3 \\ \bar{\mu} &\approx 0.6 \\ \bar{\lambda} &\approx 0.65\end{aligned}$$

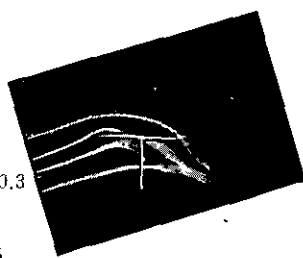


Fig. 8

$$\begin{aligned}\bar{\kappa} &\approx -0.5 \\ \bar{\mu} &\approx 1.7 \\ \bar{\lambda} &\approx 0.3\end{aligned}$$

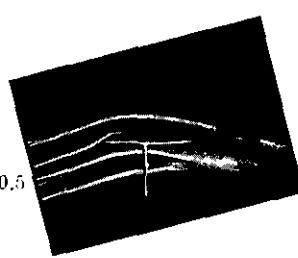


Fig. 9

$$\begin{aligned}\bar{\kappa} &\approx -0.6 \\ \bar{\mu} &\approx 2.2 \\ \bar{\lambda} &\approx 0\end{aligned}$$



Fig. 10

$$\begin{aligned}\bar{\kappa} &\approx -0.4 \\ \bar{\mu} &\approx 0.6 \\ \bar{\lambda} &\approx 1.0\end{aligned}$$

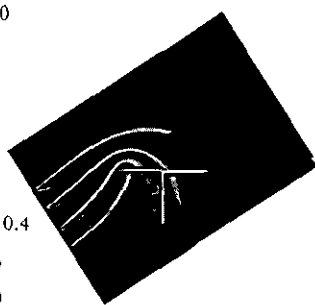


Fig. 11

$$\begin{aligned}\bar{\kappa} &\approx -0.7 \\ \bar{\mu} &\approx 1.0 \\ \bar{\lambda} &\approx 0.5\end{aligned}$$

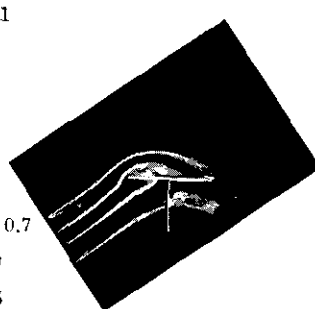


Fig. 12

$$\begin{aligned}\bar{\kappa} &\approx -0.9 \\ \bar{\mu} &\approx 1.3 \\ \bar{\lambda} &\approx 0\end{aligned}$$

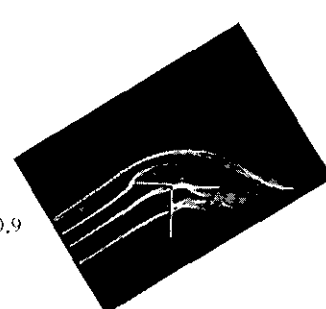


Fig. 13

$$\begin{aligned}\bar{\kappa} &\approx -0.8 \\ \bar{\mu} &\approx 0.4 \\ \bar{\lambda} &\approx 0.75\end{aligned}$$

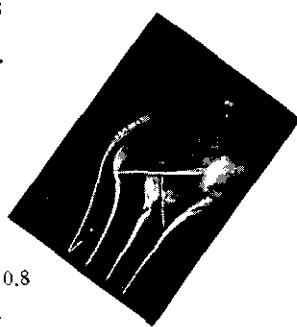


Fig. 14

$$\begin{aligned}\bar{\kappa} &\approx -1 \\ \bar{\mu} &\approx 0.5 \\ \bar{\lambda} &\approx 0.4\end{aligned}$$

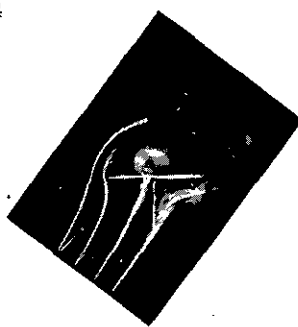
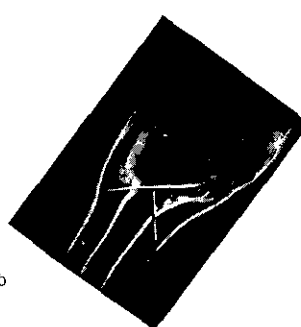
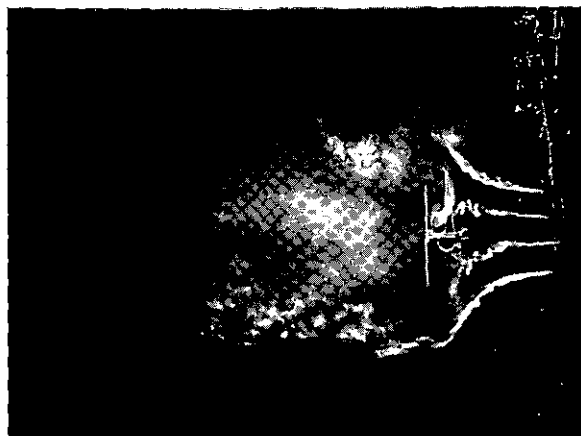
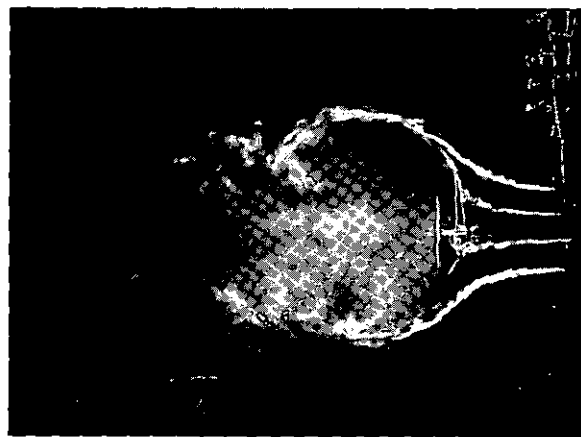
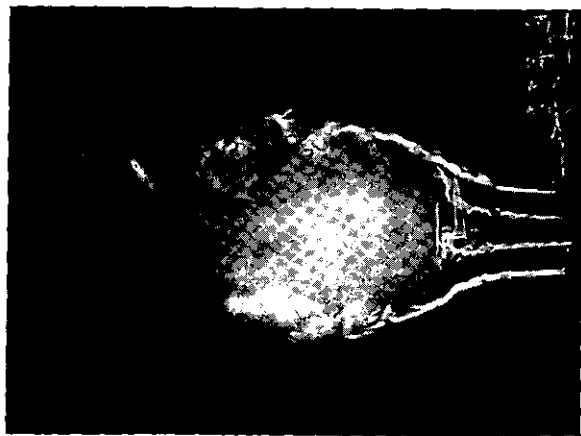


Fig. 15

$$\begin{aligned}\bar{\kappa} &\approx -1.0 \\ \bar{\mu} &\approx 0.7 \\ \bar{\lambda} &\approx 0\end{aligned}$$





1

2

3



4

5

Fig. 17. Vertical descending flight.

Application of Experimental Aerodynamic Coefficients to Flutter Calculations

by

H. BERGH and J. JEFF.

Summary.

Experimental aerodynamic coefficients of an oscillating wing in two-dimensional flow have been used in bending-torsion flutter calculations of several rectangular wings. The experimental aerodynamic coefficients are given in the form of graphs and tables for values of the reduced frequency ω from 0.08 to 1. It is found that the flutter speed, obtained by aid of the experimental aerodynamic coefficients, may be higher as well as lower than the theoretical flutter speed. The differences in flutter speed depend on the values of the relative density parameter, the ratio of the natural frequencies, and the positions of elastic and inertia axes and, in general, they will not be negligible. Though the experimental aerodynamic coefficients have been given in three decimals only, the results show that this is sufficiently accurate for flutter calculations.

1 Introduction.

Nearly all modern flutter calculations are being performed by using the theoretical values of the aerodynamic forces (ref. 1), because no systematic experimental data were available. Recently, experimental values of the aerodynamic coefficients of an oscillating wing without control surface in two-dimensional flow, for values of the reduced frequency ω between 0.08 and 1, have been obtained by BERGH and VAN DE VOOREN (ref. 2, 3, 4 and 5). The final results of that investigation have been collected also in this report (table 1 and figs. 1 to 4). These results differ slightly from those of report R104, since they have been corrected for an error of computation

This investigation has been carried out by order of the Netherlands Aircraft Development Board (N.I.V.).

Contents.

- 1 Introduction.
- 2 Procedure.
- 3 Results and discussion.
- 4 Final remark.
- 5 Conclusions.
- 6 List of symbols.
- 7 List of references.
- 1 table.
- 8 figures.

Experimental aerodynamic coefficients, obtained by smoothing the computed points.

TABLE 1

ω	k_a	k_p	m_a	m_p
0.08	-0.070 + 0.173!	1.553 - 0.129!	+ 0.020 - 0.003!	-0.041 + 0.055!
0.10	-0.060 + 0.200!	1.513 - 0.103!	+ 0.022 - 0.003!	-0.038 + 0.074!
0.15	-0.037 + 0.265!	1.451 - 0.101!	+ 0.022 - 0.004!	-0.031 + 0.118!
0.20	-0.018 + 0.322!	1.400 + 0.082!	+ 0.019 - 0.005!	-0.027 + 0.161!
0.30	+ 0.007 + 0.424!	1.326 + 0.295!	-0.003 - 0.007!	-0.032 + 0.245!
0.40	-0.001 + 0.513!	1.274 + 0.491!	-0.039 - 0.008!	-0.052 + 0.326!
0.50	-0.027 + 0.597!	1.236 + 0.679!	-0.087 - 0.005!	-0.088 + 0.406!
0.60	-0.074 + 0.678!	1.198 + 0.850!	-0.142 + 0.007!	-0.135 + 0.488!
0.70	-0.148 + 0.760!	1.147 + 1.003!	-0.206 + 0.032!	-0.187 + 0.568!
0.80	-0.243 + 0.837!	1.072 + 1.124!	-0.249 + 0.078!	-0.236 + 0.644!
0.90	-0.356 + 0.921!	0.966 + 1.204!	-0.258 + 0.170!	-0.296 + 0.724!
1.00	-0.484 + 0.996!	0.812 + 1.215!	-0.222 + 0.332!	-0.358 + 0.803!

in the calculation of the tunnel wall-interference.

With these experimental values of the aerodynamic coefficients some flutter calculations have been performed for the case of bending-torsion flutter of a rectangular wing, rigidly fixed at the root, with several values of the relative density

parameter μ and the positions of elastic and inertia axes.

The results have been compared with those, obtained with theoretical values of the aerodynamic coefficients.

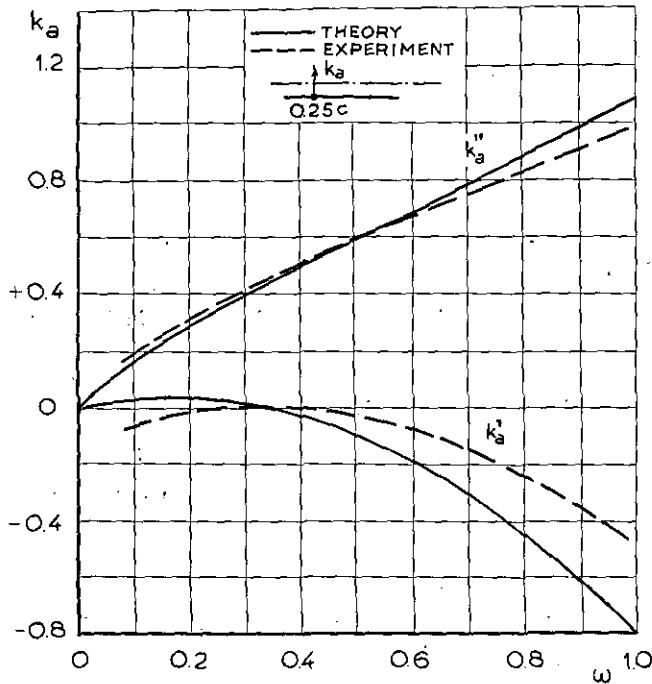


Fig. 1. Aerodynamic force coefficient, due to translation.

$$k_a = k'_a + i k''_a$$

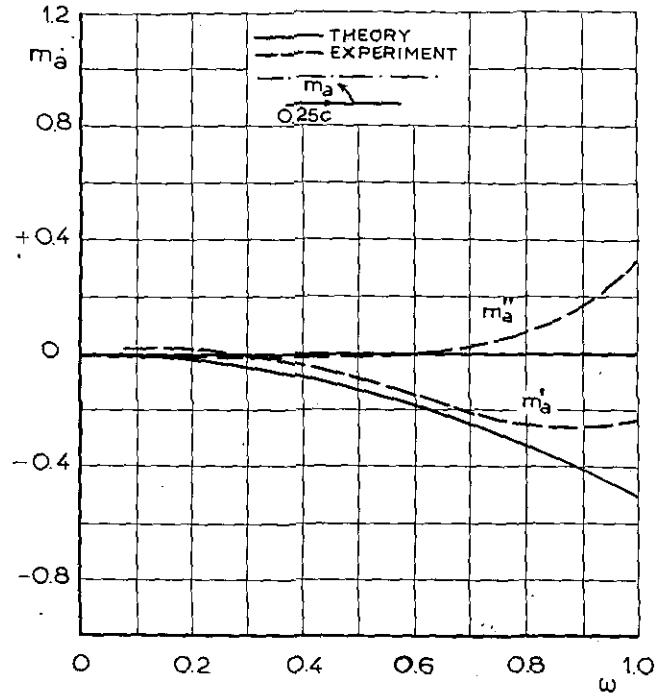


Fig. 3. Aerodynamic moment coefficient, due to translation.

$$m_a = m'_a + i m''_a$$

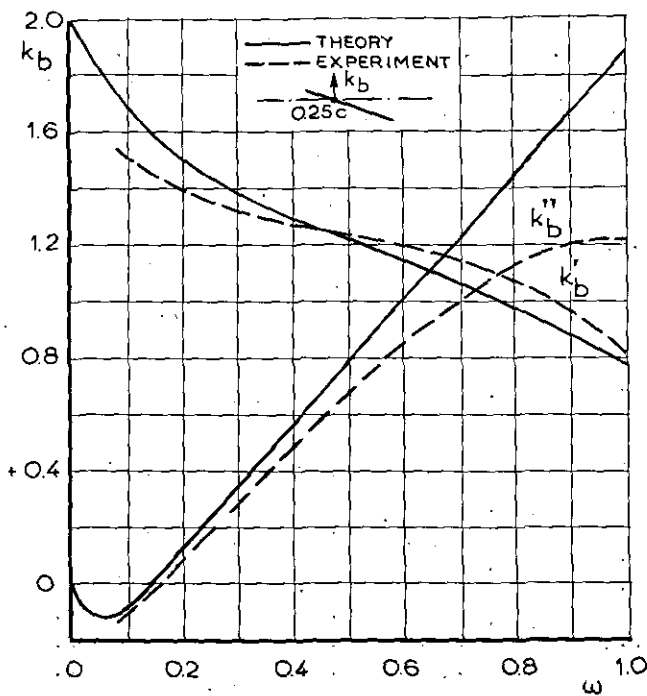


Fig. 2. Aerodynamic force coefficient, due to rotation.

$$k_b = k'_b + i k''_b$$

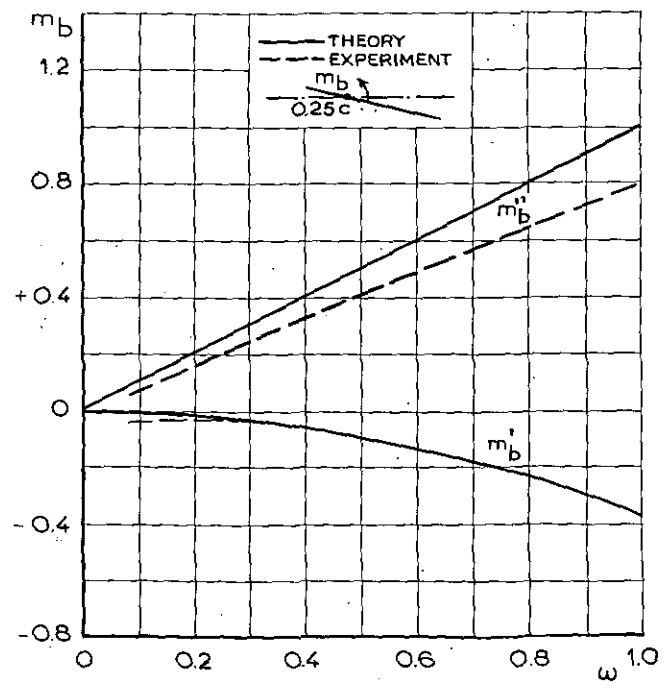


Fig. 4. Aerodynamic moment coefficient, due to rotation.

$$m_b = m'_b + i m''_b$$

2 Procedure.

The bending-torsion flutter calculations have been carried out for a rectangular wing, fixed at the root.

According to the linearized theory of ref. 1, the aerodynamic force K acting on the wing and the moment M about the quarter chord axis, both for unit span, can be written as:

$$K = \frac{\pi}{2} \cdot \rho \cdot v^2 \cdot c \cdot [k_a \cdot A + k_b \cdot B] \cdot e^{i\omega t},$$

$$M = \frac{\pi}{4} \cdot \rho \cdot v^2 \cdot c^2 \cdot [m_a \cdot A + m_b \cdot B] \cdot e^{i\omega t},$$

where $\frac{Ac}{2}$ denotes the amplitude of translation at the quarter chord axis and B the amplitude of rotation. The force K is positive when directed upward and the moment M is positive when it is nose-heavy. The theoretical values of the coefficients k_a , k_b , m_a and m_b have been obtained from ref. 1, while the experimental values of the coefficients have been obtained from ref. 5 and are given in table 1 of this report.

In order to reduce the number of degrees of freedom of the mechanical system with continuously distributed elasticity and mass from infinite to two, it has been assumed that bending and torsion are determined each by one prescribed deformation function.

Thus:

$$z = \frac{1}{2} q_1 \cdot z_1 \cdot c \cdot e^{i\omega t} \quad \text{and} \quad \varphi = q_2 \cdot \varphi_1 \cdot c \cdot e^{i\omega t},$$

where q_1 and q_2 denote the new variables and z_1 and φ_1 the assumed deformation functions for bending of the elastic axis and torsion respectively. The functions z_1 and φ_1 are given in the following table.

spanwise coordinate	0	1/8 b	2/8 b	3/8 b	4/8 b	5/8 b	6/8 b	7/8 b	b
bending z_1	0	0.0169	0.0682	0.1547	0.2752	0.4268	0.6039	0.7983	1
torsion φ_1	0	0.1490	0.3170	0.4890	0.6511	0.7921	0.9029	0.9745	1

The two equations of motion have been solved by aid of the GALERKIN procedure. The two prescribed deformation functions have also been chosen as weight functions. (RAYLEIGH-RITZ analysis).

The flutter determinant has been solved for several values of the reduced frequency ω with $\frac{v^2}{v_B^2}$ and $\frac{v^2}{v_T^2}$ as unknown quantities, where v_B and v_T are the natural angular frequencies of the wing in vacuum for bending and torsion.

The non-dimensional flutter speed coefficient $\frac{2 v_{cr}}{v_T \cdot c}$ then follows from the formula

$$\frac{2 v_{cr}}{v_T \cdot c} = \frac{1}{\omega} \sqrt{\frac{v^2}{v_B^2} \cdot \frac{v_B^2}{v_T^2}}.$$

The procedure means physically that, for an assumed value of the reduced frequency, a harmonic oscillation is only possible, when the calculated value of the ratio $\frac{v_B^2}{v_T^2}$ corresponds with the actual value of that ratio.

Several different wings have been investigated with the following values of the positions of elastic and inertia axes, EA and IA respectively, and of the relative density parameter μ .

EA	0.2 c	0.2 c	0.3 c	0.3 c	0.3 c	0.4 c	0.4 c
IA	0.4 c	0.4 c	0.4 c	0.4 c	0.4 c	0.5 c	0.5 c
μ	5	15	5	15	30	5	30

The radius of gyration of the aerofoil about the inertia axis has been chosen 0.3 c for all cases. It has been assumed that no internal damping is present.

3 Results and discussion.

The results of the calculations are given in the figures 5 to 7. In the figures 5a to 7a, the non-dimensional flutter speed coefficient $\frac{2 v_{cr}}{v_T \cdot c}$

is plotted against the ratio $\frac{v_B^2}{v_T^2}$, while in the figures 5b, c, d to 7b, c, d cross-plots of figures 5a to 7a are given for three values of $\lambda = \frac{v_B^2}{v_T^2}$.

The figures 5a to 7a show, that the experimental curves lie partly below and partly above the theoretical curves. In some cases, flutter becomes impossible for small values of the frequency ratio $\frac{v_B^2}{v_T^2}$, if the experimental coefficients are used (fig. 5a

and 6a). The boundary curve through the points of intersection between the theoretical and the experimental curves for different values of the relative density parameter μ is also plotted in the figures 5a to 7a. It is seen, that the position of these boundary curves varies for the different cases investigated. This means, that the question, whether the flutter speed is increased or decreased by using the experimental aerodynamic coefficients instead of the theoretical values, does not only depend on the parameters $\frac{v_B^2}{v_T^2}$ and μ , but also on the positions of elastic and inertia axes. From the present investigation, it is impossible to derive general rules about this change in flutter speed for the different wing configurations.

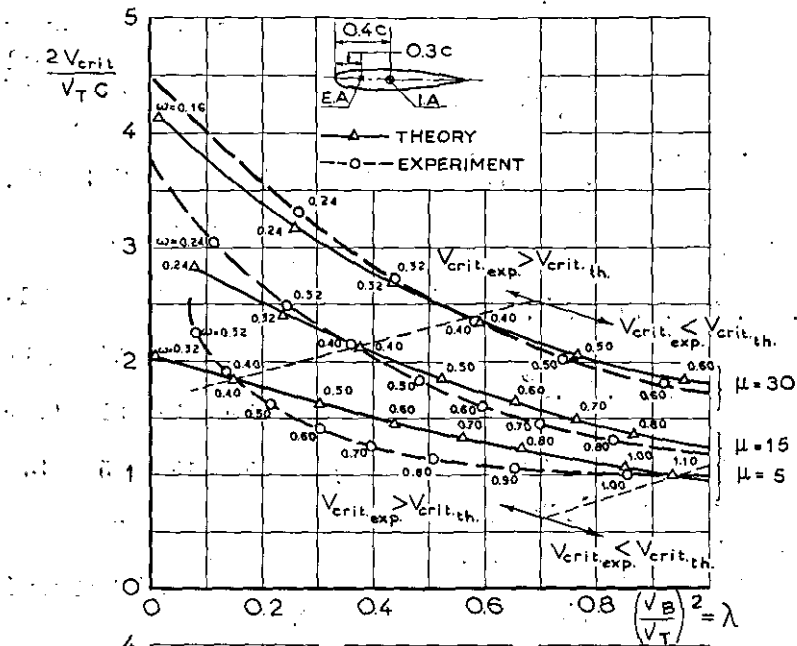


Fig. 5a.

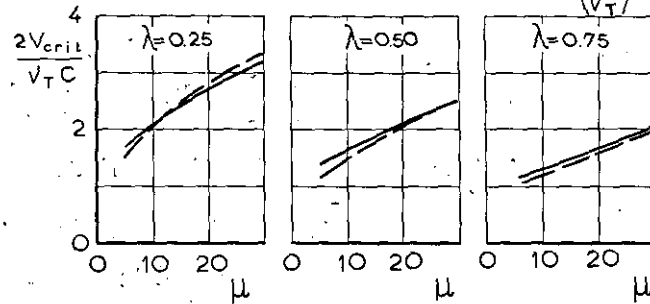


Fig. 5b

Fig. 5c

Fig. 5d

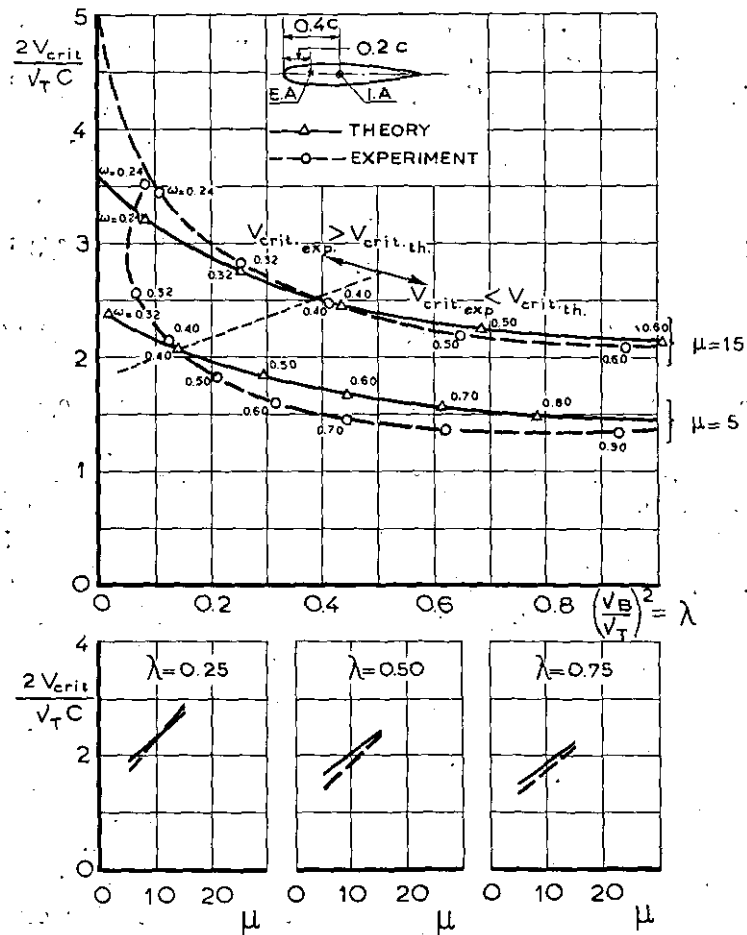


Fig. 6a.

Fig. 6b

Fig. 6c

Fig. 6d

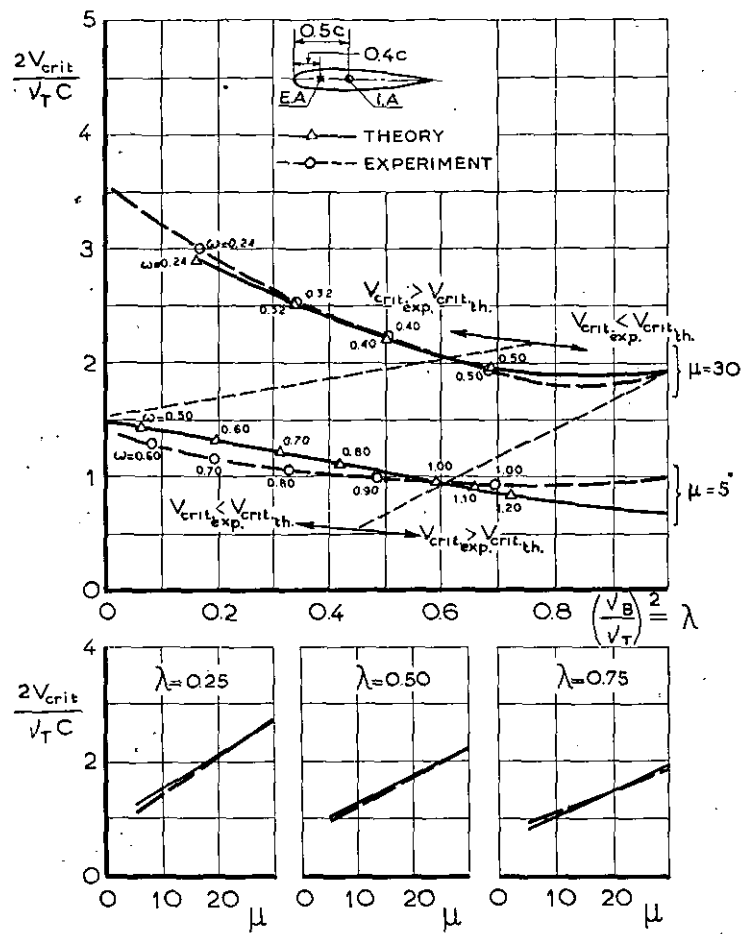


Fig. 7a.

Fig. 7b

Fig. 7c

Fig. 7d

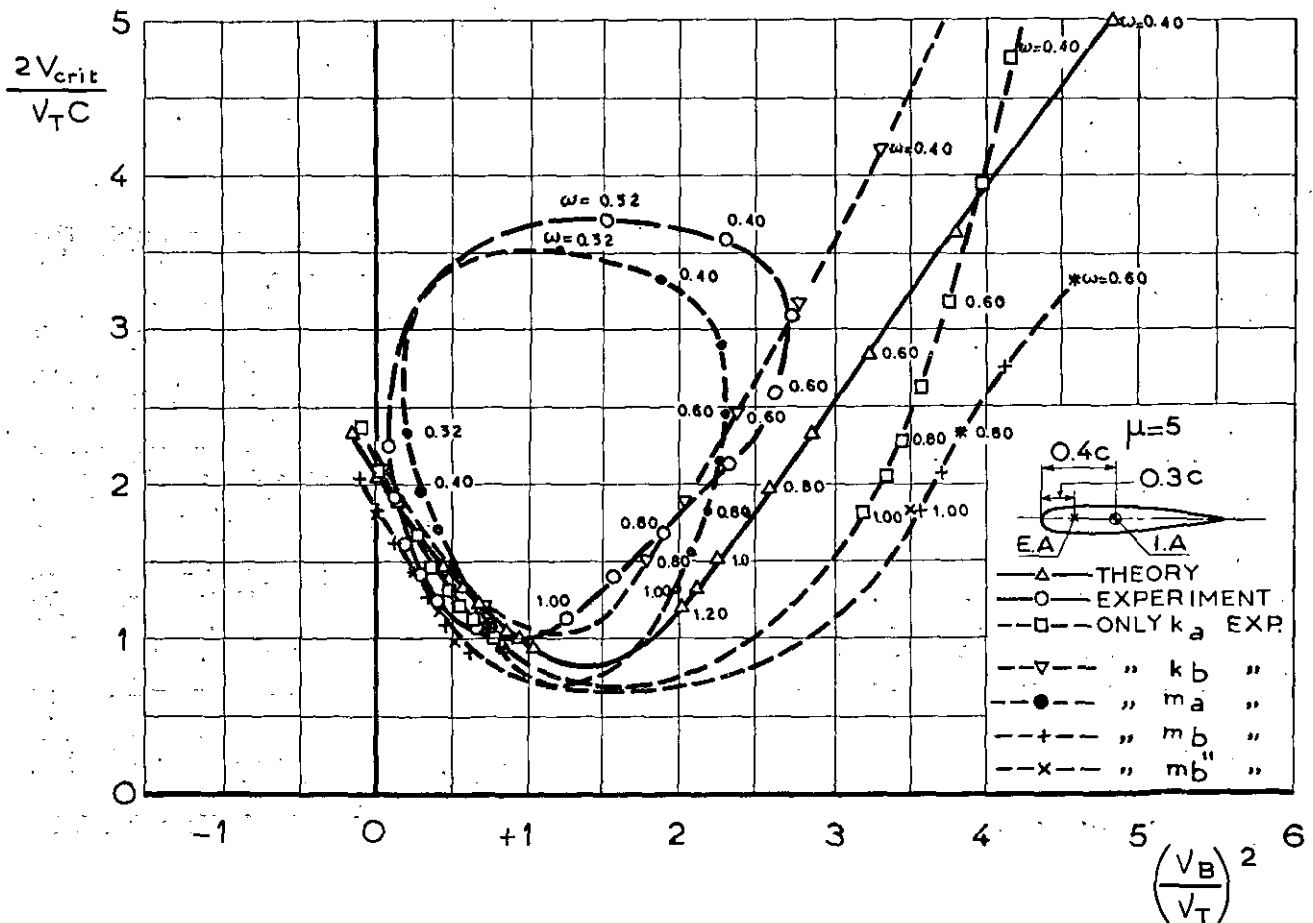


Fig. 8.

Considering the fact, that the calculations with experimental coefficients give a reduction of the theoretical flutter speed up to a maximum of 20 per cent in the cases investigated, it will be recommendable to use the experimental aerodynamic coefficients for future flutter calculations.

An analysis has been made about the influence of the separate experimental aerodynamic coefficients on the flutter speed.

This has been done by replacing alternatively one of the theoretical coefficients by an experimental one in the calculations. The results of this investigation, which has been performed only for one case, are given in figure 8. It is seen that,

for the values of the frequency ratio $\frac{v_B^2}{v_T^2}$ which

may occur in practice ($\frac{v_B^2}{v_T^2} < 1$), the imaginary

part of the coefficient m_b is chiefly responsible for the decrease of the flutter speed. The fact, that the experimental curve is closed, is caused presumably by the coefficient m_a . However, it is not certain whether this conclusion will hold also for other wing configurations.

Since the experimental aerodynamic coefficients are given only in three decimals, it can be discussed, whether this is sufficiently accurate. The results show that the points, computed with the experimental values of the aerodynamic coefficients, lie on smooth curves without any perceptible scatter. Therefore, it may be concluded that the given experimental aerodynamic coefficients are accurate enough for flutter calculations.

4. Final remark.

The question can rise, whether flutter experiments would give results, which agree with the flutter speed, calculated with the experimental aerodynamic coefficients. Though it will be considered, whether such experiments will be carried out in due time, it may be remarked, that some reasons exist, which make it probable that the experiments will confirm the calculations. The first reason is, that the experimental aerodynamic coefficients have been determined from the equation of motion by measuring the response of a wing model, which is given forced motions by means of springs ("forcing through a spring"). Since in flutter experiments also the response of the model is measured and since, moreover, the assumption of linearity of the system has been confirmed in the present experiments, it may be expected that the experimental flutter speed agrees with the calculated one.

Finally, it may be added, that in the experiments the REYNOLDS number had only a small influence, provided that the boundary layer transition was fixed by a disturbance wire (ref. 2).

5 Conclusions.

The following conclusions can be drawn from the present investigation:

- i It is recommendable to use the experimental aerodynamic coefficients, because the discrepancies, as compared with theory, are not negligible. A decrease in flutter speed up to 20 per cent is found by using the experimental coefficients instead of the theoretical ones.
- ii For flutter calculations, the given experimental aerodynamic coefficients have a sufficient accuracy.

6 List of symbols.

- A amplitude of translation at the quarter chord axis divided by semi-chord.
- B amplitude of rotation.
- K aerodynamic force on the wing per unit span.
- M aerodynamic moment about the quarter chord axis per unit span.
- b semi-span.
- c chord.
- t time.
- v airspeed.
- v_{cr} flutter speed.
- z translation of the elastic axis.
- z_1 prescribed function of translation of the quarter chord axis.
- μ relative density parameter (ratio of wing mass to mass of cylinder of air with diameter equal to wing chord).
- ν frequency (rad/sec).
- ν_B uncoupled angular frequency of wing bending in vacuum.
- ν_T uncoupled angular frequency of torsional vibration about the elastic axis in vacuum.
- ρ air density.
- φ coordinate of rotation.
- φ_1 prescribed function of rotation.
- ω reduced frequency $\left(\frac{\nu \cdot c}{2 \cdot v}\right)$.

7 List of references.

- 1 KÜSSNER, H. G. Zusammenfassender Bericht über den instationären Auftrieb von Flügeln. Luftfahrtforschung. Vol. 13, p. 140, 1936.
- 2 GREIDANUS, J. H., v. D. VOOREN, A. I. and BERGH, H. Experimental Determination of the Aerodynamic Coefficients of an Oscillating Wing in Incompressible, Two-Dimensional Flow. Part I. Wing with Fixed Axis of Rotation. Nat. Aero. Res. Inst. Rep. F. 101, 1952.
- 3 v. D. VOOREN, A. I. and BERGH, H. Experimental Determination of the Aerodynamic Coefficients of an Oscillating Wing in Incompressible, Two-Dimensional Flow. Part II. Wing with Moving Axis of Rotation. Nat. Aero. Res. Inst. Rep. F. 102, 1952.
- 4 BERGH, H. Experimental Determination of the Aerodynamic Coefficients of an Oscillating Wing in Incompressible, Two-Dimensional Flow. Part III. Experiments at Zero Airspeed. Nat. Aero. Res. Inst. Rep. F. 103, 1952.
- 5 BERGH, H. and v. D. VOOREN, A. I. Experimental Determination of the Aerodynamic Coefficients of an Oscillating Wing in Incompressible, Two-Dimensional Flow. Part IV. Calculation of the Coefficients. Nat. Aero. Res. Inst. Rep. F. 104, 1952.

Completed: November 1952.

REPORT F. 118

Influence of Compressibility on the Calculated Flexure-Torsion Flutter Speed of a Family of Rectangular Cantilever Wings

by

J. IJFF.

Summary.

The flutter speed of 27 wings with different positions of elastic and inertia axes and different values of the relative density parameter has been calculated for three values of the Mach number.

It has been found that the influence of compressibility can be as well favorable as unfavorable, depending upon the case investigated. All results are presented in a number of diagrams which also show the influence of the other parameters on the flutter speed.

Contents.

- 1 Introduction.
- 2 Procedure.
- 3 Influence of compressibility on flutter speed.
- 4 Influence of other parameters on the flutter speed.
- 5 Conclusions.
- 6 List of symbols.
- 7 List of references.

30 figures.

This investigation has been performed by order of the Netherlands Aircraft Development Board (N.I.V.).

1 Introduction.

The rise of aeroplane speeds during the last two decennaries has made flutter calculations, based on the aerodynamic theory of a compressible flow, of increasing importance.

Now that the aerodynamic theory of an oscillating wing in two-dimensional subsonic compressible flow has been developed by TIMMAN in a rigorous analytical way and the numerical results of that theory have become available (ref. 1), it is possible to correctly investigate the influence of compressibility upon the flutter speed.

For this purpose a number of flutter calculations, referring to rectangular wings with various values of the relative density parameter, the positions of elastic and inertia axes and the flexural-torsional stiffness ratio, has been performed for the Mach numbers 0, 0.5 and 0.7.

This work can be seen as a continuation of older work (ref. 2) carried out at the Nat. Aero. Res. Inst., where only incompressible flow was considered. Besides the introduction of compressibility, a further difference with ref. 2 is that the wings of ref. 2 have a taper ratio of $1/3$. The reason for this difference is that calculations for a tapered wing would have required the aerodynamic coefficients in a compressible flow to be known for more values of the reduced frequency ω than are given in ref. 1. This would compel to extensive interpolation in the tables of ref. 1, which has been performed in the mean time, but which was not yet available when commencing the present investigation.

This difference entails the additional advantage of permitting a comparison between the flutter speeds for a rectangular and a tapered wing, provided the flow is incompressible.

Results obtained will also be compared with those of GARRICK (ref. 3), who has made some flutter calculations based on aerodynamic coefficients as computed by FRASER and SKAN from POSSIO's integral equation.

2 Procedure.

Calculations for bending-torsion flutter of rectangular wings, rigidly fixed at the root, and moving in a non-viscous compressible fluid, have been performed on the basis of the aerodynamic theory of ref. 1. The aerodynamic forces and moments, acting on the three-dimensional wings, have been obtained by aid of strip-theory.

Bending and torsion are determined by one prescribed deformation function each, thus introducing a system of two degrees of freedom. The assumed deformation functions are given in the following table:

spanwise coordinate	0	1/8 b	2/8 b	3/8 b	4/8 b	5/8 b	6/8 b	7/8 b	b
bending	0	0.0169	0.0682	0.1547	0.2752	0.4268	0.6039	0.7983	1
torsion	0	0.1490	0.3170	0.4890	0.6511	0.7921	0.9029	0.9745	1

The two equations of motion have been solved by aid of the GALERKIN procedure. The weight functions have been taken identically to the deformation functions. (RAYLEIGH-RTZ analysis).

The flutter determinant has been solved for several assumed values of the reduced frequency ω with $\frac{v_B^2}{v_T^2}$ and $\frac{v^2}{v_B^2}$ as unknown quantities. v_B and v_T are the uncoupled frequencies of the wing for bending and torsion in vacuum. The non-dimensional flutter speed $\frac{2v}{v_T \cdot c}$ then follows from the formula

$$\frac{2v_{cr}}{v_T \cdot c} = \frac{1}{\omega} \sqrt{\frac{v_B^2}{v_T^2} \cdot \frac{v^2}{v_B^2}}$$

In this way results are obtained which have the physical meaning that for the chosen value of the reduced frequency ω those values of the ratio $\frac{v_B^2}{v_T^2}$ are determined, for which the wing can perform a harmonic oscillation.

Mathematically it is possible that a negative value of $\frac{v_B^2}{v_T^2}$ will be found, but it will be clear that no physical meaning can be ascribed to negative values of $\frac{v_B^2}{v_T^2}$. In actual wing constructions the values of $\frac{v_B^2}{v_T^2}$ will range from 0 to about 1.

The positions of the elastic axis (EA), the inertia axis (IA) and the value of the relative density parameter μ have been varied and the following values have been used:

EA	0.2 c	0.3 c	0.4 c
IA	0.3 c	0.4 c	0.5 c
μ	5	15	30

Thus the flutter speed has been calculated for 27 cases, each for three values of the Mach number.

The radius of gyration of the aerofoil about the inertia axis has been assumed to be 0.3 c for all positions of the inertia axis. Internal damping has been neglected in all cases.

The results of the flutter calculations are given in the figs. 1 to 30. The non-dimensional flutter speed $\frac{2v}{v_T \cdot c}$ has been plotted against the ratio $\frac{v_B^2}{v_T^2}$ in the figs. 1 to 27 for each combination of the

parameters which have been varied. Six combinations show no flutter possibility at all ($EA = IA = 0.3$ c and $EA = 0.4$ c, $IA = 0.3$ c).

In fig. 28 the non-dimensional flutter speed $\frac{2v}{v_T \cdot c}$ has been plotted against the relative density parameter μ for three values of the stiffness ratio $\frac{v_B^2}{v_T^2}$ (1, 0.5, 0). In the same way the non-dimensional flutter speed $\frac{2v}{v_T \cdot c}$ has been plotted in fig. 29 against the position of the inertia axis and in fig. 30 against the position of the elastic axis.

It is possible that for a certain value of the airspeed, the divergence speed, the steady moment of the aerodynamic forces about the elastic axis exceeds the restraining elastic moment (static instability). By putting $v = 0$ (and $\omega = 0$) in the flutter determinant it is possible to calculate the divergence speed and the results of that calculations can also be found in the figs. 1 to 27, where it is seen that the divergence speed is independent of the ratio $\frac{v_B}{v_T}$.

It will be clear that the divergence speed forms an upper limit to the speed range of the wing, just as the flutter speed, but it is seen that in all cases where a finite flutter speed is found the flutter speed is the lower limit.

The divergence speed increases with the relative density parameter μ . This can be explained, since the increase in μ can be realized either by decreasing air density or by increasing wing density; in the first case the aerodynamic forces are diminished, while in the second case the elastic moment is increased.

When the elastic axis lies forward of the quarter chord axis, the moment of the aerodynamic forces is always stabilizing and thus the divergence speed is infinite (cases 1 to 9).

3 Influence of compressibility on flutter speed.

In ref. 4 it is suggested that the effect of compressibility can be taken into account by adding a correction factor $\sqrt{1-M^2}$, based on the PRANDTL-GLAUERT rule, to the critical speed, determined by aid of an incompressible aerodynamic theory. This means that compressibility would always lower the flutter speed.

However, it has been shown by GARRICK (ref. 3) and it is confirmed by the more complete calculations in this report that, depending on the value of other parameters (stiffness ratio and relative density parameter), compressibility may as well rise as lower the flutter speed.

It follows from figs. 1 to 27 that compressibility is favorable if $v_B > v_T$; however, for the more important region $v_B < v_T$ its favorable effect exists only for values of the relative density parameter μ smaller than 15 (see fig. 28). In general, the conclusion of GARRICK (ref. 3) that the influence of compressibility is small, can be retained if $v_B < v_T$, though there are some cases where larger differences appear (e.g. $EA = 0.2$ c, $IA = 0.3$ c and $EA = IA = 0.4$ c).

In conclusion, it may be remarked that present airworthiness requirements for flutter speeds in compressible flow, which are based on the PRANDTL-GLAUERT rule, will in most cases be far too conservative for large Mach numbers.

4 Influence of other parameters on the flutter speed.

Although these calculations have been primarily intended to study the influence of compressibility on the flutter speed, it is possible to study also the influence of some other parameters, viz. positions of elastic and inertia axes, relative density parameter μ , uncoupled wing frequencies v_B and v_T of the first uncoupled bending and torsion mode and the taper.

Some conclusions about the influence of these parameters on the flutter speed can be taken from the older NLL work (ref. 2), while a general survey of British work has been presented by WILLIAMS (ref. 5).

Since in an early stage of the development of a new design it is very difficult to obtain rather accurate data concerning the positions of the elastic and inertia axes, it is important to know how the flutter speed varies with the positions of elastic and inertia axes. This can be found in figs. 29 and 30. The following conclusions can be drawn:

- a) for positions of the elastic axis aft of the inertia axis no flutter is possible unless both axes are far behind the quarter chord axis (e.g. is 0.4 c). In the latter case, the aerodynamic coupling may induce flutter. Hence it is more advisable to diminish the distance between the two axes by shifting forward the inertia axis than by shifting backward the elastic axis.
- b) varying the position of the elastic axis ahead of the position of the inertia axis, it is seen (fig. 30) that there exists a minimum in flutter speed when the distance between both axes is about 0.1 c. As this is a common case it is seen that either a small variation in the position of the elastic axis or a small variation in the position of the inertia axis causes in general very small variations in the flutter speed.

A further important parameter in a flutter calculation is the relative density parameter μ .

It follows from fig. 28 that in general an increase in μ causes an increase in flutter speed, provided the frequencies are kept constant. This, for instance, is realised when the air density ρ is

diminished. The same is found in ref. 2 for a wing with a taper ratio of $1/3$, but the increase in flutter speed with μ is slower in the case of ref. 2. This result is confirmed by the measurements of refs. 6 and 7.

The increase in flutter speed with increasing value of μ is such that the critical dynamic pressure $\frac{1}{2} \rho v^2$ decreases towards an asymptotic value.

This conclusion, which holds independently whether μ increases by decrease of air density or by increase of wing density, provided this occurs uniformly all over the wing, can be shown as follows:

Let it first be assumed that the non-dimensional flutter speed coefficient $\frac{2v}{v_T \cdot c}$ varies proportionally to $\sqrt{\mu}$. Since $\mu = \frac{m}{\rho} = \frac{\text{constant}}{\rho v_T^2}$, it follows

immediately that $\frac{1}{2} \rho v^2$ will be constant. As in reality the flutter speed coefficient increases less than proportionally to $\sqrt{\mu}$, the conclusion is that $\frac{1}{2} \rho v^2$ decreases slightly with increasing μ .

The influence of the uncoupled frequencies of bending and torsion v_B and v_T on the flutter speed can be examined from figs. 1 to 27. It must be kept in mind that the values of $\frac{v_B^2}{v_T^2}$, occurring in actual wing constructions, are nearly always smaller than 1 and hence, only the part of the diagrams for which $\frac{v_B^2}{v_T^2}$ is between 0 and 1, has to be considered.

When the bending frequency v_B is increased, the flutter speed will first decrease to a certain minimum and then increase to infinity. The minimum is in nearly all cases of any importance found at values of $\frac{v_B^2}{v_T^2}$ between 0.6 and 1.4 and hence it

may be concluded that for actual values of $\frac{v_B^2}{v_T^2}$ an increase in v_B will decrease the flutter speed.

It is well known that one of the most effective ways in which v can be increased is to increase the torsional stiffness, i.e. v_T .

Indeed, if all other parameters, including the ratio $\frac{v_B^2}{v_T^2}$, are kept constant, the flutter speed will

be proportional to v_T . If, however, v_B and not $\frac{v_B^2}{v_T^2}$ is kept constant, it follows from nearly all figures that for $\frac{v_B}{v_T}$ between 0 and 1, the flutter speed increases more than proportionally to v_T .

For other values of the Mach number the same conclusions hold. As has already been mentioned in sec. 3, the influence of compressibility on the flutter speed is changing at a certain value of $\frac{v_B^2}{v_T^2}$ from unfavorable to favorable.

The results of the present calculations referring to $M = 0$ have been compared with those of ref. 2, were a wing with a taper ratio of $1/3$ (tip chord = $1/3$ root chord) was considered. Comparing a rectangular wing and a tapered wing with equal mean

area, i.e. equal mean chord, and taper ratio $1/3$, it follows that the ordinates of the figures in ref. 2 must be multiplied by a factor 1.5, since the flutter speed is then made dimensionless in both cases by aid of the mean semi-chord. This leads to the dotted lines in figs. 1 to 27. It is seen that in the region $0 < \frac{v_B}{v_T} < 1$ the tapered wing, in general, has a smaller flutter speed than the rectangular wing if v_T and v_B are assumed to be the same.

To simplify the evaluation of the aerodynamic forces, flutter calculations for a tapered wing are sometimes made by assuming a rectangular wing with the same reference chord as the tapered wing. The reference section is usually taken at $0.75 b$. For comparing results the ordinates of the figures in ref. 2 have to be multiplied by 2, i.e. the ordinates of the dotted lines in the present report by 1.33. It then follows that the dotted lines come usually above the drawn lines for $M=0$ and hence, the approximation by a rectangular wing of the same reference chord at $y=0.75 b$ and the same uncoupled frequencies will mostly be conservative. Taking the chord of the rectangular wing equal to that of the tapered wing in the section $y=0.7 b$, would for taper ratio $1/3$ yield results which, on the average, are slightly better.

The conclusion that a tapered wing has a smaller flutter speed than a rectangular wing of equal area and frequencies is in agreement with ref. 8, where the same conclusion is reached for a coefficient $K = \frac{v}{v_T c}$, \bar{v}_T denoting the coupled torsional frequency. It is shown also in ref. 8, that if instead of frequencies stiffnesses are kept constant, the flutter speed increases if the wing becomes more highly tapered.

5. Conclusions.

The flutter speed of 27 rectangular wings with different positions of elastic and inertia axes and different values of the relative density parameter has been calculated for Mach numbers equal to 0, 0.5 and 0.7. The main conclusions are:

- 1°) For values of μ smaller than 15 the influence of compressibility on the flutter speed is favorable, but for larger values of μ the effect may be adverse, especially if $v_B < v_T$.
- 2°) The well known fact, that increase in the relative density parameter μ causes an increase in the flutter speed, is not generally valid when compressibility has been taken into account. Then, there are cases where a minimum in flutter speed exists for a certain value of μ .
- 3°) The rapid increase in flutter speed, which occurs when the inertia and elastic axes approach each other, is, in general, more pronounced for higher Mach numbers.

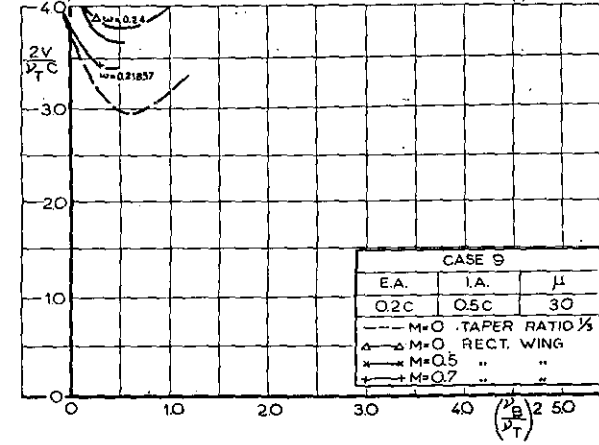
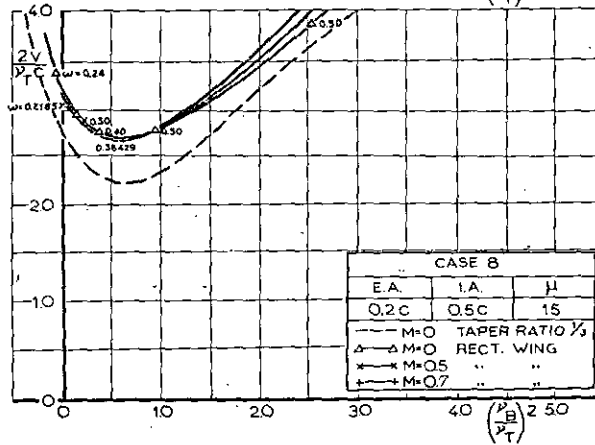
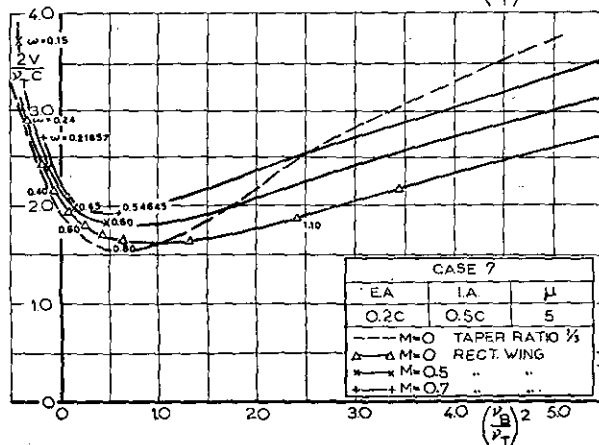
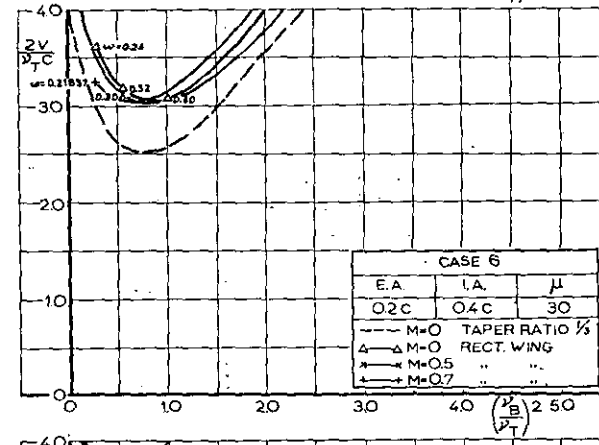
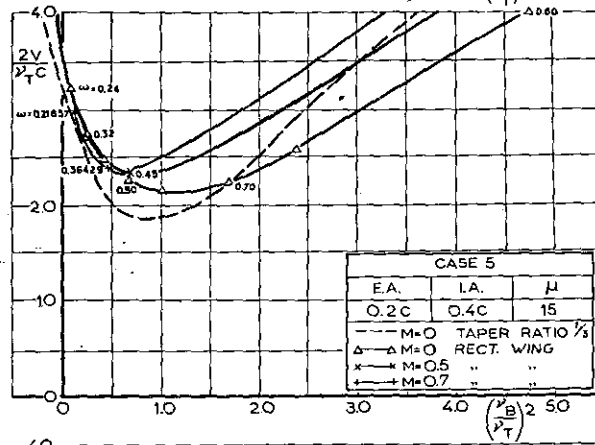
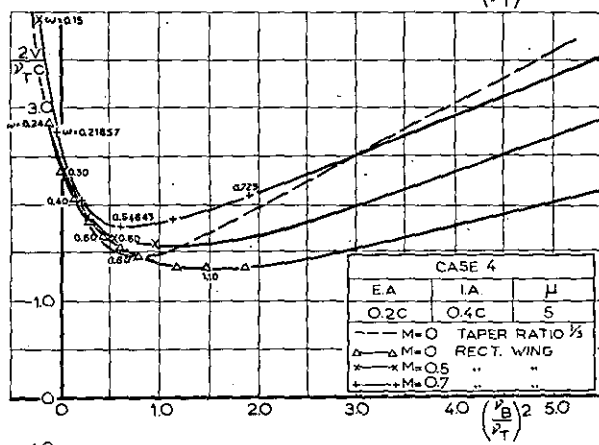
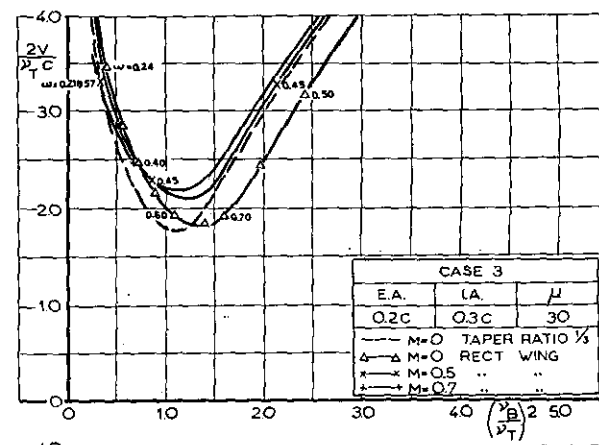
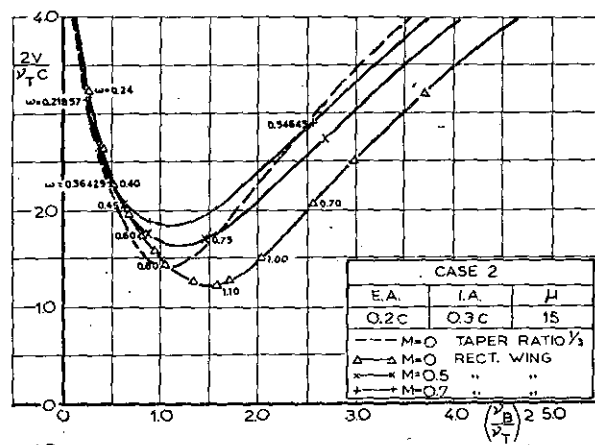
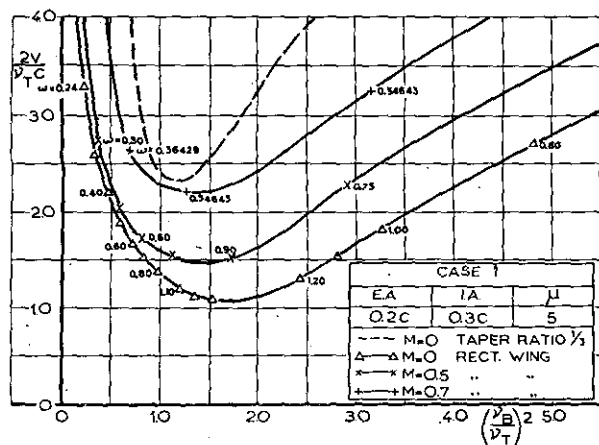
- 4°) The conclusion that for fixed position of the inertia axis and varied position of the elastic axis, the flutter speed becomes minimal if the elastic axis lies about $0.1 c$ ahead of the inertia axis, holds for all Mach numbers.
- 5°) In the actual range of values of the ratio of the bending and the torsional frequency $\frac{v_B}{v_T}$ (from 0 to 1), an increase in bending frequency decreases the flutter speed while increase in torsional frequency increases this speed very rapidly. This conclusion holds also for all Mach numbers, though both effects are less pronounced for values of the ratio $\frac{v_B^2}{v_T^2}$ near 1, if the Mach number is higher.

6. List of symbols.

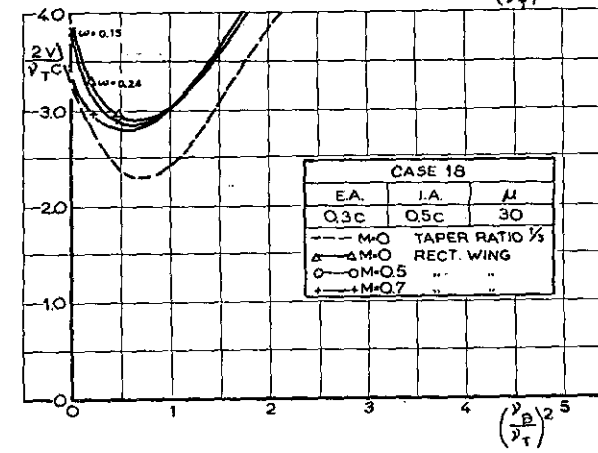
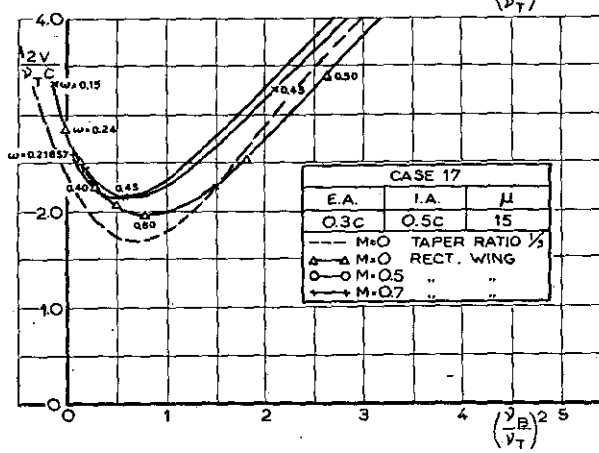
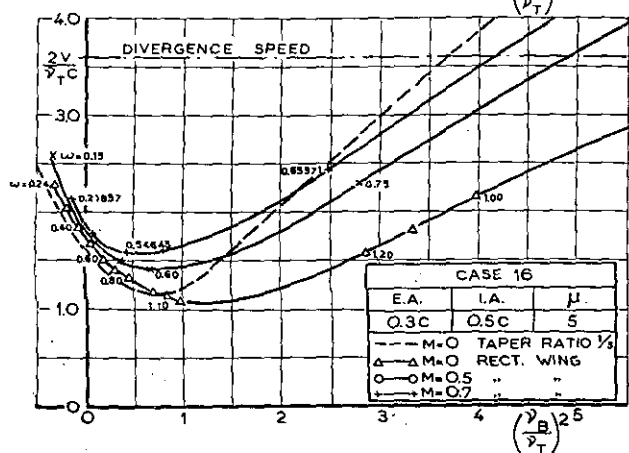
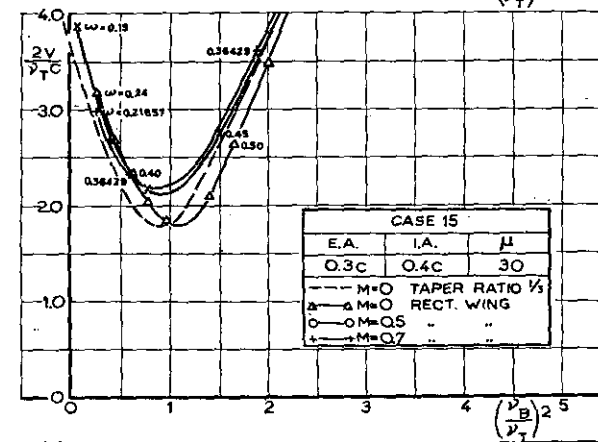
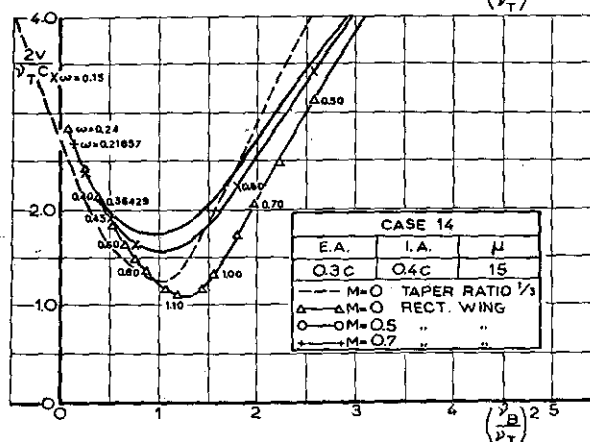
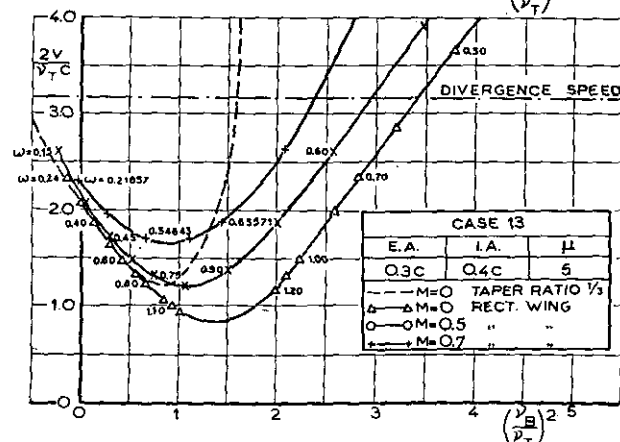
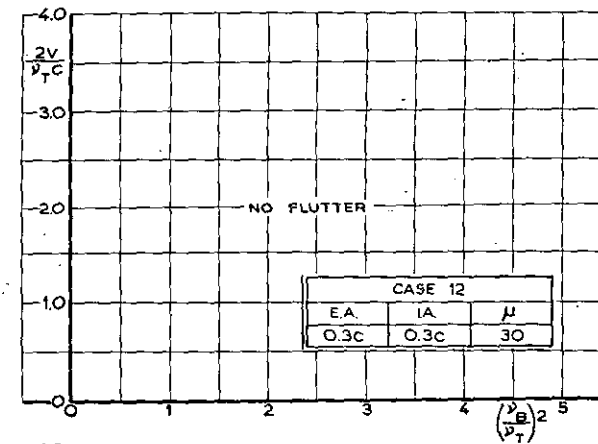
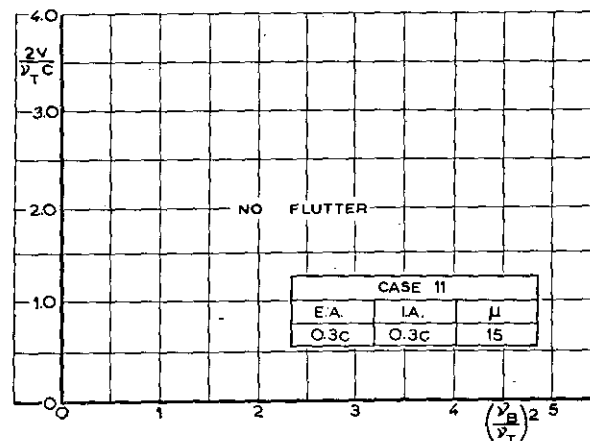
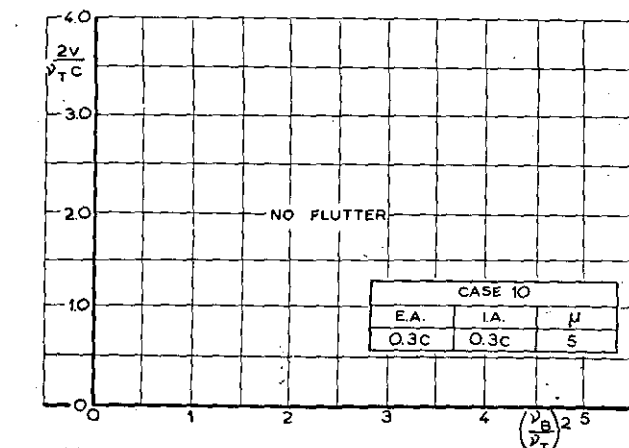
- M — Mach number.
 b — semi span.
 c — wing chord.
 l — semi chord.
 v — flutter speed.
 μ — relative density parameter (ratio of mass of wing to mass of cylinder of air of diameter equal to chord of wing, both taken for equal length along span).
 \dot{v} — frequency (rad/sec).
 v_B — uncoupled frequency of wing bending in vacuum (rad/sec).
 v_T — uncoupled frequency of torsional vibrations about the elastic axis, in vacuum (rad/sec).
 ρ — air density.
 ω — reduced frequency $\frac{v l}{v}$.

7. List of references.

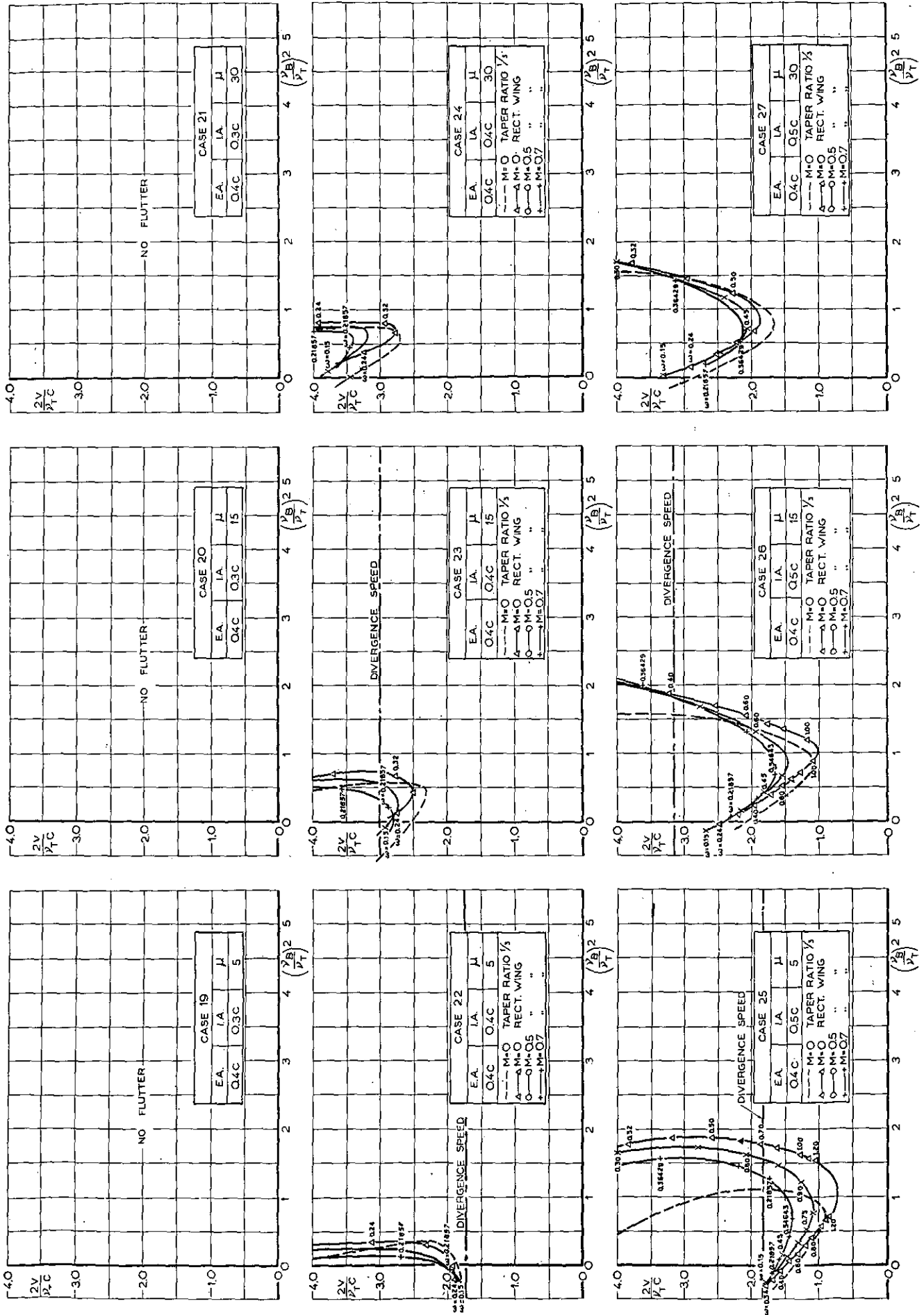
1. TEMMAN, R., VAN DE VOOREN, A. I. and GREIDANUS, J. H. "Aerodynamic Coefficients of an Oscillating Airfoil in Two-Dimensional Subsonic Flow". J. Aero. Sci. 18, no. 12, Dec. 1951.
2. VAN DE VOOREN, A. I. and GREIDANUS, J. H. "Diagrams of Critical Flutter Speed for Wings of a Certain Standard Type". Report V. 1297, Nat. Aero. Res. Inst., Amsterdam 1947.
3. GARRICK, I. E. "Bending-Torsion Flutter Calculations Modified by Subsonic Compressibility Corrections". NACA TR 836, 1946.
4. THEODORSEN, T. and GARRICK, I. E. "Mechanism of Flutter — A Theoretical and Experimental Investigation of the Flutter Problem". NACA TR 685, 1940.
5. WILLIAMS, J. "Aircraft Flutter". R. and M 2492, 1948.
6. CASTLE, G. E. and HERR, R. W. "Some Effects of Density and Mach Number on the Flutter Speed of Two Uniform Wings". NACA TN 1989, 1949.
7. WOOLSTON, D. S. and CASTLE, G. E. "Some Effects of Variations in Several Parameters Including Fluid Density, on the Flutter Speed of Light Uniform Cantilever Wings". NACA TN 2558, 1951.
8. DUNCAN, W. J. and GRIFFITH, C. L. T. "The Influence of Wing Taper on the Flutter of Cantilever Wings". R and M 1869, 1939.



Figs. 1-9.



Figs. 10-18.



Figs. 19-27.

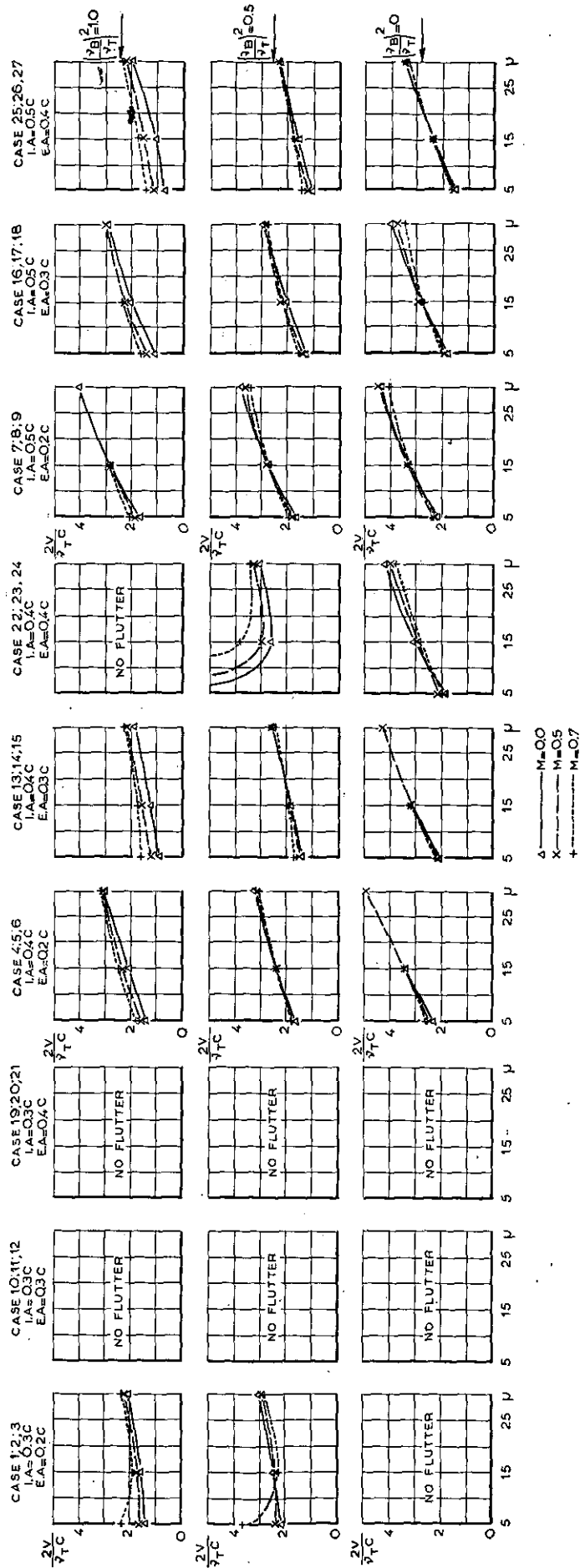


Fig. 28

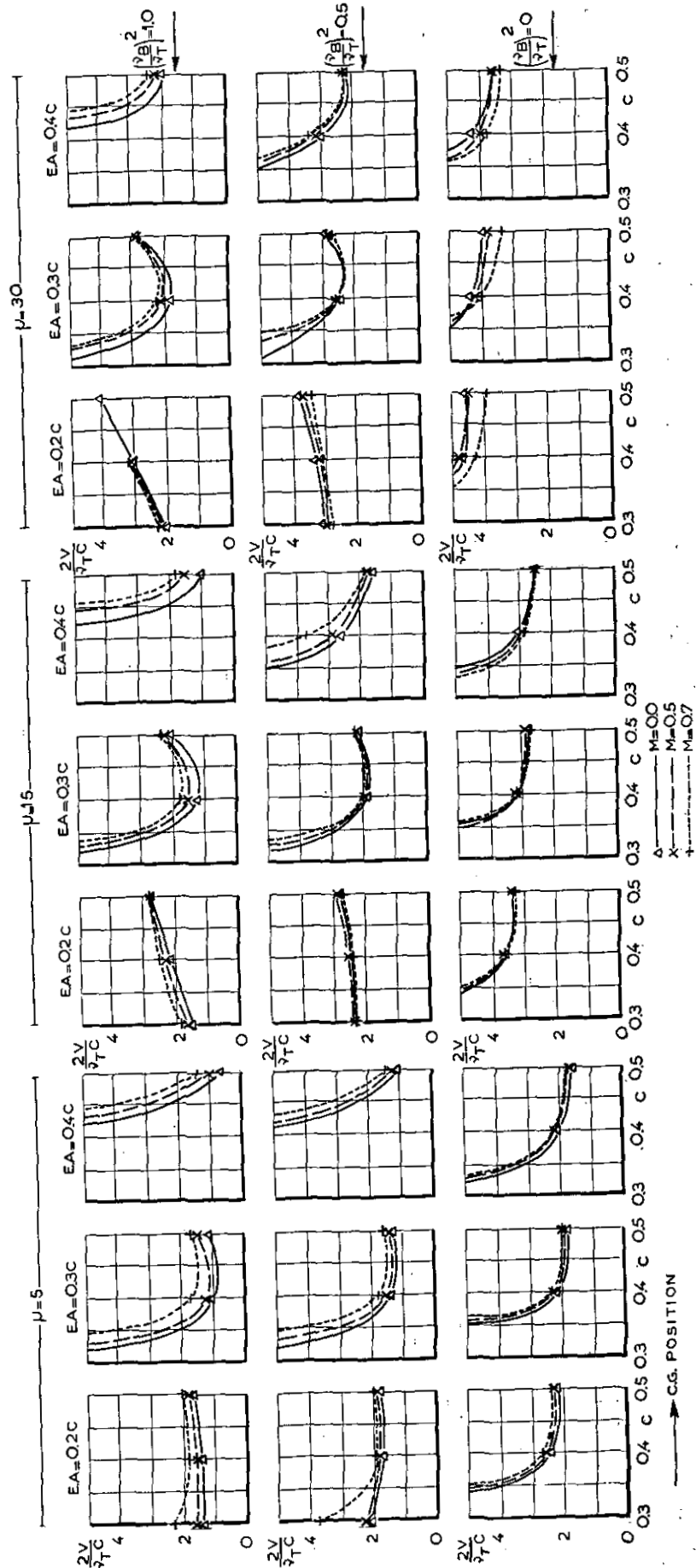


Fig. 29

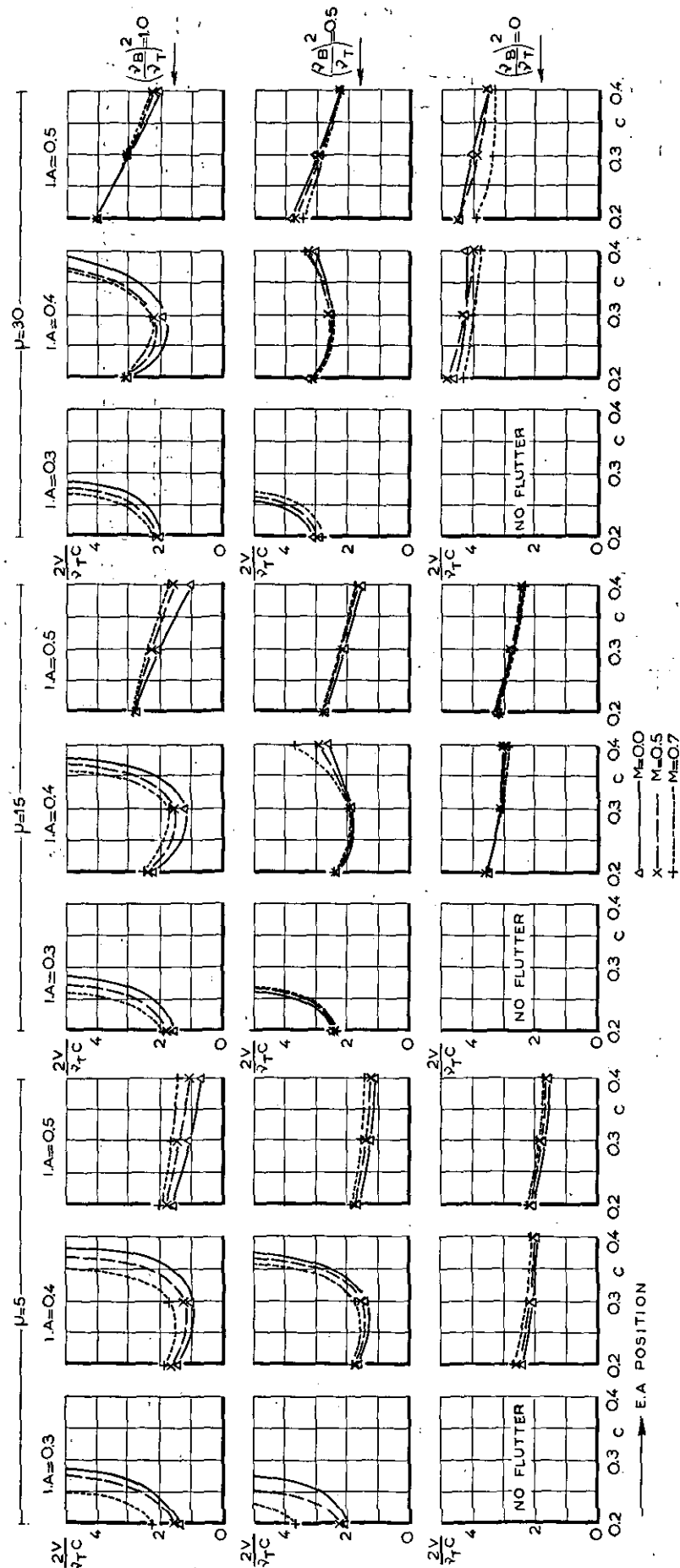


Fig. 30

REPORT F.118

Influence of Compressibility on the Calculated Flexure-Torsion Flutter Speed of a Family of Rectangular Cantilever Wings

by

J. IJFF.

Summary.

The flutter speed of 27 wings with different positions of elastic and inertia axes and different values of the relative density parameter has been calculated for three values of the Mach number.

It has been found that the influence of compressibility can be as well favorable as unfavorable, depending upon the case investigated. All results are presented in a number of diagrams which also show the influence of the other parameters on the flutter speed.

Contents.

- 1 Introduction.
 - 2 Procedure.
 - 3 Influence of compressibility on flutter speed.
 - 4 Influence of other parameters on the flutter speed.
 - 5 Conclusions.
 - 6 List of symbols.
 - 7 List of references.
- 30 figures.

This investigation has been performed by order of the Netherlands Aircraft Development Board (N. I. V.).

1 Introduction.

The rise of aeroplane speeds during the last two decennaries has made flutter calculations, based on the aerodynamic theory of a compressible flow, of increasing importance.

Now that the aerodynamic theory of an oscillating wing in two-dimensional subsonic compressible flow has been developed by TIMMAN in a rigorous analytical way and the numerical results of that theory have become available (ref. 1), it is possible to correctly investigate the influence of compressibility upon the flutter speed.

For this purpose a number of flutter calculations, referring to rectangular wings with various values of the relative density parameter, the positions of elastic and inertia axes and the flexural-torsional stiffness ratio, has been performed for the Mach numbers 0, 0.5 and 0.7.

This work can be seen as a continuation of older work (ref. 2) carried out at the Nat. Aero. Res. Inst., where only incompressible flow was considered. Besides the introduction of compressibility, a further difference with ref. 2 is that the wings of ref. 2 have a taper ratio of $1/3$. The reason for this difference is that calculations for a tapered wing would have required the aerodynamic coefficients in a compressible flow to be known for more values of the reduced frequency ω than are given in ref. 1. This would compel to extensive interpolation in the tables of ref. 1, which has been performed in the mean time, but which was not yet available when commencing the present investigation.

This difference entails the additional advantage of permitting a comparison between the flutter speeds for a rectangular and a tapered wing, provided the flow is incompressible.

Results obtained will also be compared with those of GARRICK (ref. 3), who has made some flutter calculations based on aerodynamic coefficients as computed by FRASER and SKAN from POSSIO's integral equation.

2 Procedure.

Calculations for bending-torsion flutter of rectangular wings, rigidly fixed at the root, and moving in a non-viscous compressible fluid, have been performed on the basis of the aerodynamic theory of ref. 1. The aerodynamic forces and moments, acting on the three-dimensional wings, have been obtained by aid of strip-theory.

Bending and torsion are determined by one prescribed deformation function each, thus introducing a system of two degrees of freedom. The assumed deformation functions are given in the following table:

spanwise coordinate	0	1/8 b	2/8 b	3/8 b	4/8 b	5/8 b	6/8 b	7/8 b	b
bending	0	0.0169	0.0682	0.1547	0.2752	0.4268	0.6039	0.7983	1
torsion	0	0.1490	0.3170	0.4890	0.6511	0.7921	0.9029	0.9745	1

The two equations of motion have been solved by aid of the GALERKIN procedure. The weight functions have been taken identically to the deformation functions. (RAYLEIGH-RITZ analysis).

The flutter determinant has been solved for several assumed values of the reduced frequency ω with $\frac{v_B^2}{v_T^2}$ and $\frac{v^2}{v_B^2}$ as unknown quantities. v_B and v_T are the uncoupled frequencies of the wing for bending and torsion in vacuum. The non-dimensional flutter speed $\frac{2v}{v_T \cdot c}$ then follows from the formula

$$\frac{2v_{cr}}{v_T \cdot c} = \frac{1}{\omega} \sqrt{\frac{v_B^2}{v_T^2} \cdot \frac{v^2}{v_B^2}}$$

In this way results are obtained which have the physical meaning that for the chosen value of the reduced frequency ω those values of the ratio $\frac{v_B^2}{v_T^2}$ are determined, for which the wing can perform a harmonic oscillation.

Mathematically it is possible that a negative value of $\frac{v_B^2}{v_T^2}$ will be found, but it will be clear that no physical meaning can be ascribed to negative values of $\frac{v_B^2}{v_T^2}$. In actual wing constructions the values of $\frac{v_B^2}{v_T^2}$ will range from 0 to about 1.

The positions of the elastic axis (EA), the inertia axis (IA) and the value of the relative density parameter μ have been varied and the following values have been used:

EA	0.2 c	0.3 c	0.4 c
IA	0.3 c	0.4 c	0.5 c
μ	5	15	30

Thus the flutter speed has been calculated for 27 cases, each for three values of the Mach number.

The radius of gyration of the aerofoil about the inertia axis has been assumed to be 0.3 c for all positions of the inertia axis. Internal damping has been neglected in all cases.

The results of the flutter calculations are given in the figs. 1 to 30. The non-dimensional flutter speed $\frac{2v}{v_T \cdot c}$ has been plotted against the ratio $\frac{v_B^2}{v_T^2}$ in the figs. 1 to 27 for each combination of the

parameters which have been varied. Six combinations show no flutter possibility at all ($EA = IA = 0.3 c$ and $EA = 0.4 c$, $IA = 0.3 c$).

In fig. 28 the non-dimensional flutter speed $\frac{2v}{v_T \cdot c}$ has been plotted against the relative density parameter μ for three values of the stiffness ratio $\frac{v_B^2}{v_T^2}$ (1, 0.5, 0). In the same way the non-dimensional flutter speed $\frac{2v}{v_T \cdot c}$ has been plotted in fig. 29 against the position of the inertia axis and in fig. 30 against the position of the elastic axis.

It is possible that for a certain value of the airspeed, the divergence speed, the steady moment of the aerodynamic forces about the elastic axis exceeds the restraining elastic moment (static instability). By putting $v = 0$ (and $\omega = 0$) in the flutter determinant it is possible to calculate the divergence speed and the results of that calculations can also be found in the figs. 1 to 27, where it is seen that the divergence speed is independent of the ratio $\frac{v_B}{v_T}$.

It will be clear that the divergence speed forms an upper limit to the speed range of the wing, just as the flutter speed, but it is seen that in all cases where a finite flutter speed is found the flutter speed is the lower limit.

The divergence speed increases with the relative density parameter μ . This can be explained, since the increase in μ can be realized either by decreasing air density or by increasing wing density; in the first case the aerodynamic forces are diminished, while in the second case the elastic moment is increased.

When the elastic axis lies forward of the quarter chord axis, the moment of the aerodynamic forces is always stabilizing and thus the divergence speed is infinite (cases 1 to 9).

3 Influence of compressibility on flutter speed.

In ref. 4 it is suggested that the effect of compressibility can be taken into account by adding a correction factor $\sqrt{1-M^2}$, based on the PRANDTL-GLAUERT rule, to the critical speed, determined by aid of an incompressible aerodynamic theory. This means that compressibility would always lower the flutter speed.

However, it has been shown by GARRICK (ref. 3) and it is confirmed by the more complete calculations in this report that, depending on the value of other parameters (stiffness ratio and relative density parameter), compressibility may as well rise as lower the flutter speed.

It follows from figs. 1 to 27 that compressibility is favorable if $v_B > v_T$; however, for the more important region $v_B < v_T$ its favorable effect exists only for values of the relative density parameter μ smaller than 15 (see fig. 28). In general, the conclusion of GARRICK (ref. 3) that the influence of compressibility is small, can be retained if $v_B < v_T$, though there are some cases where larger differences appear (e.g. $EA = 0.2$ c, $IA = 0.3$ c and $EA = IA = 0.4$ c).

In conclusion, it may be remarked that present airworthiness requirements for flutter speeds in compressible flow, which are based on the PRANDTL-GLAUERT rule, will in most cases be far too conservative for large Mach numbers.

4 Influence of other parameters on the flutter speed.

Although these calculations have been primarily intended to study the influence of compressibility on the flutter speed, it is possible to study also the influence of some other parameters, viz. positions of elastic and inertia axes, relative density parameter μ , uncoupled wing frequencies v_B and v_T of the first uncoupled bending and torsion mode and the taper.

Some conclusions about the influence of these parameters on the flutter speed can be taken from the older NLL work (ref. 2), while a general survey of British work has been presented by WILLIAMS (ref. 5).

Since in an early stage of the development of a new design it is very difficult to obtain rather accurate data concerning the positions of the elastic and inertia axes, it is important to know how the flutter speed varies with the positions of elastic and inertia axes. This can be found in figs. 29 and 30. The following conclusions can be drawn:

- a) for positions of the elastic axis aft of the inertia axis no flutter is possible unless both axes are far behind the quarter chord axis (e.g. is 0.4 c). In the latter case, the aerodynamic coupling may induce flutter. Hence it is more advisable to diminish the distance between the two axes by shifting forward the inertia axis than by shifting backward the elastic axis.
- b) varying the position of the elastic axis ahead of the position of the inertia axis, it is seen (fig. 30) that there exists a minimum in flutter speed when the distance between both axes is about 0.1 c. As this is a common case it is seen that either a small variation in the position of the elastic axis or a small variation in the position of the inertia axis causes in general very small variations in the flutter speed.

A further important parameter in a flutter calculation is the relative density parameter μ .

It follows from fig. 28 that in general an increase in μ causes an increase in flutter speed, provided the frequencies are kept constant. This, for instance, is realised when the air density ρ is

diminished. The same is found in ref. 2 for a wing with a taper ratio of $1/3$, but the increase in flutter speed with μ is slower in the case of ref. 2. This result is confirmed by the measurements of refs. 6 and 7.

The increase in flutter speed with increasing value of μ is such that the critical dynamic pressure $\frac{1}{2} \rho v^2$ decreases towards an asymptotic value.

This conclusion, which holds independently whether μ increases by decrease of air density or by increase of wing density, provided this occurs uniformly all over the wing, can be shown as follows:

Let it first be assumed that the non-dimensional flutter speed coefficient $\frac{2v}{v_T \cdot c}$ varies proportionally to $\sqrt{\mu}$. Since $\mu = \frac{m}{\rho} = \frac{\text{constant}}{\rho v_T^2}$, it follows immediately that $\frac{1}{2} \rho v^2$ will be constant. As in reality the flutter speed coefficient increases less than proportionally to $\sqrt{\mu}$, the conclusion is that $\frac{1}{2} \rho v^2$ decreases slightly with increasing μ .

The influence of the uncoupled frequencies of bending and torsion v_B and v_T on the flutter speed can be examined from figs. 1 to 27. It must be kept in mind that the values of $\frac{v_B^2}{v_T^2}$, occurring in actual wing constructions, are nearly always smaller than 1 and hence, only the part of the diagrams for which $\frac{v_B^2}{v_T^2}$ is between 0 and 1, has to be considered.

When the bending frequency v_B is increased, the flutter speed will first decrease to a certain minimum and then increase to infinity. The minimum is in nearly all cases of any importance found at values of $\frac{v_B^2}{v_T^2}$ between 0.6 and 1.4 and hence it

may be concluded that for actual values of $\frac{v_B^2}{v_T^2}$ an increase in v_B will decrease the flutter speed.

It is well known that one of the most effective ways in which v can be increased is to increase the torsional stiffness, i.e. v_T .

Indeed, if all other parameters, including the ratio $\frac{v_B^2}{v_T^2}$, are kept constant, the flutter speed will

be proportional to v_T . If, however, v_B and not $\frac{v_B^2}{v_T^2}$ is kept constant, it follows from nearly all figures that for $\frac{v_B}{v_T}$ between 0 and 1, the flutter speed increases more than proportionally to v_T .

For other values of the Mach number the same conclusions hold. As has already been mentioned in sec. 3, the influence of compressibility on the flutter speed is changing at a certain value of $\frac{v_B^2}{v_T^2}$ from unfavorable to favorable.

The results of the present calculations referring to $M = 0$ have been compared with those of ref. 2, where a wing with a taper ratio of $1/3$ (tip chord = $1/3$ root chord) was considered. Comparing a rectangular wing and a tapered wing with equal mean

area, i.e. equal mean chord, and taper ratio $1/3$, it follows that the ordinates of the figures in ref. 2 must be multiplied by a factor 1.5, since the flutter speed is then made dimensionless in both cases by aid of the mean semi-chord. This leads to the dotted lines in figs. 1 to 27. It is seen that in the region $0 < \frac{v_B}{v_T} < 1$ the tapered wing, in general, has a smaller flutter speed than the rectangular wing if v_T and v_B are assumed to be the same.

To simplify the evaluation of the aerodynamic forces, flutter calculations for a tapered wing are sometimes made by assuming a rectangular wing with the same reference chord as the tapered wing. The reference section is usually taken at $0.75 b$. For comparing results the ordinates of the figures in ref. 2 have to be multiplied by 2, i.e. the ordinates of the dotted lines in the present report by 1.33. It then follows that the dotted lines come usually above the drawn lines for $M=0$ and hence, the approximation by a rectangular wing of the same reference chord at $y=0.75 b$ and the same uncoupled frequencies will mostly be conservative. Taking the chord of the rectangular wing equal to that of the tapered wing in the section $y=0.7 b$, would for taper ratio $1/3$ yield results which, on the average, are slightly better.

The conclusion that a tapered wing has a smaller flutter speed than a rectangular wing of equal area and frequencies is in agreement with ref. 8, where the same conclusion is reached for a

coefficient $K = \frac{v}{v_T c}$, $\overline{v_T}$ denoting the coupled torsional frequency. It is shown also in ref. 8, that if instead of frequencies stiffnesses are kept constant, the flutter speed increases if the wing becomes more highly tapered.

5. Conclusions.

The flutter speed of 27 rectangular wings with different positions of elastic and inertia axes and different values of the relative density parameter has been calculated for Mach numbers equal to 0, 0.5 and 0.7. The main conclusions are:

- 1°) For values of μ smaller than 15 the influence of compressibility on the flutter speed is favorable, but for larger values of μ the effect may be adverse, especially if $v_B < v_T$.
- 2°) The well known fact, that increase in the relative density parameter μ causes an increase in the flutter speed, is not generally valid when compressibility has been taken into account. Then, there are cases where a minimum in flutter speed exists for a certain value of μ .
- 3°) The rapid increase in flutter speed, which occurs when the inertia and elastic axes approach each other, is, in general, more pronounced for higher Mach numbers.

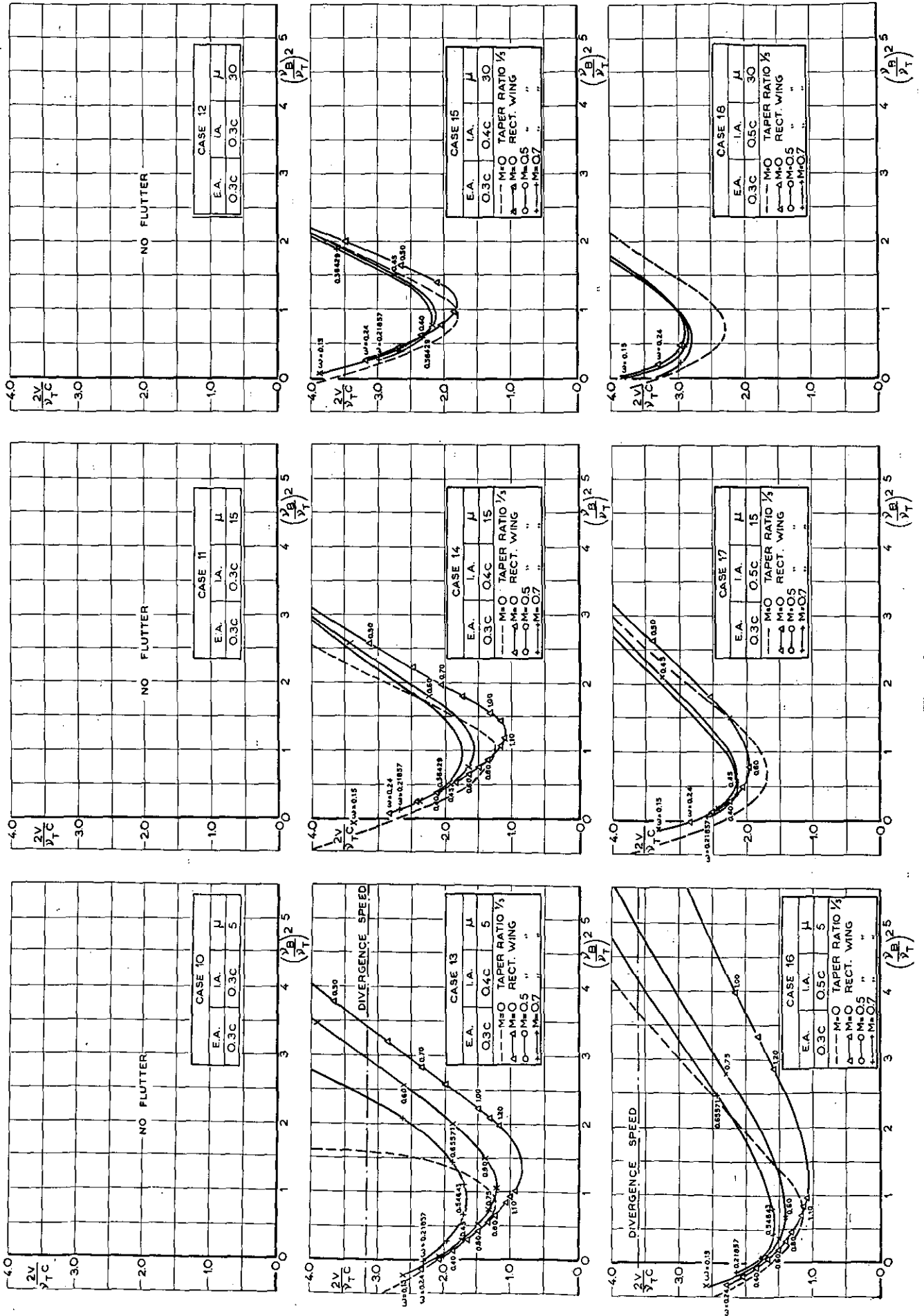
- 4°) The conclusion that for fixed position of the inertia axis and varied position of the elastic axis, the flutter speed becomes minimal if the elastic axis lies about 0.1 c ahead of the inertia axis, holds for all Mach numbers.
- 5°) In the actual range of values of the ratio of the bending and the torsional frequency $\frac{v_B}{v_T}$ (from 0 to 1), an increase in bending frequency decreases the flutter speed while increase in torsional frequency increases this speed very rapidly. This conclusion holds also for all Mach numbers, though both effects are less pronounced for values of the ratio $\frac{v_B^2}{v_T^2}$ near 1, if the Mach number is higher.

6. List of symbols.

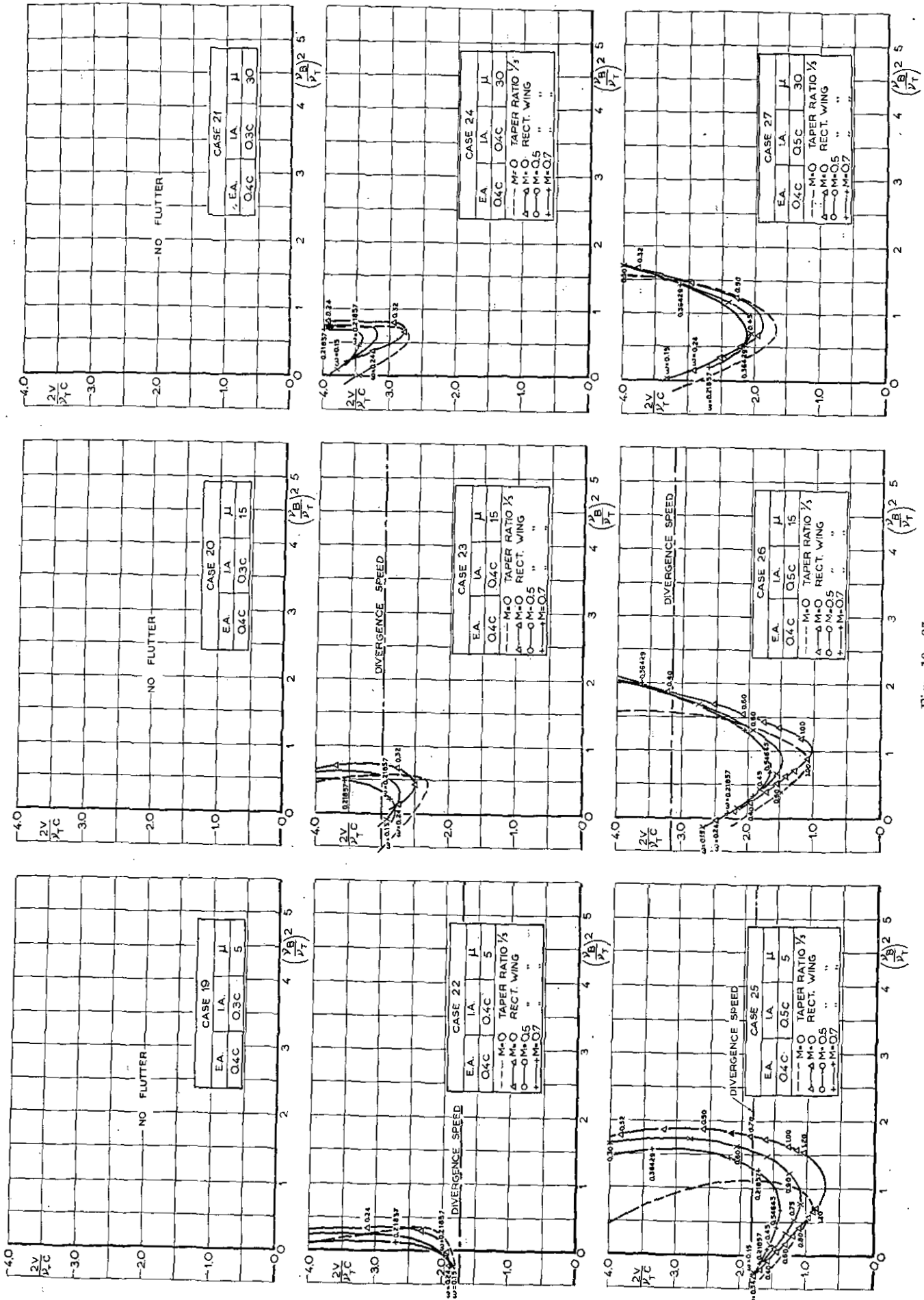
- M — Mach number.
 b — semi span.
 c — wing chord.
 l — semi chord.
 v — flutter speed.
 μ — relative density parameter (ratio of mass of wing to mass of cylinder of air of diameter equal to chord of wing, both taken for equal length along span).
 ν — frequency (rad/sec).
 ν_B — uncoupled frequency of wing bending in vacuum (rad/sec).
 ν_T — uncoupled frequency of torsional vibrations about the elastic axis, in vacuum (rad/sec).
 ρ — air density.
 ω — reduced frequency $\frac{\nu l}{v}$.

7. List of references.

1. TIMMAN, R., VAN DE VOOREN, A. I. and GREIDANUS, J. H. "Aerodynamic Coefficients of an Oscillating Airfoil in Two-Dimensional Subsonic Flow". J. Aero. Sci. 18, no. 12, Dec. 1951.
2. VAN DE VOOREN, A. I. and GREIDANUS, J. H. "Diagrams of Critical Flutter Speed for Wings of a Certain Standard Type". Report V.1297, Nat. Aero. Res. Inst., Amsterdam 1947.
3. GARRICK, I. E. "Bending-Torsion Flutter Calculations Modified by Subsonic Compressibility Corrections". NACA TR 836, 1946.
4. THEODORSEN, T. and GARRICK, I. E. "Mechanism of Flutter — A Theoretical and Experimental Investigation of the Flutter Problem". NACA TR 685, 1940.
5. WILLIAMS, J. "Aircraft Flutter". R and M 2492, 1948.
6. CASTLE, G. E. and HERR, R. W. "Some Effects of Density and Mach Number on the Flutter Speed of Two Uniform Wings". NACA TN 1989, 1949.
7. WOOLSTON, D. S. and CASTLE, G. E. "Some Effects of Variations in Several Parameters Including Fluid Density, on the Flutter Speed of Light Uniform Cantilever Wings". NACA TN 2558, 1951.
8. DUNCAN, W. J. and GRIFFITH, C. L. T. "The Influence of Wing Taper on the Flutter of Cantilever Wings". R and M 1869, 1939.



Figs. 10-18.



Figs. 19-27.

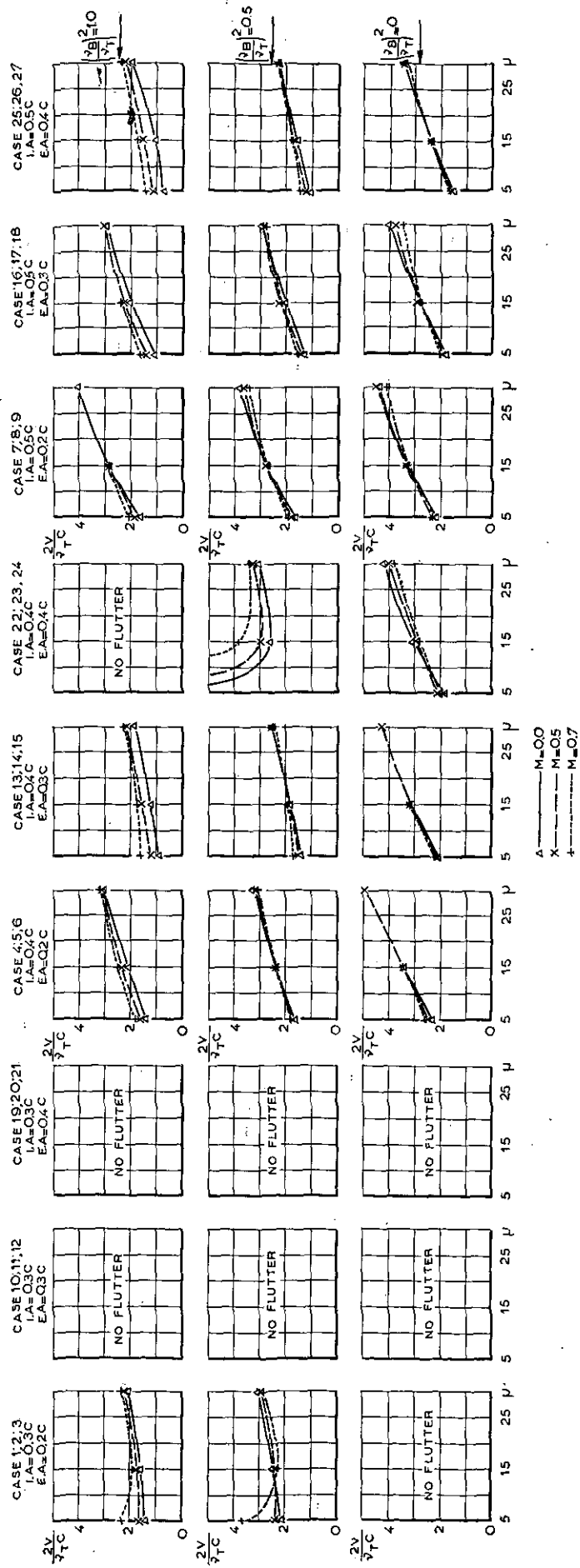


Fig. 28

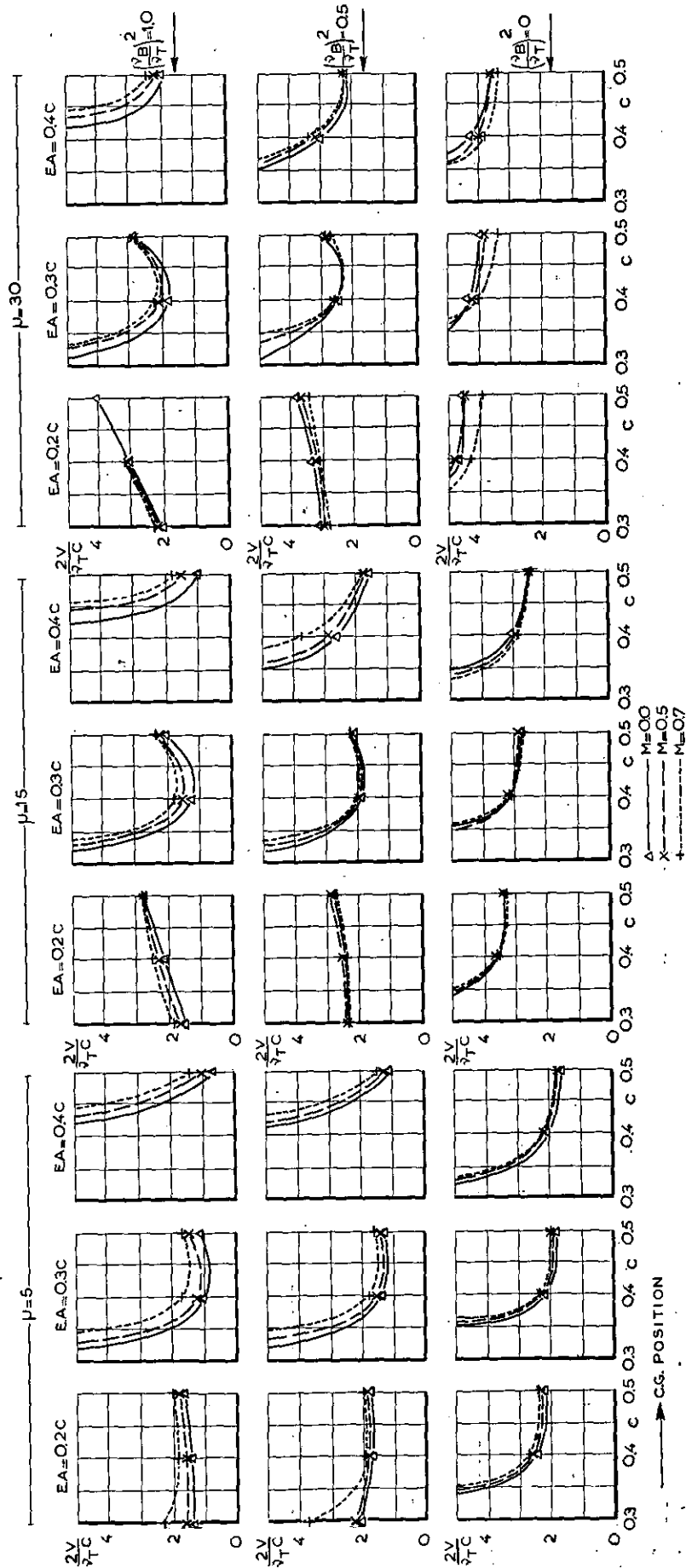


Fig. 29

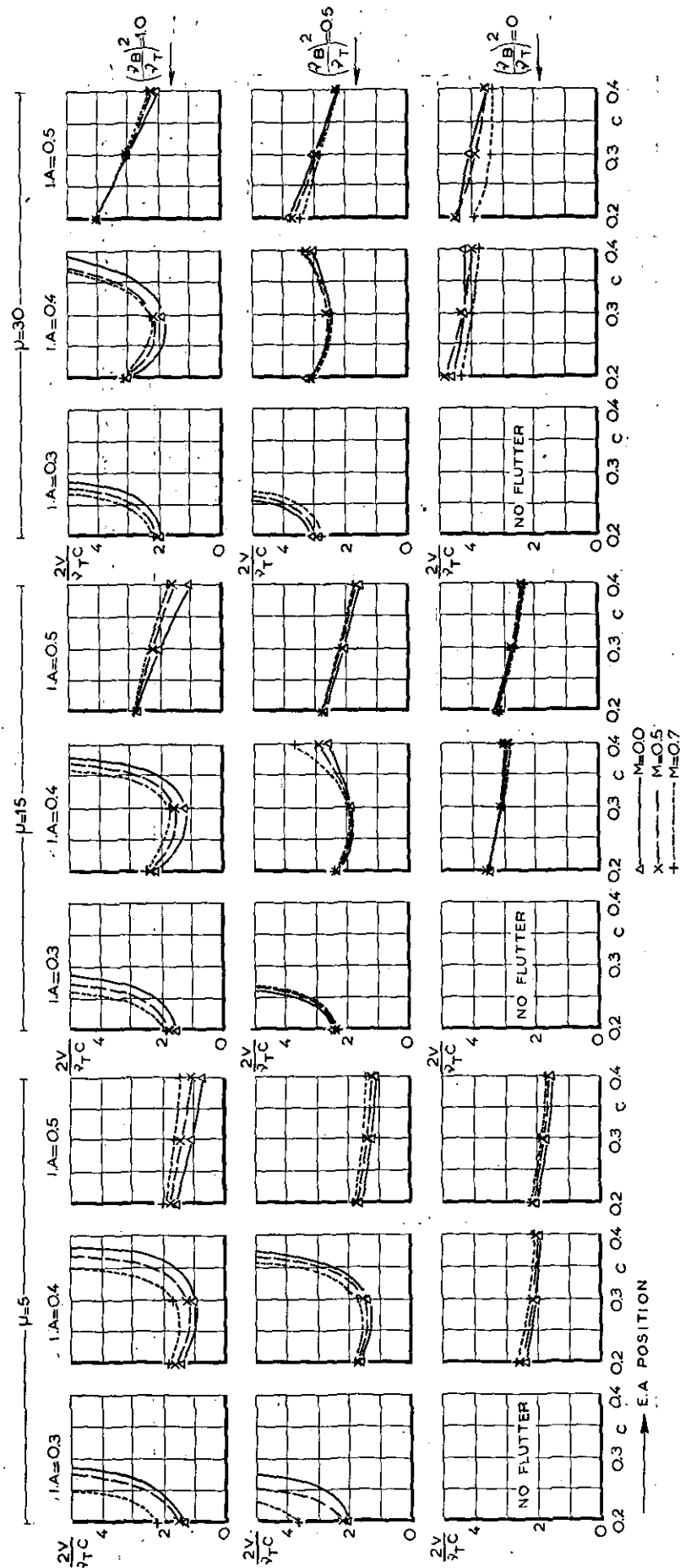


Fig. 30

REPORT F.129

An Approach to Lifting Surface Theory

by

A. I. VAN DE VOOREN.

Summary.

By using a series expansion for the chordwise vorticity distribution, a set of integral equations for the coefficients in this expansion is obtained. In the simplest case this set of integral equations simplifies into WEISSINGER's equation. All chordwise integrations can be performed by aid of pivotal points for which the best positions are derived. A function, given explicitly in the report, must be evaluated in these points.

Contents.

- 1 Introduction.
- 2 List of symbols.
- 3 The integral equation of a lifting surface.
- 4 Calculation of the function $J(\xi_0, \eta_0; \xi, \eta)$.
- 5 Isolation of the two-dimensional downwash term.
- 6 Investigation of the function $K(\xi_0, \eta_0; \xi, \eta)$.
- 7 Introduction of chordwise vorticity distribution.
- 8 Approximate solution. Choice of pivotal points.
- 9 Approximations based on lift, first and higher moments.
- 10 Comparison with WEISSINGER's result.
- 11 Recapitulation.
- 12 List of references.
- Appendix 1. More rigorous derivation of eq. (3.19).
- „ 2. The best position of the pivotal points.
- 3 tables.
- 5 figures.

This investigation has been performed by order of the Netherlands Aircraft Development Board (N.I.V.).

1 Introduction.

In report F.121 (ref. 1) a generalization of PRANDTL's equation has been given for swept wings. Like the original PRANDTL equation it yields good approximations to the actual pressure distribution on the wing as long as the aspect ratio is not too small. For the case of small aspect ratios one has to resort to more accurate methods, such as there are on one side WEISSINGER's method (ref. 2) which, however, yields only the lift but not the moment distribution, and on the other side methods more closely related to lifting surface theory. Among the lifting surface theories there are available

FALKNER's method (ref. 3) and a recent method developed by MULTHOPP (ref. 4).

Though MULTHOPP's method will probably be sufficiently accurate for many practical problems, it still has the disadvantage of being restricted to chordwise pressure distributions of the type

$$A_0 \cot \frac{\vartheta}{2} + A_1 \sin \vartheta, \quad (1.1)$$

where ϑ is the chordwise angular coordinate ($\vartheta = 0$ corresponds to the leading edge). It is true that by a refined choice of the points where the downwash is taken into account (pivotal points), the influence of the omitted term $A_2 \sin 2\vartheta$ upon lift and moment of the wing is diminished, but only in a two-dimensional flow this influence vanishes exactly. Even if the wing is parabolically cambered, the pressure distribution will be more or less different from the type (1.1) due to the effect of "induced camber", that is due to the chordwise varying downwash induced by the trailing vortices. And if, moreover, the profile is S-shaped or "cambered" as a result of flap deflection, pressure distributions strongly differing from (1.1) will occur. Though the formulae of the present report neither can be applied immediately to the case of a deflected control surface, the method seems liable to extension in that direction.

The present method is developed as a generalization of REISSNER's derivation (refs. 5 and 6) of WEISSINGER's method. The generalization involves that this derivation now also applies to tapered or swept wings and, moreover, that in principle no restriction needs to be made about the pressure distribution. This latter feature allows the presentation as a lifting surface theory and makes the method also applicable to wings of small aspect ratio.

It would not have been possible to present a method which can handle more intricate pressure distributions than (1.1) if no simplification with regard to MULTHOPP's method would have been found. This simplification is obtained by remarking a certain duality between the accuracy re-

quired for the integration over the vortices (in MULTHOPP's method the evaluation of the influence coefficients i and j) and the number of terms assumed in the series for the pressure distribution. It will be shown (Sec. 8) that after splitting off the two-dimensional downwash, the integration over the vortices can be performed by aid of as many pivotal points as are used for the determination of the downwash. This principle has also been employed by WEISSINGER to reduce his F -method to the L -method without any significant loss of accuracy.

Finally, the best position for the pivotal points is given. For the pivotal points required in determining the downwash, the result agrees with that of MULTHOPP. The pivotal points required for the integration of the downwash lie at equal distance but at the opposite side of the mid-chord line as the first mentioned set of pivotal points.

It is expected that the present method will be particularly useful in cases of small aspect ratio, where the number of chordwise pivotal points has to be increased, while the number of spanwise stations may be diminished. The spanwise integration is not considered in this report, but it is advised to perform this in the way described by MULTHOPP (ref. 7).

2 List of symbols.

b	semispan
f	the x -coordinate of the wing mid-chord line
l	semichord at arbitrary section
l_r	semichord at root section
r	$\sqrt{(x-x_0)^2 + (y-y_0)^2}$
w	downwash (positive downward)
x	coordinate in flight direction (positive backward)
y	coordinate in spanwise direction (positive to starboard)
x_0, y_0	x, y -coordinates of the point, where the downwash is calculated
α	local angle between lines $\xi = \text{constant}$ and $\eta = \text{constant}$
ξ, η	coordinates defined by eq. (3.2)
γ_x, γ_y	vorticity components along X- and Y-axes
γ_ξ, γ_η	vorticity components in the directions of flight and mid-chord line
ϵ	ratio of root chord to wing span, $\frac{l_r}{b}$
τ	taper ratio
φ	angle of sweep
Γ	circulation
J	function defined by eq. (3.18)
K	function defined by eq. (5.3)

3 The integral equation of a lifting surface.

The expression for the downwash in an arbitrary point x_0, y_0 of the lifting surface is found by application of BIOT and SAVART's law as

$$w(x_0, y_0) = -\frac{1}{4\pi} \iint_A \frac{x-x_0}{r^3} \gamma_y dx dy + \frac{1}{4\pi} \iint_{A+A'} \frac{y-y_0}{r^3} \gamma_x dx dy. \quad (3.1)$$

The X-axis coincides with the direction of undisturbed flow relative to the wing (see fig. 3.1), while the Y-axis is perpendicular to the X-axis in the plane of the wing. γ_x and γ_y are the vorticity components in X- and Y-directions, while r

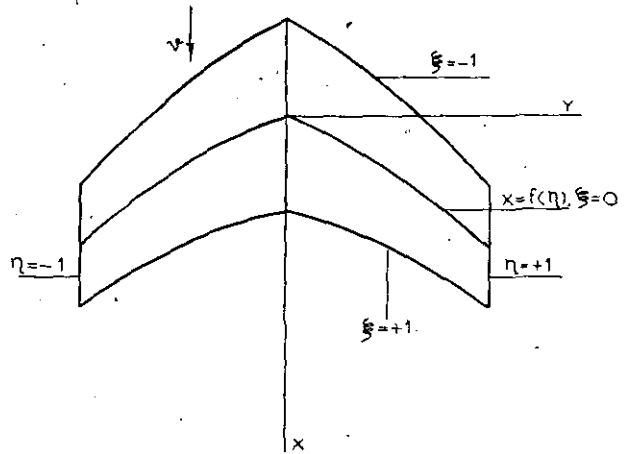


Fig. 3.1. Wing plan form.

denotes the distance between the points x_0, y_0 and x, y , i. e.

$$r = \sqrt{(x-x_0)^2 + (y-y_0)^2}.$$

A denotes the wing area and A' the area of the wake. In the wake γ_y vanishes and γ_x is constant in X-direction.

It has been shown by REISSNER (ref. 5) how for rectangular wings without sweepback eq. (3.1) can be reduced to a form from which PRANDTL's integral equation for the lifting line as well as WEISSINGER's L - and F -methods follow by suitable approximations. The reduction given by REISSNER is only valid if both the leading and the trailing edges are perpendicular to the main stream velocity. However, it appears to be possible to generalize this reduction to wings of general plan form provided new coordinates, ξ and η are introduced by the transformation

$$\left. \begin{aligned} x &= f(\eta) + \xi l(\eta) \\ y &= b \eta \end{aligned} \right\} \quad (3.2)$$

where $x=f(\eta)$, i. e. in the new coordinates $\xi=0$, denotes the mid-chord line (fig. 3.1) and $l(\eta)$ stands for the semi-chord; $\xi=-1$ and $\xi=1$ determine the leading and trailing edges respectively, while $\eta=\pm 1$ denote the two tip-chords.

Consequently the vorticity vector $\vec{\gamma}$ is now decomposed (see fig. 3.2) into

$$\left. \begin{aligned} \gamma_\xi &= \gamma_x - \gamma_y \tan \alpha \\ \gamma_\eta &= \frac{\gamma_y}{\cos \alpha} \end{aligned} \right\} \quad (3.3)$$

where α denotes the local angle between the lines $\xi = \text{constant}$ and $\eta = \text{constant}$. In general, α will vary over the whole plane of the wing. It is determined by the formula

$$\tan \alpha = \left(\frac{\partial x}{\partial y} \right)_{\xi} = \frac{\left(\frac{\partial x}{\partial \eta} \right)_{\xi}}{\left(\frac{\partial y}{\partial \eta} \right)_{\xi}} = \frac{1}{b} (f' + \xi l'), \quad (3.4)$$

the accent denoting differentiation toward η .

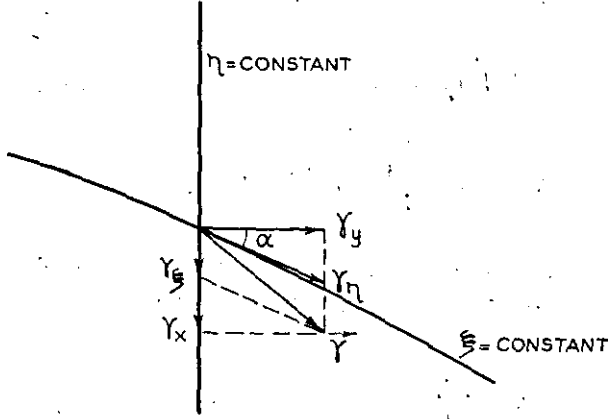


Fig. 3.2. Decomposition of vorticity vector $\vec{\gamma}$.

The reverse formulae of (3.3) are

$$\left. \begin{aligned} \gamma_x &= \gamma_{\xi} + \gamma_{\eta} \sin \alpha \\ \gamma_y &= \gamma_{\eta} \cos \alpha \end{aligned} \right\} \quad (3.5)$$

The advantage of the transformation (3.2) is that at the leading edge $\vec{\gamma}$ lies in η -direction which means that γ_{ξ} vanishes. Due to this property a transformation of eq. (3.1) by aid of partial integration becomes possible, which could not be performed in the x, y coordinates. This partial integration is based upon the following formulae in x, y -coordinates

$$\left. \begin{aligned} \frac{x-x_0}{r^3} &= \frac{\partial}{\partial y} \frac{y-y_0}{r(x-x_0)} \\ \text{and} \quad \frac{y-y_0}{r^3} &= \frac{\partial}{\partial x} \frac{x-x_0}{r(y-y_0)} \end{aligned} \right\} \quad (3.6)$$

which easily can be verified. In the ξ, η coordinates the operators $\frac{\partial}{\partial y}$ and $\frac{\partial}{\partial x}$ are to be replaced by

$$\frac{\partial \xi}{\partial y} \frac{\partial}{\partial \xi} + \frac{\partial \eta}{\partial y} \frac{\partial}{\partial \eta} \quad \text{and} \quad \frac{\partial \xi}{\partial x} \frac{\partial}{\partial \xi} + \frac{\partial \eta}{\partial x} \frac{\partial}{\partial \eta} \quad (3.7)$$

Since

$$\xi = \frac{x-f}{l} \quad \text{and} \quad \eta = \frac{y}{b},$$

it follows that

$$\left. \begin{aligned} \frac{\partial \xi}{\partial x} &= \frac{1}{l}, \quad \frac{\partial \xi}{\partial y} = -\frac{f' + \xi l'}{bl} = -\frac{\tan \alpha}{l}, \\ \frac{\partial \eta}{\partial x} &= 0, \quad \frac{\partial \eta}{\partial y} = \frac{1}{b} \end{aligned} \right\} \quad (3.8)$$

Hence, eqs. (3.6) can be replaced by

$$\frac{x-x_0}{r^3} = \left\{ -\frac{\tan \alpha}{l} \frac{\partial}{\partial \xi} + \frac{1}{b} \frac{\partial}{\partial \eta} \right\} \frac{y-y_0}{r(x-x_0)}$$

and

$$\frac{y-y_0}{r^3} = \frac{1}{l} \frac{\partial}{\partial \xi} \frac{x-x_0}{r(y-y_0)} \quad (3.9)$$

As final preparation for the transformation of eq. (3.1) into ξ and η coordinates, it is remarked that the surface element $dx dy$ must be replaced by

$$\left| \begin{array}{cc} \frac{\partial x}{\partial \xi} & \frac{\partial x}{\partial \eta} \\ \frac{\partial y}{\partial \xi} & \frac{\partial y}{\partial \eta} \end{array} \right| d\xi d\eta = bl d\xi d\eta. \quad (3.10)$$

By aid of eqs. (3.5) and (3.10), formula (3.1) now becomes

$$\begin{aligned} w &= -\frac{1}{4\pi} \int_{-1}^1 \int_{-1}^1 \frac{x-x_0}{r^3} \gamma_{\eta} \cos \alpha bl d\xi d\eta + \\ &+ \frac{1}{4\pi} \int_{-1}^1 \int_{-1}^{\infty} \frac{y-y_0}{r^3} (\gamma_{\xi} + \gamma_{\eta} \sin \alpha) bl d\xi d\eta, \end{aligned}$$

while after application of eqs. (3.9) the result is

$$\begin{aligned} w &= \frac{b}{4\pi} \int_{-1}^1 \int_{-1}^1 \gamma_{\eta} \sin \alpha \frac{\partial}{\partial \xi} \left\{ \frac{y-y_0}{r(x-x_0)} + \right. \\ &\quad \left. + \frac{x-x_0}{r(y-y_0)} \right\} d\xi d\eta - \\ &- \frac{1}{4\pi} \int_{-1}^1 \int_{-1}^1 l \gamma_{\eta} \cos \alpha \frac{\partial}{\partial \eta} \frac{y-y_0}{r(x-x_0)} d\xi d\eta + \\ &+ \frac{b}{4\pi} \int_{-1}^1 \int_{-1}^{\infty} \gamma_{\xi} \frac{\partial}{\partial \xi} \frac{x-x_0}{r(y-y_0)} d\xi d\eta, \quad (3.11) \end{aligned}$$

where use has been made of the fact that $\gamma_{\eta} = 0$ for $\xi \gg 1$.

Similarly, the equation of continuity

$$\frac{\partial \gamma_x}{\partial x} + \frac{\partial \gamma_y}{\partial y} = 0$$

will now be transformed to ξ - and η -coordinates. By aid of eqs. (3.5), (3.7) and (3.8) it is obtained that

$$\begin{aligned} \frac{1}{l} \frac{\partial (\gamma_{\xi} + \gamma_{\eta} \sin \alpha)}{\partial \xi} - \frac{\tan \alpha}{l} \frac{\partial \gamma_{\eta} \cos \alpha}{\partial \xi} + \\ + \frac{1}{b} \frac{\partial \gamma_{\eta} \cos \alpha}{\partial \eta} = 0 \end{aligned}$$

or

$$\begin{aligned} \frac{1}{l} \frac{\partial \gamma_{\xi}}{\partial \xi} + \frac{\gamma_{\eta}}{l} \frac{\partial \sin \alpha}{\partial \xi} - \frac{\gamma_{\eta} \tan \alpha}{l} \frac{\partial \cos \alpha}{\partial \xi} + \\ + \frac{1}{b} \frac{\partial \gamma_{\eta} \cos \alpha}{\partial \eta} = 0. \end{aligned}$$

By using eq. (3.4) it is found that

$$\begin{aligned}\frac{\partial \sin \alpha}{\partial \xi} &= \tan \alpha \frac{\partial \cos \alpha}{\partial \xi} + \cos \alpha \frac{\partial \tan \alpha}{\partial \xi} = \\ &= \tan \alpha \frac{\partial \cos \alpha}{\partial \xi} + \frac{b'}{b} \cos \alpha,\end{aligned}$$

and the continuity equation becomes

$$\frac{1}{l} \frac{\partial \gamma_\xi}{\partial \xi} + \frac{\gamma_\eta}{l} \frac{b'}{b} \cos \alpha + \frac{1}{b} \frac{\partial \gamma_\eta \cos \alpha}{\partial \eta} = 0$$

or

$$b \frac{\partial \gamma_\xi}{\partial \xi} + \frac{\partial}{\partial \eta} (l \gamma_\eta \cos \alpha) = 0. \quad (3.12)$$

Integration to ξ between $\xi = -1$ and $\xi = +1$ yields for the wake vorticity (i. e. $\xi \geq 1$)

$$\gamma_\xi = -\frac{1}{b} \frac{d\Gamma}{d\eta}, \quad (3.13)$$

where the circulation Γ is given by

$$\Gamma(\eta) = l \int_{-1}^1 \gamma_\eta \cos \alpha d\xi = l \int_{-1}^1 \gamma_\eta d\xi. \quad (3.14)$$

In deriving eq. (3.13) use has been made of the first and second of the following boundary conditions

$$\begin{aligned}\xi = -1, \gamma_\xi = 0; \quad \xi \geq 1, \gamma_\eta = 0; \\ \eta = \pm 1, \gamma_\eta = 0.\end{aligned} \quad (3.15)$$

By partial integration to ξ the last term of eq. (3.11) becomes equal to

$$\begin{aligned}&\frac{b}{4\pi} \int_{-1}^1 \frac{(\gamma_\xi)_{\xi=\infty}}{y-y_0} d\eta - \\ &- \frac{b}{4\pi} \int_{-1}^1 \int_{-1}^1 \frac{x-x_0}{r(y-y_0)} \frac{\partial \gamma_\xi}{\partial \xi} d\xi d\eta,\end{aligned}$$

which by aid of eqs. (3.12) and (3.13) may be replaced by

$$\begin{aligned}&-\frac{1}{4\pi b} \int_{-1}^1 \frac{d\Gamma/d\eta}{\eta-\eta_0} d\eta + \\ &+ \frac{1}{4\pi} \int_{-1}^1 \int_{-1}^1 \frac{x-x_0}{r(y-y_0)} \frac{\partial (l \gamma_\eta \cos \alpha)}{\partial \eta} d\xi d\eta\end{aligned}$$

and this is equal to

$$\begin{aligned}&-\frac{1}{4\pi b} \int_{-1}^1 \frac{d\Gamma/d\eta}{\eta-\eta_0} d\eta - \\ &-\frac{1}{4\pi} \int_{-1}^1 \int_{-1}^1 l \gamma_\eta \cos \alpha \frac{\partial}{\partial \eta} \frac{x-x_0}{r(y-y_0)} d\xi d\eta.\end{aligned}$$

Since

$$\frac{x-x_0}{r(y-y_0)} + \frac{y-y_0}{r(x-x_0)} = \frac{r}{(x-x_0)(y-y_0)},$$

this yields together with the first and second terms of the right hand side of eq. (3.11) the following expression for the downwash

$$\begin{aligned}w(\xi_0, \eta_0) &= \\ &= \frac{b}{4\pi} \int_{-1}^1 \int_{-1}^1 \gamma_\eta \sin \alpha \frac{\partial}{\partial \xi} \frac{r}{(x-x_0)(y-y_0)} d\xi d\eta - \\ &- \frac{1}{4\pi} \int_{-1}^1 \int_{-1}^1 l \gamma_\eta \cos \alpha \frac{\partial}{\partial \eta} \frac{r}{(x-x_0)(y-y_0)} d\xi d\eta - \\ &- \frac{1}{4\pi b} \int_{-1}^1 \frac{d\Gamma/d\eta}{\eta-\eta_0} d\eta.\end{aligned}$$

Making use of eqs. (3.7) and (3.8) and replacing moreover $\gamma_\eta \cos \alpha$ by γ_η , it is obtained that

$$\begin{aligned}w(\xi_0, \eta_0) &= \\ &= \frac{b}{4\pi} \int_{-1}^1 \int_{-1}^1 l \gamma_\eta \frac{\partial}{\partial \eta} \frac{r}{(x-x_0)(y-y_0)} d\xi d\eta - \\ &- \frac{1}{4\pi b} \int_{-1}^1 \frac{d\Gamma/d\eta}{\eta-\eta_0} d\eta,\end{aligned} \quad (3.16)$$

where the differentiation to y must be performed by keeping x constant. Thus

$$\frac{\partial}{\partial y} \frac{r}{(x-x_0)(y-y_0)} = -\frac{x-x_0}{r(y-y_0)^2}. \quad (3.17)$$

Let this form be put equal to

$$\frac{1}{b^2} \frac{\partial J}{\partial \eta} = -\frac{x-x_0}{r(y-y_0)^2}$$

or

$$J(\xi_0, \eta_0; \xi, \eta) = -b^2 \int \frac{x-x_0}{r(y-y_0)^2} d\eta. \quad (3.18)$$

The function J is only determined by its derivative to η and hence it is equal to the indefinite integral given in (3.18). J appears to be a function which has a finite discontinuity in those sections η , where either leading or trailing edge has a kink. Assuming that this occurs only in the centre section, partial integration to η of the first term of eq. (3.16) leads, after substitution of eqs. (3.17) and (3.18) to

$$\begin{aligned}w(\xi_0, \eta_0) &= \frac{1}{4\pi b} \int_{-1}^1 \int_{-1}^1 J \frac{\partial (l \gamma_\eta)}{\partial \eta} d\xi d\eta - \\ &- \frac{1}{4\pi b} \int_{-1}^1 \frac{d\Gamma/d\eta}{\eta-\eta_0} d\eta + \\ &+ \frac{1}{4\pi b} \int_{-1}^1 \{ J(\xi_0, \eta_0; \xi, 0^+) - \\ &- J(\xi_0, \eta_0; \xi, 0^-) \} (l \gamma_\eta)_{\eta=0} d\xi\end{aligned} \quad (3.19)$$

since

$$\int_{-1}^{0^-} l_{\gamma y} \frac{\partial J}{\partial \eta} d\eta + \int_{0^+}^1 l_{\gamma y} \frac{\partial J}{\partial \eta} d\eta = J \cdot l_{\gamma y} \Big|_{-1}^{0^-} + J \cdot l_{\gamma y} \Big|_{0^+}^1 - \int_{-1}^{0^-} J \frac{\partial l_{\gamma y}}{\partial \eta} d\eta - \int_{0^+}^1 J \frac{\partial l_{\gamma y}}{\partial \eta} d\eta =$$

$$\{ J(\xi_0, \eta_0; \xi, 0^-) - J(\xi_0, \eta_0; \xi, 0^+) \} (l_{\gamma y})_{\eta=0} - \int_{-1}^1 J \frac{\partial l_{\gamma y}}{\partial \eta} d\eta.$$

If there are more sections where J has a finite discontinuity, eq. (3.19) can easily be generalized.

Hence, in lifting surface theory, the downwash in a point x_0, y_0 is, without any approximation, given by a formula of the type of eq. (3.19). This expression contains a single unknown function, viz. the function $\gamma_y(\xi, \eta)$ in the wing region A . The

By substitution of eqs. (4.1) and (4.2) into eq. (3.2) it is found that

$$x = b |\eta| \tan \varphi + l_r (1 - \tau |\eta|) \xi,$$

$$y = b \eta.$$

Assuming η_0 to be positive, it is obtained that

$$\left. \begin{aligned} x - x_0 &= b(\eta - \eta_0) \tan \varphi + l_r \{ \xi - \xi_0 - \tau(\eta \xi - \eta_0 \xi_0) \} \\ r &= \sqrt{[b(\eta - \eta_0) \tan \varphi + l_r \{ \xi - \xi_0 - \tau(\eta \xi - \eta_0 \xi_0) \}]^2 + [b(\eta - \eta_0)]^2} \end{aligned} \right\} \text{ if } \eta > 0 \quad (4.3)$$

$$\left. \begin{aligned} x - x_0 &= -b(\eta + \eta_0) \tan \varphi + l_r \{ \xi - \xi_0 + \tau(\eta \xi + \eta_0 \xi_0) \} \\ r &= \sqrt{[-b(\eta + \eta_0) \tan \varphi + l_r \{ \xi - \xi_0 + \tau(\eta \xi + \eta_0 \xi_0) \}]^2 + [b(\eta - \eta_0)]^2} \end{aligned} \right\} \text{ if } \eta < 0. \quad (4.4)$$

function $J(\xi_0, \eta_0; \xi, \eta)$ can be evaluated for any given wing plan form.

The derivation of eq. (3.19) is not quite rigorous since the first term of the right hand side of eq. (3.16) contains an improper integral of which the principal value in the sense of CAUCHY does not exist. However, a more careful but also more laborious derivation is possible by calculating the downwash in the point (x_0, y_0, z_0) , and then letting approach z_0 the value 0. This leads to the same equation (3.19) as is shown in Appendix I.

Finally, it may be remarked that for an unswept wing, where $\frac{\partial}{\partial y} = \frac{1}{b} \frac{\partial}{\partial \eta}$, it follows from eqs. (3.17) and (3.18) that

$$J = b \frac{r}{(x - x_0)(y - y_0)},$$

which is in accordance with refs. 5 and 6.

4 Calculation of the function $J(\xi_0, \eta_0; \xi, \eta)$.

For any given plan form of the wing the function J can be calculated; this calculation will now be performed for the case that each semi-wing is of trapezoidal form.

Then the mid-chord line has the equation

$$x \equiv f(\eta) = b |\eta| \tan \varphi, \quad (4.1)$$

where φ is the angle of sweepback. The chord is determined by the relation

$$l = l_r \{ 1 - \tau |\eta| \}, \quad (4.2)$$

where l_r denotes the root chord and τ the taper ratio defined by $\frac{l_r - l_t}{l_r}$ if l_t is the tip chord.

Hence $\tau = 0$ denotes a wing of constant chord and $\tau = 1$ a triangular wing.

With the substitution $\eta - \eta_0 = t$, the integral (3.18) becomes of the type

$$J = - \int \frac{\alpha + \beta t}{t^2 \sqrt{(\alpha + \beta t)^2 + b^2 t^2}} dt,$$

which is equal to

$$J = \frac{\sqrt{(\alpha + \beta t)^2 + b^2 t^2}}{\alpha t}, \quad (4.5)$$

where for $\eta > 0$

$$\begin{aligned} \alpha &= \alpha^+ = l_r (1 - \tau \eta_0) (\xi - \xi_0) \\ \beta &= \beta^+ = b \tan \varphi - l_r \tau \xi \end{aligned} \quad (4.6)$$

and for $\eta < 0$

$$\begin{aligned} \alpha &= \alpha^- = l_r \{ \xi - \xi_0 + \tau \eta_0 (\xi + \xi_0) \} - 2 b \eta_0 \tan \varphi \\ \beta &= \beta^- = -b \tan \varphi + l_r \tau \xi. \end{aligned} \quad (4.7)$$

It follows from eq. (4.5) that J is discontinuous for $\eta = 0$. In fact

$$J(\xi_0, \eta_0; \xi, 0^+) = - \frac{\sqrt{(\alpha^+ - \beta^+ \eta_0)^2 + b^2 \eta_0^2}}{\alpha^+ \eta_0}$$

and

$$J(\xi_0, \eta_0; \xi, 0^-) = - \frac{\sqrt{(\alpha^- - \beta^- \eta_0)^2 + b^2 \eta_0^2}}{\alpha^- \eta_0}, \quad (4.8)$$

which, in general, are two different values.

5 Isolation of the two-dimensional downwash term.

In chordwise direction the function J becomes infinitely large for

$$\xi = \xi_0 \quad \text{if } \eta > 0 \quad (5.1)$$

$\xi = \xi_0'$; where

$$\xi_0' = \frac{l_r (1 - \tau \eta_0) \xi_0 + 2 b \eta_0 \tan \varphi}{l_r (1 + \tau \eta_0)} \quad \text{if } \eta < 0;$$

$\xi = \xi_0'$ denotes the line of constant ξ -coordinates on the left wing passing through $P(\xi_0, \eta_0)$, see fig. 5.1. This follows by remarking that $BP = l_r(1 - \tau\eta_0)\xi_0$, $BC = CD = b\eta_0 \tan \varphi$ and $DE = l_r(1 + \tau\eta_0)$. It may occur, as in fig. 5.1, that the

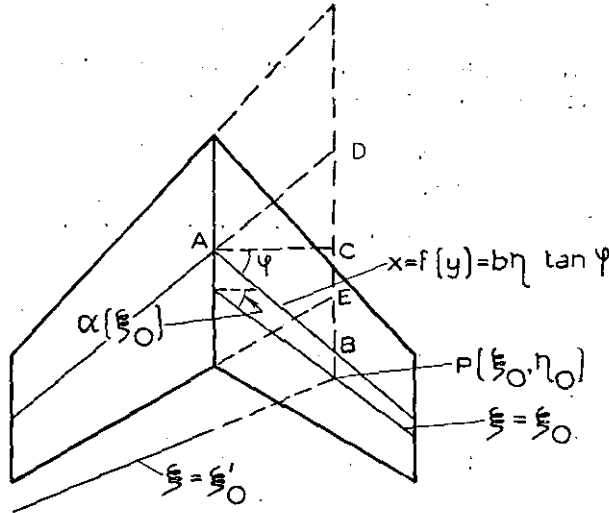


Fig. 5.1. Positions of the lines $\xi = \xi_0$ and $\xi = \xi_0'$.

line $\xi = \xi_0'$ falls behind the trailing edge of the left wing ($\xi_0' > 1$). In such case the chordwise integration on the left wing does not contain the singular point but it remains advisable to split off the singularity.

It will now be shown that separation of this singularity is identical to isolation of the two-dimensional downwash.

It follows from eqs. (4.5) through (4.7) that the singular part (i.e. singular in ξ) of the function $J(\xi_0, \eta_0; \xi, \eta)$ is given by

$$\left. \begin{aligned} \lim_{\xi \rightarrow \xi_0} J(\xi_0, \eta_0; \xi, \eta) &= \frac{|\eta - \eta_0|}{(\eta - \eta_0)(\xi - \xi_0)} \frac{\sqrt{(b \tan \varphi - l_r \tau \xi_0)^2 + b^2}}{l_r(1 - \tau\eta_0)} \text{ if } \eta > 0, \\ \lim_{\xi \rightarrow \xi_0} J(\xi_0, \eta_0; \xi, \eta) &= \frac{|\eta - \eta_0|}{(\eta - \eta_0)(\xi - \xi_0')} \frac{\sqrt{(b \tan \varphi - l_r \tau \xi_0')^2 + b^2}}{l_r(1 + \tau\eta_0)} \text{ if } \eta < 0. \end{aligned} \right\} \quad (5.2)$$

Hence the function $K(\xi_0, \eta_0; \xi, \eta)$, defined by

$$\left. \begin{aligned} K &= \frac{\sqrt{\{\varepsilon(1 - \tau\eta_0)(\xi - \xi_0) + (\tan \varphi - \varepsilon \tau \xi)(\eta - \eta_0)\}^2 + (\eta - \eta_0)^2} - |\eta - \eta_0| \sqrt{(\tan \varphi - \varepsilon \tau \xi_0)^2 + 1}}{\varepsilon(1 - \tau\eta_0)(\xi - \xi_0)(\eta - \eta_0)} \text{ if } \eta > 0, \\ K &= \frac{\sqrt{\{\varepsilon(1 + \tau\eta_0)(\xi - \xi_0') - (\tan \varphi - \varepsilon \tau \xi)(\eta - \eta_0)\}^2 + (\eta - \eta_0)^2} - |\eta - \eta_0| \sqrt{(\tan \varphi - \varepsilon \tau \xi_0')^2 + 1}}{\varepsilon(1 + \tau\eta_0)(\xi - \xi_0')(\eta - \eta_0)} \text{ if } \eta < 0, \end{aligned} \right\} \quad (5.3)$$

where

$$\varepsilon = \frac{l_r}{b}, \quad (5.4)$$

is regular in ξ .

It will now be investigated what is the contribution of the singular part of J to the right hand side of eq. (3.19). When substituting eqs. (5.2) into the first term of the right hand side of eq. (3.19), the integration to η can be carried out.

The substitution gives rise to the following integrals to η :

$$\begin{aligned} \int_{-1}^0 \frac{|\eta - \eta_0|}{\eta - \eta_0} \frac{\partial(l\gamma_y)}{\partial \eta} d\eta &= \\ &= - \int_{-1}^0 \frac{\partial(l\gamma_y)}{\partial \eta} d\eta = - (l\gamma_y)_{\eta=0-}, \\ \int_0^1 \frac{|\eta - \eta_0|}{\eta - \eta_0} \frac{\partial(l\gamma_y)}{\partial \eta} d\eta &= \\ &= - \int_0^{\eta_0} \frac{\partial(l\gamma_y)}{\partial \eta} d\eta + \int_{\eta_0}^1 \frac{\partial(l\gamma_y)}{\partial \eta} d\eta = \\ &= -2(l\gamma_y)_{\eta=\eta_0} + (l\gamma_y)_{\eta=0+}. \end{aligned}$$

Hence, the first and third terms of the R.H.S. of eq. (3.19) become after substitution of eqs. (5.2) for J equal to

$$- \frac{1}{2\pi} \int_{-1}^1 \frac{\sqrt{(b \tan \varphi - l_r \tau \xi_0)^2 + b^2}}{l_r(1 - \tau\eta_0)b} \frac{l\gamma_y(\xi, \eta_0)}{\xi - \xi_0} d\xi, \quad (5.5)$$

as can easily be verified.

It follows from eq. (3.4) that

$$\cos \alpha = \frac{b}{\sqrt{(f' + \xi'')^2 + b^2}}$$

and, from eqs. (4.1) and (4.2) that $f' = b \tan \varphi$ and $f'' = -l_r \tau$ (if $\eta > 0$). Hence

$$\cos \alpha = \frac{b}{\sqrt{(b \tan \varphi - l_r \tau \xi)^2 + b^2}}$$

and (5.5) may be replaced by

$$- \frac{1}{2\pi \cos \alpha(\xi_0)} \int_{-1}^1 \frac{\gamma_y(\xi, \eta_0)}{\xi - \xi_0} d\xi. \quad (5.6)$$

It will be clear that $\frac{\gamma_y(\xi, \eta_0)}{\cos \alpha(\xi_0)}$ is the component of the vorticity parallel to the line $\xi - \xi_0$. If τ were zero, i.e. α constant, (5.6) would represent

exactly the two-dimensional downwash. In order that the conception two-dimensional downwash exists for a tapered wing, it has to be interpreted as that value of the downwash in P which would occur if the dimensions in the local spanwise direction at P are stretched infinitely, compared with chordwise dimensions. In this generalized sense, (5.6) represents also for a tapered wing the two-dimensional downwash.

The result is that instead of eq. (3.19) one may write

$$w(\xi_0, \eta_0) = -\frac{1}{2\pi \cos \alpha(\xi_0)} \int_{-1}^1 \frac{\gamma_\nu(\xi, \eta_0)}{\xi - \xi_0} d\xi - \frac{1}{4\pi b} \int_{-1}^1 \frac{d\Gamma/d\eta}{\eta - \eta_0} d\eta + \frac{1}{4\pi b} \int_{-1}^1 \int_{-1}^1 K \frac{\partial(l\gamma_\nu)}{\partial\eta} d\xi d\eta + \frac{1}{4\pi b} \int_{-1}^1 \{K(\xi_0, \eta_0; \xi, 0^+) - K(\xi_0, \eta_0; \xi, 0^-)\} (l\gamma_\nu)_{\eta=0} d\partial. \quad (5.7)$$

6 Investigation of the function $K(\xi_0, \eta_0; \xi, \eta)$.

This function will first be investigated as function of ξ and η for fixed values of ξ_0 and η_0 , while η_0 is positive.

1°. The region where $|\xi - \xi_0| \ll |\eta - \eta_0|$ (Region I in fig. 6.1). After substitution of $\xi = \xi_0 + \delta$ into the first equation (5.3) the result is

$$K = \frac{\sqrt{\{\varepsilon(1 - \tau\eta_0)\delta + (\tan \varphi - \varepsilon\tau\xi_0)(\eta - \eta_0)\}^2 + (\eta - \eta_0)^2} - |\eta - \eta_0| \sqrt{(\tan \varphi - \varepsilon\tau\xi_0)^2 + 1}}{\varepsilon(1 - \tau\eta_0)\delta(\eta - \eta_0)}$$

$$\left. \begin{aligned} K(\xi_0, \eta_0; \xi, 0^+) &= \frac{\sqrt{\{\varepsilon(1 - \tau\eta_0)(\xi - \xi_0) - (\tan \varphi - \varepsilon\tau\xi)\eta_0\}^2 + \eta_0^2} - |\eta_0| \sqrt{(\tan \varphi - \varepsilon\tau\xi_0)^2 + 1}}{\varepsilon(1 - \tau\eta_0)(\xi - \xi_0)\eta_0} \\ K(\xi_0, \eta_0; \xi, 0^-) &= \frac{\sqrt{\{\varepsilon(1 + \tau\eta_0)(\xi - \xi_0') + (\tan \varphi - \varepsilon\tau\xi)\eta_0\}^2 + \eta_0^2} - |\eta_0| \sqrt{(\tan \varphi - \varepsilon\tau\xi_0')^2 + 1}}{\varepsilon(1 + \tau\eta_0)(\xi - \xi_0')\eta_0} \end{aligned} \right\} \quad (6.5)$$

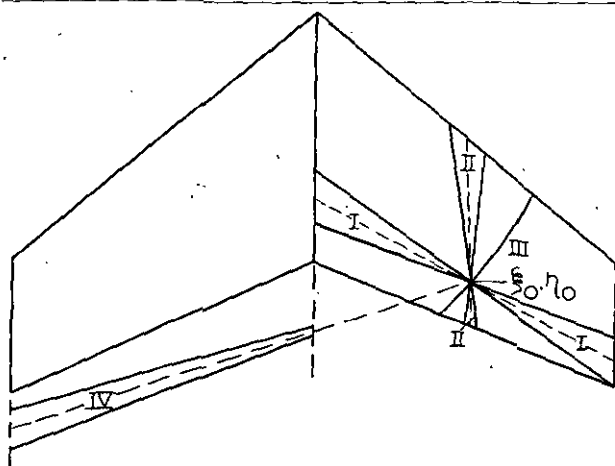


Fig. 6.1. Positions of different regions.

Making use of the assumption $|\delta| \ll |\eta - \eta_0|$, the function can be approximated in region I by

$$K = \frac{1}{|\eta - \eta_0|} \frac{\tan \varphi - \varepsilon\tau\xi_0}{\sqrt{(\tan \varphi - \varepsilon\tau\xi_0)^2 + 1}} + 0(\delta), \eta > 0. \quad (6.1)$$

The sign of K is determined by that of $\tan \varphi - \varepsilon\tau\xi_0$; it is independent of η . For most swept-back wings, K will be positive in region I. If the point ξ_0, η_0 is chosen in such a way that $\varepsilon\tau\xi_0 = \tan \varphi$, K vanishes at the line $\xi = \xi_0$.

In the neighbourhood of the line $\xi = \xi_0'$ at the left wing (region IV) K is given similarly by

$$K = \frac{1}{|\eta - \eta_0|} \frac{\tan \varphi - \varepsilon\tau\xi_0'}{\sqrt{(\tan \varphi - \varepsilon\tau\xi_0')^2 + 1}} + 0(\delta), \eta < 0. \quad (6.2)$$

2°. The region where $|\eta - \eta_0| \ll |\xi - \xi_0|$ (Region II in fig. 6.1).

Eq. (5.3) leads immediately to the approximation in region II:

$$K = \frac{|\xi - \xi_0|}{\xi - \xi_0} \cdot \frac{1}{\eta - \eta_0}. \quad (6.3)$$

3°. The curve where K vanishes (III in fig. 6.1).

The nominator of the first eq. (5.3) becomes equal to 0 if

$$\xi = \left(\frac{1 - \tau\eta_0}{1 - \tau\eta} \right)^2 \xi_0 - \left\{ \frac{\tau(\eta - \eta_0)}{1 - \tau\eta} \right\}^2 \xi_0 - \frac{2 \tan \varphi}{\varepsilon(1 - \tau\eta)} (\eta - \eta_0). \quad (6.4)$$

4°. The function K is discontinuous in η for $\eta = 0$.

From eqs. (5.3) it is obtained that

Since the right hand sides of these two expressions are unequal, K is discontinuous in η for $\eta = 0$.

Fig. 6.2 shows lines of constant K values on the wing for the particular case

$$\varepsilon = 1/2, \quad \tau = 1/2, \quad \varphi = \pi/4, \\ \xi_0 = 1/2, \quad \eta_0 = 1/2.$$

The function will now be investigated for the case that $\eta_0 = 0$. According to eq. (5.1) ξ_0' is then equal to ξ_0 .

1°. Near the lines $\xi = \xi_0$ and $\xi = \xi_0'$ the function K is determined by eqs. (6.1) and (6.2) if $\eta_0 = 0$ is substituted.

2°. At both sides of the centre section K follows from eq. (6.3) with $\eta_0 = 0$.

3°. K vanishes at the curve obtained by substitution of $\eta_0 = 0$ in eq. (6.4) while η may assume both positive and negative values.

4°. The discontinuity in K for $\eta = 0$ remains finite if η_0 approaches 0, since eqs. (6.5) yield that both $K(\xi_0, \eta_0; \xi, 0^+)$ and $K(\xi_0, \eta_0; \xi, 0^-)$ behave as $-\frac{1}{\eta_0}$ for $\eta_0 \rightarrow 0$.

eq. (7.3) yields the following infinite set of integral equations in 1 variable:

$$\begin{aligned} w_0(\eta_0) = & \\ = & \frac{1}{2l} c_0(\eta_0) + \frac{1}{4\pi b} \sum_{n=0}^{\infty} \int_{-1}^1 K_{n0}(\eta_0, \eta) c_n'(\eta) d\eta + \\ & + \frac{1}{4\pi b} \sum_{n=0}^{\infty} \{K_{n0}(\eta_0, 0^+) - K_{n0}(\eta_0, 0^-)\} c_n(0) - \\ & - \frac{1}{4b} \int_{-1}^1 \frac{c_0'(\eta) + c_1'(\eta)}{\eta - \eta_0} d\eta, \quad (7.9) \end{aligned}$$

$$\begin{aligned} w_m(\eta_0) = & -\frac{1}{2l} c_m(\eta_0) + \\ & + \frac{1}{4\pi b} \sum_{n=0}^{\infty} \int_{-1}^1 K_{nm}(\eta_0, \eta) c_n'(\eta) d\eta + \\ & + \frac{1}{4\pi b} \sum_{n=0}^{\infty} \{K_{nm}(\eta_0, 0^+) - K_{nm}(\eta_0, 0^-)\} c_n(0), \\ & m=1, 2, \dots \quad (7.10) \end{aligned}$$

Together with the boundary conditions $c_i(\pm 1)=0$, these determine the unknown functions $c_i(\eta)$.

8 Approximate solution. Choice of pivotal points.

In practice only a few, say r , of the functions $c_i(\eta)$ will be taken into account. Hence, $i=0, 1, \dots, r-1$. However, the method to be dealt with in this section should only be applied for $r \geq 3$. If r is taken equal to 1 or 2, the method of Sec. 9 is to be preferred since it allows in these cases a more accurate determination of lift and moment than the method given in this section.

If only the functions $c_i(\eta)$, $i=0, 1, \dots, r-1$ are considered, eq. (7.10) is left out of account for $m \geq r$, while the summations occurring in the remaining equations must be taken from $n=0$ to $n=r-1$. This means that the functions K_n , eqs. (7.4), are neglected for $n \geq r$. The problem is then to determine the functions K_n for $n < r$, i.e. integrals of the types

$$\begin{aligned} & \int_{-1}^1 f(\xi) \cot \frac{\vartheta}{2} d\xi \text{ and} \\ & \int_{-1}^1 f(\xi) \sin n\vartheta d\xi, \quad n=1, 2, \dots, r-1 \quad (8.1) \end{aligned}$$

with such an accuracy that the error is of the order

$$\int_{-1}^1 f(\xi) \sin n\vartheta d\xi, \quad n \geq r,$$

since the latter integrals are neglected. This means that the following approximation for $f(\xi)$ may be used:

$$f(\xi) = a_0 + 2 \sum_{m=1}^r a_m \cos m\vartheta. \quad (8.2)$$

By giving the value of $f(\xi)$ in $r+1$ arbitrary values of ξ , the function is completely determined provided it is of the type (8.2). The integrals (8.1) then can be calculated. However, it appears to be possible to choose r special values of ξ , so-called *pivotal points*, and if $f(\xi)$ is known in these points and is, moreover, of the type (8.2), the integrals (8.1) can also be obtained exactly. This procedure is the same as that used in a similar case by MULTHOFF (ref. 4) for $r=1$ and 2.

The integrals will become equal to

$$\int_{-1}^1 f(\xi) \cot \frac{\vartheta}{2} d\xi = \sum_{s=1}^r p_{0s} f(\xi_s), \quad (8.3)$$

$$\int_{-1}^1 f(\xi) \sin n\vartheta d\xi = \sum_{s=1}^r p_{ns} f(\xi_s) \quad n=1, 2, \dots, r-1.$$

It appears (see App. 2) that the position of the pivotal points is determined by the general formula

$$\vartheta_s = \frac{2s-1}{2r+1} \pi, \quad s=1, 2, \dots, r.$$

The values of the quantities p_{is} are obtained by substituting eq. (8.3) into eq. (8.2) and equating the coefficients of a_m .

The values of the quantities ξ_s and p_{is} are given in table 8.1 for $r=1$.

If it is assumed, as has been done by eq. (8.2), that $K(\xi_0, \eta_0; \xi, \eta)$ is a polynomial of degree r in ξ , eqs. (5.3) and (5.4) show that it may also be assumed that $K(\xi_0, \eta_0; \xi, \eta)$ is a polynomial of degree r in ξ_0 . In case of an untapered wing ($\tau=0$) the assumptions are exactly equivalent. Moreover, no greater errors will be involved if it is assumed that

$$K(\xi_0, \eta_0; \xi, \eta) \cos \alpha(\xi_0) \text{ and } w(\xi_0, \eta_0) \cos \alpha(\xi_0)$$

are also polynomials of degree r in ξ_0 . Hence for the evaluation of the integrals (7.7) and (7.8), i.e. of integrals of the type

$$\int_0^\pi h(\xi_0) \cos m\vartheta_0 d\vartheta_0, \quad m=0, 1, \dots, r-1. \quad (8.4)$$

it may be assumed that

$$h(\xi_0) = b_0 + 2 \sum_{n=1}^r b_n \cos n\vartheta_0. \quad (8.5)$$

Similar to eqs. (8.3) the integrals (8.4) become equal to

$$\begin{aligned} & \int_0^\pi h(\xi_0) \cos m\vartheta_0 d\vartheta_0 = \\ & = \sum_{s=1}^r q_{ms} h(\xi_{0,s}), \quad m=0, 1, \dots, r-1. \quad (8.6) \end{aligned}$$

Since for any value of m the left hand side of eq. (8.6) is independent of b_r , the right hand side must also be independent of b_r . Hence, it can be concluded at once that the pivotal points are determined by the condition

TABLE 8.1

Quantities required for the evaluation of the integrals (8.3).

r	s	ϑ_s	ξ_s	p_{0s}	p_{1s}	p_{2s}	p_{3s}
1	1	$\frac{1}{3}\pi$	-0.5	3.1416			
2	1	$\frac{1}{5}\pi$	-0.8090	2.2733	0.4342		
2	2	$\frac{3}{5}\pi$	+0.3090	0.8683	1.1367		
3	1	$\frac{1}{7}\pi$	-0.9010	1.7063	0.1690	0.3045	
3	2	$\frac{3}{7}\pi$	-0.2225	1.0973	0.8532	0.3797	
3	3	$\frac{5}{7}\pi$	+0.6235	0.3380	0.5487	-0.6842	
4	1	$\frac{1}{9}\pi$	-0.9397	1.3542	0.0817	0.1535	0.2068
4	2	$\frac{3}{9}\pi$	-0.5000	1.0472	0.5236	0.5236	0
4	3	$\frac{5}{9}\pi$	+0.1736	0.5769	0.6771	-0.2352	-0.5954
4	4	$\frac{7}{9}\pi$	+0.7660	0.1633	0.2885	-0.4419	0.3886

TABLE 8.2

Quantities required for the evaluation of the integrals (9.4).

r	s	ϑ_s	ξ_s	p_{0s}	p_{1s}	p_{2s}	p_{3s}
1	1	$\frac{2}{3}\pi$	+0.5	3.1416			
2	1	$\frac{2}{5}\pi$	-0.3090	0.8683	1.1367		
2	2	$\frac{4}{5}\pi$	+0.8090	2.2733	0.4342		
3	1	$\frac{2}{7}\pi$	-0.6235	0.3380	0.5487	0.6842	
3	2	$\frac{4}{7}\pi$	+0.2225	1.0973	0.8532	-0.3797	
3	3	$\frac{6}{7}\pi$	+0.9010	1.7063	0.1690	-0.3045	
4	1	$\frac{2}{9}\pi$	-0.7660	0.1633	0.2885	0.4419	0.3886
4	2	$\frac{4}{9}\pi$	-0.1736	0.5769	0.6771	0.2352	-0.5954
4	3	$\frac{6}{9}\pi$	+0.5000	1.0472	0.5236	-0.5236	0
4	4	$\frac{8}{9}\pi$	+0.9397	1.3542	0.0817	-0.1535	0.2068

TABLE 8.3.

Quantities required for the evaluation of the integrals (8.4).

r	s	ϑ_s	ξ_s	p_{0s}	p_{1s}	p_{2s}	p_{3s}
1	1	$\frac{1}{2}\pi$	0	3.1416			
2	1	$\frac{1}{4}\pi$	-0.7071	1.5708	1.1107		
2	2	$\frac{3}{4}\pi$	+0.7071	1.5708	-1.1107		
3	1	$\frac{1}{6}\pi$	-0.8660	1.0472	0.9069	0.5236	
3	2	$\frac{1}{2}\pi$	0	1.0472	0	-1.0472	
3	3	$\frac{5}{6}\pi$	+0.8660	1.0472	-0.9069	0.5236	
4	1	$\frac{1}{8}\pi$	-0.9239	0.7854	0.4512	0.5554	0.6011
4	2	$\frac{3}{8}\pi$	-0.3827	0.7854	0.6011	-0.5554	-1.4512
4	3	$\frac{5}{8}\pi$	+0.3827	0.7854	-0.6011	-0.5554	-1.4512
4	4	$\frac{7}{8}\pi$	+0.9239	0.7854	-1.4512	0.5554	-0.6011

$$\cos r\vartheta_s = 0 \text{ or } \vartheta_s = \frac{2s-1}{2r}\pi \quad s=1, 2, \dots, r.$$

Table 8.3 contains the resulting values for $\xi_{0,s}$ and q_{is} for $r=1$ to $r=4$.

In this way all quantities in eqs. (7.9) and (7.10) are known except the unknown functions $c_i(\eta)$. This integral equation can be solved by one of the known methods (ref. 7), which will not be considered here furthermore.

9 Approximations based on lift, first and higher moments.

Instead of operating with the expansion coefficients $c_i(\eta)$ it is possible to use the integral quantities

$$g_0(\eta) = \Gamma(\eta) = l \int_{-1}^1 \gamma_y d\xi,$$

$$g_n(\eta) = l \int_{-1}^1 \gamma_y \cos n\vartheta d\xi, \quad n=0, 1, \dots \quad (9.1)$$

denoting lift, first and higher moments respectively. By substitution of eqs. (7.1) and (7.2) into eq. (9.1) the following relations are found:

$$g_0(\eta) = \pi \{ c_0(\eta) + c_1(\eta) \},$$

$$g_1(\eta) = \frac{1}{2}\pi \{ c_0(\eta) + c_2(\eta) \}, \quad (9.2)$$

$$g_n(\eta) = \frac{1}{2}\pi \{ -c_{n-1}(\eta) + c_{n+1}(\eta) \} \text{ if } n \geq 2.$$

The advantage of the functions $g_i(\eta)$ compared with the functions $c_i(\eta)$ is that two of them, viz. $g_0(\eta)$ and $g_1(\eta)$ determine already lift and moment of the wing, while three of the c_i -functions are required to attain the same purpose. Before proceeding to the special cases $r=1$ and 2, the general set of integral equations, based on the use of the g_i -functions will be derived.

This is performed by multiplying eq. (7.3) with

$$\cos \alpha(\xi_0) \tan \frac{\vartheta_0}{2}, \cos \alpha(\xi_0) \sin m\vartheta_0,$$

$$m=1, 2, \dots \quad (9.3)$$

respectively and integrating to ξ_0 from -1 to $+1$. Since

$$\int_{-1}^{+1} \left\{ c_0(\eta_0) - 2 \sum_{n=1}^{\infty} c_n(\eta_0) \cos n\vartheta_0 \right\} \tan \frac{\vartheta_0}{2} d\xi_0 = g_0(\eta_0),$$

$$\int_{-1}^{+1} \left\{ c_0(\eta_0) - 2 \sum_{n=1}^{\infty} c_n(\eta_0) \cos n\vartheta_0 \right\} \sin m\vartheta_0 d\xi_0 = g_m(\eta_0)$$

and introducing moreover

$$K_{n0}(\eta_0, \eta) = \int_{-1}^{+1} K_n(\xi_0, \eta_0; \eta) \cos \alpha(\xi_0) \tan \frac{\vartheta_0}{2} d\xi_0, \quad (9.4)$$

$$K_{nm}(\eta_0, \eta) = \int_{-1}^{+1} K_n(\xi_0, \eta_0; \eta) \cos \alpha(\xi_0) \sin m\vartheta_0 d\xi_0,$$

the result is:

$$l \int_{-1}^{+1} w(\xi_0, \eta_0) \cos \alpha(\xi_0) \tan \frac{\vartheta_0}{2} d\xi_0 = \frac{1}{2} g_0(\eta_0) - \frac{l}{4\pi b} \int_{-1}^{+1} \cos \alpha(\xi_0) \tan \frac{\vartheta_0}{2} d\xi_0 \int_{-1}^{+1} \frac{g_0'(\eta)}{\eta - \eta_0} d\eta +$$

$$+ \frac{l}{4\pi b} \sum_{n=0}^{\infty} \int_{-1}^{+1} K_{n0}(\eta_0, \eta) c_n'(\eta) d\eta + \frac{l}{4\pi b} \sum_{n=0}^{\infty} \{K_{n0}(\eta_0, 0^+) - K_{n0}(\eta_0, 0^-)\} c_n(0), \quad (9.5)$$

$$l \int_{-1}^{+1} w(\xi_0, \eta_0) \cos \alpha(\xi_0) \sin m\vartheta_0 d\xi_0 = \frac{1}{2} g_m(\eta_0) - \frac{l}{4\pi b} \int_{-1}^{+1} \cos \alpha(\xi_0) \sin m\vartheta_0 d\xi_0 \int_{-1}^{+1} \frac{g_0'(\eta)}{\eta - \eta_0} d\eta +$$

$$+ \frac{l}{4\pi b} \sum_{n=0}^{\infty} \int_{-1}^{+1} K_{nm}(\eta_0, \eta) c_n'(\eta) d\eta + \frac{l}{4\pi b} \sum_{n=0}^{\infty} \{K_{nm}(\eta_0, 0^+) - K_{nm}(\eta_0, 0^-)\} c_n(0). \quad (9.6)$$

Apart from the factor $\cos \alpha(\xi_0)$ the weight functions (9.3) are the same as those introduced by FLAX (ref. 8) when solving the basic integral equation of lifting surface theory by aid of the adjoint variational principle.

It may be remarked that if in eq. (7.3)

$$K_n(\xi_0, \eta_0; \eta) c_n'(\eta)$$

is replaced by $\bar{K}_n(\xi_0, \eta_0; \eta) g_n'(\eta)$,

where

$$\bar{K}_0(\xi_0, \eta_0; \eta) = \frac{1}{\pi} \int_0^\pi K(\xi_0, \eta_0; \xi, \eta) d\vartheta,$$

$$\bar{K}_n(\xi_0, \eta_0; \eta) = \frac{2}{\pi} \int_0^\pi K(\xi_0, \eta_0; \xi, \eta) \cos n\vartheta d\vartheta, \quad n \geq 1$$

and a similar reduction is made for the last term in eq. (7.3), eqs. (9.5) and (9.6) can be written in terms of the g_i -functions only.

However, when taking into account only r unknown functions, larger errors are made when $g_r(\eta)$ is neglected than when $c_r(\eta)$ is neglected. This is due to the fact that $g_r(\eta)$ is of the same order as $c_{r-1}(\eta)$ according to eq. (9.2). Hence, the best way is to retain the terms containing $c_n(\eta)$ functions in the form in which they are given in eqs. (9.5) and (9.6) and to express $c_n(\eta)$, $n = 0, 1, \dots, r-1$ into $g_n(\eta)$, $n = 0, 1, \dots, r-1$ by aid of the first r equations of the set (9.2) while neglecting $c_r(\eta)$. This leads to the same result as would be obtained when $g_r(\eta)$ is replaced by the linear combination of $g_0(\eta), g_1(\eta), \dots, g_{r-1}(\eta)$ which follows from eqs. (9.2) and then substituted into the form $\bar{K}_n(\xi_0, \eta_0; \eta) g_n'(\eta)$.

For $r=2$, eqs. (9.2) yield

$$c_0(\eta) = \frac{2}{\pi} g_1(\eta), \quad c_1(\eta) = \frac{1}{\pi} g_0(\eta) - \frac{2}{\pi} g_1'(\eta).$$

while for $r=1$

$$c_0(\eta) = \frac{1}{\pi} g_0(\eta).$$

The most accurate way for evaluating integrals of the type (9.4) when using r pivotal points is similar to that described in Sec. 8 when referring to the integrals (8.1).

By substitution of $\vartheta = \pi - \vartheta_0$ the integrals (8.1) transform into integrals of the type (9.4). Hence the pivotal points are determined by the formula

$$\vartheta_s = \frac{2s}{2r+1} \pi, \quad s = 1, 2, \dots, r$$

while the coefficients p_{is} are closely related to those used in Sec. 8 (see table 8.2).

After having performed the integration to ξ_0 the integral equations (9.5) and (9.6) can be solved for the unknown functions $g_i(\eta)$.

10 Comparison with Weissinger's result.

For the particular case $r=1$ it might be expected that the present result becomes identical to that of WEISSINGER's L -method (ref. 2). Indeed for $r=1$, eq. (9.5) becomes equal to

$$l \int_{-1}^{+1} w(\xi_0, \eta_0) \cos \alpha(\xi_0) \tan \frac{\vartheta_0}{2} d\xi_0 = \frac{1}{2} g_0(\eta_0) -$$

$$- \frac{l}{4\pi b} \int_{-1}^{+1} \cos \alpha(\xi_0) \tan \frac{\vartheta_0}{2} d\xi_0 \int_{-1}^{+1} \frac{g_0'(\eta)}{\eta - \eta_0} d\eta +$$

$$+ \frac{l}{4\pi^2 b} \int_{-1}^{+1} K_{00}(\eta_0, \eta) g_0'(\eta) d\eta +$$

$$+ \frac{l}{4\pi^2 b} \{K_{00}(\eta_0, 0^+) - K_{00}(\eta_0, 0^-)\} g_0(0)$$

or, after performing the integration to ξ_0 by aid of the pivotal point $\xi_0 = 1/2$,

$$w(\frac{1}{2}, \eta_0) = \frac{g_0(\eta_0)}{2\pi l \cos \alpha(\frac{1}{2})} - \frac{1}{4\pi b} \int_{-1}^{+1} \frac{g_0'(\eta)}{\eta - \eta_0} d\eta +$$

$$+ \frac{1}{4\pi^2 b} \int_{-1}^{+1} K_0(\frac{1}{2}, \eta_0; \eta) g_0'(\eta) d\eta +$$

$$+ \frac{1}{4\pi^2 b} \{K_0(\frac{1}{2}, \eta_0; 0^+) - K_0(\frac{1}{2}, \eta_0; 0^-)\} g_0(0).$$

After performing also the integration to ξ involved in K_0 by aid of the pivotal point $\xi = -1/2$ the result is

$$w(\frac{1}{2}, \eta_0) = \frac{g_0(\eta)}{2\pi l \cos \alpha(\frac{1}{2})} - \frac{1}{4\pi b} \int_{-1}^1 \frac{g_0'(\eta)}{\eta - \eta_0} d\eta +$$

$$+ \frac{1}{4\pi b} \int_{-1}^1 K_0(\frac{1}{2}, \eta_0; -\frac{1}{2}, \eta) g_0'(\eta) d\eta +$$

$$+ \frac{1}{4\pi b} \{ K_0(\frac{1}{2}, \eta_0; -\frac{1}{2}, 0^+) -$$

$$- K_0(\frac{1}{2}, \eta_0; -\frac{1}{2}, 0^-) \} g_0(0). \quad (10.1)$$

It has been shown by REISSNER (ref. 5, see also ref. 6) that for the case of a rectangular unswept wing WEISSINGER's L -method leads to an equation identical to that resulting from (10.1) when τ and φ are taken equal to 0. It can easily be verified that WEISSINGER's general result used in the L -method corresponds to eq. (10.1).

11 Recapitulation.

By a suitable reduction of the expression for the downwash in an arbitrary point of a lifting surface, an integral equation in two variables for the pressure distribution is obtained. This equation contains a function $J(\xi_0, \eta_0; \xi, \eta)$ which is wholly determined by the planform of the wing. This function is evaluated in Sec. 4, where it appears that J is singular on the right wing if $\eta = \eta_0$ or $\xi = \xi_0$ and singular on the left wing if $\xi = \xi_0'$ (ξ_0' being the ξ -coordinate of the point (ξ_0, η_0)) if this point is considered as a point of the elongated left wing, see fig. 5.1). The ξ -singularity can be avoided by splitting off the two-dimensional downwash. The remaining function, called $K(\xi_0, \eta_0; \xi, \eta)$ is singular in the section $\eta = \eta_0$, while it has like J a discontinuity for $\eta = 0$. This function has been investigated in Sec. 6.

By introducing a series expansion for the chordwise vorticity distribution the integral equation in two variables can be transformed into an infinite set of integral equations for an infinite number of functions of one variable. If the series is cut off after, say r terms, a set of r integral equations for r functions is obtained. It is shown that with this approximation certain integrals may also be approximated by evaluating them by aid of r pivotal points. The position of these pivotal points is chosen in such a way that the errors become minimum.

If only 1 or 2 terms of the series expansion are taken into account, the procedure is slightly varied since it is advantageous to identify then the unknown functions with the lift and moment distributions. It is shown that for $r=1$ the method becomes identical to that of WEISSINGER.

12 List of references.

1. VAN DE VOOREN, A. I. "The Generalization of PRANDTL's Equation for Yawed and Swept Wings". Report F.121, Nat. Aero. Res. Inst. 1952.
2. WEISSINGER, J. "Ueber eine Erweiterung der Prandtl'schen Theorie der tragenden Linie". Math. Nachr. 2 Band Heft 1/2, p. 45-106, 1949.
3. FALKNER, V. M. "The Calculation of the Aerodynamic Loading on Surfaces of any Shape". R. and M. 1910, 1943.

4. MÜLTHOPP, H. "Methods for Calculating the Lift Distribution of Wings (Subsonic Lifting Surface Theory)". R. A. E. Report Aero 2353, 1950.
5. REISSNER, E. "Note on the Theory of Lifting Surfaces." Proc. of the Nat. Acad. of Sciences, Vol. 35, p. 208-215, April 1949.
6. BOSSCHAART, A. C. A. and VAN DE VOOREN, A. I. "Overzicht van enkele theorieën voor draagkrachtsverdeling van vleugels met grote slankheid." (in Dutch). Report F.92, Nat. Aero. Res. Inst., 1952.
7. MÜLTHOPP, H. "Die Berechnung der Auftriebsverteilung von Tragflügeln". Luftfahrtforschung Vol. 15, p. 153-169, 1938.
8. FLAX, A. H. "General Reverse Flow and Variational Theorems in Lifting-Surface Theory." J. of the Aero. Sci., Vol. 19, p. 361-374, 1952.

APPENDIX 1.

More rigorous derivation of eq. (3.19).

Since in the derivation of eq. (3.19) as given in the main text, integrals have been used of which no Cauchy principal value exists, a more rigorous derivation is presented here. Then the downwash is first calculated in a point (x_0, y_0, z_0) just above the lifting surface (z_0 small, but $\neq 0$), while only at the end the transition $z \rightarrow 0$ is made.

It can easily be verified that for $z_0 \neq 0$ BIOT and SAVART's formula (3.1) remains unchanged, provided

$$r = \sqrt{(x - x_0)^2 + (y - y_0)^2 + z_0^2}.$$

Eqs. (3.6) are to be replaced by

$$\frac{x - x_0}{r^3} = \frac{\partial}{\partial y} \left\{ \frac{(x - x_0)(y - y_0)}{\{(x - x_0)^2 + z_0^2\} r} \right\}$$

and

$$\frac{y - y_0}{r^3} = \frac{\partial}{\partial x} \left\{ \frac{(x - x_0)(y - y_0)}{\{(y - y_0)^2 + z_0^2\} r} \right\}$$

Pursuing the reduction leading to eq. (3.11), it is found that eq. (3.11) has to be changed into

$$w = \frac{b}{4\pi} \int_{-1}^1 \int_{-1}^1 \gamma_\eta \sin \alpha \frac{\partial}{\partial \xi} \left\{ \frac{(x - x_0)(y - y_0)}{\{(x - x_0)^2 + z_0^2\} r} \right. \\ \left. + \frac{(x - x_0)(y - y_0)}{\{(y - y_0)^2 + z_0^2\} r} \right\} d\xi d\eta -$$

$$- \frac{1}{4\pi} \int_{-1}^1 \int_{-1}^1 b \gamma_\eta \cos \alpha \frac{\partial}{\partial \eta} \left\{ \frac{(x - x_0)(y - y_0)}{\{(x - x_0)^2 + z_0^2\} r} \right\} d\xi d\eta +$$

$$+ \frac{b}{4\pi} \int_{-1}^1 \int_{-1}^1 \gamma_\xi \frac{\partial}{\partial \xi} \left\{ \frac{(x - x_0)(y - y_0)}{\{(y - y_0)^2 + z_0^2\} r} \right\} d\xi d\eta.$$

Partial integration of the last term leads finally to

$$- \frac{1}{4\pi b} \oint \frac{d\Gamma/d\eta}{\eta - \eta_0} d\eta -$$

$$- \frac{1}{4\pi} \int_{-1}^1 \int_{-1}^1 b \gamma_\eta \cos \alpha \frac{\partial}{\partial \eta} \left\{ \frac{(x - x_0)(y - y_0)}{\{(y - y_0)^2 + z_0^2\} r} \right\} d\xi d\eta.$$

Since

$$\frac{1}{(x-x_0)^2+z_0^2} + \frac{1}{(y-y_0)^2+z_0^2} = \frac{r^2+z_0^2}{\{(x-x_0)^2+z_0^2\}\{(y-y_0)^2+z_0^2\}},$$

the final formula for the downwash replacing eq. (3.16) becomes:

$$w(\xi_0, \eta_0) = -\frac{b}{4\pi} \int_{-1}^1 \int_{-1}^1 l_{\gamma} \frac{\partial}{\partial y} \frac{x-x_0}{\{(x-x_0)^2+z_0^2\}} \frac{y-y_0}{\{(y-y_0)^2+z_0^2\}} \frac{r^2+z_0^2}{r} d\xi d\eta - \frac{1}{4\pi b} \int_{-1}^1 \frac{d\Gamma/d\eta}{\eta-\eta_0} d\eta.$$

The function J is then introduced as

$$J(\xi_0, \eta_0; \xi, \eta) = b^2 \int \frac{\partial}{\partial y} \frac{x-x_0}{\{(x-x_0)^2+z_0^2\}} \frac{y-y^2}{\{(y-y_0)^2+z_0^2\}} \frac{r^2+z_0^2}{r} d\eta$$

and in this indefinite integral the limit $z_0 \rightarrow 0$ can be taken, which leads to the original definition of J as given by eq. (3.18). Since eq. (3.19) is also obtained in this way, it is clear that the results are the same, whether or not a small value of z_0 is introduced.

APPENDIX 2.

The best position of the pivotal points.

When calculating the integrals (8.1) the position of the pivotal points is determined by eqs. (8.3). After substitution of eq. (8.2), the following set of r equations is obtained:

$$\begin{aligned} \pi(a_0 + a_1) &= \sum_{s=1}^r p_{0s} \{ a_0 + 2 \sum_{m=1}^r a_m \cos m\vartheta_s \}, \\ \frac{1}{2} \pi(a_{n-1} - a_{n+1}) &= \\ &= \sum_{s=1}^r p_{ns} \{ a_n + 2 \sum_{m=1}^r a_m \cos m\vartheta_s \}, \\ n &= 1, 2, \dots, r-1. \quad (\text{A } 2.1) \end{aligned}$$

All these equations must be identities in the coefficients a_j . This means that any equation yields $r+1$ new equations and hence (A 2.1) is equivalent to $r(r+1)$ equations. The unknowns are r^2 quantities p_{js} together with r values of ϑ_s . These unknowns can be determined uniquely.

The position of the pivotal points can be found in the following way, given by Mr. E. M. DE JAGER.

The r equations (A 2.1) subsequently lead to the following sets of equations

$n=0$	$n=1$	$n=2$	etc:
$\sum_{s=1}^r p_{0s} = \pi$	$\sum_{s=1}^r p_{1s} = \frac{1}{2} \pi$	$\sum_{s=1}^r p_{2s} = 0$	to $n=r-1$
$\sum_{s=1}^r p_{0s} \cos \vartheta_s = \frac{1}{2} \pi$	$\sum_{s=1}^r p_{1s} \cos \vartheta_s = 0$	$\sum_{s=1}^r p_{2s} \cos \vartheta_s = \frac{1}{4} \pi$	
$\sum_{s=1}^r p_{0s} \cos 2\vartheta_s = 0$	$\sum_{s=1}^r p_{1s} \cos 2\vartheta_s = -\frac{1}{4} \pi$	$\sum_{s=1}^r p_{2s} \cos 2\vartheta_s = 0$	
$\sum_{s=1}^r p_{0s} \cos 3\vartheta_s = 0$	$\sum_{s=1}^r p_{1s} \cos 3\vartheta_s = 0$	$\sum_{s=1}^r p_{2s} \cos 3\vartheta_s = -\frac{1}{4} \pi$	
\vdots	\vdots	\vdots	
$\sum_{s=1}^r p_{0s} \cos r\vartheta_s = 0$	$\sum_{s=1}^r p_{1s} \cos r\vartheta_s = 0$	$\sum_{s=1}^r p_{2s} \cos r\vartheta_s = 0$	

For the right values of ϑ_s each set must be solvable in the coefficients p_{js} . This means that between the $r+1$ equations of each set a relation of the type

$$\lambda_0 + \lambda_1 \cos \vartheta_s + \lambda_2 \cos 2\vartheta_s + \dots + \lambda_r \cos r\vartheta_s = 0$$

must exist, where $\lambda_0, \dots, \lambda_r$ are suitably chosen constants. These constants follow immediately from the right hand sides of the equations. Hence

$$2\lambda_0 + \lambda_1 = 0, \quad 2\lambda_0 - \lambda_2 = 0, \quad \lambda_1 - \lambda_3 = 0 \dots$$

and it is seen that the relation

$$1 - 2 \cos \vartheta_s + 2 \cos 2\vartheta_s - 2 \cos 3\vartheta_s + \dots \pm 2 \cos r\vartheta_s = 0 \quad (\text{A } 2.2)$$

is sufficient to make the equations within any set linearly dependent.

Multiplication of eq. (A 2.2) throughout by $\cos \vartheta_s/2$ yields

$$\cos \frac{2r+1}{2} \vartheta_s = 0$$

or

$$\vartheta_s = \frac{2s-1}{2r+1} \pi, \quad s=1, 2, \dots, r.$$

Since integrals of the type (9.4) are, apart from a possible change in sign, transformed into the integrals (8.1) by replacing ϑ_0 by $\pi - \vartheta$, the best position of the pivotal points for evaluating these integrals follows immediately to be

$$\vartheta_{0,s} = \frac{2s}{2r+1} \pi, \quad s=1, 2, \dots, r.$$

REPORT M. 1857.

A Comparative Investigation on the Fatigue Strength at Fluctuating Tension of Several Types of Riveted Lap Joints, a Series of Bolted and some Series of Glued Lap Joints of 24 ST Alclad

by

Ir A. HARTMAN and G. C. DUYN

Summary.

The report contains the results of fatigue tests at fluctuating tension on various standard types of riveted joints in 24 ST alclad. Included in the investigation are some tests on bolted and glued single lap joints.

The most important results are:

In line or staggered riveting had no influence on the endurance strength of the specimens with thin sheets. In fatigue loading all the riveted joints gave nearly the same failing stresses.

Larger static strength was not coupled with increased fatigue strength.

The bonded joint at low stress level and the bolted joint at both high and low stress level had somewhat higher fatigue strengths than the riveted joint.

Contents.

- 1 Introduction.
- 2 Test pieces, test equipment and procedure.
 - 2.1 Test pieces.
 - 2.2 Static and fatigue testing.
 - 2.3 Strain measurements.
- 3 Results of the strain measurements on some test pieces with snap rivets.
- 4 Results of the static tests.
- 5 Results of the fatigue tests.
 - 5.1 Fatigue tests on test pieces with snap rivets (type Pb).
 - 5.2 Fatigue tests on test pieces with countersunk rivets (type Vf).
 - 5.3 Fatigue tests on test pieces with countersunk rivets (type Vd).
 - 5.4 Fatigue tests on test pieces with countersunk rivets (type Ve).
 - 5.5 Fatigue tests on test pieces with countersunk rivets (type V).
 - 5.6 Fatigue tests on test pieces with steel snap rivets.
 - 5.7 Fatigue tests on test pieces with 1/8" T.L.P. Monell-pop rivets.
 - 5.8 Fatigue tests on test pieces with steel bolts.
 - 5.9 Fatigue tests on test pieces with glued joint.
 - 5.10 Comparison of the results.
- 6 Conclusions.
- 7 References.

1 Introduction.

In the technical literature a number of papers have been published dealing with the fatigue strength of riveted joints (see e.g. the review of the literature up to about 1950, given in ref. 1). However, the test results prove to depend to a large extent on details of the fabrication technique and the form of the test specimens, so that it is only possible to derive general trends from the published information, but no quantitative results for particular applications.

When it was therefore desired to obtain some knowledge of the fatigue properties of various types of joints used as standard types by the Netherlands aircraft industry, it was necessary to carry out a fairly extensive programme of fatigue tests in fluctuating tension. This programme was established by the Fatigue Committee of the Netherlands Aircraft Development Board (N.I.V.) and also incorporated the fatigue testing of a series of bolted lap joints — sometimes used for repair jobs — and a series of glued lap joints, which by the development of metal adhesives like Redux in many fields are competitive to riveted joints. The results of the experiments on two types of riveted lap joints have already been published in ref. 2 and those of previous tests on glued lap joints of smaller dimensions in ref. 3. Both reports are in Dutch and for convenience of the readers, who do not understand this language the most important results are repeated in this report.

The whole investigation was carried out in charge of the Netherlands Aircraft Development Board.

2 Test pieces, test equipment and procedure.

2.1 Test pieces.

Materials of the test pieces.

The 24ST alclad sheet material for the test pieces was supplied by the Nederlandse Aluminium-maatschappij N.V. at Utrecht. The mechanical properties of the alloy, determined from normal static tensile test pieces, cut at random from riveted test pieces, are given in the table.

There is a marked difference between the mechanical properties "with grain" and "cross grain".

All rivets were 17 S, riveted cold in the solution-treated temper.

fig. 2b — type *Vf* — front sheet half sunk, half dimpled — rear sheet dimpled.

fig. 2c — type *Vd* — both sheets dimpled.

fig. 2d — type *Ve* — front sheet dimpled — rear sheet sunk.

fig. 2e — type *V* — front sheet sunk — rear sheet flat.

fig. 2f — type *Pb* — both sheets flat — steel snap rivets.

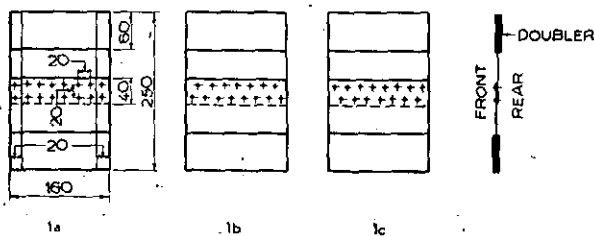
fig. 2g — type Monell-poprivet — both sheets flat — monell poprivets.

fig. 2h — bolted — both sheets flat — steel bolts, with duralumin nuts, assembled with 5 to 10 in-lbs torque.

Material	Thickness	Grain direction	Yield strength $\sigma_{0.2}$ kg/mm ²	Ultimate strength σ_u kg/mm ²	Elongation δ in % $l = 5.65 \sqrt{A}$
24 ST alclad	0.8 mm	with	36.5	45.0	22
"	"	"	36.9	45.2	22
"	"	"	37.6	46.7	23
"	"	"	36.4	47.1	22
"	"	cross	29.9	43.6	21
"	"	"	29.9	44.1	21
"	"	"	29.5	43.2	22
"	"	"	26.6	43.9	24
"	1.2 mm	with	37.7	47.1	22
"	"	"	38.5	46.9	22

Dimensions and shape of the test pieces.

The riveted test pieces were single lap joints with two rows of rivets (bolts) placed either in line or staggered. The 3 types of test pieces are shown in figs 1a to 1c incl. The dimensions of the bonded lap joints are given in figs 1d to 1g incl. In most of the joints the grain direction of the sheet material was perpendicular to the direction of loading.



— RIVET HEAD (BOLT)

Fig. 1. Shape and dimensions of the riveted, bolted and glued specimens.

1a to c. Riveted or bolted joints.

Type of joint.

The various types of riveted and bolted joints are given in the figures 2a to 2h incl.

fig. 2a — type *Pb* — both sheets flat — snap rivets.

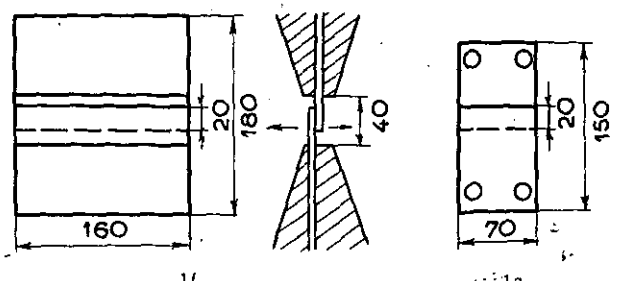
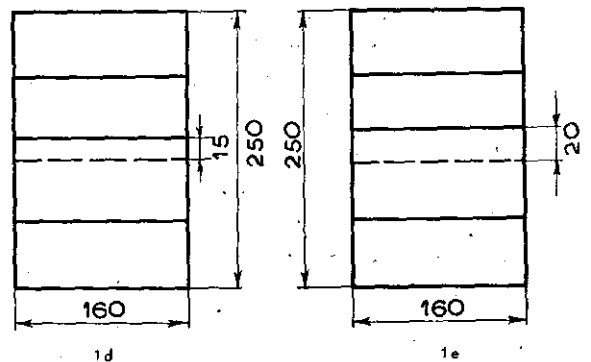


Fig. 1d to g. Glued joints.

For the glued joints (figs 1d to g incl.) "Redux" was used. All test pieces were made at the Fokker Aircraft Co according to common practice, except

same width. The 10 tons dynamometer of the pulsator was used for the static tests and the 2 tons dynamometer for the fatigue tests. The

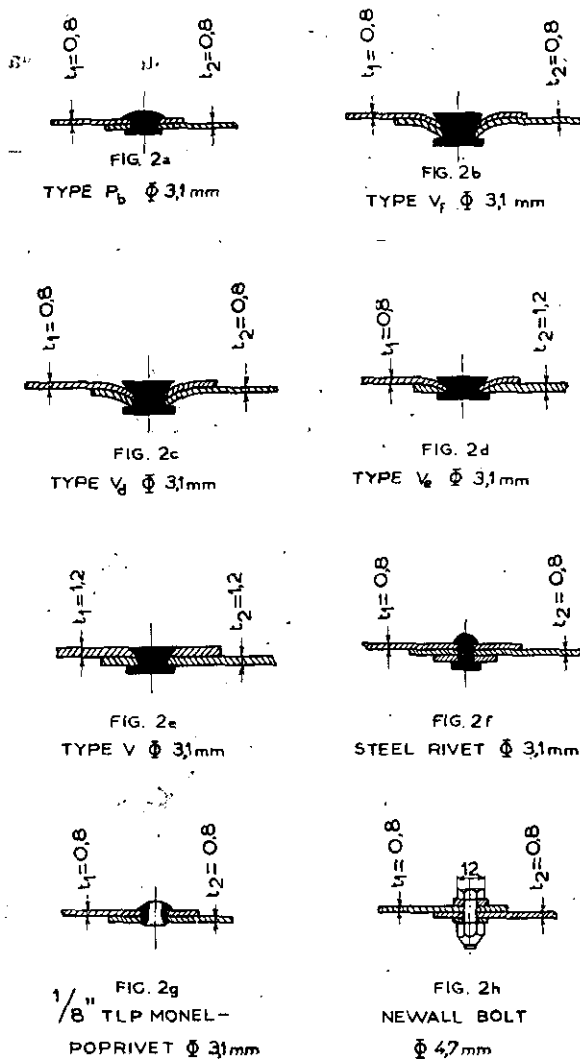


Fig. 2. Types of riveted and bolted joints.

8 specimens according to fig. 1g which were made at N.L.L.

The procedure for the bonding with Redux was as follows:

- (1) Degreasing with trichlorethylene.
- (2) Pickling according to DTD 915 A.
- (3) Applying a thin layer of Redux liquid (with brush), sprinkling with Redux powder, tapping off surplus powder.
- (4) Setting of the glue by heating on electrically heated press. Pressure on the glue 7 kg/cm², temperature of the glue 142° C, duration 20 minutes.

2.2 Static and fatigue testing.

The static and fatigue testing of the riveted, bolted and glued joints according to the figs 1 and 2 was carried out in an Amsler high-frequency pulsating machine (Vibraphore) of 10 tons capacity. As can be seen from fig. 3 the test pieces were bolted to two steel clamping heads of the

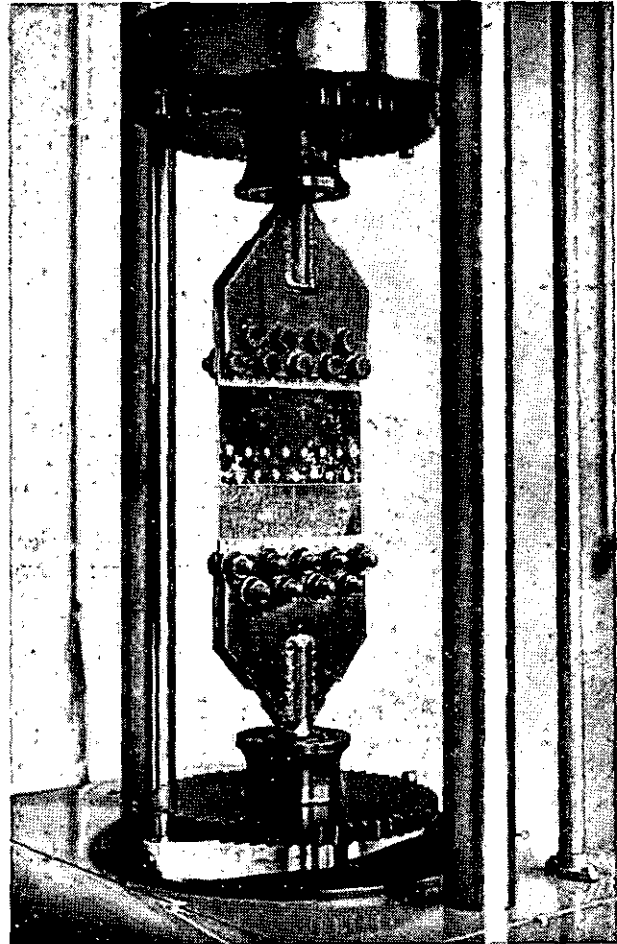


Fig. 3. Test set up in Amsler vibraphore.

fatigue testing of the bonded joints of fig. 1g was made in an Amsler high frequency pulsating machine of 2 tons capacity also with clamping heads of the same width as the test pieces.

The Wöhler curves (S-N curves) were determined for fluctuating tension with a minimum load of 100 kg. The frequency of the load reversals was about 8000/minute. If after about 50.10⁶ load reversals the test piece was not cracked the test was stopped. Otherwise the end of the test was the cracking of the specimen in the joint or in the clamping head. By adjusting the switch-off relay always in the same way it was achieved that the switching-off took place at the same degree of crack formation. It is expected that complete failure of the specimen would have occurred soon afterwards. Some specimens were tested with a small compressive lower load limit to check the influence of load inversion.

2.3 Strain measurements.

To investigate the load distribution across the width of the specimen at first mechanical and afterwards electrical strain measurements were carried out.

The mechanical strain measurements were carried out by means of six Huggenberger tensometers, mounted in pairs at both sides of the specimen between the clamping heads and the riveted joint (fig. 4). For these measurements it turned out to

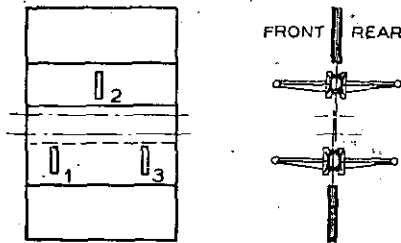


Fig. 4. Location of the Huggenberger tensometers.

be almost impossible to mount tensometers at more than three places on one side of the specimen.

Moreover these mechanical measurements have no better accuracy than about 3 %.

Therefore, it was decided to apply electrical strain-gauges on two specimens of the type shown in fig. 1c.

One of these specimens was very well finished and flat, the other one was less well finished and visibly warped.

The method of measuring made it possible to determine more accurately the local strains between the rivets and to determine the changes of the mean strains during dynamic loading (see below under "dynamic loads").

The Philips type strain-gauges were located on the specimens as shown in fig. 5. Using a switch-

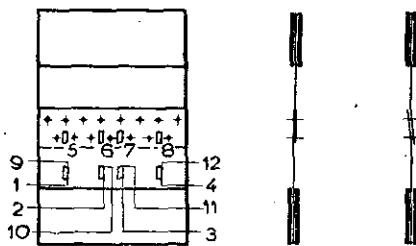


Fig. 5a. Location of the strain gauges. Fig. 5b. Unloaded and loaded specimen.

Gauges 1, 2, 3, 4, 5, 6, 7, and 8: front.

Gauges 9, 10, 11 and 12: rear.

board, it was possible to take readings of the Baldwin Strain Indicator for each strain-gauge separately. For temperature compensation the strain-gauges of the unloaded specimen were used as dummy gauges.

In fig. 6 the test set-up is shown.

Strains were measured for the following conditions:

Static loads. Loads read from the scale of the 10 tons Amsler H. F. Pulsator, equipped with a 2 tons dynamometer.

- (a) Specimen hanging loosely on the bolts of the upper clamping head.
- (b) Specimen fixed in upper and lower clamping head; in this condition the loads varied from 0 to 1000 kilogrammes, with increments of 100 or 200 kilogrammes.

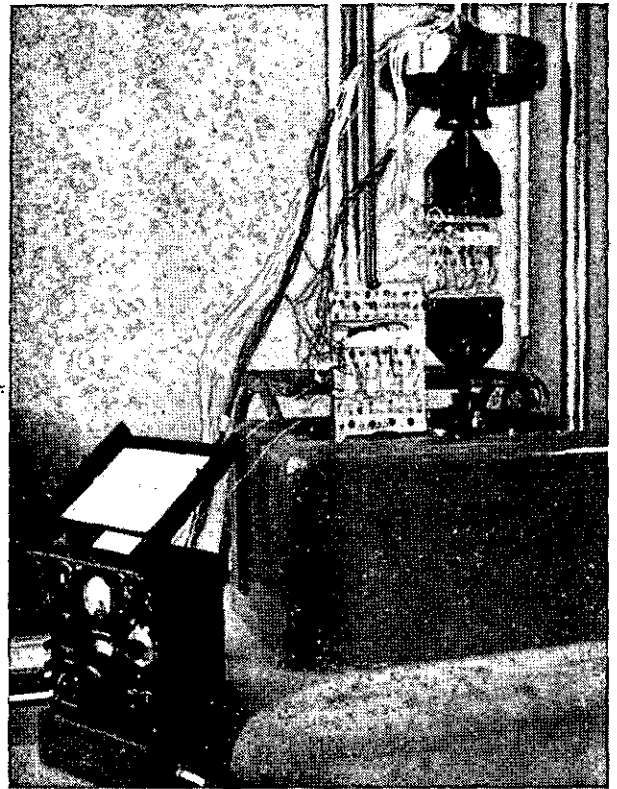


Fig. 6. Set-up for electrical strain measurements (c.f. section 2.3).

Dynamic loads. Average load 550 kilogrammes, read from the scale of the H. F. Pulsator (limits 100 kg and 1000 kg).

Strains were read at six numbers of reversals as indicated by the cycle-counter of the testing-machine.

The test set-up was exactly the same as during the static tests.

Due to the high frequency of the testing machine (about 8000 cycles/min), the reading of the galvanometer of the strain indicator gave no extra difficulties; during dynamic loading the inertia of the indicating mechanism caused the pointer to indicate the mean strain. Only the wiring of the gauges in the vicinity of the specimen sometimes suffered some damage due to fatigue; this damage was always easy to repair.

3 Results of the strain measurements on some test pieces with snap rivets.

The results of the mechanical strain measurements are given in table 1. In this table, for several specimens, the strains at the tensometers

TABLE 1.

Results of mechanical strain measurements.

Specimen no.	Load in kgs	Measured strain computed strain ¹⁾		
		Position (see fig. 4)		
		1	2	3
1b	300	—	—	—
	800	0.98	0.93	0.95
	1200	1.01	0.97	1.00
	1600	1.01	0.97	0.98
	1800	1.01	0.98	0.98
2b	800	—	—	—
	1000	1.13	0.99	1.20
	1400	1.03	0.96	1.11
	1800	0.98	0.94	1.07
	2200	0.98	0.98	1.09
3b	300	—	—	—
	800	1.05	0.97	1.02
	1200	1.03	0.98	1.05
	1600	1.06	1.00	1.08
	1750	1.08	1.01	1.09
4b	300	—	—	—
	800	0.98	0.96	0.98
	1200	1.05	1.00	1.03
	1600	1.06	1.02	1.02
5b	300	—	—	—
	800	0.94	1.02	0.97
	1200	0.97	1.03	0.97
	1600	0.98	1.06	0.98

¹⁾ The strains are all with respect to the first reading at 300 kg or 800 kg.

1, 2 and 3, (see fig. 4) taken at different loads, are given as percentages of the calculated average strain, using a modulus of elasticity of 7000 kg/mm².

The results show that the uniformity of the strain distribution is very good for specimens 1b and 4b and somewhat less for the other three specimens.

One has to consider the fact that strains were read from three tensometers which were not situated in line. Moreover, the horizontal position of the Huggenberger tensometers may induce fairly large errors caused by the unequal loading of the knife edges.

The results obtained from the electrical strain measurements are given in the tables 2 and 3 and in the figures 7 and 8.

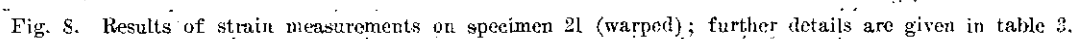
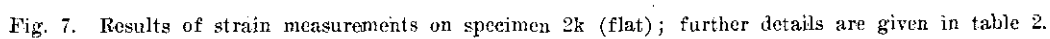
In these figures the strains of the gauges 1

and 9, 2 and 10, 3 and 11, 4 and 12 were added to compensate for strains, caused by bending of the specimen.

From the graphs of these pairs for the *static measurements* (strain versus load) it is evident that the load distribution is very satisfactory.

Taking the zero-position indicated on the scale of the testing machine as a reference, the largest scatter measured amounts to about 7 % for the flat specimen and 4 % for the warped specimen. Though at this location the scatter for the flat specimen exceeded that for the warped one, the stress distribution at the rivet line was, as could be expected, more favourable for the flat specimen.

For the gauges 5, 6, 7 and 8 bending was not compensated for, as it was not possible to attach opposite strain gauges at the same half of the specimen because of the lap joint. The heavy



bending of the specimen near the joint was due to asymmetry (fig. 5b).

This asymmetry caused a compressive stress at the place where the gauges were attached. In the graphs this compressive stress results in pronounced curvature of the lower part of the load-strain curves 5, 6, 7 and 8.

In the flat specimen 2 k the bending stresses were about the same at all four gauges 5 to 8.

In specimen 2 l, however, at strain gauge 8 extra low strains were measured. This meant that at the same specimen half, but at the inside of the joint extra high tensile stresses occurred.

The bending stress near gauge 8 is about 3 times as high as near gauges 5 and 6. As was to be expected the first cracks developed near this gauge 8. Nevertheless, the life of the poorly finished specimen 2 l is only about 10 % less than that of the better specimen 2 k.

The influence of the clamping of the specimen in the clamping heads is shown by the sloping, dotted lines. This clamping caused local prestressing, varying between 0.3 and 0.6 kg/mm².

During the *dynamic tests* (lower parts of tables 2 and 3 and curves B in figs 7 and 8), at about 70 % of the life of the specimen a considerable increase of the strains was observed at a number of gauges, in particular at gauges between the rivets. At these places the first cracks were observed. Strain gauge 8 of specimen 2 k failed in consequence of cracks which originated from the neighbouring rivets.

4 Results of the static tests.

Table 4 gives the results of the static tests, which are also indicated in fig. 18. The scatter in the results of these static tests is less than 5 % with the exception of the results for the type *Ve* and the strength of the specimens riveted in line is slightly higher than that of the specimens with staggered rivet rows. Because the failure was by shearing of the rivets and the staggered specimen has one rivet less than the specimens riveted in line, these results are quite reasonable. Because shearing of the rivets was critical it is clear that the heavier sheet of the type *V* has no important influence on the ultimate strength. For the riveted joints with steel rivets and the bolted and glued joints failure always occurred at the clamping head. The real ultimate load of the joint is higher than the value indicated in fig. 18.

The joints with pop rivets have the lowest strength.

5 Results of the fatigue tests.

5.1 Fatigue tests on test pieces with snap rivets (type *Pb*).

The results of these tests are given in table 5 and in fig. 9, in which is also drawn the scatter band. From the situation of the points in the scatter band it is clear that there is no marked difference in fatigue strength of the 3 types of test pieces 1a to 1c. The mean endurance strength at a minimum load of 100 kg for a life of $5 \cdot 10^7$

cycles is estimated at 550 kg. In nearly all cases the crack initiated in the front plate at the lower row of rivets ((fig. 1), i. e. at the side of the pre-formed rivet heads and regardless of whether there were 7 or 8 rivets in this row. It can therefore be concluded that the damage and stress concentration caused to the front plate during the riveting operation is critical in fatigue testing (for this type of rivets).

In this report the fatigue strength of this type of lap joint with snap rivets has been taken as standard of comparison and for this purpose the scatter band of fig. 9 has been redrawn in the figures of all other joints.

5.2 Fatigue tests on test pieces with countersunk rivets (type *Vf*).

Table 6 and fig. 10 give the results for these riveted lap joints. The situation of the points in fig. 10 indicates that probably the fatigue strength at 10^6 cycles for the test pieces riveted in line is somewhat higher than for the staggered specimens, but the difference is unimportant. As a whole the fatigue strength of the joints type 2a and 2b is the same. Contrary to that for joints of type *Pb* the start of the crack for joints of type *Vf* was not in the front plate, but in the rear plate, beginning at the shank of the rivets, i. e. at the head formed during riveting.

As is shown in fig. 10 the result of test piece 1 l with a compressive lower limit fits well in the scatter band for tests with tensile loads only. To plot this result with the compressive lower limit in the same figure a fatigue load from $+x$ to $-y$ kg was taken equivalent to a load from $+(x+y+100)$ kg to 100 kg.

5.3 Fatigue tests on test pieces with countersunk rivets (type *Vd*).

In this and in the following series the number of test pieces according to the figs 1b and 1c was diminished, because the results for the specimens of the two preceding series indicated no significant differences between these two types. The results of the tests are given in table 7 and in fig. 11. All the results are within the scatter band for the lap joints with snap rivets; there is a slight indication that the mean life at low stress levels is somewhat higher for the type *Vd*.

5.4 Fatigue tests on test pieces with countersunk rivets (type *Ve*).

Table 8 and fig. 12 give the results for the specimens with countersunk rivets and with 0.8 and 1.2 mm sheets. Here also all the points are within the scatter band for the lap joints with snap rivets in thin plate. As could be expected the formation of the crack was always in the thin plate (the front plate). In fig. 12 like in fig. 10 the result of a test piece with a compressive lower limit fits well in the scatter band for tests with tensile loads only.

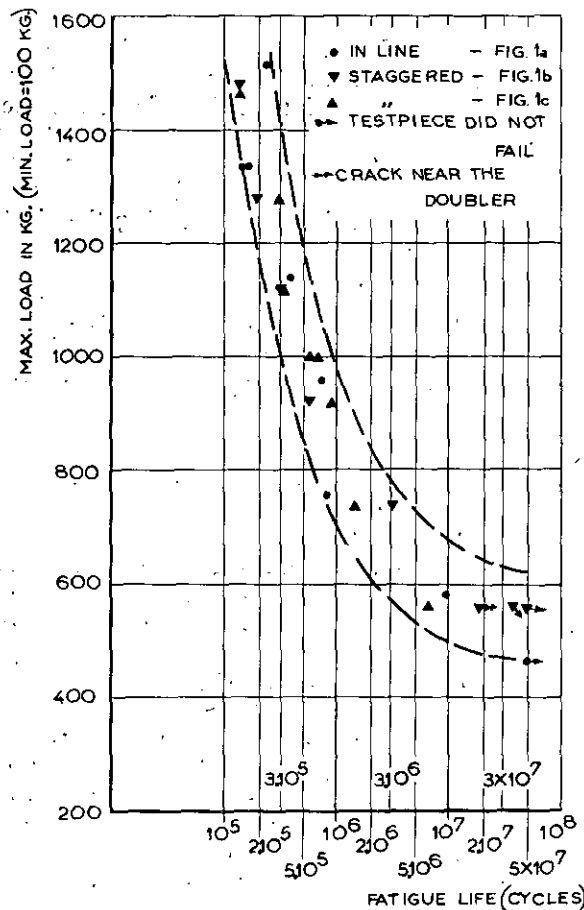


Fig. 9. Results of fatigue tests with fluctuating tension on 24 ST alclad single lap joints riveted with 17 S snap rivets.

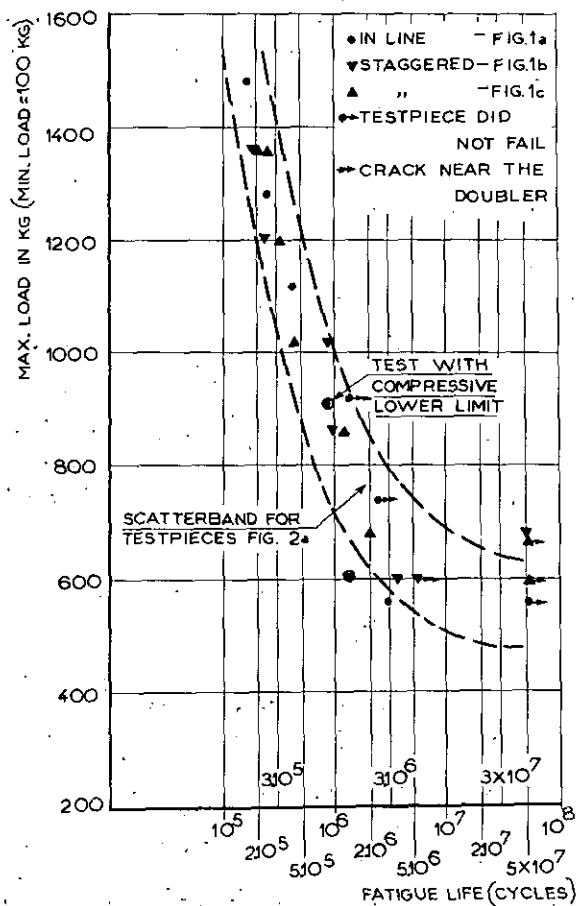


Fig. 10. Results of fatigue tests with fluctuating tension on 24 ST alclad single lap joints riveted with 17 S countersunk rivets (fig. 2b).

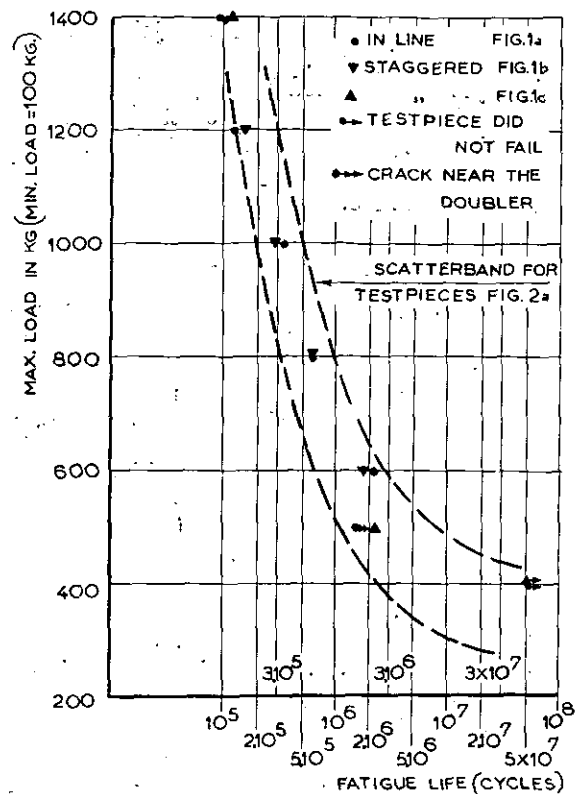


Fig. 11. Results of fatigue tests with fluctuating tension on 24 ST alclad single lap joints riveted with 17 S countersunk rivets (fig. 2c).

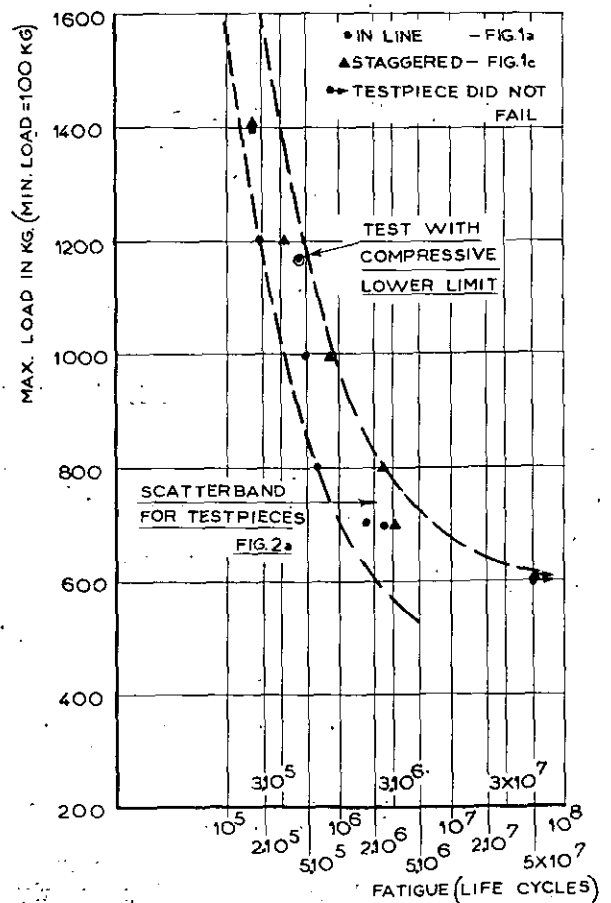


Fig. 12. Results of fatigue tests with fluctuating tension on 24 ST alclad single lap joints riveted with 17 S countersunk rivets (fig. 2d).

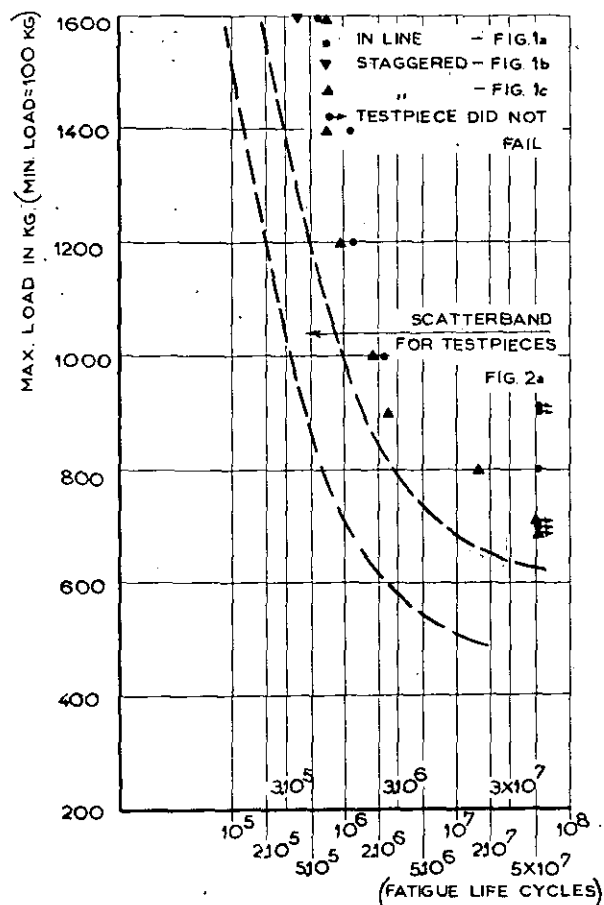


Fig. 13. Results fatigue tests with fluctuating tension on 24 ST alclad single lap joints riveted with 17 S countersunk rivets (fig. 2e).

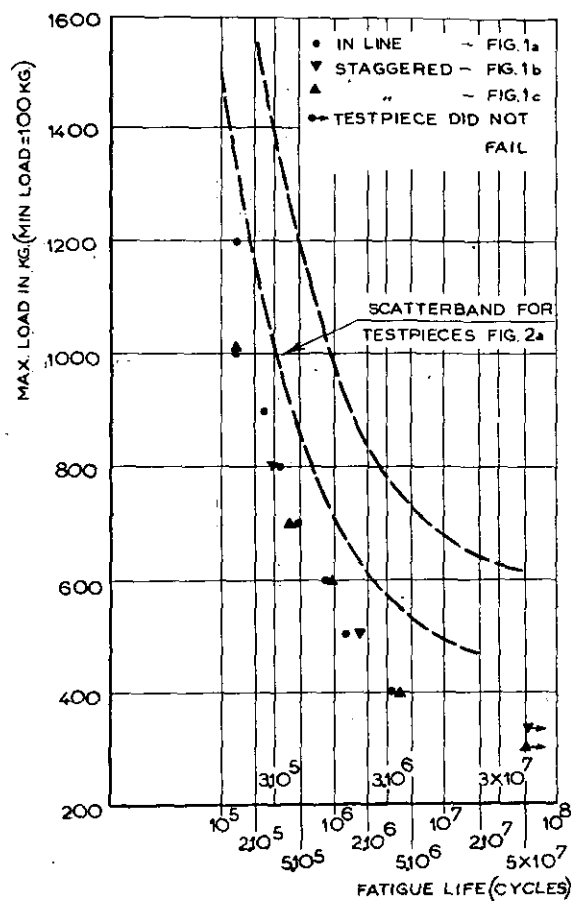


Fig. 15. Results fatigue tests with fluctuating tension on 24 ST alclad single lap joints riveted with Monell pop rivets (fig. 2g).

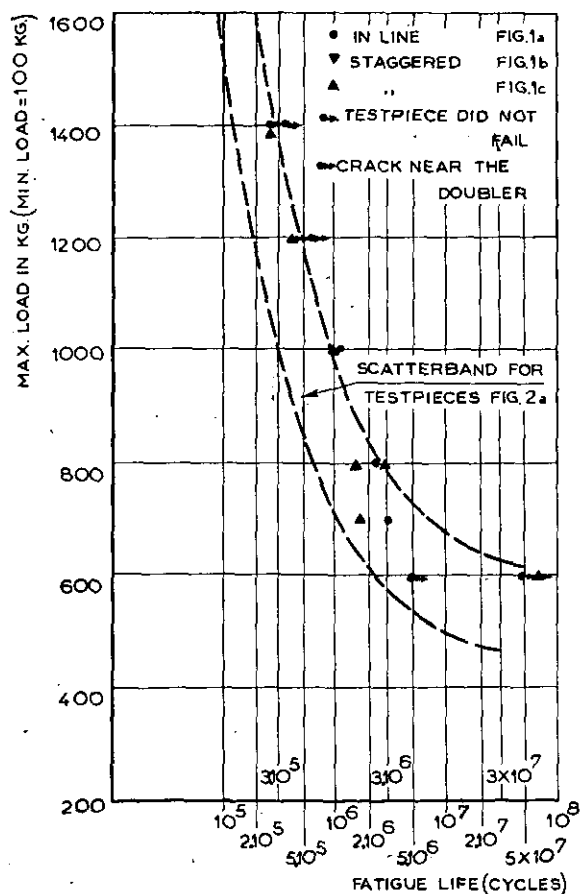


Fig. 14. Results fatigue tests with fluctuating tension on 24 ST alclad single lap joints riveted with steel snap rivets (fig. 2f).

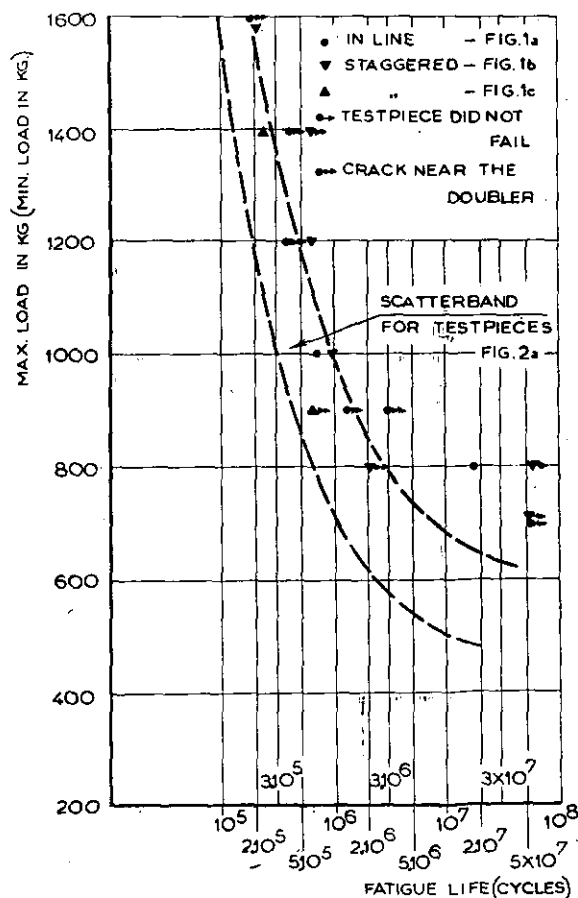


Fig. 16. Results fatigue tests with fluctuating tension on 24 ST alclad bolted single lap joints (fig. 2h).

5.5 Fatigue tests on test pieces with countersunk rivets (type V).

The results of these tests are given in table 9 and in fig. 13.

The points in fig. 13 indicate a marked increase in fatigue strength as compared to the specimens with snap rivets and at low stress levels greater lives for the test pieces riveted in line than for those with staggered rivets. The endurance strength at 50.10^6 cycles for the test pieces in line amounts to 900 kg and for the staggered test pieces to 750 kg. This increase in fatigue strength has to be chiefly attributed to the greater sheet thickness. The ratio between the endurance strengths of test pieces riveted in line according to figs 2c and 2a, viz. $\frac{900}{550}$, nearly equals the ratio between the sheet thickness, $\frac{1.2}{0.8}$, so the tensile stress in both test pieces is practically the same.

The cause of the failure of these test pieces with 1.2 mm sheet thickness was in all cases cracking of the plate.

5.6 Fatigue tests on test pieces with steel snap rivets.

The results for the test pieces with steel rivets are collected in table 10 and in fig. 14. At low stress levels all points lie in the scatter band for similar test pieces with 17 S rivets; at high stress levels the cracking of the plate in the clamping head indicates greater strength for the specimens with steel rivets but the difference does not seem to be large. If the cracking started near the rivets this occurred in all cases in the rear plate which is just the reverse of the behaviour of specimens with 17 S rivets.

5.7 Fatigue tests on test pieces with $\frac{1}{8}$ " T.L.P. Monell-poprivets.

Table 11 and fig. 15 give the results. The situation of the points in fig. 15 clearly demonstrates that these pop-riveted joints have lower fatigue strengths than the corresponding snap-riveted joints. The ratios between fatigue strength and static strength are for both types almost the same (see table beneath).

Life in cycles	10^6	5.10^7
snap rivet	0.23	0.14
pop rivet	0.20	0.12

The scatter for the pop-riveted joints is surprisingly low.

5.8 Fatigue tests on test pieces with steel bolts.

The results for the bolted joints are given in table 12 and fig. 16. Many specimens broke at

the clamping head which makes it difficult to draw a conclusion. The points in fig. 16 indicate both at low and at high stress levels a somewhat higher fatigue strength for the bolted than for the riveted joints.

5.9 Fatigue tests on test pieces with glued joint.

The results of the fatigue tests on the various glued joints are given in table 13 and plotted in fig. 17. Also included in this figure are the scatter

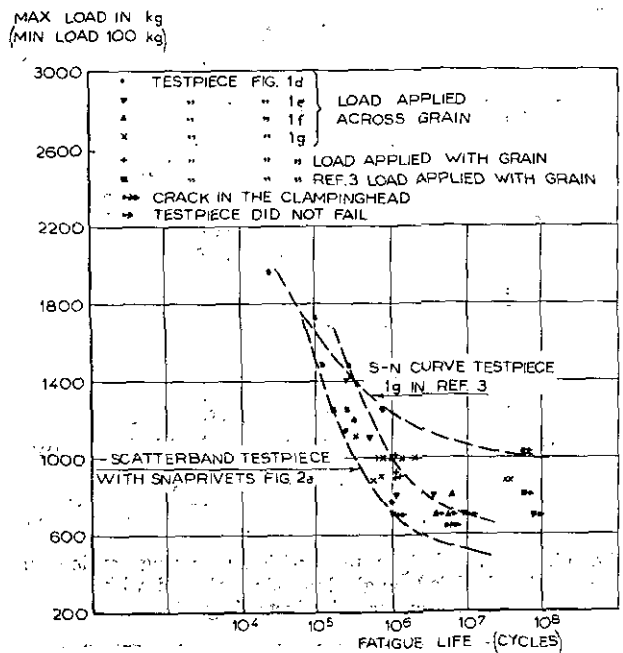


Fig. 17. Results fatigue tests with fluctuating tension on glued 24 ST alclad single lap joints.

band for the test pieces with 17 S snap rivets and the results of the tests of ref. 3 on glued joints in 0.8 mm sheet according to fig. 1g.

The loads on the specimens 1g have been multiplied by $160/70 = 2.29$ before plotting them in fig. 17, in order to make them comparable with the other results. Also, slight corrections have been made to reduce all results to a lower load limit of 100 kg at 160 mm width.

The test results show the usual scatter and it is not possible to draw any definite conclusions with regard to the influence of the length of the glue line (15 or 20 mm), the free length of the specimen (150 or 40 mm) and the width of the specimen (160 or 70 mm). Also there seems to be no influence of the grain direction of the sheet material with respect to the direction of load application, despite the marked differences in static strength.

The glued joints may be said to be somewhat superior to the snap-riveted joints according to fig. 2a, but most of the results lie considerably below the S-N curve from ref. 3. Actually, the discrepancies between this curve and the test results for specimens 1d and 1e prompted the execution of the further tests on specimens 1f and 1g. It should be observed that the tests of ref. 3 do not properly cover the range of $N >$

2.5×10^5 and in drawing the $S-N$ curve too much stress was apparently laid on the few test results for high values of N . Another possible explanation is suggested by the lens shape of the glue line with the specimens of ref. 3, which may have caused a more favourable stress distribution than will normally be encountered, giving high fatigue strengths at the lower stress levels.

For practical purposes it must be concluded that the bonded joints were somewhat superior to the snap-riveted joints, but did not show the large superiority indicated in ref. 3¹).

5.10 Comparison of the results.

To facilitate a survey of the most significant results the static strength and fatigue strengths at 10^6 and 10^8 cycles for the different types of joint are collected in fig. 18.

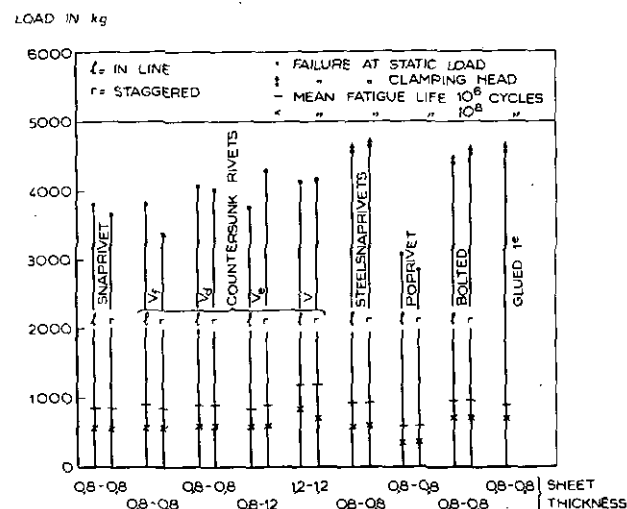


Fig. 18. Principal results of static and fatigue tests on 24 ST alclad lap joints.

Under static load the riveted joint with steel rivets, the bolted joint and the glued joint in strength far outmeasure the other riveted joints. The real ultimate strength of these test pieces could not be determined owing to cracking in the plate at the clamping head.

As expected the pop-riveted joint had the lowest strength.

The large difference in static strength of test pieces riveted with 17 S and with steel snap rivets does not greatly affect the fatigue strength.

At high stresses the steel rivet has some advantage but at fatigue lives of 10^8 cycles no improvement is apparent.

The remaining types of test pieces with high static strength, viz. the bolted and glued joints, have some superiority at low stress level. Except for pop rivets the endurance strength is about the same for all types of riveted joints in 0.8 mm 24 ST alclad, indicating that the stress concentration in the plate is almost independent of the

type of riveting used. The cracking of the plates in joints type 2c with 1.2 mm plate at the same nominal tensile stress as in joints with 0.8 mm plate confirms this assumption.

The greater fatigue strength of the joints type V has to be attributed to the greater sheet thickness.

With the exception of the type V the endurance strength was not influenced by the rivet pattern (rivets in line or staggered).

The results of the two tests with a negative tensile stress on the fatigue cycle indicate (see fig. 10 and fig. 12) that with a low positive or negative minimum load the amplitude of the cycle determines the fatigue life. The change of the stress ratio (R) from low positive to low negative values causes no jump in fatigue strength.

No results have been found in the literature on the fatigue strength of riveted single lap joints of 24 ST alclad suitable for a direct comparison with the results of this report. In ref. 4 it is stated that riveting in line or staggered has no influence on the fatigue strength, which agrees with the results in this report.

6 Conclusions.

- 1 The load distribution over the width of the test piece was excellent.
- 2 The bending stresses in the plate near the rivets of flat test pieces did not vary over the width of the test piece, as they did for the warped ones (see figs 7 and 8).
- 3 The clamping of the test pieces caused a pre-stress (tension and compression) of about 0.3 to 0.6 kg/mm² (see figs 7 and 8).
- 4 Increase of the mean strain (at constant mean load and amplitude of the fatigue load) in the plate between the rivets did not appear until 70 % of the fatigue life had been passed. Thereafter the strain change, as well as the cracking had a strongly progressive character.
- 5 With the exception of the results for test pieces type V (1.2 mm sheet) there was no difference in fatigue strength by riveting in line or staggered.
- 6 Change of 17 S snap rivets to steel rivets gave a higher static strength, but no higher endurance strength. High static strength is not coupled with high endurance strength.
- 7 All types of riveted joints (except pop rivets) have given almost the same stress concentration in the plate. The greater strength of joints type V has to be attributed to greater sheet thickness.
- 8 The pop-riveted joints had smaller static and fatigue strengths than the other joints. The ratio between static strength and endurance strength was almost the same as for snap-riveted joints.
- 9 The bolted joints had both at high and at low stress levels somewhat greater fatigue strengths than the riveted joints in the same sheet thickness.

¹) A review of all tests on bonded joints carried out to date in this country will shortly be issued as a report of the Fokker Aircraft Co.

- 10 The fatigue strength of the bonded joints of 0.8 mm 24 ST — alclad sheet with a normal glueline was somewhat superior to that of the riveted joints, but did not show the large superiority indicated in ref. 3.

7 References.

1. VAN MEER, H. P. and HARTMAN, A. Literatuurgegevens over de vermoeiingssterkte van lichte metalen. Report S. 381, Nationaal Luchtvaartlaboratorium, Amsterdam (1951). (Unpublished).
2. HARTMAN, A. and DUYN, G. C. Vergelijkend onderzoek van verschillende typen van klinkverbindingen bij pulserende belasting. I. Report M. 1735, Nationaal Luchtvaartlaboratorium, Amsterdam (1951).
3. — Vermoeiingsproeven op enkelvoudige lapnaden van 24 ST alclad gelijmd met Redux en 1 serie geklonken proefstukken uit 24 ST alclad plaat en 24 S nagels. Report M. 1627, Nationaal Luchtvaartlaboratorium, Amsterdam (1950).
4. RUSSELL, H. W. a.o. Fatigue strength and related characteristics of aircraft joints. I. NACA Wartime Report W 56 (ARR 4 F 01), 1944.

Completed: October 1952.

471

TABLES

(For table 1 see p. M5)

TABLE 2.

Electrical strain measurements on specimen 2 k. Static loading.

Load	Measured strain in micro-ins/in in strain-gauges no.: ¹⁾											
	1	2	3	4	5	6	7	8	9	10	11	12
Specimen hanging loosely on the bolts	—68	—174	—182	—149	—92	—69	—27	59	4	100	—7	+251
Vibraphore indication: 0 kg	0	0	0	0	0	0	0	0	0	0	0	0
"	55	63	63	40	9	12	18	42	149	127	131	180
"	200	152	150	131	38	53	59	92	257	241	241	320
"	400	361	351	320	130	159	160	200	467	443	429	542
"	600	522	570	530	252	282	281	319	654	645	620	753
"	800	732	790	737	393	430	420	451	850	851	820	963
"	1000	931	1000	942	532	575	553	582	1041	1051	1017	1172

Dynamic loading. Average load 550 kg (min 100 kgs; max 1000 kgs).

Indication cycle-counter ²⁾	Changes of the strains in micro-ins/in											
	1	2	3	4	5	6	7	8	9	10	11	12
Reference indication: 036925	0	0	0	0	0	0	0	0	0	0	0	0
" 037090	—4	—5	+8	+210	—1	8	—9	0	—15	—6	—1	—2
" 037200	—14	—28	0		0	8	—11	—10	—25	—9	—8	
" 037314	—10		+13		0	8	—8	8	—25	—4	—2	
" 037440	—11	³⁾	+29	³⁾	+8	6	—5	—28	—15	+1	0	³⁾
" 037600	—5		+50		+5	+230	+2	+253	—15	—10	+8	

¹⁾ All measured strains are reduced to the strains in clamped specimen at vibraphore-loading of 0 kgs.+ tensile strain.
— compressive strain.²⁾ 1 unit = 1000 reversals.³⁾ These readings could not be taken.

+ : deviation in direction of tension.

— : deviation in direction of compression.

TABLE 3.

Electrical strain measurements on specimen 2 L. Static loading.

Load		Measured strain in micro-ins/in in strain-gauges no.: ¹⁾											
		1	2	3	4	5	6	7	8	9	10	11	12
Specimen hanging loosely on the bolts		+ 177	+ 39	+ 21	+ 286	+ 41	+ 86	+ 88	+ 3	- 282	- 129	- 138	- 206
Vibraphore indication:		0	0	0	0	0	0	0	0	0	0	0	0
0 kg		99	155	140	250	30	17	- 13	- 131	108	99	60	- 57
100 "		197	280	287	460	58	48	- 1	- 161	180	177	120	- 56
200 "		451	512	538	790	138	141	77	- 136	331	337	260	14
400 "		699	744	766	1079	250	258	184	- 56	490	508	428	134
600 "		939	964	990	1340	420	398	307	62	657	690	600	285
800 "		1158	1171	1208	1588	600	556	455	191	827	880	792	459
1000 "													
Dynamic loading. Average load 550 kg (min 100 kgs; max 1000 kgs).													
Indication cycle-counter ²⁾		Changes of the strains in micro-ins/in											
		1	2	3	4	5	6	7	8	9	10	11	12
Reference indication:		0	0	0	0	0	0	0	0	0	0	0	0
036308			+ 3			- 10	+ 9	- 24	+ 15	- 8	0	0	+ 7
036432			+ 15			- 1	+ 13	- 2	+ 17	+ 14	+ 16	+ 9	+ 15
036570			+ 25	³⁾	³⁾	- 1	+ 10	+ 55	+ 10	+ 10	+ 22	- 13	+ 16
036781			+ 44			- 25	0	+ 2368	+ 68	- 9	0	- 43	- 38
036800			+ 57			+ 27	+ 399	+ 2831	+ 156		+ 16	- 337	+ 159
036925													

¹⁾ All measured strains are reduced to the strains in clamped specimen at vibraphore-loading of 0 kgs.

+ tensile strain.

- compressive strain.

²⁾ 1 unit = 1000 reversals.³⁾ These readings could not be taken.

+ : deviation in direction of tension.

- : deviation in direction of compression.

TABLE

Results of static tension tests on 24 ST alclad

Number of test piece	Test piece according to		Sheet thickness in mm	Type	Load at failure in kg
3a	fig. 1a	fig. 2a	0.8	<i>Pb</i> — 17 S snap rivets	3800
3b	"	"	"	" " " "	3800
4a	fig. 1b	"	"	" " " "	3700
4b	"	"	"	" " " "	3600
2a	fig. 1c	"	"	" " " "	3750
2b	"	"	"	" " " "	3550
1a	fig. 1a	fig. 2b	"	<i>Vf</i> front plate partly sunk — rear plate dimpled	3850
1b	"	"	"	" " " " " " " "	3750
6a	fig. 1b	"	"	" " " " " " " "	3400
6b	"	"	"	" " " " " " " "	3500
5a	fig. 1c	"	"	" " " " " " " "	3400
5b	"	"	"	" " " " " " " "	3000
8a	fig. 1a	fig. 2c	"	<i>Vd</i> both plates dimpled	4100
8b	"	"	"	" " " " "	4050
9a	fig. 1b	"	"	" " " " "	3850
9b	fig. 1c	"	"	" " " " "	4000
14a	fig. 1a	fig. 2d	0.8 and 1.2	<i>Ve</i> rear plate sunk — front plate dimpled	3450
14b	"	"	" " "	" " " " " " "	4050
19a	fig. 1c	"	" " "	" " " " " " "	4500
19b	"	"	" " "	" " " " " " "	4150
13a	fig. 1a	fig. 2e	1.2	<i>V</i> front plate sunk	4250
13b	"	"	"	" " " "	4000
18a	fig. 1c	"	"	" " " "	4050
18b	fig. 1b	"	"	" " " "	4250
12a	fig. 1a	fig. 2f	0.8	<i>Pb</i> steel rivets	4600
17a	fig. 1c	"	"	" " "	4650
11a	fig. 1a	fig. 2g	"	1/8" Monell T. L. P. pop rivets	3000
11b	"	"	"	" " " "	3200
16a	fig. 1b	"	"	" " " "	2800
16b	"	"	"	" " " "	2850
10a	fig. 1a	fig. 2h	"	steel bolts	4400
15a	fig. 1b	"	"	" "	4550
20a	fig. 1c	"	"	glued	4550

L.

riveted, bolted and glued simple lap joints.


σ_{max} in sheet $W = 160 \text{ mm}$	τ_{max} in rivet $\phi = 3.1 \text{ mm}$	Remarks
29.6	31.6	Failure by shearing of all rivets — little distortion of rivet holes
29.6	31.6	" " " " " " " " " " "
28.9	32.6	Rear plate teared at rivets of lower rivet row
28.1	31.8	Failure by shearing of all rivets — little distortion of rivet holes
29.3	33.1	" " " " " " " " " " "
27.7	31.4	" " " " " " " " " " "
30.1	31.9	Upper rivet row pulled through the plate — lower rivet row sheared
29.3	31.1	Rivets pulled through the plate
26.6	30.0	Some rivets sheared, all others pulled through the plate
27.4	31.0	" " " " " " " " " " "
26.6	30.0	Some rivets pulled through the plate, all others sheared
23.4	26.5	" " " " " " " " " " "
32.0	34.0	Failure by shearing of all rivets — large distortion of rivet holes
31.6	33.6	" " " " " " " " " " "
30.1	34.0	Crack at the clamping head under the doublers
31.2	35.3	Failure by shearing of all rivetheads in longitudinal direction 
27.0	28.6	" " " " " " " " " " "
31.6	33.6	Rivets pulled through the front plate
35.1	39.7	Crack at the clamping head under the doublers
32.4	36.6	Failure by shearing of all rivets
22.2	35.2	" " " " " " " " " " "
20.8	33.2	" " " " " " " " " " "
21.1	35.7	" " " " " " " " " " "
22.2	37.6	" " " " " " " " " " "
35.9	38.1	Crack at the clamping head under the doublers
36.3	41.7	" " " " " " " " " " "
23.4	24.9	Shank of the rivets pulled through the rear plate
25.0	26.5	" " " " " " " " " " "
21.9	24.7	" " " " " " " " " " "
22.3	25.1	" " " " " " " " " " "
34.3	—	Crack at the clamping head under the doublers
35.6	—	" " " " " " " " " " "
35.6	—	" " " " " " " " " " "

TABLE 5.

Results of fatigue tests with fluctuating tension on 24 ST alelad single lap joints riveted with 17 S snap rivets (fig. 2a).

Number of the test piece	Test piece according to	Load in kg		Life (cycles) $\times 10^3$	σ_{\max} in sheet kg/mm^2 $t = 0.8 \text{ mm}$ $w = 160 \text{ mm}$	τ_{\max} in rivet kg/mm^2 $\phi 3.1 \text{ mm}$	Remarks
		min	max				
3c	fig. 1a	100	1520	243	11.9	12.6	crack in the front plate in the lower rivet row
3d	"	"	1340	151	10.5	11.1	" " " rear " " " upper " "
3k	"	"	1340	169	10.5	11.1	" " " front " " " lower " "
3e	"	"	1140	410	8.9	9.4	" " " " " " " " " "
3f	"	"	960	784	7.5	7.9	" " " " " " " " " "
3g	"	"	760	812	5.9	6.3	" " " rear " " " upper " "
3h	"	"	580	9488	4.5	4.8	" " " front " " " lower " "
3l	"	"	460	> 52518	3.6	3.8	test piece did not fail
4c	fig. 1b	"	1480	144	11.6	13.1	crack in front plate in the lower rivet row
4d	"	"	1280	202	10.0	11.3	" " " " " " " " " "
4e	"	"	1120	340	8.7	9.9	" " " " " " " " " "
4f	"	"	920	600	7.2	8.1	" " " " " " " " " "
4g	"	"	740	3412	5.8	6.5	" " " " " " " " " "
4h	"	"	560	> 50734	4.4	5.0	test piece did not fail
4k	"	"	560	2084	4.4	5.0	crack in front plate near the riveted reinforcing plates
4l	"	"	560	40144	4.4	5.0	" " " " " " " " " "
2c	fig. 1c	"	1480	140	11.6	13.1	" " " " " in the lower rivet row
2d	"	"	1280	301	10.0	11.3	" " " " " " " " " "
2e	"	"	1120	342	8.7	9.9	" " " " " " " " " "
2k	"	"	1000	720	7.8	8.9	" " " " " " " " " "
2l	"	"	1000	617	7.8	8.9	" " " " " " " " " "
2f	"	"	920	950	7.2	8.1	" " " " " " " " " "
2g	"	"	740	1553	5.8	6.5	" " " " " " " " " starting
2h	"	"	560	7225	4.4	5.0	from the edge of the plate crack in the rear plate in the upper rivet row

The test pieces 2 k and 2 l were used for the measurements with strain gauges.

TABLE 6.

Results of fatigue tests with fluctuating tension on 24 ST alclad single lap joints riveted with 17 S countersunk rivets (type Vf, fig. 2b).

Number of the test piece	Test piece according to	Load in kg		Life (cycles) $\times 10^3$	σ_{\max} in sheet kg/mm ² $t = 0.8$ mm $w = 160$ mm	τ_{\max} in rivet kg/mm ² $\phi = 3.1$ mm	Remarks
		min	max				
1c	fig. 1a	100	1480	173	11.6	12.2	crack in the rear plate in the upper rivet row
1d	"	"	1280	259	10.0	10.6	" " " " " "
1e	"	"	1120	440	8.7	9.2	" " " " " "
1f	"	"	920	1451	7.2	7.6	" " " " near the riveted reinforcing plates
1g	"	"	740	2657	5.8	6.1	" " " " " "
1h	"	"	560	3144	4.4	4.6	" " " " in the upper rivet row
1k	"	"	560	> 57490	4.4	4.6	test piece did not fail
1l	"	—50	760		5.9	6.3	crack in the rear plate in the upper rivet row
6c	fig. 1b	100	1360	194	10.6	12.0	" " " " " "
6d	"	"	1200	227	9.4	10.6	" " " " " "
6e	"	"	1020	884	8.0	9.0	" " " " lower " "
6f	"	"	860	973	6.7	7.6	" " " " upper " "
6g	"	"	680	64973	5.3	6.0	" " " " " "
6h	"	"	600	444	4.7	5.3	" " " " " "
6k	"	"	600	5125	4.7	5.3	(strong transverse vibration of the test piece)
6l	"	"	600	3635	4.7	5.3	crack in the rear plate near the riveted reinforcing plates
5c	fig. 1c	"	1360	220	10.6	12.0	" " " " in the upper rivet row
5l	"	"	1360	272	10.6	12.0	" " " " " "
5d	"	"	1200	324	9.4	10.6	" " " " lower " "
5e	"	"	1020	467	8.0	9.0	" " " " upper " "
5f	"	"	860	1365	6.7	7.6	" " " " " "
5g	"	"	680	2080	5.3	6.0	" " " " front " "
5k	"	"	680	> 52730	5.3	6.0	test piece did not fail
5h	"	"	600	> 52091	4.7	5.3	" " " " " "

TABLE 7.

Results of fatigue tests with fluctuating tension on 24 ST alelad single lap joints riveted with 17 S countersunk rivets (type Vd fig. 2c).

Number of the test piece	Test piece according to	Load in kg		Life (cycles) $\times 10^3$	σ_{\max} in sheet kg/mm^2 $t=0.8 \text{ mm}$ $w=160 \text{ mm}$	τ_{\max} in rivet kg/mm^2 $\phi 3.1 \text{ mm}$	Remarks
		min	max				
8c	fig. 1a	100	1600	85	12.5	13.3	crack in the rear plate in the upper rivet row
8k	"	"	1600	99	12.5	13.3	" " " " " " " " " "
8d	"	"	1400	124	11.0	11.7	" " " " " " " " " "
8e	"	"	1200	357	9.4	10.0	" " " " " " " " " "
8f	"	"	1000	643	7.8	8.4	" " " " " " " " " "
8g	"	"	800	2293	6.3	6.7	" " " " " " " " " "
8l	"	"	700	1710	5.5	5.8	" " " front " near the riveted reinforcing plate
8h	"	"	600	> 58953	4.7	5.0	test piece did not fail
9c	fig. 1c	"	1600	109	12.5	14.1	crack in the rear plate in the upper rivet row
9d	fig. 1b	"	1400	152	11.0	12.3	" " " " " " " " " "
9e	"	"	1200	273	9.4	10.6	" " " " " " " " " "
9f	"	"	1000	638	7.8	8.8	" " " " " " " " " "
9g	"	"	800	1898	6.3	7.0	" " " " " " " " " "
9k	fig. 1c	"	700	2323	5.5	6.2	" " " " " " " " " "
9h	"	"	600	> 53528	4.7	5.3	test piece did not fail

TABLE 8.

Results of fatigue tests with fluctuating tension on 24 ST alclad single lap joints riveted with 17 S countersunk rivets (type Vc fig. 2d).

Number of the test piece	Test piece according to	Load in kg		Life (cycles) $\times 10^3$	σ_{\max} in sheet kg/mm ² $t = 0.8$ mm $w = 160$ mm	τ_{\max} in rivet kg/mm ² $\phi 3.1$ mm	Remarks
		min	max				
14d	fig. 1a	100	1400	182	11.0	11.7	crack in the front plate (0.8 mm) in the lower rivet row
14e	"	"	1200	202	9.4	10.0	" " " " " " " " " "
14f	"	"	1000	504	7.8	8.4	" " " " " " " " " "
14g	"	"	800	615	6.3	6.7	" " " " " " " " " "
14k	"	"	700	1888	5.5	5.8	" " " " " " " " " "
14l	"	"	700	2501	5.5	5.8	" " " " " " " " " "
14h	"	"	600	> 56220	4.7	5.0	test piece did not fail
14m	"	— 60	1000	492	7.8	8.4	crack in the front plate in the lower rivet row
19d	fig. 1c	100	1400	179	11.0	12.3	" " " " " " " " " "
19e	"	"	1200	336	9.4	10.6	" " " " " " " " " "
19f	"	"	1000	851	7.8	8.8	" " " " " " " " " "
19g	"	"	800	2600	6.3	7.0	" " " " " " " " " "
19h	"	"	700	3197	5.5	6.2	" " " " " " " " " "
19k	"	"	600	> 51138	4.7	5.3	test piece did not fail

TABLE 9.

Results of fatigue tests with fluctuating tension on 24 ST alclad single lap joints riveted with 17 S countersunk rivets (type V fig. 2e).

Number of the test piece	Test piece according to	Load in kg		Life (cycles) $\times 10^3$	σ_{\max} in sheet kg/mm ² $t = 1.2$ mm $w = 160$ mm	τ_{\max} in rivet kg/mm ² ϕ 3.1 mm	Remarks
		min	max				
13c	fig. 1a	100	1600	633	8.4	13.3	crack in the front plate in the lower rivet row
13d	"	"	1400	1158	7.3	11.7	" " " rear " " " upper " "
13e	"	"	1200	1182	6.3	10.0	" " " " " " " " " " "
13f	"	"	1000	2346	5.2	8.4	" " " " " " " " " " "
13l	"	"	900	> 54979	4.7	7.5	test piece did not fail
13m	"	"	900	> 55036	4.7	7.5	" " " " " "
13g	"	"	800	> 57961	4.2	6.7	" " " " " "
13h	"	"	700	> 58077	3.6	5.8	" " " " " "
18e	fig. 1b	"	1600	400	8.4	14.1	crack in the front and in the rear plate
18l	fig. 1c	"	1600	746	8.4	14.1	" " " rear plate in the upper rivet row
18d	"	"	1400	746	7.3	12.3	" " " " " " " " " " "
18e	"	"	1200	993	6.3	10.6	" " " " " " " " " " "
18f	"	"	1000	1833	5.2	8.8	" " " " " " " " " " "
18g	"	"	900	2471	4.7	7.9	" " " front " " " lower " "
18m	"	"	800	16895	4.2	7.0	" " " rear " " " upper " "
18h	"	"	700	> 56700	3.6	6.2	test piece did not fail
18k	"	"	700	> 57850	3.6	6.2	" " " " " "

TABLE 10.

Results of fatigue tests with fluctuating tension on 24 ST alclad single lap joints riveted with steel snap rivets (fig. 2f).

Number of the test piece	Test piece according to	Load in kg		Life (cycles) $\times 10^3$	σ_{\max} in sheet kg/mm ² $t = 0.8$ mm $w = 160$ mm	τ_{\max} in rivet kg/mm ² $\phi 3.1$ mm	Remarks
		min	max				
12d	fig. 1a	100	1400	287	10.9	11.7	crack in the rear plate near the reinforcing plate
12m	"	"	1400	340	10.9	11.7	" " " " " " " " " "
12e	"	"	1200	658	9.4	10.0	" " " " " " " " " "
12f	"	"	1000	1175	7.8	8.4	" " " " " in the upper rivet row
12g	"	"	800	2566	6.2	6.7	" " " " " " " " " "
12h	"	"	700	3021	5.5	5.8	" " " " " " " " " "
12k	"	"	600	5309	4.7	5.0	" " " " " near the reinforcing plate
12l	"	"	600	> 53458	4.7	5.0	test piece did not fail
17d	fig. 1c	"	1400	280	10.9	12.3	crack in the rear plate in the upper rivet row
17e	"	"	1200	425	9.4	10.6	" " " front " near the reinforcing plate
17f	"	"	1000	1072	7.8	8.8	" " " rear " in the upper rivet row
17g	"	"	800	1771	6.2	7.0	" " " " " " " " " "
17h	"	"	800	2801	6.2	7.0	" " " " " " " " " "
17k	"	"	700	1869	5.5	6.2	" " " " " " " " " "
17l	fig. 1b	"	600	> 66742	4.7	5.3	test piece did not fail
17m	"	— 40	1000	291	7.8	8.8	crack in the rear plate in the upper rivet row
17c	"	— 50	1000	390	7.8	8.8	" " " " " near the reinforcing plate

TABLE 11.

Results of fatigue tests with fluctuating tension on 24 ST alelad single lap joints riveted with Monell pop rivets (fig. 2g).

Number of the test piece	Test piece according to	Load in kg		Life (cycles) $\times 10^3$	σ_{\max} in sheet kg/mm^2 $t = 0.8 \text{ mm}$ $w = 160 \text{ mm}$	τ_{\max} in rivet kg/mm^2 $\phi 3.1 \text{ mm}$	Remarks
		min	max				
11d	fig. 1a	100	1200	137	9.4	10.0	crack in the rear plate in the upper rivet row
11e	"	"	1000	144	7.8	8.4	" " " " " " " " " "
11e	"	"	900	254	7.0	7.5	" " " " " " " " " "
11f	"	"	800	338	6.2	6.7	" " " " " " " " " "
11g	"	"	700	504	5.5	5.8	" " " " " " " " " "
11h	"	"	600	865	4.7	5.0	" " " " " " " " " "
11k	"	"	500	1381	3.9	4.2	" " " " " " " " " "
11l	"	"	400	3420	3.1	3.3	" " " " " " " " " "
16l	fig. 1c	"	1000	135	7.8	8.8	" " " " " " " " " "
16k	fig. 1b	"	800	314	6.2	7.0	" " " " " " " " " "
16h	fig. 1c	"	700	435	5.5	6.2	" " " " " " " " " "
16g	"	"	600	909	4.7	5.3	" " " " " " " " " "
16f	fig. 1b	"	500	1784	3.9	4.4	" " " " " " " " " "
16e	fig. 1c	"	400	4117	3.1	3.5	" " " " " " " " " "
16e	fig. 1b	"	340	> 51874	2.6	3.0	test piece did not fail
16d	fig. 1c	"	300	> 55699	2.3	2.6	" " " " " " " " " "

TABLE 12.

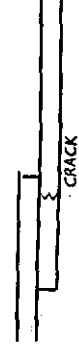
Results of fatigue tests with fluctuating tension on 24 ST Alclad single lap joints
(fig. 2h).

Number of the test piece	Test piece according to	Load in kg		Life (cycles) $\times 10^3$	σ_{max} in sheet kg/mm^2 $t = 0.8 \text{ mm}$ $w = 160 \text{ mm}$	τ_{max} in bolt kg/mm^2 $\phi 4.7 \text{ mm}$	Remarks
		min	max				
10h	fig. 1a	100	1600	199	12.5	5.8	crack in the front plate near the reinforcing plate
10d	"	"	1400	499	10.9	5.1	" " " " " " " "
10l	"	"	1200	390	9.4	4.3	" " " " " " " "
10e	"	"	1000	664	7.8	3.6	" " " " " in the lower bolt row
10g	"	"	900	1392	7.0	3.3	" " " " " near the reinforcing plate
10k	"	"	900	3295	7.0	3.3	" " " rear " " " "
10l	"	"	800	18939	6.2	2.9	" " " front " in the lower bolt row
10f	"	"	700	> 51220	5.5	2.5	test piece did not fail
15g	fig. 1b	"	1600	197	12.5	6.2	crack in the rear plate in the upper bolt row
15d	"	"	1400	602	10.9	5.4	" " " " " near the reinforcing plate
15l	fig. 1c	"	1200	261	10.9	5.4	" " " " " in the upper bolt row
15h	fig. 1b	"	1400	629	9.4	4.6	" " " front " " " lower " "
15e	"	"	1000	1029	7.8	3.9	" " " rear " " " upper " "
15m	fig. 1c	"	900	638	7.0	3.5	" " " front " near the reinforcing plate
15f	"	"	800	2357	6.2	3.1	" " " " " " " "
15k	"	"	800	> 60129	6.2	3.1	test piece did not fail
15e	"	"	700	> 52406	5.5	2.7	" " " " "

TABLE 13.

Results of fatigue tests with fluctuating tension on 24 ST alclad glued single lap joints.

Number of the test piece	Sheet thickness in mm	Length of the glue line in mm	Width of the test piece in mm	Distance between clamping heads in mm	Load in kg		Life (cycles) $\times 10^3$	σ_{max} in sheet kg/mm ²	Remarks
					min	max			
7b	0.8	15	160	150	100	1520	277	11.9	crack in plate at edge of joint
7c	"	"	"	"	"	1140	237	8.9	" " " " " "
7d	"	"	"	"	"	760	1082	5.9	" " " " " "
7e	"	"	"	"	"	580	5741	4.5	" " " " " " also crack at the clamping head
20c	"	20	"	"	"	1400	250	10.9	" " " " " "
20d	"	"	"	"	"	1100	496	8.6	" " " " " "
20e	"	"	"	"	"	800	1376	6.3	" " " " " " at clamping head under reinforcing plates
20f	"	"	"	"	"	800	3535	"	" " " " " " in plate at edge of joint
20b	"	"	"	"	"	700	1149	5.5	" " " " " " at the clamping head under the reinforcing plates
20g	"	"	"	"	"	700	43348	"	" " " " " "
20h	"	"	"	"	"	700	7926	"	" " " " " "
21c	"	"	"	40	"	1200	312	9.4	" " " " " " plate at edge of joint
21d	"	"	"	"	"	1000	1006	7.8	" " " " " " at clamping head under the reinforcing plates
21e	"	"	"	"	"	800	6500	6.3	" " " " " " in plate at edge of joint
21f	"	"	"	"	"	700	4169	5.5	" " " " " " at clamping head under the reinforcing plates
21g	"	"	"	"	"	700	4912	"	" " " " " "
20b-1	"	"	69	"	40	560	522	10.2	" " " " " " plate at edge of joint
20e-1	"	"	"	"	"	560	280	"	" " " " " "
20g-1	"	"	"	"	"	560	440	"	" " " " " "
20b-2	"	"	"	"	"	440	1301	8.0	" " " " " "
20e-2	"	"	"	"	"	440	1962	"	" " " " " "
20h-1	"	"	"	"	"	440	788	"	" " " " " " in the glue line
20g-2	"	"	"	"	"	380	585	6.9	" " " " " "
20h-2	"	"	"	"	"	380	38328	"	" " " " " "
2b	"	"	"	"	60	500	342	8.9	" " " " " " at edge of joint — load applied across grain
1b	"	"	"	"	60	450	715	8.1	" " " " " "
2a	"	"	"	"	60	410	708	7.3	" " " " " "
1a	"	"	"	"	50	400	87133	7.2	" " " " " "
4b	"	"	"	"	50	450	1250	8.1	" " " " " " with grain
3b	"	"	"	"	50	400	1150	7.2	" " " " " "
4a	"	"	"	"	50	400	1286	7.2	" " " " " "
3a	"	"	"	"	50	400	1256	7.2	" " " " " "



REPORT S 416¹⁾.

Comparative Fatigue Tests with 24 S-T Alclad Riveted and Bonded Stiffened Panels

by

J. H. RONDEEL, R. KRUTHOF and F. J. PLANTEMA.

Summary.

The purpose of the investigation was to compare the fatigue strengths of bonded and riveted flat sheet-stringer panels of identical construction except for the sheet-stringer joints.

The results of fatigue tests on panels stiffened with angle section stringers and top-hat stringers are given.

The bonded panels proved to be superior both in static strength and in fatigue strength and showed no dangerous propagation of damages.

Contents.

- 1 Introduction.
- 2 The test programme, the specimens and the test set-up.
 - 2.1 The test programme.
 - 2.2 The specimens.
 - 2.3 The test set-up.
- 3 The test results.
 - 3.1 Description of failures.
 - 3.2 Discussion.
- 4 Conclusions.
- 5 References.
- Acknowledgement.
- Appendix A.

1 Introduction.

Considerable interest for the application of metal-to-metal bonding for aircraft structures has developed in this country, and both at the Fokker Aircraft Co and the National Aeronautical Research Institute a number of investigations in this field have been and are being made. These investigations deal with static and dynamic tests of bonded specimens in shear, peeling tests, as well as manufacturing and testing of bonded aircraft components. At the Fokker factory an experimental installation for manufacturing such parts has been developed and the experience gained with this installation led to the decision to install a glueing press having platens of 2×1 metres, which is now in operation.

An excellent summary of most of the investigations carried out so far with structural components has been published in refs. 1 and 2. Among others, static tests with stiffened panels showed

a superiority in failing load of about 20 % of bonded panels as compared with riveted panels. It could be expected that the absence of stress raisers and the larger stability due to the continuous attachment between stiffener and sheet with bonded panels would cause similar advantages in fatigue loading. On the other hand, information received from abroad suggested that fatigue failure of bonded panels might progress very rapidly, once cracks or peeling between stiffener and sheet had started.

Under sponsorship of the Netherlands Aircraft Development Board a fairly extensive series of comparative fatigue tests with riveted and bonded stiffened panels was therefore carried out. The panels were manufactured at the Fokker factory and tested in the 50 tons hydraulic pulsator of the N.L.L.

Preliminary results of these tests have already been published in ref. 1. In this report the results will be given in a more definite and detailed form.

2 The test programme, the specimens and the test set-up.

2.1 The test programme.

The purpose of the investigation was to compare the fatigue strengths of stiffened panels, which only differed in the joining of the stiffeners to the sheet, viz. Redux bonded and riveted.

Two types of panels were tested: type I with angle-section stiffeners, and type II with hat-section stiffeners.

From each type at least one bonded and one riveted panel were loaded statically to failure and then the other panels were tested in fluctuating compression. The static load the panel could sustain at the end of the fatigue test was determined in a number of cases. The fatigue loads ranged

¹⁾ Abbreviated version of Report S 411 (unpublished).

from 1000 kg as a lower limit to about 45, 60 or 75 % of the static failing load.

The minimum load of 1000 kg was decided upon because this simplified the test procedure to a large extent. Some reserve panels were fabricated and the tests on these were made depending on the results of the tests already carried out.

The following tests were made:

2.2 The specimens.

The sheet material used for the panels was 24 ST alclad, the thickness for the type I panels being 0.6 mm and for the type II panels 0.5 mm. The mean values of panel and stringer thicknesses are given in table 2.1.

The panels type I were provided with four 24 ST alclad angle sections $20 \times 20 \times 1.5$ mm,

Panel		Number of panels loaded				Total number of panels
		static	from 1000 kg to about ¹⁾			
			75 %	60 %	45 % of static load	
type I	{ riveted	1	1	1	1	4
	{ bonded	2	3	3	2	10
type II	{ riveted	1	1	1	1	4
	{ bonded	1	3	3	2	9

¹⁾ See figs. 3.20 and 3.22 for actual percentages.

In this report the panels are indicated as appears from the following examples:

Ib—75—2 and IIr—s—1.

I and II refer to the type of stringers.

b or r refer to bonded or riveted.

45-60-75 indicate the maximum fluctuating load in % of the static strength.

s indicates the statically loaded panel.

1-2-3 serialnumber.

bent from sheet material (fig. 2.1). The width of the panels was 600 mm and the stiffeners were spaced 150 mm apart. On the riveted panels 3 mm snap rivets were used to attach the angle sections, the pitch being 20 mm.

The panels type II were stiffened with four hat section stringers, spaced 150 mm apart. For the riveted panels the same rivets were used as with the type I panels. Originally the width of these panels was also 600 mm, but as it appeared

TABLE 2.1.

Mean thickness of panels and stringers.

Panel no.	Mean thickness in mm		Panel no.	Mean thickness in mm	
	Sheet	Stringer		Sheet	Stringer
Ib-s-1	0.64	1.56	IIb-s-1	0.54	1.01
Ib-s-2	0.60	1.56			
Ib-45-1	0.59	1.56	IIb-45-1	0.54	1.01
Ib-45-2	0.60	1.54	IIb-45-2	0.53	1.00
Ib-60-1	0.67	1.54	IIb-60-1	0.53	1.01
Ib-60-2	0.64	1.57	IIb-60-2	0.53	1.00
Ib-60-3	0.61	1.57	IIb-60-3	0.53	1.01
Ib-75-1	0.67	1.53	IIb-75-1	0.54	1.00
Ib-75-2	0.64	1.57	IIb-75-2	0.54	1.00
Ib-75-3	0.61	1.57	IIb-75-3	0.54	1.00
Ir-s-1	0.60	1.51	IIr-s-1	0.53	1.01
Ir-45-1	0.67	1.53	IIr-45-1	0.53	1.01
Ir-60-1	0.64	1.52	IIr-60-1	0.54	1.00
Ir-75-1	0.61	1.59	IIr-75-1	0.54	1.00

from the tests on the type I panels that peeling of the glue joint mostly started at the outer edges of the outer stiffeners because of the heavy buckling of the strips outside of these stiffeners,

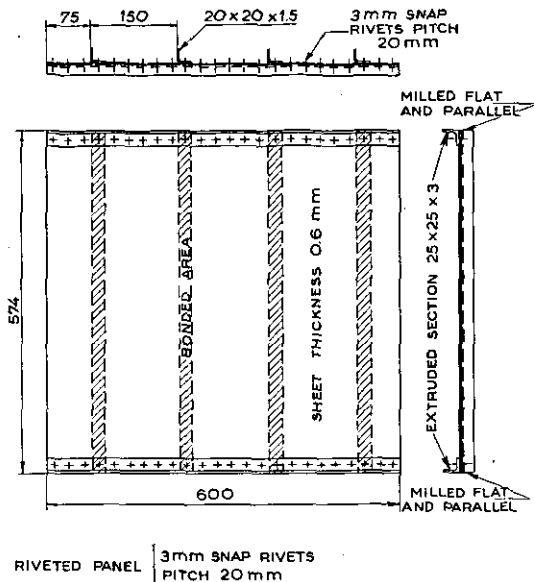


Fig. 2.1. Nominal dimensions of the panels, type I.

these strips were removed. Thus the total width of the type II panels ranged from 510 to 515 mm (fig. 2.2).

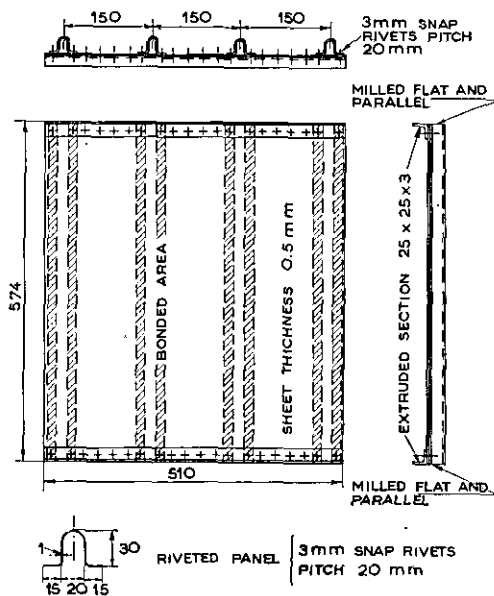


Fig. 2.2. Nominal dimensions of the panels, type II.

For introducing the load into the panels, the top and bottom ends of each panel were provided with heavy extruded angle sections $25 \times 25 \times 3$ mm riveted to the sheet. The ends of a panel were finally milled flat and parallel to each other, to obtain an even load distribution.

The total height of the panels thus became about 574 mm.

All panels were manufactured at the Fokker factory. Some particulars of the bonding process are given in Appendix A.

2.3 The test set-up.

The tests were run in a standard 50 tons Amsler hydraulic pulsating machine.

As the platens of this machine are too small to apply an evenly distributed load to the panels, two rigid loading beams were designed and fastened to the platens. They consisted of two beams (Dutch specification NP 10, i. e. 10 cm height and 5 cm width of flanges) welded together in such a manner as to form a box beam. To the top and bottom planes of this beam steel plates of 10 mm thickness were welded. These plates were milled flat and parallel and then the beams were bolted to the platens of the pulsating machine. The beams are clearly shown in fig. 3.17. Between these beams and the specimen a strip of fibre of about 1 mm thickness was inserted.

In this manner an even distribution of the load over the panel width was obtained, as could be seen from the regular pattern of the buckles in the panels during the tests. Moreover, the panels were placed as accurately as possible with the neutral axis in the centre line of the machine, and were prevented from moving perpendicularly to their plane by small clamps on the beams. Such a movement might occur when the panel started collapsing.

With the first few tests, the panels were pulsated at about 260 load reversals per minute. To accelerate the test programme, later on 525 reversals per minute were applied. Before this was done the amplitudes of the buckles of two panels were determined at each frequency over about three wave lengths. It appeared that in both cases the amplitudes were exactly the same, so that the wave formation was not diminished by the higher frequency of load application.

3 The test results.

3.1 Description of failures.

A review of the principal results of the fatigue tests is given in tables 3.1 and 3.2, while figures 3.1 to 3.19 incl. show details of the appearance of the fractures in the sheets and the length and location of the peeling of the bonded joints during and at the end of the tests. The depth of the peeling was measured with a thickness gauge of 0.05 mm. If no depth of the peeling is indicated the flange of the stiffener was separated completely from the sheet (complete peeling) over the marked distance.

3.1.1 The riveted panels, type I.

The statically loaded panel failed at a load of 4550 kg and thus the fatigue panels were subjected to a pulsating compression load varying from 1000 kg to 2000, 2700 or 3400 kg respectively. The tests were ended after 2.65, 4.07 and 2.68×10^6 load reversals had been applied. The static loads after the tests were 4910, 4200 and 3700 kg.

A great difficulty with the tests was the choice of the useful life, at which the tests should be stopped. It was not intended to continue the test

TABLE 3.1.

Principal results of the fatigue tests on panels type I (fig. 2.1).

Panel no.	Number of loading cycles $\times 10^{-6}$ endured before									Total Number of loading cycles applied $\times 10^{-6}$	Ultimate static load in kg at the end of the test
	cracking of the sheet			partly peeling of the bonded joint.			total peeling of the bonded joint				
	1st crack	2nd	3rd	1st peeling	2nd	3rd	1st	2nd	3rd		
Ir-s-1	—	—	—	—	—	—	—	—	—	—	4,550
Ir-45-1	1.18 ¹⁾ 1.43 (3 \times)	1.87 ¹⁾ 2.57	2.57 ¹⁾ 2.65							2.65	4,910
Ir-60-1	0.27	0.67 ¹⁾ 1.11	1.15							4.07	4,200
Ir-75-1	0.026 ¹⁾ 0.75 (5 \times)	0.87 ¹⁾ 1.16 (6 \times)	1.60 ¹⁾ 1.88 (4 \times)							2.68	3,700
Ib-s-1	—	—	—	—	—	—	—	—	—	—	5,500
Ib-s-2	—	—	—	—	—	—	—	—	—	—	4,580
Ib-45-1	0.70	1.08	—	0.70	0.83	—	1.08	—	—	1.10	—
Ib-45-2	0.30	0.37	0.68	0.30	1.03	1.79	—	—	—	3.04	—
Ib-60-1	1.99	—	—	—	—	—	—	—	—	2.79 ²⁾	—
Ib-60-2	0.11	0.36	—	0.11	0.22	—	—	—	—	0.37	—
Ib-60-3	0.11	—	—	0.11	—	—	0.11	0.13	—	0.24	3,800
Ib-75-1	0.25	0.32	0.39	0.29	—	—	0.35	0.63	—	0.64	—
Ib-75-2	0.07	0.09	0.10	0.05	—	—	0.10	—	—	0.11	—
Ib-75-3	0.010	0.012	0.019	0.009	—	—	0.017	—	—	0.026	—

¹⁾ At the first number of cycles the panel was inspected without cracks being found. The number between the brackets indicates the number of cracks detected simultaneously.²⁾ This panel failed by trouble of the pulsator.

to complete destruction of the panel, but to stop it when the panel was considered to be "severely" damaged. This condition is, of course, not clearly defined and that the choice made was rather arbitrary is illustrated by comparing the numbers of load reversals at which the first fracture in

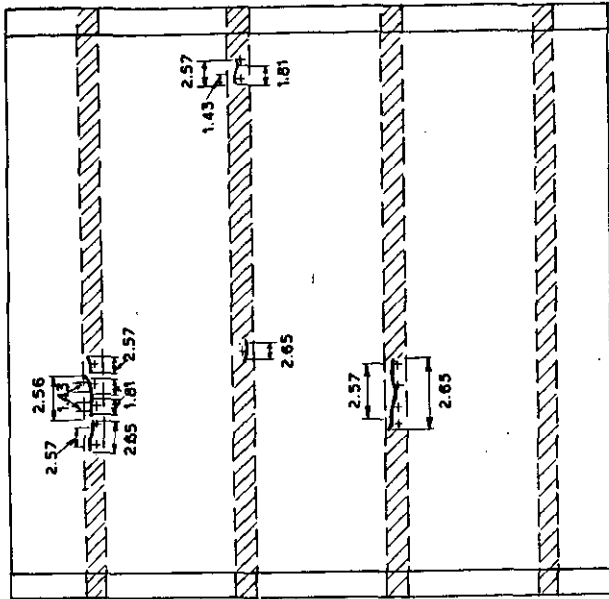


Fig. 3.1. The cracks in panel Ir-45-1. $n = 2.65 \times 10^6$. The numbers indicate the loading cycles $\times 10^{-6}$ at which the crack in the sheet had the indicated length; + rivets.

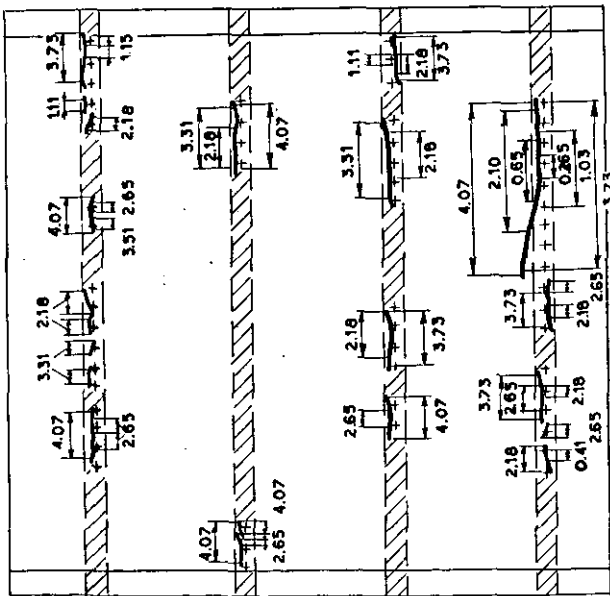


Fig. 3.2. The cracks in panel Ir-60-1. $n = 4.07 \times 10^6$. (Also see fig. 3.1).

the sheet occurred with the total numbers of loading cycles applied to each panel (table 3.1). The first number appears to be roughly inversely proportional to the maximum pulsating load. The last number did not correspond to an equal degree of crack formation for different panels, as may be seen from figs. 3.1 to 3.3. They clearly show that the number of fractures in the 45 % panel is far less than that in the 60 % or even in the 75 % panel. Thus the fatigue tests on panel Ir-45-1

and Ir-75-1 should have been continued to a larger number of loading cycles to obtain a life comparable to that of panel Ir-60-1, though it is evident, by comparing the fractures, that the 75 % panel was nearer to this condition than the 45 % panel.

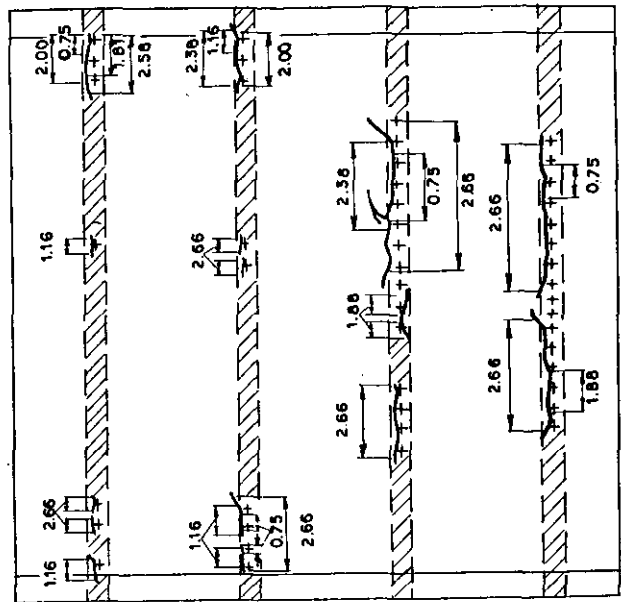
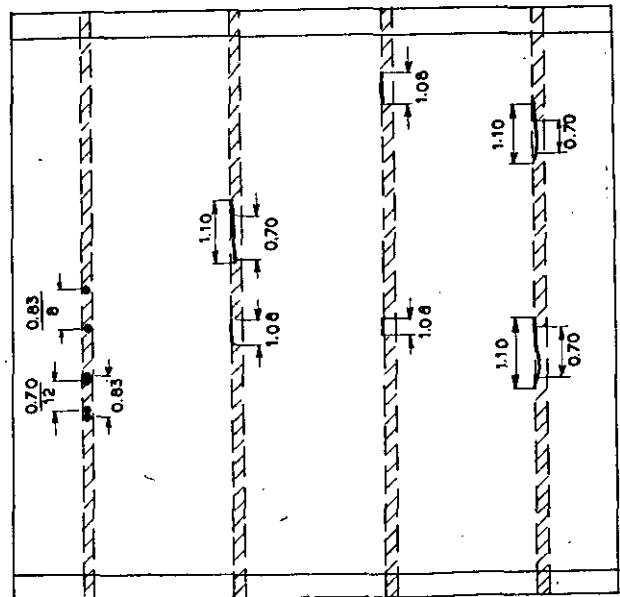


Fig. 3.3. The cracks in panel Ir-75-1. $n = 2.68 \times 10^6$. (Also see fig. 3.1).

3.1.2 The bonded panels, type I.

The first panel of this series failed at a static load of 5500 kg and the maximum pulsating loads were calculated from this value. During the tests on the riveted panels, which were investigated after nearly all bonded panels, type I were tested,



— = cracking of the sheet.
 . . = peeling of the glue joint.
 0.70 = number of load cycles $\times 10^{-6}$ when the crack or total peeling had the indicated length.

$\frac{0.70}{12}$ = after 0.70 $\times 10^6$ load cycles the peeling was 12 mm deep.

Fig. 3.4 The cracks and peeling of panel Ib-45-1. $n = 1.10 \times 10^6$.

it proved desirable to evaluate the static load of the panels Ib once again (c.f. static load of Ir-s-1 and Ir-45-1). The last panel of series Ib was therefore again loaded statically and its ultimate load was 4580 kg. This discrepancy can partly be explained by the difference in thickness of the sheets of both panels (c.f. table 2.1) and must further be due to normal scatter.

Figs. 3.4 to 3.8 incl. give typical examples of

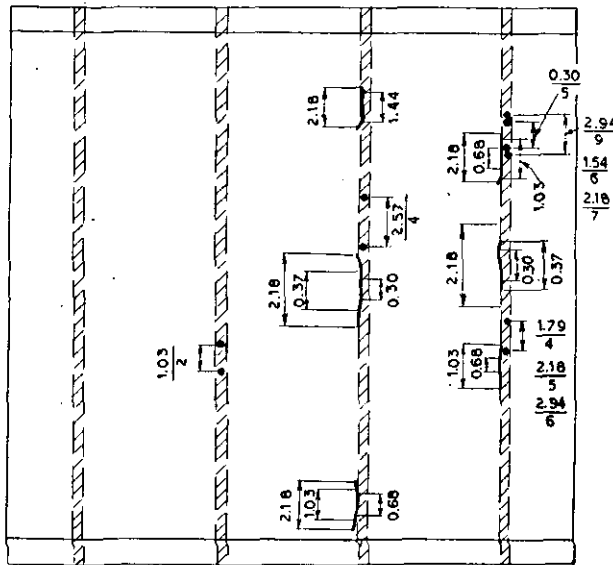


Fig. 3.5. The cracks and peeling of panel Ib-45-2.
 $n = 3.04 \times 10^6$. (Also see fig. 3.4).

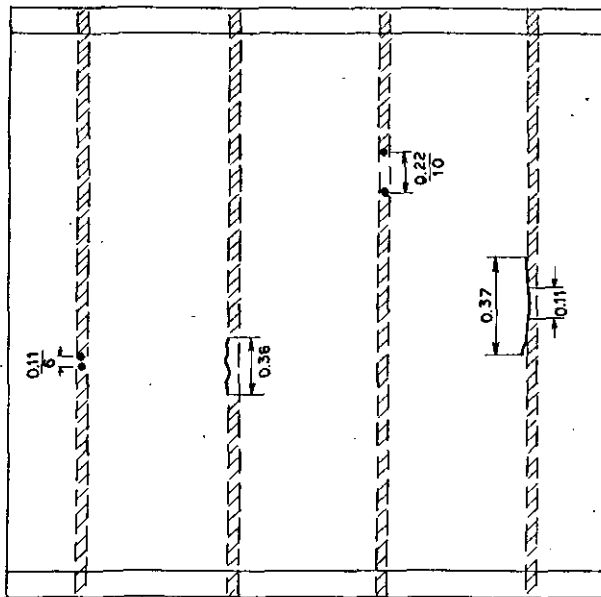


Fig. 3.6. The cracks and peeling of panel Ib-60-2.
 $n = 0.37 \times 10^6$. (Also see fig. 3.4).

the location and length of the fractures in the sheets and the peeling of the bonded joints at the end of the tests.

It must be remarked that panel Ib-60-1, being the first panel investigated, was only subjected to a maximum pulsating load of 55 % of the static load mentioned before and that the panel failed after 2.79×10^6 load reversals by trouble of the pulsator.

As stated in 3.1.1 the tests were stopped when the panels were considered to show "severe damage" and the degree of damage with different panels is rather variable.

Considering the figures it is clear that many panels might have endured a higher number of load cycles than were applied. Only panels Ib-75-1 and Ib-75-3 failed by a crack in the free leg of the angle section and may thus be considered to have reached their fatigue life. The fracture in the first panel was probably caused by peeling

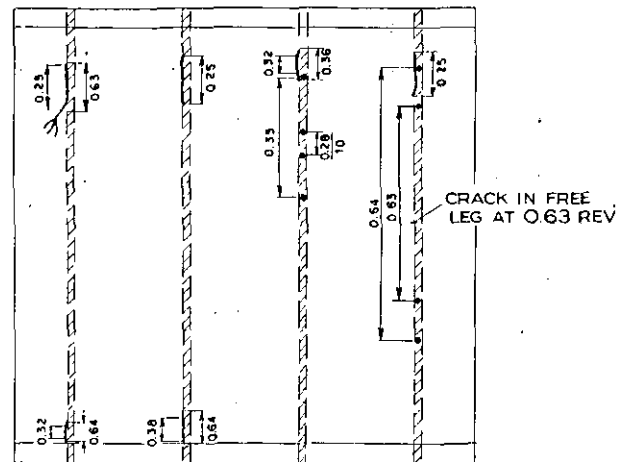


Fig. 3.7. The cracks and peeling of panel Ib-75-1.
 $n = 0.64 \times 10^6$. (Also see fig. 3.4).

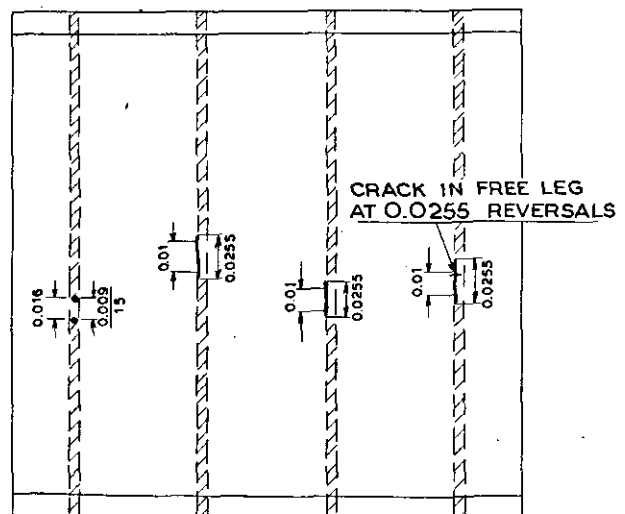


Fig. 3.8. The cracks and peeling of panel Ib-75-3.
 $n = 0.026 \times 10^6$. (Also see fig. 3.4).

of the greater part of the stiffener, thus causing the stiffener to bend. The fracture in the other stiffener was not accompanied by peeling, and was perhaps caused by bending of the sheet-stringer as a whole.

The panels Ib-45-2 and Ib-60-3 were rather heavily damaged at the end of the test and were perhaps near to complete destruction.

Only with four panels type I, peeling test specimens were manufactured, giving peeling strengths of 10.2, 13.8, 16.0 and 18.8 kg (c.f. Appendix A).

3.1.3 The riveted panels, type II.

The static load of one of these panels was 10,050 kg and the pulsating loads were calculated according to this load.

The erratic results of the tests on the type I panels gave rise to the decision to test the type II panels until complete destruction of at least one of the stiffeners occurred.

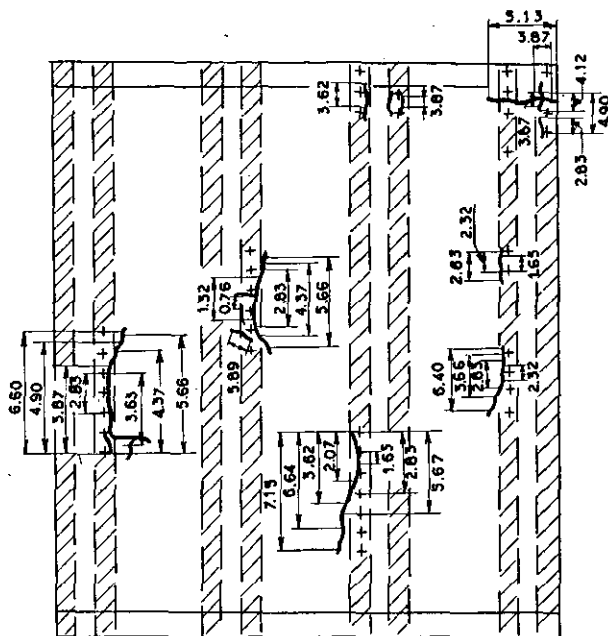


Fig. 3.9. The cracks in panel IIr-45-1. $n = 7.23 \times 10^6$.
(Also see fig. 3.1).

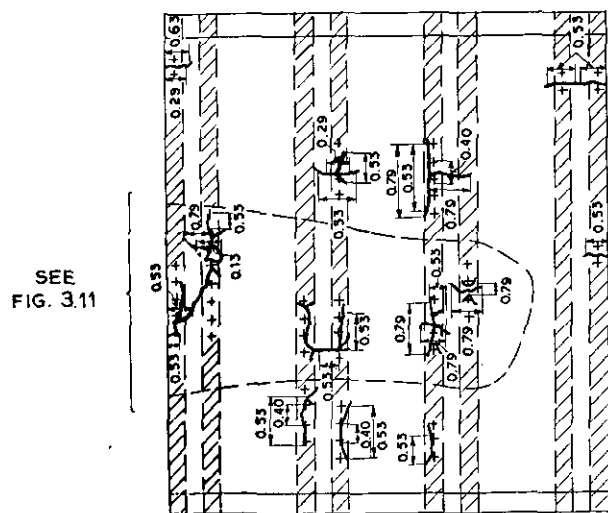


Fig. 3.10. The cracks in panel IIr-60-1. $n = 0.80 \times 10^6$.
(Also see fig. 3.1).

In figs. 3.9 to 3.12 incl. the cracks in the panels at the end of the tests are given. The cracks in these panels differed from those in the panels type I, where only cracks in the direction of the load occurred. The horizontal cracks caused the hat sections to take a much greater part of the load and consequently failure of the stiffener took place.

In one corner of panel IIr-45-1 horizontal cracks appeared after some vertical ones and this caused

a hole in the sheet. Then after some load cycles the hat section failed at this spot (fig. 3.9).

In panel IIr-60-1 horizontal cracks appeared in many places, and after some further load cycles three stiffeners failed at those spots as can be seen from figs. 3.10 and 3.11.

Panel II-R75-1 showed far less cracks in the sheet, but nevertheless the horizontal cracks caused two stiffeners to fail after 0.099×10^6 load cycles (fig. 3.12).

The static loads of the panels, sustained after the fatigue tests were performed, were nearly proportional to the number of undamaged stiffeners, as might be expected.

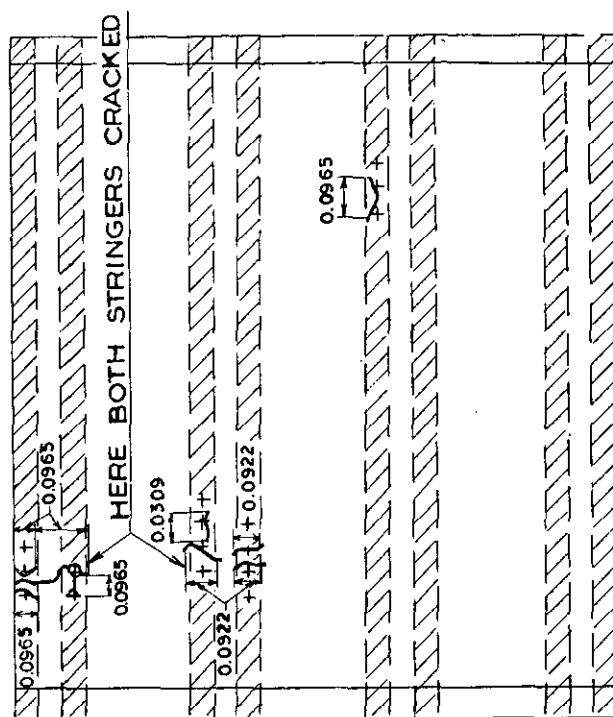


Fig. 3.12. The cracks in panel IIr-75-1. $n = 0.099 \times 10^6$.
(Also see fig. 3.1).

3.1.4 The bonded panels, type II.

The static load of one of these panels was 11,930 kg. This was in very good accordance with the static load of panel IIb-45-2, which after having endured 20.22×10^6 load cycles without any visible damage collapsed at a static load of 12,300 kg.

As for the riveted panels (c.f. 3.1.3) the fatigue tests were continued to complete destruction of at least one of the stiffeners except that the test on panel IIB-45-2 was stopped after reaching 20 million cycles without any visible damage.

Panel IIb-45-1 showed a beginning of peeling after 3.41×10^6 load cycles, while cracks in the sheet and total peeling occurred after 5.35 and 6.57×10^6 load cycles. At last the stiffener collapsed after 20.44×10^6 load cycles.

The three panels loaded between 1000 kg and 60 % of the static load behaved quite differently. Two panels (IIB-60-1 and 3) showed complete peeling after nearly the same number of load cycles and only minor cracks in the sheets. Panel IIB-60-2



Fig. 3.11. View of panel Iir-60-1 after the test.
(Reverse side of area indicated in fig. 3.10).

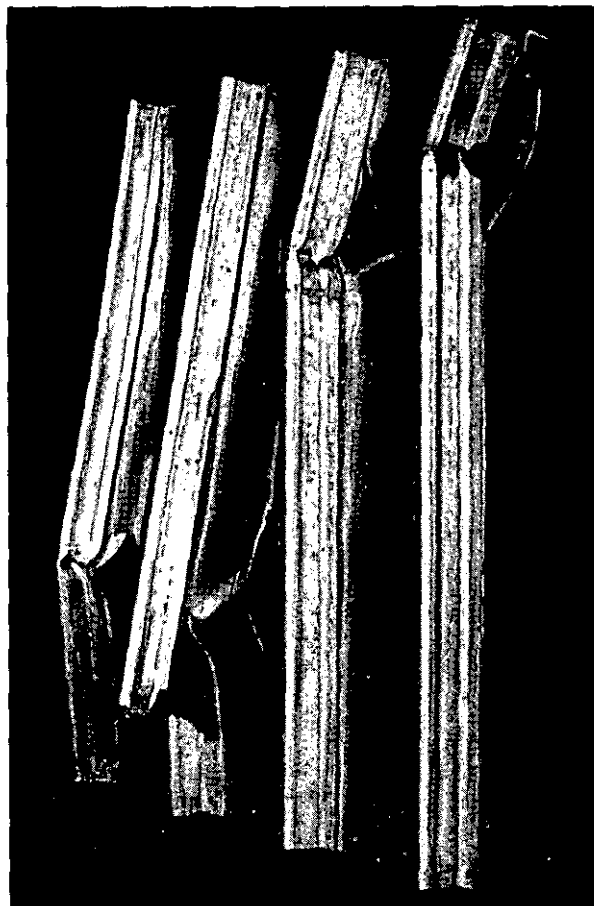
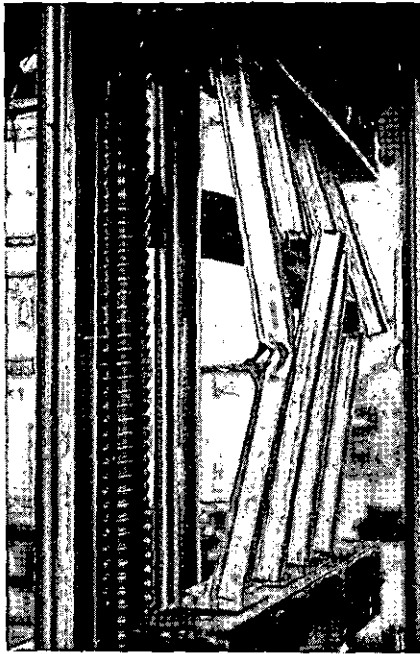
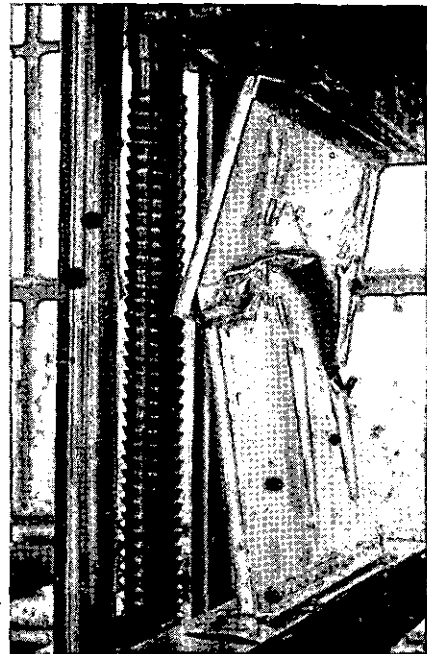


Fig. 3.15. View of panel IIb-60-2 after the test
(same side as fig. 3.14).



a



b

Fig. 3.17. Panel IIb-75-1 at the end of the test in the testing machine. $n = 0.25 \times 10^6$.

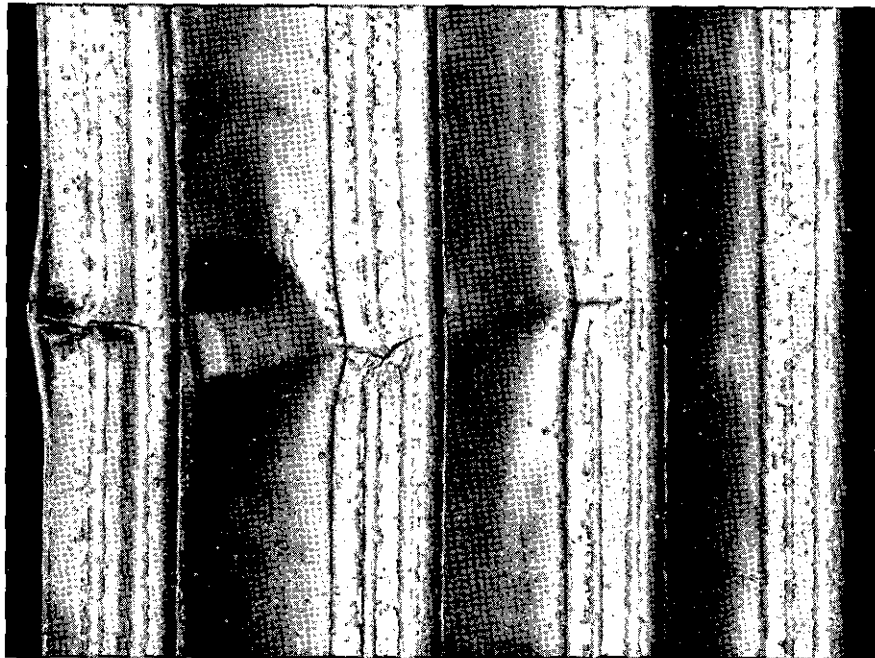


Fig. 3.19. View of panel IIb-75-3 after the test
(same side as shown in fig. 3.18).

panel was tested overnight no description of the starting of the fractures can be given. The numbers of load cycles from these panels are in rather good accordance. With panel IIb-75-2 failure of the hat section stiffeners again started when complete peeling had reached a certain extent.

Panel IIb-75-3 showed an exceptional behaviour. Here again the first stiffener collapsed because

should be expected, owing to the fairly arbitrary choice made in stopping the tests. This expectation is confirmed and it is therefore impossible to draw any definite conclusions with regard to the fatigue lives of panels of this type. Part of the scatter will probably be due to variations in the static strengths of the panels, which may apparently be fairly large (table 3.1). In fig. 3.20 the static

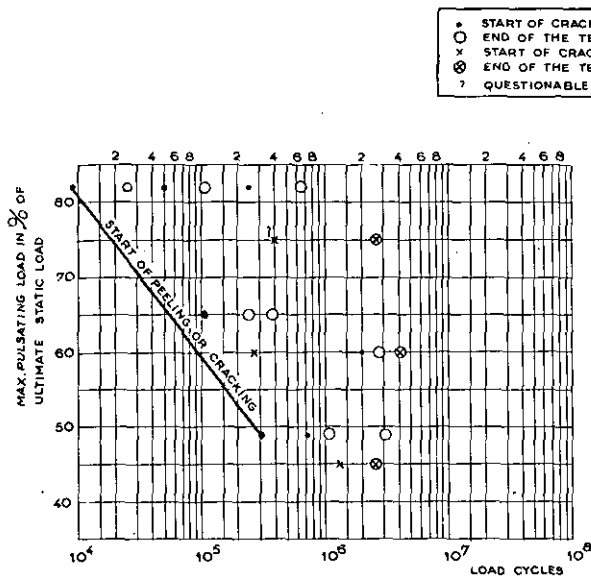


Fig. 3.20.

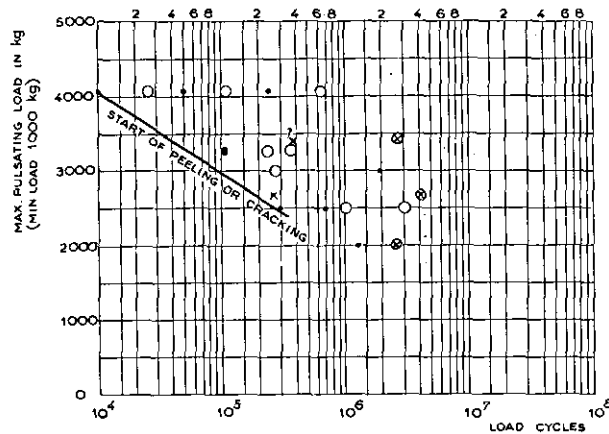


Fig. 3.21.

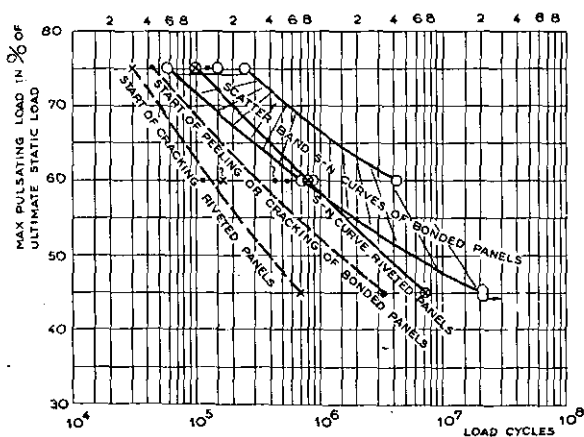


Fig. 3.22.

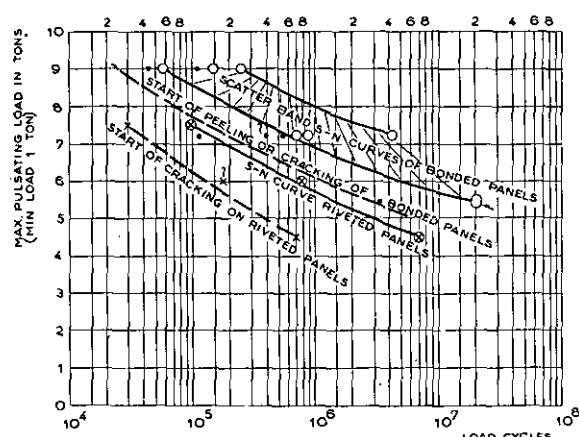


Fig. 3.23.

the peeling exceeded a certain limit. Then two other stiffeners collapsed without peeling from the attached sheet. (c.f. figs. 3.18 and 3.19).

The results of the peeling tests of the specimens manufactured with the panels are given in Appendix A and table 3.2.

3.2 Discussion.

3.2.1 Panels type I.

Figures 3.20 and 3.21 give diagrams of the number of load cycles against the percentage of static load of the panel, and against the maximum pulsating load.

From the description of the tests in sections 3.1.1 and 3.1.2 it is clear that a large scatter

failing load for the bonded panels has been taken as 5040 kg, being the average of the results for panels Ib-s-1 and Ib-s-2, whereas the static strength of the riveted panels was assumed to be 4730 kg, the average for panels Ir-s-1 and Ir-45-1. It may be assumed that the prior fatigue loading will hardly have affected the static strength of the latter panel. The lower load limit of 1000 kg corresponds to 20 % and 21 % respectively.

In view of the foregoing, only curves indicating a lower limit for the start of cracking or peeling have been drawn in figures 3.20 and 3.21. However, here again it should be observed that the results were influenced by the presence of the strips of sheet outside of the outer stiffeners, which showed more severe buckling than the sheet between two stiffeners. Therefore, the results are

TABLE 3.2.

Principal results of the fatigue tests on panels type II (fig. 2.2).

Panel no.	Number of loading cycles $\times 10^{-6}$ endured before									Peeling strength in kg	Total Number of loading cycles applied $\times 10^{-6}$	Ultimate static load in kg at the end of the test
	cracking of the sheet			partly peeling of the bonded joint			total peeling of the bonded joint					
	1st crack	2nd	3rd	1st peeling	2nd	3rd	1st	2nd	3rd			
IIr-s-1	—	—	—	—	—	—	—	—	—	—	—	10,050
IIr-45-1	0.65 0.76	— 1.32	— 1.65	—	—	—	—	—	—	—	7.23	7,480
IIr-60-1	0.04 0.29	— 0.40	— 0.53	—	—	—	—	—	—	—	0.80	4,580
IIr-75-1	0.031	0.097	—	—	—	—	—	—	—	—	0.099	—
IIb-s-1	—	—	—	—	—	—	—	—	—	—	—	11,930
IIb-45-1	5.31 5.35	—	—	3.16 3.41	— 3.89	—	— 6.57	— 7.30	—	—	20.44	10,550
IIb-45-2	—	—	—	—	—	—	—	—	—	15.6	20.22 ¹⁾	12,300
IIb-60-1	0.18 0.68	—	—	—	—	—	— 0.68	— 0.82	—	—	0.88	8,050
IIb-60-2	0.54	0.75	0.78	2.11 2.19	—	—	2.82	3.60	—	≈ 3	4.25	0
IIb-60-3	0.11	—	—	—	—	—	0.61	0.70	—	22.8	0.72	—
IIb-75-1	—	—	—	—	—	—	—	—	—	26.2	0.25	0
IIb-75-2	0.12	0.15	—	—	—	—	0.12	0.13	0.14	18.9	0.15	—
IIb-75-3	0.058 ²⁾	—	—	0.043	—	—	0.049	—	—	22.2	0.058	—

¹⁾ After 20.22×10^6 load cycles the panel was still undamaged.²⁾ At the location of peeling a crack in the stiffener appeared after 0.047×10^6 load reversals.

not representative for practical applications of this type of panel, but will be on the conservative side.

All cracks in the sheet of the riveted panels ran just along the heads of the rivets and appeared sooner in the case of the higher loads, as might be expected from the heavier buckling of the sheets under these loads.

The ultimate compressive load of these panels was not very much influenced by those cracks (c.f. table 3.1). In one case (panel Ir-45-1) it was even 10 % higher than of the statically loaded panel, but this was partly caused by the greater thickness of the sheet (c.f. table 2.1).

All cracks in the sheets of the bonded panels, and in nearly all riveted panels, appeared near the corner of the angle section. This may be due to the greater stiffness of the sheet-stiffener combination at these points in a plane perpendicular to the sheet than on the free side of the stiffener, where the bonded leg of the angle section followed the buckling of the sheet to a certain degree.

From figs. 3.1 to 3.8 incl. it may be concluded that small cracks in the sheets generally propagate rather slowly and do not influence the strength of the panel, so that there is ample warning of any impending fatigue failure both for the riveted and for the bonded panels.

3.2.2 Panels type II.

Figs. 3.22 and 3.23 give diagrams of the total number of load cycles endured against the percentage of the static load and the maximum pulsating load. Also the points giving the start of cracking or peeling are included.

Except on panel IIb-45-2, which showed no damage after having sustained more than 20×10^6 load cycles, the fatigue tests on all panels were continued until failure of one or more stringers occurred.

It may therefore be expected that the scatter will be much less than with the panels of type I and this is confirmed by the test results.

The decrease of scatter may also have been caused by a greater uniformity of the static strengths of the panels. This is indicated by the results of panel IIb-45-2.

In fig. 3.22 the average results for failure of the bonded panels are more favourable than those for the riveted panels. Two of the three riveted panel results are, however, within the scatter band for the bonded panels, so that it is not possible to say more than that the bonded panels appear to be at least as good as the riveted panels when compared in percentages of their static strengths. The difference in the lower load limits, being 8 % and 10 % respectively, makes the comparison slightly in favour of the riveted panels. When compared in absolute maximum loads at the same lower load limit, the bonded panels are superior to the riveted panels, as shown in fig. 3.23. The fatigue lives of the former range between 4 and 14 times those of the latter.

Cracking of the sheet of the riveted panels starts earlier than cracking or peeling of the bonded panels; at the same load fig. 3.23 shows ratio's

of 5 to 11 of the numbers of cycles. An important result is that after the start of cracking or peeling the damage propagates only gradually until at a much higher number of cycles cracks occur in one or more stiffeners. With the riveted panels these cracks followed upon the development of horizontal cracks in the sheet due to inter-rivet buckling, after which the stiffener had to carry more load locally. With the bonded panels cracks in the stiffener develop after peeling has occurred over a certain distance, by which cause the stiffener has to carry more load and its flange is left unsupported by the sheet.

After cracking of the stiffener it loses bending stiffness and starts to bend out of the plane of the panel. Collapse of the stiffener then follows quickly. The static loads the panels could carry at the end of the fatigue test were reduced approximately in proportion to the number of failed stiffeners.

The superiority of the bonded panels over the riveted panels can be ascribed to the continuous joint between stiffener flanges and sheet. The rivets give only local attachments and permit inter-rivet buckling at high loads.

4 Conclusions.

4.1 Tests were carried out with two types of bonded and riveted panels, which were of identical construction except for the sheet-stringer joints.

The tests on the panels of type I (angle section stiffeners) must be considered as preliminary tests from which no quantitative conclusions can be drawn. They gave rise to some improvements of the testing technique and showed that after cracking or peeling first occurs, the damage to both riveted and bonded panels progresses only gradually.

4.2 The static strength of the bonded panels is higher than that of the riveted panels, which can be explained by the stabilizing effect of the continuous glue joint.

4.3 The fatigue strength of the bonded panels of type II is at least equal to that of the riveted panels when both are expressed as percentages of the static strength. Hence, the absolute fatigue strength is higher for the bonded panels than for the riveted panels. At the same load the fatigue lives of the bonded panels were 4 to 14 times those of the riveted panels.

4.4 Cracking of the sheet of the riveted panels starts earlier than cracking or peeling with the bonded panels, the ratio's between the corresponding numbers of reversals at the same load ranging from 5 to 11.

4.5 For all panels the propagation of cracking or peeling was very gradual. When these damages had reached such an extent that cracks in the stiffeners developed, collapse of those stiffeners followed quickly.

4.6 The static strengths of the panels after the fatigue tests were reduced roughly in proportion to the number of failed stiffeners.

5 References.

1. SCHLIEKELMANN, R. J. De toepassing van gelijmde metaalverbindingen in vliegtuigconstructies. De Ingenieur, Deel 64, no. 16, blz. L 14—L 18, 18 April 1952. Translated into English and published as: Bonded joints in the construction of metal aircraft, Aero Research Technical Note no. 114, June 1952, Aero Research Ltd, Duxford, Cambridge.
2. SCHLIEKELMANN, R. J. The application of metal-to-metal adhesives in composite spar booms. Report R-16, Fokker Aircraft Co. 1951.

Acknowledgement. The test programme was prepared by the Structures Department of the Fokker Aircraft Co. and the tests were executed in consultation with Messrs E. J. VAN BEEK and R. J. SCHLIEKELMANN of the said department, whose valuable assistance is gratefully acknowledged.

APPENDIX A.

The Manufacturing of the Bonded Panels.

All panels were manufactured in an experimental press by the Fokker Aircraft Company, Holland, using the "Redux" process.

The surfaces to be bonded were carefully degreased in a chromic-sulphuric acid according to DTD-915 A. Before application of the liquid component of the glue they were rinsed thoroughly in cold and hot water. Curing was carried out at temperatures of 140—145° C for 15—20 minutes at a pressure of 7 kg per sq.cm. After curing, the joints were cooled to 100° C before release of pressure.

With some of the type I panels (angle section stiffeners) and with all type II panels (hat section stiffeners) standard peeling test specimens (0.8 mm sheet, width 25 mm, length of bonded part 180 mm) were pretreated and fabricated simultaneously.

The results of the peeling tests which were taken at the Fokker factory, together with some particulars of the fabrication of the panels are given in the following table.

Panel no.	Mean Peeling strength in kg	Particulars
Type I	very low 13.8 16.0 18.8 10.2	The first five panels fabricated had a very low peeling strength, because of a too high curing temperature; colour of the bond dark-red. The corresponding panel numbers could not be ascertained.
IIb-s-1	—	No pressure on the peeling test specimen; colour of the bond light red.
IIb-45-1	21.8	Curing temperature temporarily too high; colour of the bond dark-red.
IIb-45-2	15.6	
IIb-60-1	24.8	
IIb-60-2	≈ 3	
IIb-60-3	22.8	
IIb-75-1	26.2	
IIb-75-2	18.9	
IIb-75-3	22.2	

Completed: December 1952.

REPORT S. 426

Note on the General Stress-Strain Relations of Some Ideal Bodies Showing the Phenomena of Creep and of Relaxation

by

J. P. BENTHEM.

Summary.

The general stress-strain relations of the Kelvin-Solid and the Maxwell-Liquid are derived from the cases of pure change of shape and of pure change of volume. It is shown that the relations of the Kelvin-Solid in pure tension may be much more complicated. The extension of the Kelvin-Solid and Maxwell-Liquid to general Linear Bodies is indicated.

Some remarks are made about viscosity effects, which may accompany plastic deformation.

Contents:

- 1 Introduction.
- 2 Linear Bodies.
 - 2.1 The Hookian Solid.
 - 2.2 The compressible viscous liquid (Newtonian Liquid).
 - 2.3 The Kelvin-Solid.
 - 2.3.1 Stress-strain relations.
 - 2.3.2 Mechanical and electrical model.
 - 2.3.3 Creep of the Kelvin-Solid.
 - 2.4 The Maxwell-Liquid.
 - 2.4.1 Stress-strain relations.
 - 2.4.2 Mechanical and electrical model.
 - 2.4.3 Creep and relaxation of the Maxwell-Liquid.
 - 2.5 Generalized Linear Bodies.
- 3 Plastic deformation in pure shear.
 - 3.1 Plastic deformation without viscosity effects.
 - 3.2 Plastic deformation with viscosity effects.
- 4 Notations.
- 5 References.
- 14 figures.

1 Introduction.

A one-dimensional model of the stress-strain relations of the Hookian Solid is a spring showing a displacement linear to the applied force. A model for the Newtonian Liquid is a dashpot, whose resistance to the displacement of the piston is proportional to the velocity of this displacement (in fact the shear-stress is proportional to the rate of shear-strain). Bodies, whose stress-strain relations may be represented by models consisting of more or less complicated combinations of such linear springs and dashpots, linked in series or parallel, are called Linear Bodies. It is not necessary, and mostly even not desirable to inter-

pret these models as a picture of the behaviour of the molecules of the material and of their mutual forces and velocities. These models do not serve any other purpose than to give a simplified picture of a mathematical relation.

The report deals with the general stress-strain relations of isotropic Linear Bodies and something is said about the viscosity phenomena which may accompany plastic deformation. For this case, however, only states of pure (and non-rotating) shear are considered in order to avoid a discussion of the many questions which arise, even if viscosity effects are not present at all, if plastic deformation for arbitrary states of stress and stress-histories is considered. For a survey of the extensive literature on (non-viscous) plastic deformation, see e.g. refs. 1, 2, 3.

2 Linear Bodies.

2.1 The Hookian Solid.

The isotropic Hookian Solid has various elasticity constants, the elasticity modulus E , modulus of rigidity G , the Poisson-ratio ν , the bulk modulus k , Lodes' coefficient λ (the other coefficient of Lode being G). Only two of these coefficients, however, are independent and choosing these two, the stress-strain relations may be written in different forms. The most natural form seems to be

$$\sigma_{ij} = 2G \epsilon_{ij} + k \delta_{ij} \epsilon_{aa}, \quad (2.1)$$

where $i = 1, 2, 3$; $j = 1, 2, 3$; $\delta_{ij} = 0$ if $i \neq j$;
 $\delta_{ij} = 1$ if $i = j$;

σ_{11} , σ_{22} , σ_{33} are the normal-stress components;

$\sigma_{12} = \sigma_{21}$, $\sigma_{13} = \sigma_{31}$, $\sigma_{23} = \sigma_{32}$ are the shear-stress components;

ϵ_{11} , ϵ_{22} , ϵ_{33} are the normal-strain components;

$2 \epsilon_{12} = 2 e_{21}$ etc. are the shear-strain components;

$\epsilon_{aa} = \epsilon_{11} + \epsilon_{22} + \epsilon_{33}$; e_{ij} is the strain-deviator;

$$e_{ij} = \epsilon_{ij} - \frac{1}{3} \delta_{ij} \epsilon_{aa};$$

$$e_{11} + e_{22} + e_{33} = 0.$$

The first term of the right hand side of (2.1) refers to the change of shape, the second to the change of volume. Equation (2.1) can also be written as two independent relations

$$s_{ij} = 2 G e_{ij}, \quad (2.2)$$

$$\sigma_{aa} = 3 k \epsilon_{aa}, \quad (2.3)$$

where s_{ij} is the stress-deviator,

$$s_{ij} = \sigma_{ij} - \frac{1}{3} \delta_{ij} \sigma_{aa},$$

$$s_{11} + s_{22} + s_{33} = 0,$$

$$\text{and } \sigma_{aa} = \sigma_{11} + \sigma_{22} + \sigma_{33}.$$

Again (2.2) refers to the change of shape, and (2.3) to the change of volume.

If $G=0$ the Hookian-Solid degenerates into a non-viscous compressible fluid. Rubber e.g., which for small strains (and vanishing rates of strain) may be considered as a Hookian-Solid, is nearly incompressible compared to its resistance to change of shape (k is very large compared to G).

The inverse relations of (2.1) to (2.3) incl. are

$$\epsilon_{ij} = \frac{1}{2 G} s_{ij} + \frac{1}{9 k} \delta_{ij} \sigma_{aa}, \quad (2.4)$$

or the two independent relations

$$e_{ij} = \frac{1}{2 G} s_{ij}, \quad (2.5)$$

$$\epsilon_{aa} = \frac{1}{3 k} \sigma_{aa}. \quad (2.6)$$

2.2 The compressible viscous liquid (Newtonian Liquid).

The stress-strain relations of the compressible viscous liquid are

$$\sigma_{ij} = k \delta_{ij} \epsilon_{aa} + 2 \mu \dot{e}_{ij} + \mu_v \delta_{ij} \dot{\epsilon}_{aa}. \quad (2.7)$$

The dot indicates the derivative with respect to time t . The first term of the right hand side is identical to the right hand side of (2.1) if $G=0$. The second and the third terms together are a differential form of the complete right hand side of (2.1). Equation (2.7) is equivalent to the two independent relations for change of shape and change of volume respectively

$$s_{ij} = 2 \mu \dot{e}_{ij}, \quad (2.8)$$

$$\sigma_{aa} = 3 k \dot{\epsilon}_{aa} + 3 \mu_v \dot{\epsilon}_{aa}. \quad (2.9)$$

The coefficient μ is the viscosity coefficient (of change of shape) and μ_v is the volume-viscosity coefficient. Very little is known about this coefficient μ_v , mainly due to the fact that in liquids a non-vanishing volume-strain-velocity $\dot{\epsilon}_{aa}$ is in general only possible for a very short time, because the volume strain ϵ_{aa} remains small (k is

large), and soon approaches its equilibrium value, at which $\epsilon_{aa}=0$. After a sudden application of a constant state of stress, the term $\mu_v \delta_{ij} \dot{\epsilon}_{aa}$ in (2.7) may be of comparable magnitude to the other terms during a short time. This duration of time can only last longer if the change of shape develops very slowly due to an extraordinarily high viscosity-coefficient μ . Some further remarks on the volume-viscosity will be made in sec. 2.3. In general, however, the volume-viscosity in Newtonian Liquids need not be considered. For 1-atomic gases it has been proved on theoretical grounds that $\mu_v=0$, and in aerodynamics μ_v may be assumed to vanish.

2.3 The Kelvin-Solid.

2.3.1 Stress-strain relations.

The stress-strain relations of the Kelvin-Solid are

$$\begin{aligned} \sigma_{ij} = & 2 G e_{ij} + k \delta_{ij} \epsilon_{aa} + \\ & + 2 \mu \dot{e}_{ij} + \mu_v \delta_{ij} \dot{\epsilon}_{aa}. \end{aligned} \quad (2.10)$$

The first and second terms of the right hand side together are identical to the right hand side of (2.1), whereas the third and fourth terms are identical to the differential form of the right hand side of (2.1). Equation (2.10) may again be written as two relations for change of shape and change of volume

$$s_{ij} = 2 G e_{ij} + 2 \mu \dot{e}_{ij}, \quad (2.11)$$

$$\sigma_{aa} = 3 k \epsilon_{aa} + 3 \mu_v \dot{\epsilon}_{aa}. \quad (2.12)$$

If $G=0$ the Kelvin-Solid degenerates into the Newtonian Liquid. In contrast to the Newtonian Liquid, the Kelvin-Solid has two viscosity coefficients μ and μ_v of equal importance, owing to the existence of both moduli k and G .

A problem in which only G and μ play a role is that of a cylindrical rod executing torsional vibrations, or that of a vibrating helical spring. These are not only cases of pure change of shape, but also of pure shear (there is, in a suitable co-ordinate system, only one non-vanishing component σ_{ij} , viz. $\sigma_{12} = \sigma_{21} = s_{12} = s_{21} = \tau$ and the relation

$$\tau = G \gamma + \mu \dot{\gamma} \quad (2.13)$$

is valid; $\gamma (= 2 \epsilon_{12} = 2 e_{12})$ is the shear-strain.

The relations for pure tension are not of such a simple form. From (2.10) follow the linear simultaneous differential equations

$$\left. \begin{aligned} \sigma = & \frac{4}{3} G (\epsilon - \epsilon_t) + k (\epsilon + 2 \epsilon_t) + \\ & + \frac{4}{3} \mu (\dot{\epsilon} - \dot{\epsilon}_t) + \mu_v (\dot{\epsilon} + 2 \dot{\epsilon}_t), \\ 0 = & -\frac{2}{3} G (\epsilon - \epsilon_t) + k (\epsilon + 2 \epsilon_t) - \\ & - \frac{2}{3} \mu (\dot{\epsilon} - \dot{\epsilon}_t) + \mu_v (\dot{\epsilon} + 2 \dot{\epsilon}_t), \end{aligned} \right\} \quad (2.14)$$

where σ is the tensile stress, ϵ the longitudinal strain and ϵ_t the transverse strain. If $\mu = \mu_v = 0$, it can easily be derived that $\sigma = 9 k G \epsilon / (3 k + G) = E \epsilon$ (E = elasticity modulus). REINER (ref. 4) exten-

sively treats the tensile test with a rod of a very viscous liquid ($G=0$, and μ very large), subjected to constant tension (TROUTON's experiment). If in this experiment it may be assumed that the volume-strain-velocity, which approaches zero ($\dot{\epsilon} + 2\dot{\epsilon}_t \rightarrow 0$), has become small with respect to the change of shape, then the relations (2.14) are reduced to

$$\left. \begin{aligned} \sigma &= k(\epsilon + 2\epsilon_t) + \frac{4}{3}\mu(\epsilon - \epsilon_t), \\ 0 &= k(\epsilon + 2\epsilon_t) - \frac{2}{3}\mu(\epsilon - \epsilon_t), \end{aligned} \right\} \quad (2.15)$$

or

$$\sigma = 2\mu(\epsilon - \epsilon_t) = 3\mu\epsilon. \quad (2.16)$$

It should be remembered that the relations (2.11) and (2.12) of the Kelvin-Solid are generalizations of the relations (2.2) and (2.3) of the Hookian law which refer to the change of shape and the change of volume respectively. It is also possible mathematically, though less evident physically, to start from equivalent expressions of the Hookian law, e.g. referring to pure tension and pure hydrostatic pressure,

$$\sigma = E\epsilon; \quad \sigma_{aa} = 3k\epsilon_{aa}.$$

Generalization of these relations leads to

$$\sigma = E\epsilon + \mu_t\dot{\epsilon}, \quad (2.17)$$

$$\sigma_{aa} = 3k\epsilon_{aa} + 3\mu_v\dot{\epsilon}_{aa}. \quad (2.18)$$

The difference in (2.17) and the two relations (2.14) illustrates the relativity of the starting point. Conversely, the γ, τ relation following from (2.17) and (2.18) will then be much more complicated than (2.13). But it must be repeated, that without the knowledge of the true forces between the molecules, the separate treatment of the change of shape and of the change of volume is the most natural, and in fact the only right way for the Newtonian-Liquid ($G=0$) and the Maxwell-Liquid (par. 2.4).

2.3.2 Mechanical and electrical model.

The stress-strain relations (2.13) for pure shear and (2.12) for a hydrostatic state of stress may be illustrated by the mechanical model of fig. 2.1, consisting of an elastic spring and a dashpot (filled with a viscous liquid) coupled in parallel. The spring has a linear force-displacement relation, and the force on the piston of the dashpot linearly depends on the velocity of displacement. By frictionless arrangements, the rods AB and CD cannot rotate. It will be seen that the relation between the displacement of the point Q and the applied force P is

$$P = c_1 d + c_2 \dot{d}, \quad (2.19)$$

being of the form (2.13) and (2.12). The force P is the image of stress and the displacement d of point Q the image of strain. As equation (2.13)

also completely defines the general stress-strain relations (2.11), the model is also valuable for general change of shape.

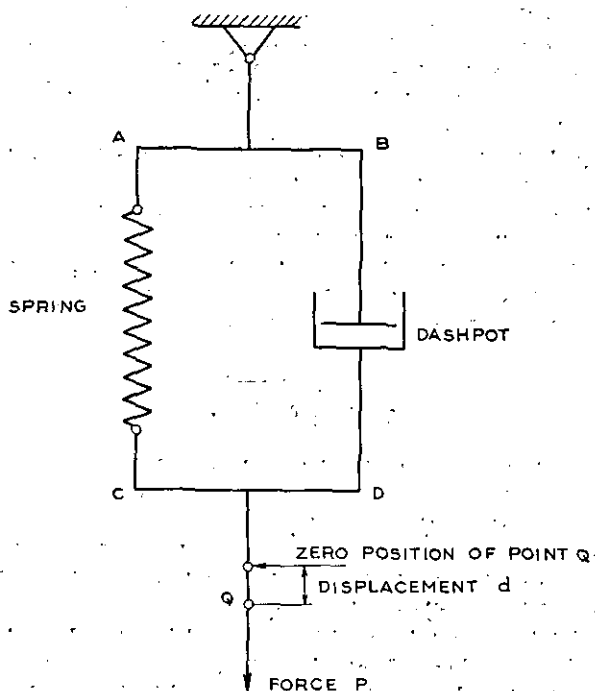


Fig. 2.1. Mechanical model of the Kelvin-Solid.

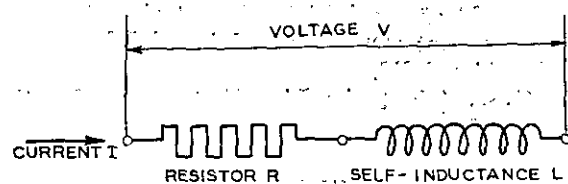


Fig. 2.2. Electrical model of the Kelvin-Solid.

In fig. 2.2 a resistor R and a self-inductance L are coupled in series. The relation between the voltage V and the current I is

$$V = RI + L\dot{I}. \quad (2.20)$$

and comparing with (2.13) and (2.12), it follows that the voltage V is the image of stress and the current I the image of strain. The model of the Hookian-Solid is a pure resistor, the model of the change of shape of a Newtonian-Liquid a pure self-inductance. Somewhat different electrical models are used by ALFREY (ref. 5) and BURGERS (ref. 6).

2.3.3 Creep of the Kelvin-Solid.

It is supposed that a part of a Kelvin-Solid material is, from an unstressed and unstrained state, instantaneously subjected to a state of pure shear at the time $t=0$. The shear strain will follow with retardation according to (2.13) and the solution is

$$\gamma = \frac{\tau}{G} \left(1 - e^{-\frac{G}{\mu} t} \right). \quad (2.21)$$

It is said that the material creeps under constant stress. For $t=0$ the strain $\gamma=0$, for $t=\infty$ the equilibrium value is reached: $\gamma=\tau/G$. To obtain the creep curve of the longitudinal strain ϵ after the application of a constant tensile stress σ , the equations (2.14) for $\sigma=\text{constant}$ and $\epsilon=0$, $\epsilon_t=0$ at $t=0$ must be solved. It must be remembered that it is actually impossible to impose an instantaneous constant stress throughout a body by instantaneous external forces, but when μ is large the solution for this ideal case will reasonably approximate actual conditions some time after the application of the load.

If from the final equilibrium state $\gamma=\tau/G$, the shear-stress is suddenly removed, the shear-strain tends to zero according to

$$\gamma = \frac{\tau}{G} e^{-\frac{G}{\mu} t} \quad (2.22)$$

This type of strain-history is called elastic after-effect. In (2.21) and (2.22) the quantity μ/G is called *retardation time* t_r .

In the Kelvin-Solid the strain follows the stress with retardation. This fact is called *delayed elasticity* or *firmité-viscosity*.

If in a certain equilibrium position the load is suddenly changed at time $t=0$, and the strain starts to change to its new equilibrium value, the difference between actual strain and final strain is after the retardation time t_r reduced to $1/e=0.368$ of the initial value at time $t=0$.

For constant strain the Kelvin-Solid behaves as the Hookian-Solid.

If $G \rightarrow 0$ (Newtonian-Liquid), the creep function (2.21) reduces to

$$\gamma = \frac{\tau t}{\mu},$$

which is also the obvious result with the stress-strain relation of the Newtonian-Liquid

$$\tau = \mu \dot{\gamma}.$$

2.4 The Maxwell-Liquid.

2.4.1 Stress-strain relations.

The differential form of the relations (2.4) of the Hookian-Solid is

$$\epsilon_{ij} = \frac{1}{2G} s_{ij} + \frac{1}{9k} \delta_{ij} \sigma_{aa}.$$

A new form of stress-strain relations can be obtained by adding to the right hand side a form identical to the non-differentiated right hand side of (2.4),

$$\epsilon_{ij} = \frac{1}{2G} s_{ij} + \frac{1}{9k} \delta_{ij} \sigma_{aa} + \frac{1}{2\mu} s_{ij} + \frac{1}{9\mu_v} \delta_{ij} \sigma_{aa}. \quad (2.23)$$

It is, however, obvious that $\mu_v = \infty$. If not, for constant hydrostatic pressure $p = -\frac{1}{3} \sigma_{aa}$

$$\epsilon_{aa} = \frac{1}{3\mu_v} \sigma_{aa}$$

would hold and an equilibrium would never be reached, which is, of course, impossible¹⁾.

From (2.23) the stress-strain relations of the Maxwell-Liquid

$$\epsilon_{ij} = \frac{1}{2G} s_{ij} + \frac{1}{9k} \delta_{ij} \sigma_{aa} + \frac{1}{2\mu} s_{ij} \quad (2.24)$$

remain.

Separation in relations for change of shape and for change of volume yields

$$\epsilon_{ij} = \frac{1}{2G} s_{ij} + \frac{1}{2\mu} s_{ij} \quad (2.25)$$

and

$$\epsilon_{aa} = \frac{1}{3k} \sigma_{aa}. \quad (2.26)$$

The physical meaning of G and μ in (2.24) and (2.25) (and also of μ_v in (2.23)), is quite different from that of the constants in (2.10). For $\mu = \infty$ in (2.24), these relations are those of the Hookian Solid (compare 2.4)). The same applies to (2.10) for $\mu = 0$ and $\mu_v = 0$. (Compare also the spring-dashpot model of the Kelvin-Solid fig. 2.1 and that for the Maxwell-Liquid fig. 2.3 to be discussed in par. 2.4.2).

For $G = \infty$ equations (2.25) and (2.26) are identical to the equations (2.8) and (2.9) for the Newtonian-Liquid with $\mu_v = 0$.

The behaviour of the Maxwell-Liquid at a hydrostatic state of stress is like that of the Hookian-Solid and Newtonian-Liquid.

In pure shear (shear stress τ , shear strain γ)

$$\gamma = \frac{1}{G} \tau + \frac{1}{\mu} \tau. \quad (2.27)$$

In pure tension (stress σ , longitudinal strain ϵ)

$$\epsilon = \frac{2k+1}{9kG} \sigma + \frac{1}{3\mu} \sigma,$$

or

$$\epsilon = \frac{\sigma}{E} + \frac{1}{3\mu} \sigma. \quad (2.28)$$

2.4.2 Mechanical and electrical model.

The stress-strain relations (2.25), (2.27) and (2.28) may be symbolized by the mechanical model fig. 2.3. The two elements used are the same as in fig. 2.1, but they are now placed in series. Obviously, the force-displacement relation of this construction is

$$\dot{d} = c_1 \dot{P} + c_2 P,$$

and the force P is the image of stress and the displacement d of point Q the image of strain.

If the stiffness of the spring is infinitely large ($G = \infty$, $c_1 = 0$) only the viscous element remains. If the viscosity of the fluid in the dashpot is infinitely large ($\mu = \infty$, $c_2 = 0$) only the elastic element remains.

¹⁾ This fact seems to have been overlooked by REINER (ref. 4), who supposes that the coefficient μ_v of the Maxwell-Liquid may have a finite value.

The electrical model (compare fig. 2.2) consists of a resistor and self-inductance coupled in parallel (fig. 2.4) and

$$\dot{I} = \frac{\dot{V}}{R} + \frac{V}{L}.$$

Again the current I is the image of the strain and the voltage V the image of the stress.

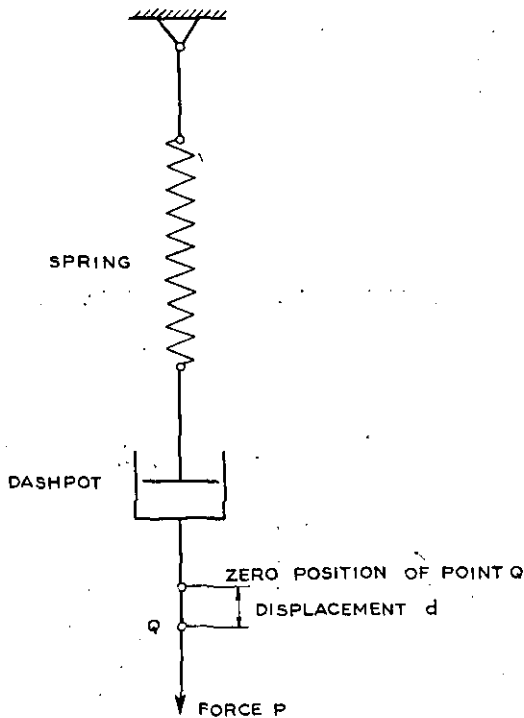


Fig. 2.3. Mechanical model for the change of shape of the Maxwell-Liquid.

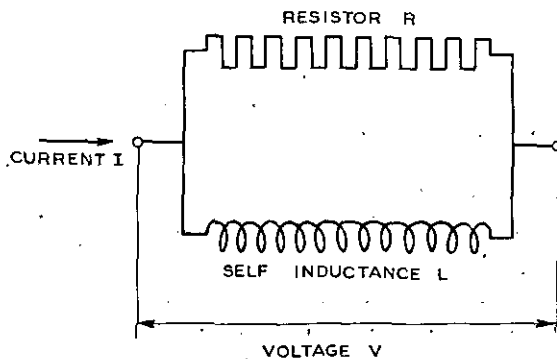


Fig. 2.4. Electrical model for the change of shape of the Maxwell-Liquid.

2.4.3 Creep and relaxation of the Maxwell-Liquid.

If a constant shear stress τ is suddenly applied, at the same moment a shear-strain $\gamma = \frac{\tau}{G}$ arises and continuously increases at the rate $\dot{\gamma} = \tau/\mu$. If a constant tension is applied, at the same moment $\epsilon = \sigma/E$, and this strain increases further at the rate $\dot{\epsilon} = \sigma/3\mu$. Also in these cases it is said that the material creeps, but this creep is of quite another type than the creep according to (2.2.1) of

the Kelvin-Solid, and does not tend to a final equilibrium value.

If a Maxwell-Liquid is suddenly forced in a state of pure shear strain γ , the corresponding shear stress is $\tau_0 = \gamma G$, and this shear stress diminishes to a final zero value according to the solution of the differential equation (c.f. (2.27))

$$0 = \frac{1}{G} \dot{\tau} + \frac{1}{\mu} \tau,$$

$$\text{i.e. } \tau = \tau_0 e^{-\frac{Gt}{\mu}}. \quad (2.29)$$

The time $t_{\text{rel}} = \mu/G$ is called *relaxation time*.

After suddenly forcing the Maxwell-Liquid in a state of pure longitudinal strain ϵ , the initial tension stress is $\sigma_0 = \epsilon E$, and this stress diminishes to a final zero value according to

$$\sigma = \sigma_0 e^{-\frac{Et}{3\eta}}, \quad (2.30)$$

the relaxation time being $3\eta/E$.

The diminishing of stress, without change of strain, is called *relaxation*.

If in a certain equilibrium position the Maxwell-Liquid is suddenly forced into a state of strain and the stress consequently follows immediately according to the Hookian Law, it will last the relaxation time t_{rel} before this stress has again reduced to $1/e = 0.368$ of the initial value.

The Maxwell-Liquid is said to show the phenomenon of *elastico-viscosity*.

2.5 Generalized Linear Bodies.

With springs and dashpots much more involved models may be constructed than are given in the figures 2.1 and 2.3 and such models may possibly serve for representing stress-strain relations for change of shape and for change of volume. The model of fig. 2.5, where a Hookian element A (spring), many (eventually a continuous distribution of) Kelvin-Solid elements B (c.f. fig. 2.1) and a viscous element C (dashpot) are linked in series, represents a general system of springs and dashpots, to which any other system may always be reduced. The force P is the image of stress, the displacement of the point Q the image of strain. An equivalent representation of fig. 2.5 is fig. 2.6, which model consists of many (eventually a continuous distribution of) Maxwell-Liquid elements (c.f. fig. 2.3) coupled in parallel. The rods AB and CD are prevented from rotation by frictionless arrangements. The force P is the image of stress, the displacement of the point Q the image of strain.

The behaviour of a continuous set of Kelvin-Solid elements in series (the set B in fig. 2.5) is completely defined by a function $J(t_r)$, such that $J(t_r)dt_r$ represents the total strain (in the model the total extension), caused after infinite time by a unit-stress (unit-load of the model), of all those elements, whose retardation times (c.f. sec. 2.3.3) lie between t_r and $t_r + dt_r$. The total strain (the total displacement in the model) of the set of

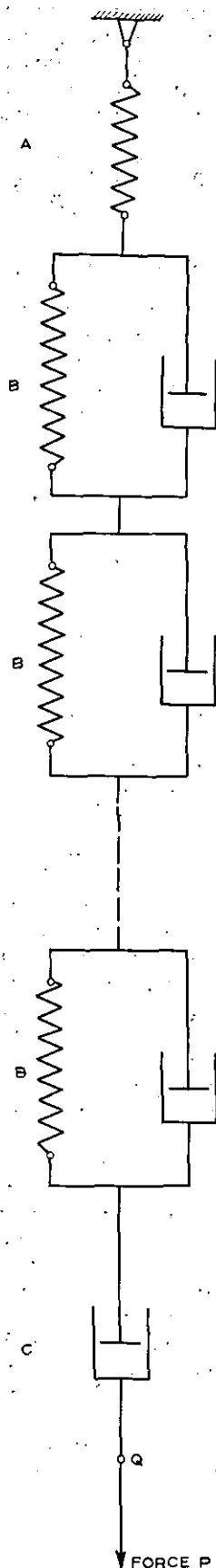


Fig. 2.5. Generalized model of the Linear Body.

continuously distributed Kelvin-Solid elements after the application of a constant stress to the

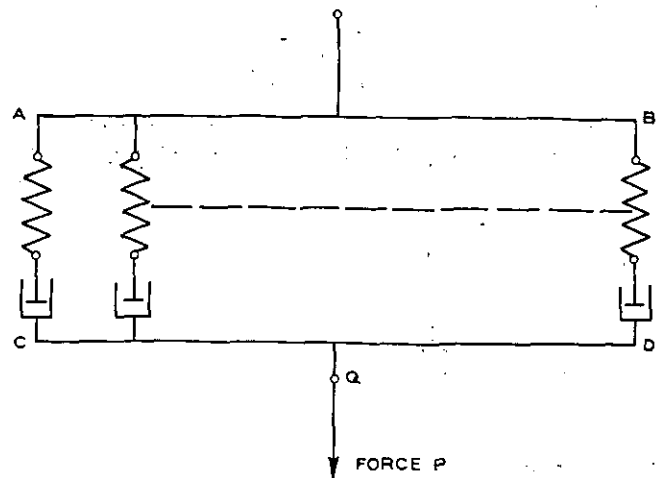


Fig. 2.6. Model equivalent to that of fig. 2.5.

unstressed and unstrained state, increases from zero till the final value according to

$$\gamma = \tau \int_0^{\infty} J(t_r) (1 - e^{-t/t_r}) dt_r \quad (2.31)$$

(supposing the model to represent relations of pure change of shape or pure shear).

To this strain γ the part of the strain represented by the spring A (fig. 2.5) $\gamma = \tau/G$ and the part represented by the dashpot $\gamma = \tau t/\eta$ must still be added. For the general differential equations of the complete model fig. 2.5 see ref. 5.

All materials, whose stress-strain relations for change of shape and change of volume may be represented by the model fig. 2.5 with linear springs and dashpots, are called Linear Bodies. As far as change of volume is concerned, the dashpot C cannot be present (compare the remark about μ_v in the discussion of the Maxwell-Liquid) (sec. 2.4.1). The stress-strain relations (2.14) concerning the behaviour of a rod in tension of the Kelvin-Solid can be represented by a generalized model fig. 2.5.

The stress-strain (force-displacement) relation of a model fig. 2.5 is not only completely determined by the constants of the springs and dashpots, and eventually by the function $J(t_r)$ if the set of Kelvin-Solid elements is continuous, but also by the creep function (change of strain after initiating a constant stress in the unstressed and unstrained state) or by the relaxation function (change of stress after initiating a constant strain in the unstressed and unstrained state).

HOHENEMSER and PRAGER (ref. 7) started from generalized stress-strain relations in pure shear:

$$C_1 + C_2 \tau + C_3 \dot{\tau} + C_4 \gamma + C_5 \dot{\gamma} = 0, \quad (2.32)$$

where C_1, \dots, C_5 are constants. With $C_1 = C_3 = 0$ (2.32) refers to the Kelvin-Solid, with $C_1 = C_5 = 0$ to the Maxwell-Liquid, with $C_3 = C_4 = C_5 = 0$ to the ideal plastic body (sec. 3.1). With only $C_1 = 0$ (2.32) corresponds to a spring-dashpot model, and it can be seen that this model may consist of a

Hookian element and a Kelvin-Solid element linked in series, or a Hookian element and a Maxwell-Liquid element coupled in parallel.

Analogous to the models fig. 2.5 and 2.6 electrical models are possible. In electrical engineering the characteristics of a network are sometimes represented in a diagram of NYQUIST, where the impedance is plotted as a function of the frequency ω of voltage and current. Similar diagrams are possible to express the stress-strain relations of arbitrary Linear Bodies¹⁾. For further work on the analogy to electrical networks, see ALFREY (ref. 5).

3 Plastic deformation in pure shear.

3.1 Plastic deformation without viscosity effects.

The ideal plastic body in pure shear has the stress-strain relation according to fig. 3.1. The

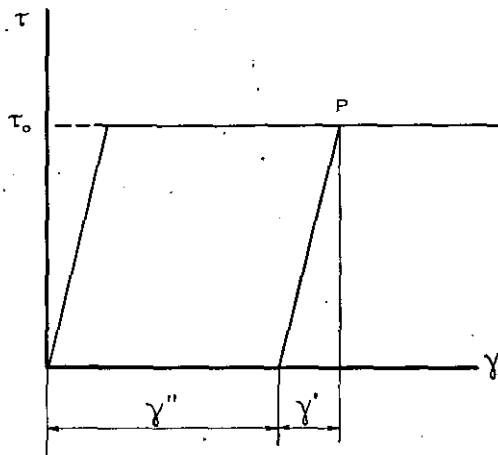


Fig. 3.1. Stress-strain relation in pure shear of the ideal plastic body.



Fig. 3.2. Model of the stress-strain relations of fig. 3.1.

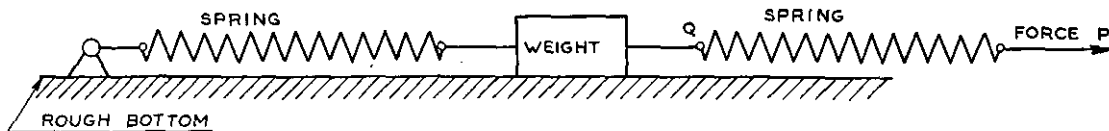


Fig. 3.3. Model of the linearly hardening material.

yield limit is the shear stress τ_0 . If $\tau < \tau_0$ the stress-strain relation is linear, if $\tau = \tau_0$ the strain may have any arbitrary value. In point P (fig. 3.1) the shear stress is τ_0 . If unloading takes place, γ'' is the permanent strain, γ' the elastic or recover-

¹⁾ It be remembered, that the real and imaginary parts of the impedance are not independent functions of the frequency.

²⁾ Other appropriate models with weights and springs coupled in parallel are possible.

able strain. This stress-strain relation may be represented by the model fig. 3.2. To a spring a weight is connected placed on a rough bottom. The weight only starts to move if a critical force is attained, and during the movement of the weight the force acting on the bottom remains constant. The force P is the image of shear stress, the displacement of point Q the image of shear strain.

The model in fig. 3.3 represents a body that shows linear strain hardening and a Bauschinger

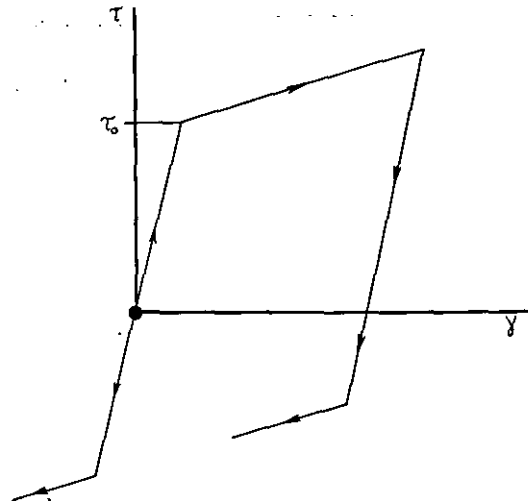


Fig. 3.4. Stress-strain relation in pure shear according to the model fig. 3.3.

effect. The corresponding stress-strain curve is shown in fig. 3.4.

Many weights with springs in series represent a more general hardening material (fig. 3.5). The corresponding stress-strain curve is given in fig. 3.6. If the set of weights is made continuous (but for the first spring and block), the sharp bends in fig. 3.6 are removed, as must be the case in a quite proper model²⁾.

If during stressing or unstressing no weights are moved, behaviour is purely elastic. If the shear-stress is increasing monotonically, the total shear-strain, and thus the plastic shear-strain is a unique function of the stress.

A noteworthy property of the plastic stress-strain relations, like those of the model fig. 3.5, is that they are independent of time.

3.2 Plastic deformation with viscosity effects.

Many extensions which may introduce viscosity effects into the model fig. 3.5 are possible, the most reasonable seem to be those shown in fig. 3.7 and fig. 3.8. Again the force P is the image of

stress and the displacement of point Q the image of strain. If a constant rate of (total) shear strain γ is applied to the model fig. 3.7, then the values of both the total shear strain and the shear-stress at initial yielding (the starting of the movement of the first block) are independent of

4. Notations.

G	modulus of rigidity.
E	modulus of elasticity.
k	bulk modulus.
σ_{ij}	stress tensor.

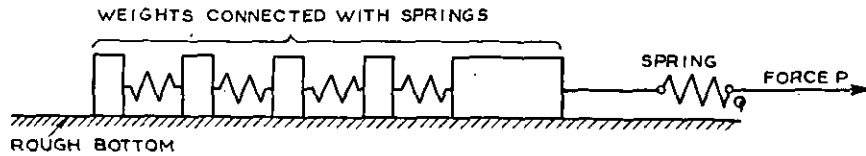


Fig. 3.5. Generalization of the model fig. 3.3.

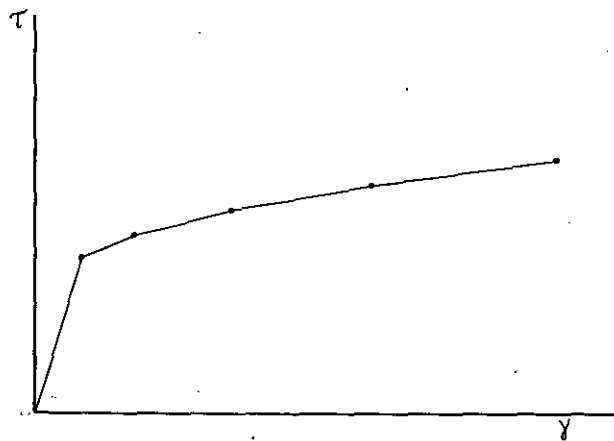


Fig. 3.6. Stress-strain relation in pure shear according to the model fig. 3.5.

$\sigma_{11}, \sigma_{22}, \sigma_{33}$	are normal stress components.
$\sigma_{12} = \sigma_{21}, \sigma_{13} = \sigma_{31}, \sigma_{23} = \sigma_{32}$	are shear stress components.
$\sigma_{11} + \sigma_{22} + \sigma_{33}$	stress deviation tensor
s_{ij}	$s_{ij} = \sigma_{ij} - \frac{1}{3} \delta_{ij} \sigma_{aa},$
s_{aa}	$s_{aa} = s_{11} + s_{22} + s_{33} = 0.$
δ_{ij}	Kronecker delta
$\delta_{ij} = 1$ if $i = j$; $\delta_{ij} = 0$ if $i \neq j$.	
τ	shear stress ($\sigma_{12} = \sigma_{21} = s_{12} = s_{21} = \tau$).
σ	tensile stress ($\sigma_{11} = \sigma$, all other σ_{ij} are zero).
ϵ_{ij}	strain tensor.
$\epsilon_{11}, \epsilon_{22}, \epsilon_{33}$	normal strain components.

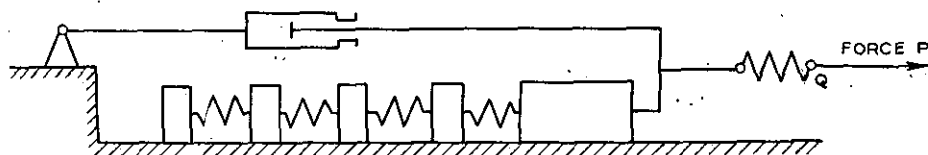


Fig. 3.7.



Fig. 3.8.

Fig. 3.7 and 3.8. Possible extensions of the model fig. 3.5, introducing viscosity effects.

the rate of strain. If the model fig. 3.8 holds, this is only true for the total shear-strain at initial yielding. The value of the shear stress at this moment, however, is increased if the rate of strain is high.

It is evident from the model fig. 3.7 that the material it represents, may show creep, i.e. change of strain at constant stress and relaxation, i.e. change of stress at constant strain. If fig. 3.8 is valid for a material, this material will show creep, but no relaxation.

$2 \epsilon_{12} = 2 \epsilon_{21}, 2 \epsilon_{13} = 2 \epsilon_{31}, 2 \epsilon_{23} = 2 \epsilon_{32}$	shear strain components.
$\epsilon_{11} + \epsilon_{22} + \epsilon_{33}$	strain deviation tensor
e_{ij}	$e_{ij} = \epsilon_{ij} - (1/3) \delta_{ij} \epsilon_{aa},$
e_{aa}	$e_{aa} = e_{11} + e_{22} + e_{33} = 0.$
γ	shear strain ($2 \epsilon_{12} = 2 \epsilon_{21} = 2 \epsilon_{12} = 2 \epsilon_{21} = \gamma$).
ϵ	longitudinal strain ($\epsilon_{11} = \epsilon$).
ϵ_t	transverse strain ($\epsilon_{12} = \epsilon_{21} = \epsilon_{13} = \epsilon_{31} = \epsilon_t$).

t	time.
σ_{ij}, σ_{aa} , etc.	differentiation with respect to time.
μ	viscosity coefficient in pure shear and in change of shape.
μ_v	viscosity coefficient in change of volume.
μ_t	viscosity coefficient in pure tension.
t_r	retardation time.
t_{rel}	relaxation time.

5 References.

1. PRAGER, W. The Stress-Strain Laws of the Mathematical Theory of Plasticity. A Survey of Recent Progress. *Journal of Applied Mechanics*, Vol. 15, No. 3, September 1948.
2. DRUCKER, D. C. Stress-Strain Relations in the Plastic Range. A Survey of Theory and Experiment. Graduate Division of Applied Mathematics, Brown University, Providence, R. I. December 1950.
3. BENTHEM, J. P. On the Stress-Strain Relations of Plastic Deformation. Report S. 398. Nationaal Luchtvaartlaboratorium, Amsterdam, December 1951.
4. REINER, M. *Deformation and Flow*, London, H. K. Lewis and Co. Ltd, 1949.
5. ALFREY, T. *Mechanical Behaviour of High Polymers*, New York, London, Interscience Publishers Inc. (Ltd), 1948.
6. First Report on Viscosity and Plasticity. *Transactions of the Royal Academy of Sciences at Amsterdam, Physical Department (First Section) Part XV*, No. 3, 1935. The second report is issued in First Section, Part XVI, No. 4, 1938.
7. HOHENEMSER, K. and PRAGER, W. Fundamental Equations and Definitions Concerning the Mechanics of Isotropic Continua. *Journal of Rheology*, Vol. III, No. 1, page 16, January 1932.

1. The first of these is the fact that the

2. second of these is the fact that the

3. third of these is the fact that the

4. fourth of these is the fact that the

5. fifth of these is the fact that the

6. sixth of these is the fact that the

7. seventh of these is the fact that the

8. eighth of these is the fact that the

9. ninth of these is the fact that the

10. tenth of these is the fact that the

11. eleventh of these is the fact that the

12. twelfth of these is the fact that the

13. thirteenth of these is the fact that the

14. fourteenth of these is the fact that the

15. fifteenth of these is the fact that the

16. sixteenth of these is the fact that the

17. seventeenth of these is the fact that the

18. eighteenth of these is the fact that the

19. nineteenth of these is the fact that the

20. twentieth of these is the fact that the

21. twenty-first of these is the fact that the

22. twenty-second of these is the fact that the

23. twenty-third of these is the fact that the

24. twenty-fourth of these is the fact that the

25. twenty-fifth of these is the fact that the

26. twenty-sixth of these is the fact that the

27. twenty-seventh of these is the fact that the

28. twenty-eighth of these is the fact that the

29. twenty-ninth of these is the fact that the

30. thirtieth of these is the fact that the

31. thirty-first of these is the fact that the

32. thirty-second of these is the fact that the

33. thirty-third of these is the fact that the

34. thirty-fourth of these is the fact that the

35. thirty-fifth of these is the fact that the

36. thirty-sixth of these is the fact that the

37. thirty-seventh of these is the fact that the

38. thirty-eighth of these is the fact that the

39. thirty-ninth of these is the fact that the

40. fortieth of these is the fact that the

41. forty-first of these is the fact that the

42. forty-second of these is the fact that the

43. forty-third of these is the fact that the

44. forty-fourth of these is the fact that the

45. forty-fifth of these is the fact that the

46. forty-sixth of these is the fact that the

47. forty-seventh of these is the fact that the

48. forty-eighth of these is the fact that the

49. forty-ninth of these is the fact that the

50. fiftieth of these is the fact that the

51. fifty-first of these is the fact that the

52. fifty-second of these is the fact that the

53. fifty-third of these is the fact that the

54. fifty-fourth of these is the fact that the

55. fifty-fifth of these is the fact that the

56. fifty-sixth of these is the fact that the

57. fifty-seventh of these is the fact that the

58. fifty-eighth of these is the fact that the

59. fifty-ninth of these is the fact that the

60. sixtieth of these is the fact that the

61. sixty-first of these is the fact that the

62. sixty-second of these is the fact that the

63. sixty-third of these is the fact that the

64. sixty-fourth of these is the fact that the

65. sixty-fifth of these is the fact that the

66. sixty-sixth of these is the fact that the

67. sixty-seventh of these is the fact that the

68. sixty-eighth of these is the fact that the

69. sixty-ninth of these is the fact that the

70. seventieth of these is the fact that the

71. seventy-first of these is the fact that the

72. seventy-second of these is the fact that the

73. seventy-third of these is the fact that the

74. seventy-fourth of these is the fact that the

75. seventy-fifth of these is the fact that the

76. seventy-sixth of these is the fact that the

77. seventy-seventh of these is the fact that the

78. seventy-eighth of these is the fact that the

79. seventy-ninth of these is the fact that the

80. eighty of these is the fact that the

81. eighty-first of these is the fact that the

82. eighty-second of these is the fact that the

83. eighty-third of these is the fact that the

84. eighty-fourth of these is the fact that the

85. eighty-fifth of these is the fact that the

86. eighty-sixth of these is the fact that the

87. eighty-seventh of these is the fact that the

88. eighty-eighth of these is the fact that the

89. eighty-ninth of these is the fact that the

90. ninetieth of these is the fact that the

91. ninety-first of these is the fact that the

92. ninety-second of these is the fact that the

93. ninety-third of these is the fact that the

94. ninety-fourth of these is the fact that the

95. ninety-fifth of these is the fact that the

96. ninety-sixth of these is the fact that the

97. ninety-seventh of these is the fact that the

98. ninety-eighth of these is the fact that the

99. ninety-ninth of these is the fact that the

100. hundred of these is the fact that the

Torsional Strength and Stiffness Tests of Wing Leading Edges

REPORT S. 421.

by

J. F. BESSSELING and W. K. G. FLOOR.

Summary.

Purpose of the investigation.

Leading edges of aeroplane wings loaded in torsion fail when the buckles that have developed in the less curved portions of the skin extend in the strongly curved nose region.

The development of buckles in the skin is accompanied by a marked decrease of the torsional stiffness of the structure.

Relevant quantitative data about the post-buckling stiffness of wing leading edges without spanwise stiffeners loaded in torsion and about the ultimate shear stresses carried by the skin in such structures were not available.

Torsion tests on wing structures of this type were carried out in order to obtain the desired information about strength and stiffness.

After the experiments had been completed, publications by other investigators dealing with the same problems became available.

In so far as they are comparable with the tests described in this report, they supplement each other.

Scope of the investigation.

The forms of the cross sections of the test specimens were similar to the nose portions of the N.A.C.A. 0009, full airfoil chord was 1250 mm and the rib spacing was 250 mm for all specimens.

For each of these nine combinations four test specimens having skin thicknesses of 0.6, 0.8, 1.0 or 1.2 mm have been tested. The thickness of the full ribs was the same for all specimens with equal skin thickness.

The closing webs and ribs were designed such that they should not fail at a lower torque than the skin nor promote failure of the structure in any way.

Results.

The torsion of the test specimen was measured at increasing and at decreasing load in several loading cycles with successively increasing maximum load. In the last cycle the ultimate load sustained by the structure was determined.

Details of the buckles occurring in the skin, especially in the nose region, were photographed at several stages of development.

The prebuckling torsional stiffness proved to be in good accordance with the Batho—Bredt formula for thin-walled tubes loaded in torsion.

An empirical formula was derived for the calculation of the ultimate shear stress in the skin of wing leading edges manufactured from 24 ST Alclad. The main parameters governing the ultimate stress are the nose radius to rib spacing ratio and the skin thickness to nose radius ratio.

The influence of the closing web position is rather small.

Contents.

1	Introduction.
2	Specimens.
2.1	Structure and dimensions.
2.2	Material properties.
3	Description of testing apparatus.
3.1	Loading frame and load measurements.
3.2	Twist measuring equipment.
4	Testprocedure.
5	Results and discussion.
5.1	Prebuckling stiffness.
5.2	Buckling stress.
5.3	Postbuckling behaviour.
5.4	Types of failure and ultimate stresses.
6	Comparison of test results from the present (N.I.V.).

7	An empirical formula for the ultimate shear strength, covering the N.L.-specimens, and analysis of test results, leading to a design chart covering all data available.
8	Concluding remarks.
9	Notations.
10	References.
28	figures.
8	tables.

This investigation has been performed by order of the Netherlands Aircraft Development Board (N.I.V.).

1 Introduction.

This paper deals with the torsional strength of thin-walled D-tubes of 24 ST Alclad. D-tubes occur in aircraft structures at the leading edge of an airfoil and their torsional strength is an important property for the structural engineer. It can not be computed by theoretical means due to the complex nature of the occurring failures. The aircraft industry was strongly interested in obtaining experimental information about the problem and thus made the first proposals for the present investigation.

Both in the design of the test specimens and in the development of the methods of conducting

Apart from one example of a complete experimentally determined torque-twist diagram the latter information is not included in this paper.

After the set up of the test programme had been completed publications on two other investigations concerning the ultimate shear strength of D-tubes became available (ref. 1 and ref. 2). The tests of ref. 1 and ref. 2 partly refer to D-tubes stiffened in both chordwise and spanwise direction, partly to specimens comparable to the specimens tested at the NLL, although the range of parameters covered was not identical. Especially the specimens described in ref. 2 differ considerably from the NLL-specimens.

After a description of the specimens (sec. 2),

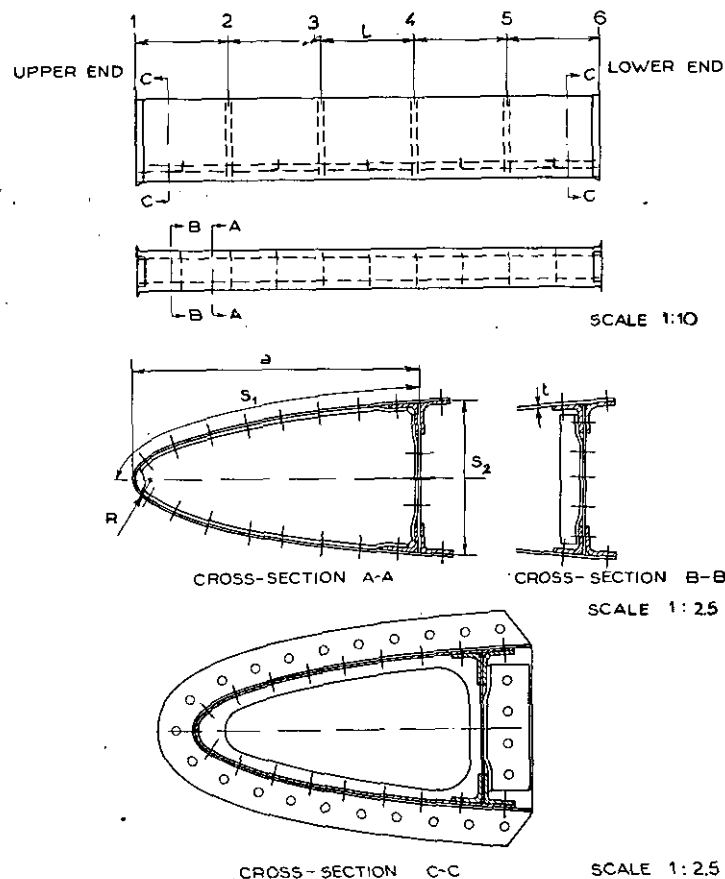


Fig. 2.1. General layout of specimens.
Dimensions vary with specimen: see table 2.1.

the tests and evaluating their results a close co-operation was maintained with the aircraft factory which manufactured the test specimens. In total 36 specimens were tested in pure torsion. The specimens had a cross-section similar to the nose portion of the NACA 0009, 0012 and 0015 airfoil sections with a closing web at 15, 20 and 25 percent of the chord. They were reinforced by equally spaced ribs, having a full web without lightening holes.

The tests were performed such as to yield information not only on the prebuckling stiffness, the buckling stress and the ultimate shear strength, but also with regard to the postbuckling stiffness and the development of permanent deformation.

the testing apparatus (sec. 3) and the test procedure (sec. 4), the test results of the present investigation are being discussed in sec. 5. As to the prebuckling stiffness substantial agreement was found with the Batho-Bredt formula. Though the buckling limit itself proved to be not well-defined, a semi-empirical formula is given for the stress at which the development of wrinkles may be expected to start.

In ref. 1 as well as in ref. 2 an empirical formula is given for the ultimate shear strength of D-tubes. In sec. 6 it is shown that neither of these covers the results of the present investigation.

In sec. 7 the ultimate shear strength is being considered as a function of the parameters of the

TABLE 2.1.

Nominal dimensions of specimens.

$$c = 1250 \text{ mm} \quad L = 250 \text{ mm} \quad R = 1.1 h^2/c$$

No.	A cm ²	t mm	t_w mm	h/c	a/c	$2 S_1$ mm	S_2 mm	Angle-section stiffeners of the spar	t_r mm
333	136.7	0.6	1.0	0.09	0.15	405	102	$20 \times 20 \times 1.5$	0.5
334		0.8	1.2			405	102		0.6
335		1.0	1.5			405	102		0.8
336		1.2	2.0			405	102		1.0
343	201.8	0.6	1.0	0.09	0.20	530	107	$20 \times 20 \times 2$	0.5
344		0.8	1.2			530	107		0.6
345		1.0	1.5			530	107		0.8
346		1.2	2.0			530	107		1.0
353	270.4	0.6	1.0	0.09	0.25	651	110	$25 \times 25 \times 2$	0.5
354		0.8	1.2			651	110		0.6
355		1.0	1.5			651	110		0.8
356		1.2	2.0			651	110		1.0
433	182.3	0.6	1.0	0.12	0.15	417	137	$20 \times 20 \times 1.5$	0.5
434		0.8	1.2			417	137		0.6
435		1.0	1.5			417	137		0.8
436		1.2	2.0			417	137		1.0
443	269.1	0.6	1.0	0.12	0.20	545	145	$20 \times 20 \times 2$	0.5
444		0.8	1.2			545	145		0.6
445		1.0	1.5			545	145		0.8
446		1.2	2.0			545	145		1.0
453	368.9	0.6	1.0	0.12	0.25	667	150	$25 \times 25 \times 2$	0.5
454		0.8	1.2			667	150		0.6
455		1.0	1.5			667	150		0.8
456		1.2	2.0			667	150		1.0
533	227.8	0.6	1.0	0.15	0.15	435	172	$20 \times 20 \times 1.5$	0.5
534		0.8	1.2			435	172		0.6
535		1.0	1.5			435	172		0.8
536		1.2	2.0			435	172		1.0
543	336.4	0.6	1.0	0.15	0.20	561	181	$20 \times 20 \times 2$	0.5
544		0.8	1.2			561	181		0.6
545		1.0	1.5			561	181		0.8
546		1.2	2.0			561	181		1.0
553	450.7	0.6	1.0	0.15	0.25	681	187	$25 \times 25 \times 2$	0.5
554		0.8	1.2			681	187		0.6
555		1.0	1.5			681	187		0.8
556		1.2	2.0			681	187		1.0

specimens. An empirical formula is obtained from the NLL-test results, giving the ultimate shear strength within the limits of the scatter of the experimental data. Analysis of the test results of ref. 1, ref. 2 and ref. 3 finally leads to a design-chart, covering all data available, its precision being less, however, than that of the formula for D-tubes, corresponding with the results observed in the NLL-specimens.

The conclusions to which the investigation has led are summarized in sec. 8.

2 Specimens.

2.1 Structure and dimensions.

The general layout of the specimens is shown in fig. 2.1. All specimens were of the same construction. The ribs were of rubberpressed sheet. The spar flanges were angle sections, bent from sheet material. Between two successive rib stations angle section stiffeners were riveted to the web to prevent buckling. The specimens were made according to normal aircraft manufacturing

standards. They were made to NACA-0009, 0012 and 0015 airfoil shapes and they had a closing web at the 15, 20 or 25 percent station. The inside skin line was the mold line.

As for the NACA airfoil sections the nose radius R is given by

$$R = 1.1 h^2/c,$$

a specimen (c.f. fig. 2.1) is fully determined, apart from the rib and the spar dimensions, by five of the six dimensions h , R , L , c , a and t , where h and c refer to the imaginary complete airfoil section of which the specimen forms the nose part. The chord c and the rib spacing L had the same value for all specimens ($c = 1250$ mm and $L = 250$ mm). By taking four values for the skin thickness t , three for the closing web position a and three for the height h (corresponding to the airfoil sections 0009, 0012 and 0015) 36 different combinations of these parameters and hence 36 specimens were obtained. The main dimensions of these specimens are listed in table 2.1. The rib

thickness, the web thickness and the size of the web stiffeners were increased and the rivetspacing was diminished as the skin thickness increased. The size of the spar flanges was varied with the web station, the size of the flanges increasing as a increased, in view of the Wagner loads (diagonal tension, field). At either end of a specimen an endfitting was riveted to the skin, the web and the sparflanges.

2.2 Material properties.

The material used for the skin, the ribs and the web was 24 ST Alclad. The grain of the skin and the web was in the direction of the longitudinal axis of the specimens.

After the specimens had been tested in torsion till failure occurred, tensile coupons were taken from the web and from the apparently undamaged parts of the skin. Table 2.2 gives the ultimate stresses for a typical group of tensile coupons. Also the results of two compression tests have been

TABLE 2.2.
Material properties.

Specimen	Part	Bay	Direction	Type	$\sigma_{0.2}$ kgmm ⁻² ¹⁾	σ_B kgmm ⁻² ²⁾	δ % ³⁾	E kgmm ⁻²
343	skin	I	longitudinal	tensile	35.6	44.3	—	7160
343	skin	V	transverse	tensile	32.4	43.4	14.0	6950
343	web	—	—	tensile	35.3	47.3	20.5	7050
344	web	—	—	tensile	35.3	47.2	19.0	6940
345	skin	III	longitudinal	tensile	33.8	45.2	17.5	6770
345	skin	V	transverse	tensile	29.8	43.4	14.3	6890
345	web	—	—	tensile	35.0	45.2	20.2	6880
454	skin	I	longitudinal	tensile	36.0	46.7	21.3	7010
454	skin	II	transverse	tensile	31.5	45.1	19.7	6750
456	skin	I	longitudinal	tensile	37.5	46.7	19.0	6700
456	skin	III	transverse	tensile	33.1	45.3	19.0	6890
456	web	—	—	tensile	35.2	43.8	17.2	6620
534	skin	I	longitudinal	tensile	—	46.3	19.0	6980
534	skin	III	transverse	tensile	29.8	44.9	20.0	6750
534	web	—	—	tensile	37.3	46.5	16.8	6830
543	skin	I	longitudinal	tensile	34.8	44.9	17.0	6880
543	skin	V	transverse	tensile	30.9	43.6	20.0	6780
543	skin	II	longitudinal	compressive	29.0	—	—	7300
543	skin	III	longitudinal	compressive	30.0	—	—	7250
543	web	—	—	tensile	34.2	43.3	16.7	6760
555	skin	I	transverse	tensile	29.2	44.0	17.8	6780
555	skin	III	longitudinal	tensile	32.2	40.5	15.0	6970
555	web	—	—	tensile	34.4	44.8	25.5	6880
556	skin	I	transverse	tensile	31.8	43.8	17.3	6780
556	skin	III	longitudinal	tensile	37.6	46.3	16.8	6730
556	web	—	—	tensile	35.7	43.8	16.2	6950

¹⁾ Normal stress producing 0.2 % permanent normal strain.

²⁾ Ultimate tensile stress.

³⁾ Permanent elongation after failure.

added. Some typical stress-strain curves, for the material of the web are plotted in fig. 2.2. Figs. 2.3 and 2.4 contain some stress-strain curves, determined on tensile coupons taken from the skin. The differences between the curves of coupons in chordwise and spanwise direction become more apparent as the skin thickness increases. This is due to the fact that the amount of plastic deformation of the material in the torsion test, before failure of the specimen occurs, increases with increasing skin thickness.

The portion of the skin volume in which plastic deformations occur before failure of the specimen becomes larger when the skin thickness increases, because buckling becomes less severe. Hence the relative magnitude of the bending strains and thus the ratio between the largest and the average strains, decreases.

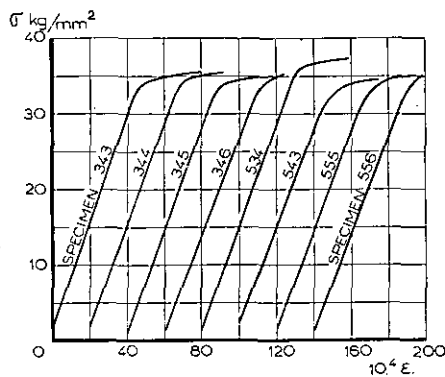


Fig. 2.2. Some typical tensile stress-strain curves for the web material.

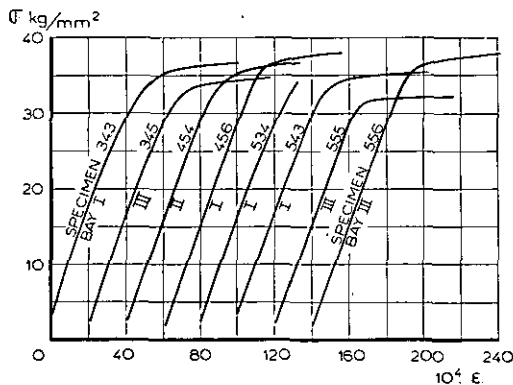


Fig. 2.3. Some typical longitudinal tensile stress-strain curves for the skin material.

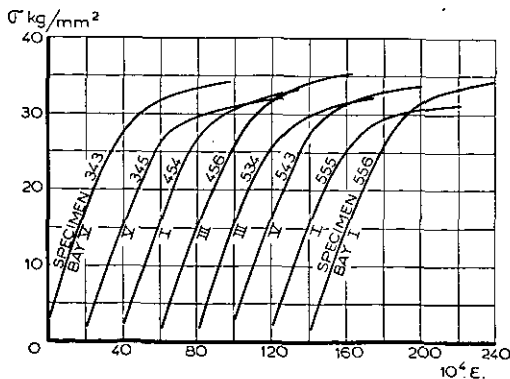


Fig. 2.4. Some typical transverse tensile stress-strain curves for the skin material.

The average modulus of elasticity was found to be

$$E = 6870 \text{ kg/mm}^2,$$

the scatter in the tension tests being $\pm 2.5\%$. The shear modulus G is given by

$$G = \frac{E}{2(1 + \nu)}.$$

With $\nu = 0.32$ it follows that

$$G = 2600 \text{ kg/mm}^2.$$

3 Description of testing apparatus.

3.1 Loading frame and load measurements.

The apparatus used to load the specimen in torsion is shown in fig. 3.1. The specimen is tested in a vertical position. The upper end of the loading jig consists of a 1 cm steel mounting plate, welded to a rigid frame work of steel channels. The flanges of the upper end fittings of the specimen are attached to this plate by bolts with 25 mm pitch. The lower end fittings are bolted, likewise with 25 mm pitch, to a 1 cm dural plate, carrying the two parts of the loading arm. The torque is applied by two opposite cable forces, working on the loading arm on either side of the specimen. By means of an adjustable cable guide the effective nominal arm length can be made 1.0 m, 1.2 m or 1.4 m. The cable forces are applied by tightening the turnbuckles, included in the cable loop. The load is measured by means of two strain gauge dynamometers, placed in the cable loop near the attachments to the loading arm. Fig. 3.2

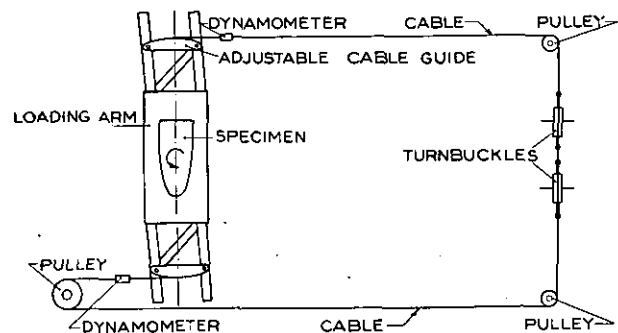


Fig. 3.2. Loading system.

gives a picture of this loading system. The pulleys are mounted on ball-bearings in order to obtain a practically pure torsion load on the specimen, by eliminating friction effects, which tend to cause unequal cable forces on either side of the specimen. Three types of dynamometers in conjunction with a Baldwin type K strain indicator have been used while carrying out the test-programme, the accuracy of their indications being 0.75 kg, 1.7 kg and 7.5 kg respectively. Table 3.1 gives the possible errors in the torque measurements.

TABLE 3.1.

Possible errors in the torque measurements.

No.	Precision of dynamometer, kg	Nominal arm length m	Possible error in the torque, kgm.
333	0.75	1.00	0.75
334	0.75	1.00	0.75
335	1.7	1.00	1.7
336	1.7	1.00	1.7
343	1.7	1.00	1.7
344	1.7	1.00	1.7
345	1.7	1.00	1.7
346	1.7	1.00	1.7
353	1.7	1.00	1.7
354	1.7	1.00	1.7
355	1.7	1.00	1.7
356	1.7	1.00	1.7
433	0.75	1.00	0.75
434	0.75	1.00	0.75
435	0.75	1.00	0.75
436	1.7	1.00	1.7
443	0.75	1.00	0.75
444	0.75	1.00	0.75
445	1.7	1.00	1.7
446	1.7	1.00	1.7
453	1.7	1.00	1.7
454	1.7	1.00	1.7
455	1.7	1.00	1.7
456	1.7	1.00	1.7
533	1.7	1.00	1.7
534	1.7	1.00	1.7
535	1.7	1.00	1.7
536	1.7	1.00	1.7
543	0.75	1.00	0.75
544	0.75	1.00	0.75
545	0.75	1.40	1.05
546	7.5	1.40	1.05
553	0.75	1.00	0.75
554	0.75; 7.5	1.20	0.90; 9.0
555	0.75; 7.5	1.40	1.05; 10.5
556	0.75; 7.5	1.40	1.05; 10.5

3.2 Twist measuring equipment.

At the stations 3, 4 and 6 (fig. 2.1) the twist of the specimen with respect to its upper end, was measured by means of two dial gauges at each station. Fig. 3.1 gives a general view of the measuring equipment.

At station 4 and at station 3 a measuring frame is attached to the specimen. The frames are supported in three points, one at the nose and two in the web. The nose support consists of a small piece of wood, fastened to the frame and fitting to the nose of the specimen. Pop rivets in the web

furnish seats for two pins attached to the frame. The pins are spring-loaded in order to provide the clamping pressure of the nose support.

At stations 4 and 6 the dial gauges are mounted on a vertical column, attached to the upper part of the loading jig. The lower dial gauges bear against fittings, bolted to the loading arm. At station 4 they bear against fittings, welded to the measuring frame at that station. The dial gauges at station 3 are attached to elevations of the measuring-frame at station 4 and they bear against fittings of the frame at station 3.

By this measuring equipment the twist was determined over the full length of the specimen, over $\frac{3}{4}$ of the length and over the part of the specimen between the ribstations 3 and 4. The latter readings should be useful to investigate if any end effects are present.

The dial gauges used were accurate to the nearest 0.01 mm. The readings at station 3 correspond with a twisting arm of 0.5 m nominal length and at stations 4 and 6 with an arm of 0.7 m nominal length.

4 Testprocedure.

After the specimen was bolted into place the reference zeros for the measuring instruments were determined. While applying the load, the full-length twist readings and the indications of the dynamometers were closely followed by making a graphical plot of the results during the test and by comparing the cable forces on either side of the specimen. If these forces showed differences of some importance or if some anomaly was found in the diagram, the testing apparatus was immediately subjected to a close inspection in order to trace the cause of the departure. This procedure proved to be advantageous in some cases, where a correction could be made in time.

The appearance of wrinkles was often accompanied by a bang. The load at which the first wrinkle was observed was recorded.

The load increment chosen depended upon the magnitude of the anticipated failing load. Usually three loading cycles were performed before failure occurred in order to investigate the development of permanent twist and permanent wrinkles. The first loading cycle was chosen such, that the permanent twist could be expected to be less than 5 % of the total twist reached in that cycle. Fig. 4.1 gives an example of a complete torque-twist diagram.

Photographs were made of the wrinkles in the specimens at different stages of loading; only a few of these have been included in this report.

At loads near the failing load the load indications were observed closely and the type of failure was recorded photographically.

5 Results and discussion.

5.1 Prebuckling stiffness.

In order to compare the Batho-Bredt theory as presented in ref. 4 with the experimental twist data, calculations were made, using the basic equation

$$\theta = T \oint \frac{ds}{t} / 4 A^2 G, \quad (5.1)$$

where s is a coordinate measured along the median line of the skin in the cross section of the tube

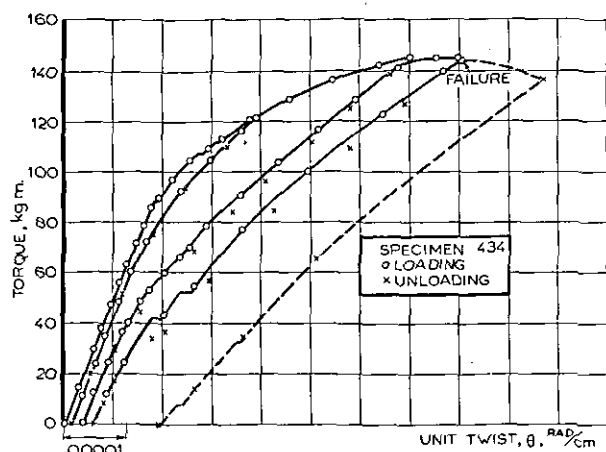


Fig. 4.1. Complete torque-twist diagram.

(fig. 5.1); the shear modulus G had the value given in sec. 2.2. The stiffness properties of a specimen were simulated by considering a simplified cross-section as shown in fig. 5.1. The rigi-

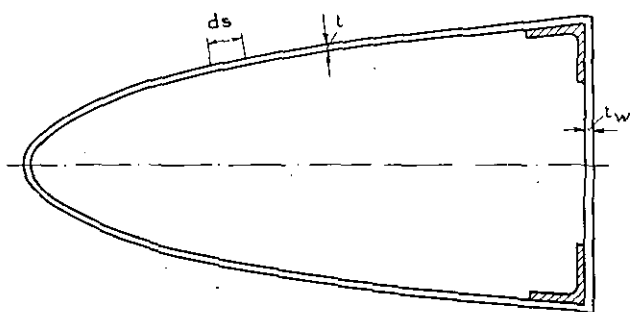


Fig. 5.1. Simplified cross-section of specimen.

a/c	0.15	0.20	0.25	0.25	0.20	0.25	0.15	0.20	0.25
h/c	0.09	0.09	0.09	0.12	0.12	0.12	0.15	0.15	0.15
No.	333	343	353	434	443	453	533	543	553
T/θ	27.6	46.4	69.4	45.5	74.4	121.8	65.5	113.9	172.8
theor.									
T_{cr}	25.6	30.5	34.4	41.8	49.7	54.9	57.1	68.2	77.3
(5.4)									

theoretical stiffness

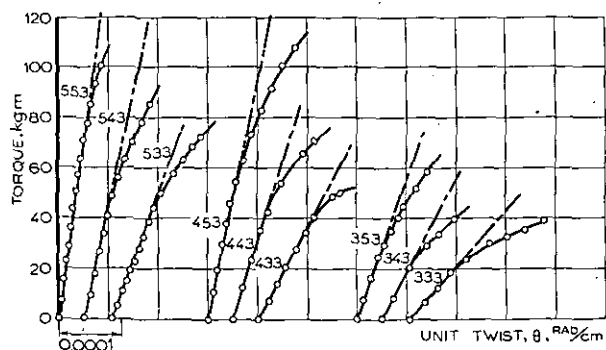


Fig. 5.2. Theoretical and experimental prebuckling stiffness, $t = 0.6$ mm.

dity of the four angle-section stiffeners of the spar was taken into account by adding the flanges of two of them to the skin and the web. The difference between the values for the stiffness, calculated with and without this contribution of the spar flanges, varied between $9\frac{1}{2}$ and 2 percent.

The measured and calculated values of unit twist have been plotted versus the torque in figs. 5.2, 5.3, 5.4 and 5.5. Substantial agreement is found between theory and experiment.

In plotting the diagrams of the figures mentioned above the full-length twist data have been used. The other twist readings were found to be less accurate for small torques. This is probably due to the not perfectly rigid attachment of the measuring frames to the specimen at stations 3 and 4. As no evident end effects proved to be present

a/c	0.15	0.20	0.25	0.15	0.20	0.25	0.15	0.20	0.25
h/c	0.09	0.09	0.09	0.12	0.12	0.12	0.15	0.15	0.15
No.	334	344	354	434	444	454	534	544	554
T/θ	36.0	60.9	91.2	59.3	101.2	159.9	85.1	148.2	226.1
theor.									
T_{cr}	49.0	58.4	66.2	80.2	95.1	105.5	109.3	130.2	147.1
(5.4)									

theoretical stiffness

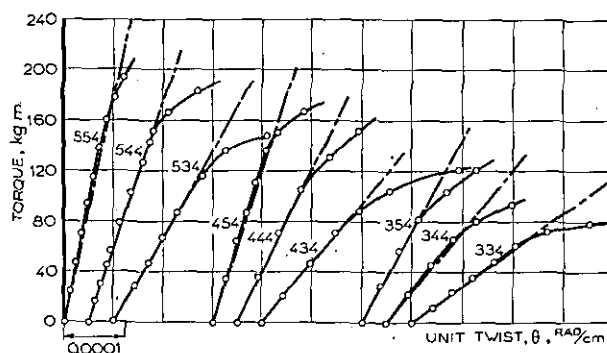


Fig. 5.3. Theoretical and experimental prebuckling stiffness, $t = 0.8$ mm.

a/c	0.15	0.20	0.25	0.15	0.20	0.25	0.15	0.20	0.25
h/c	0.09	0.09	0.09	0.12	0.12	0.12	0.15	0.15	0.15
No.	335	435	355	435	445	455	535	545	555
T/θ	44.5	75.7	112.9	73.3	125.4	197.7	105.2	108.2	279.8
theor.									
T_{cr}	80.9	96.5	109.2	132.3	157.1	174.1	180.4	214.6	243.4
(5.4)									

theoretical stiffness

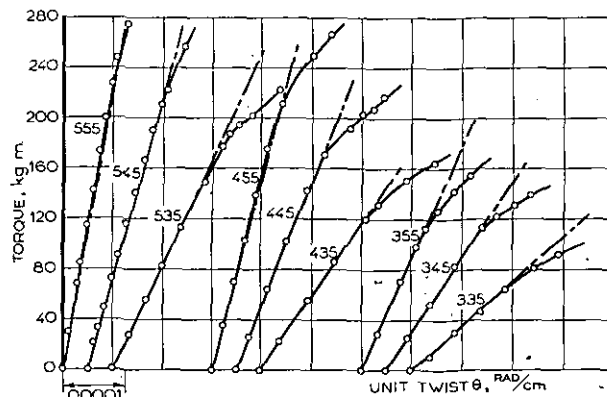


Fig. 5.4. Theoretical and experimental prebuckling stiffness, $t = 1.0$ mm.

a/c	0.15	0.20	0.25	0.15	0.20	0.25	0.15	0.20	0.25
h/c	0.09	0.09	0.09	0.12	0.12	0.12	0.15	0.15	0.15
No.	336	346	356	436	446	456	536	546	556
T/δ	53.6	91.2	135.7	88.7	151.6	238.5	127.7	222.9	338.9
theor.									
T_{cr}									
form.	122.0	145.3	164.2	199.5	237.0	263.0	272.3	323.7	366.7
(6.4)									
———— theoretical stiffness									

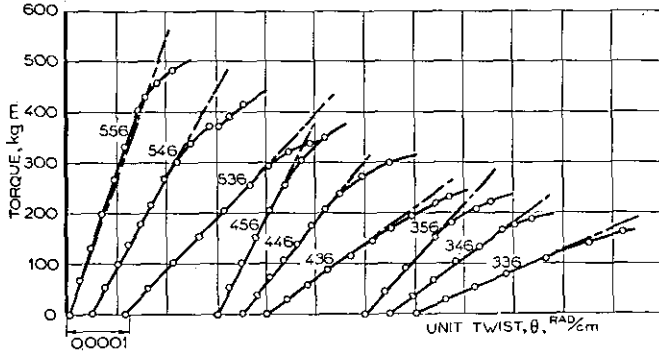


Fig. 5.5. Theoretical and experimental prebuckling stiffness, $t = 1.2$ mm.

the data obtained with these measuring frames did not require further consideration in this paper.

5.2 Buckling stress.

The buckling limit in the various tests was not well-defined. In most cases the specimens showed a continuous transition from the unbuckled to the buckled state. For several specimens there was an appreciable scatter in the loads at which the various skin panels of one specimen buckled, thus showing the large influence of small initial waviness of the skin due to imperfect fabrication.

The shearing stress in a skin panel at a given torque follows from the equation.

$$\tau = T/2 At. \quad (5.2)$$

The recordings concerning the appearance of the first wrinkles, in combination with the observed points of departure from the linear parts of the curves in the diagrams of figs 5.2, 5.3, 5.4 and 5.5, lead to a semi-empirical formula for the stress at which the development of wrinkles may be expected to start. In deriving this formula the theory of ref. 5, concerning the stability of thin-walled tubes under torsion, is taken as a starting point. Ref. 5 gives for the buckling stress of medium length circular tubes the theoretical formula

$$\tau_{cr} = A \frac{E}{1-\nu^2} (t/L)^2 (\sqrt{1-\nu^2} L^2/t\delta)^{3/4}, \quad (5.3)$$

where d represents the diameter of the tube and where

$A = 1.18$ for hinged edges;

$A = 1.29$ for clamped edges.

This formula for circular tubes has been proved to give fair agreement with experimental data. Improved formulae of a similar character are proposed in ref. 6.

The influence of the curvature of the skin panel

of a D-tube will largely depend on the parameters a/c and h/c . In the experimental investigation of ref. 1 it was already found, that a rough estimation of the critical stress for D-tubes, shaped conform to an NACA-0012 airfoil section and with $a/c = 0.30$, can be made by substituting $2a$ instead of d into (5.3). The present investigation, dealing with NACA-0009, — 0012 and — 0015 airfoil shapes and with closing-web positions $a/c = 0.15, 0.20$ and 0.25 , leads to the same result. No apparent interference was found between the value of a/c and the influence of the parameter h/c . Thus the buckling stress for D-tubes could be expressed by

$$\tau_{cr} = B \frac{E}{1-\nu^2} (t/L)^2 (L^2/ta)^{0.75}, \quad (5.4)$$

where

$$B = 0.31 \text{ for } h/c = 0.09;$$

$$B = 0.38 \text{ for } h/c = 0.12;$$

$$B = 0.415 \text{ for } h/c = 0.15.$$

An interpolation graph for B is being proposed in fig. 5.6.

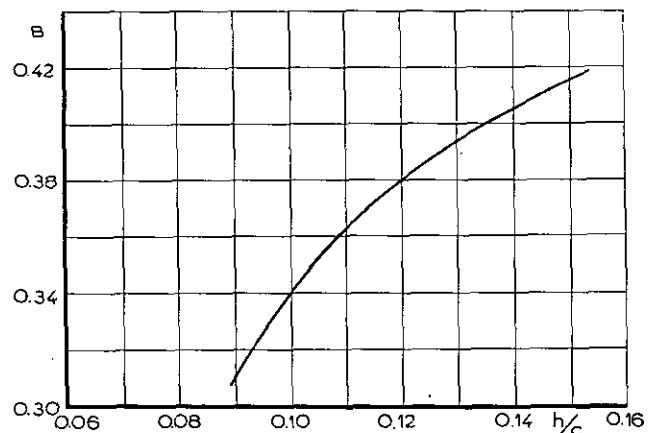


Fig. 5.6. Interpolation graph for the factor B , occurring in the formula (5.4) for the buckling stress.

The torques corresponding with the shearing-stresses calculated from (5.4) are given on figs. 5.2, 5.3, 5.4 and 5.5. It is seen that the buckling limits, estimated from the change in slope of the unit-twist curves, and the calculated buckling torques may differ considerably. For the greater part of the specimens the difference is less than 10 %, however.

It should be mentioned here, that the specimens, for which formula (5.4) has been derived, all had the same value of L/c . As interaction may exist between the parameters L/c and h/c , formula (5.4) should be used with caution for values of L/c other than $L/c = 0.2$.

5.3 Postbuckling behaviour.

Generally, the specimens were subjected to three loading cycles (sec. 4) before failure occurred. Fig. 4.1 gives an example of a complete torque-twist diagram, derived from the full-length twist data of specimen no. 434. Such diagrams are avail-

able for all three twist gauge lengths. Together with the observations and the photographic recordings of the development of wrinkles they may form the basis for a study concerning the postbuckling stiff-

ness and the growth of permanent twist. This falls beyond the scope of this paper, however, which is primarily concerned with the ultimate torsional strength of D-tubes.

TABLE 5.1.

Failure data.

No.	Type of failure	Remarks	Ultimate stress τ_u , kg/mm ²
333	A.1.b		3.27
334	A.1.b		4.02
335	A.1.b		5.16
336	A.1.b		5.91
343	A.2.b	damaged rib	2.88
344	A.1.b		4.43
345	A.1.b		4.78
346	A.1.b		5.50
353	A.2.b	damaged rib	2.67
354	B.2.a ₂	damaged rib	4.21
355	B.1.a ₂	damaged rib	4.57
356	B.1.a ₂		5.44
433	A.1.b		3.83
434	A.1.b		4.98
435	A.1.b		5.73
436	A.1.b		6.29
443	A.2.a ₂		3.28
444	B.2.a ₂		4.38
445	B.1.a ₁	failure in end panel	5.83
446	A.1.a ₁		6.58
453	B.2.a ₂		3.59
454	B.2.a ₂		4.32
455	B.2.a ₂		4.99
456	A.2.a ₁	damaged rib	6.24
533	B.2.a ₂		3.51
534	B.1.a ₂		5.50
535	B.1.a ₁		6.07
536	A.1.a ₁	failure in end panel	6.86
543	A.2.a ₂		3.09
544	A.2.a ₂		4.44
545	A.2.a ₂	{ failure in end panel; damaged rib	5.23
546	A.1.a ₁		6.47
553	B.2.a ₂		3.30
554	B.2.a ₁		4.31
555	B.2.a ₁		5.21
556	B.2.a ₁	failure in end panel	6.52

- A. Collapse after the torque had reached a maximum.
 B. Collapse before the torque had reached a maximum.
 1. Collapse with one wrinkle in a skin panel.
 2. Collapse with two wrinkles in a skin panel.
 a. First type of failure.
 a₁ Buckle crossing over the nose.
 a₂ Buckle rapidly extending into the nose.
 b. Second type of failure; bending failure of the nose.

5.4 Types of failure and ultimate stresses.

In all cases failure of a specimen was due to collapse of the strongly curved nose portion. During the tests two types of failure were observed. The typical failure for low a/c and large h/c values was characterized by a buckle crossing over or rapidly extending into the nose, usually accompanied by a sudden decrease of the load. With the second type of failure the wrinkles gradually deepened, finally leading to a kind of collapse in which the nose bent suddenly in the form of an S-curve in the plane normal to the chord after the torque had reached a maximum.

Failure occurred with one or with two wrinkles in a skin panel. The initial wrinkle started near the beam. 17 of the 36 specimens failed after a second wrinkle had appeared below the initial wrinkle. Usually failure occurred shortly after the development of this second wrinkle, as it rapidly extended into the nose in most cases.

The points of failure of the various specimens were well spread over the five skin panels of a specimen. Only four specimens failed in an end panel. It may be concluded therefore that nearly no end effect was present.

Some typical examples of failure are given in figs. 5.7, 5.8, 5.9 and 5.10. The ultimate stresses and other information concerning the failure of the specimens are supplied in table 5.1.

In some cases visible damage was done to a rib. The kind of damage was always the same: Fig. 5.11 represents a severe case. The picture shows that the ribs may be loaded perpendicular to the chordwise direction by forces from the skin in the buckled state. It is found in tables 5.1 and 2.1 that, for low values of h/a in particular, the ribs are heavily loaded when the specimen is near failure.

6 Comparison of test results from the present investigation with empirical formulae for the ultimate stress, derived in earlier investigations.

According to ref. 1 the average ultimate strength in torsion for stiffened or unstiffened D-tubes, having a cross section similar to the NACA 0012 airfoil section and a closing web at 30 percent of the chord, can be calculated from the formula:

$$(1 - \mu^2) \frac{\tau_u L^2 S_1^2}{Et^{1.75}} = 3.24 \left(\sqrt{1 - \mu^2} \frac{L^2 S_1^2}{2at} \right)^{0.74} \quad (6.1)$$

The left and right hand sides have the dimensions of the 2.25th and the 1.48th power of a length respectively.

It is thus evident that this formula can hold only for D-tubes of approximately equal size as the specimens of ref. 1. In all other cases (6.1) must lead to erroneous results.

Taking (6.1) as a starting point a dimensionless formula was obtained by putting

$$(1 - \mu^2) \frac{\tau_u L^2 S_1^2}{E t^{1.75}} = c \left(V \sqrt{1 - \mu^2} \frac{L^2 S_1^2}{2 a t} a^\eta \right)^\delta, \quad (6.2)$$

where $\eta = 2.25/\delta - 2$. The power δ has been de-

termined such as to yield the best correlation with the test data from the present investigation and the data for unstiffened D-tubes from ref. 1. The analysis resulted into the following expression for the average ultimate shear strength ($\delta = 0.68$):

$$\tau_u = 0.288 E (t/L)^{0.64} (a/S_1)^{0.21} (t/S_1)^{0.43}. \quad (6.3)$$

TABLE 6.1.

Comparison between experimental values of the ultimate stress and the results of the modified NACA-formula (6.3).

	No.	t/L	a/S_1	t/S_1	τ_u kg/mm ² formula	τ_u kg/mm ² test	percent difference
NLL	333	0.0024	0.925	0.00297	3.37	3.27	— 3
	334	0.0032	0.925	0.00396	4.59	4.02	— 12.5
	335	0.0040	0.925	0.00492	5.79	5.16	— 11
	336	0.0048	0.925	0.00591	7.05	5.91	— 16
	343	0.0024	0.943	0.00226	3.00	2.88	— 4
	344	0.0032	0.943	0.00302	4.09	4.43	+ 8
	345	0.0040	0.943	0.00377	5.19	4.78	— 8
	346	0.0048	0.943	0.00453	6.31	5.50	— 13
	353	0.0024	0.960	0.00185	2.76	2.67	— 3
	354	0.0032	0.960	0.00246	3.76	4.21	+ 12
	355	0.0040	0.960	0.00306	4.76	4.57	— 4
	356	0.0048	0.960	0.00368	5.79	5.44	— 6
	433	0.0024	0.900	0.00288	3.29	3.83	+ 16
	434	0.0032	0.900	0.00385	4.50	4.98	+ 10.5
	435	0.0040	0.900	0.00478	5.68	5.73	+ 1
	436	0.0048	0.900	0.00575	6.93	6.29	— 9
	443	0.0024	0.917	0.00220	2.95	3.28	+ 11
	444	0.0032	0.917	0.00299	4.05	4.38	+ 8
	445	0.0040	0.917	0.00366	5.09	5.83	+ 14
	446	0.0048	0.917	0.00440	6.19	6.58	+ 6
	453	0.0024	0.936	0.00180	2.72	3.59	+ 32
	454	0.0032	0.936	0.00240	3.70	4.32	+ 16.5
	455	0.0040	0.936	0.00299	4.69	4.99	+ 6
	456	0.0048	0.936	0.00359	5.69	6.24	+ 9.5
	533	0.0024	0.862	0.00276	3.22	3.51	+ 9
	534	0.0032	0.862	0.00369	4.38	5.50	+ 25.5
	535	0.0040	0.862	0.00461	5.55	6.07	+ 9.5
	536	0.0048	0.862	0.00550	6.71	6.86	+ 2
	543	0.0024	0.891	0.00214	2.90	3.09	+ 6.5
	544	0.0032	0.891	0.00286	3.95	4.44	+ 12
	545	0.0040	0.891	0.00356	5.00	5.23	+ 4.5
	546	0.0048	0.891	0.00427	6.07	6.47	+ 6.5
	553	0.0024	0.914	0.00176	2.68	3.30	+ 23
	554	0.0032	0.914	0.00235	3.65	4.31	+ 18
	555	0.0040	0.914	0.00293	4.63	5.21	+ 12.5
	556	0.0048	0.914	0.00352	5.62	6.52	+ 16
ref. 3	0006	0.00718	0.944	0.00372	7.85	6.91	— 12
	0009	0.00718	0.929	0.00366	7.75	7.10	— 8.5
	0015	0.00718	0.892	0.00351	7.55	7.54	0
	16.012	0.00718	0.969	0.00229	6.34	6.45	+ 2

TABLE 6.1 (continued).

	No.	t/L	a/S_1	t/S_1	τ_u kg/mm ² formula	τ_u kg/mm ² test	percent difference
ref. 1	1	0.000646	0.914	0.00157	1.15	0.98	— 15
	2	0.00102	0.914	0.002485	1.88	1.50	— 20
	3	0.00148	0.905	0.00357	2.78	2.54	— 8.5
	4	0.00121	0.914	0.00197	1.67	1.905	+ 14
	5	0.00204	0.914	0.002485	2.92	2.96	+ 1
	6	0.00296	0.905	0.00357	4.33	3.625	— 16.5
	7	0.001815	0.914	0.00147	2.16	2.54	+ 7.5
	8	0.003065	0.914	0.002485	3.79	3.455	— 9
	9	0.00444	0.905	0.00357	5.61	5.65	+ 1
	10	0.00387	0.914	0.00157	3.61	3.98	+ 10
	11	0.00613	0.914	0.002485	5.90	5.82	— 1.5
	12	0.00888	0.905	0.00357	8.73	8.65	— 1

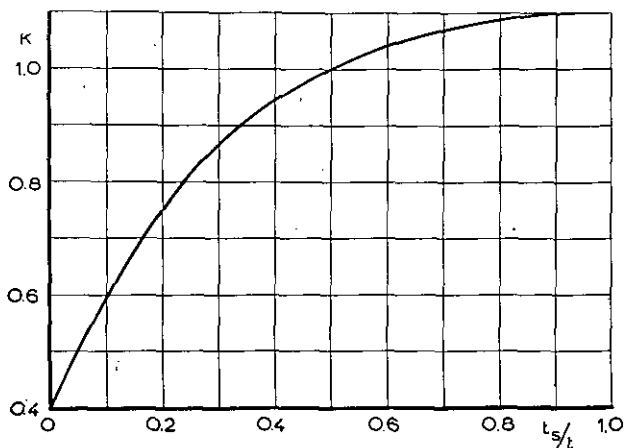


Fig. 6.1. Factor in formula (6.4) for stiffening effect of chordwise stiffeners, according to ref. 2.

In table 6.1 the calculated and experimental ultimate stresses are listed for the NACA- and the NLL-specimens. Also four unstiffened specimens from ref. 3¹⁾ have been included. It is seen that the correlation is rather good, though a systematic variation of the error with the value of h/c and with the skin thickness may be observed.

The test results of ref. 2 can not be compared with formula (6.3), as the dimensions of the specimens are given incompletely in ref. 2 (S_1 nor a is mentioned).

The formula for the ultimate shear strength of unstiffened D-tubes, proposed in ref. 2, reads

$$\tau_u = k (R/L)^{0.37} \cdot \tau_2, \quad (6.4)$$

where k depends on the rib dimensions and where τ_2 is a function of R/t . Graphs for k and τ_2 , taken from ref. 2, are included in this paper as figs. 6.1 and 6.2. The rib dimension parameter t_s follows from

$$t_s = A_r/L, \quad (6.5)$$

¹⁾ Ref. 3 is a continuation of ref. 1. The test results given in ref. 3 have not been published by the NACA.

where A_r represents the cross-sectional area of one typical chordwise stiffener or effective ribflange (for rubber pressed ribs a width of about $15 t_r$ of the rib web has to be added to the ribflange to give A_r , according to ref. 2).

Calculation of the ultimate stress with (6.4) for all specimens from ref. 1, ref. 2, ref. 3 and from the present investigation leads to results, listed in table 6.2. In many cases the correlation between calculated and experimental ultimate stress turns out to be rather poor. This could be expected, however, as the range of parameters for which formula (6.4) was derived lies outside the range of parameters covered by the other investigations. Extrapolation thus proves to give insufficient correlation.

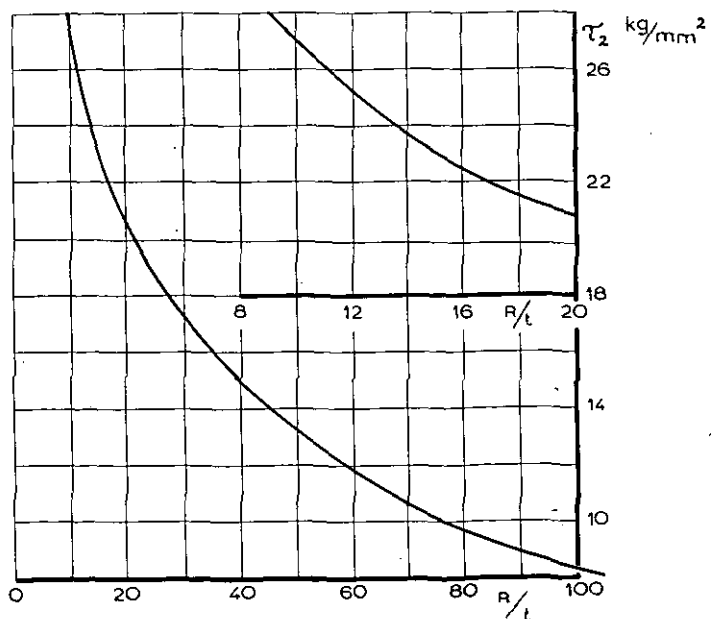


Fig. 6.2. Typical buckling stress in formula (6.4) for wing leading edges, according to ref. 2.

TABLE 6.2.

Comparison between experimental values of the ultimate stress and the results of the SAAB-formula (6.4).

	No.	R/t	$10^3 R/L$	t_s/t	τ_u kg/mm ² formula	τ_u kg/mm ² test	percent difference
NACA	333	18.57	44.56	0.0750	3.65	3.27	— 10½
	343					2.88	— 21
	353					2.67	— 27
	334					4.02	— 2
	344	13.93	44.56	0.0720	4.11	4.43	+ 8
	354					4.21	+ 2½
	335					5.16	+ 9½
	345					4.78	+ 1½
	355	11.14	44.56	0.0864	4.70	4.57	— 3
	336					5.91	+ 11½
	346					5.50	+ 4
	356					5.44	+ 3
	433	33.00	79.20	0.0750	3.52	3.83	+ 9
	443					3.28	— 7
	453					3.59	+ 2
	434					4.98	+ 24
	444	24.75	79.20	0.0720	4.01	4.38	+ 9
	454					4.32	+ 8
	435					5.73	+ 25
	445					5.83	+ 27
	455	19.80	79.20	0.0864	4.59	4.99	+ 9
	436					6.29	+ 20½
	446					6.58	+ 26
	456					6.24	+ 19½
	533	51.57	123.76	0.0750	3.32	3.51	+ 6
	543					3.09	— 7
	553					3.30	— ½
	534					5.50	+ 44
	544	38.68	123.76	0.0720	3.81	4.44	+ 16½
	554					4.31	+ 13
	535					6.02	+ 35
	545					5.23	+ 17
	555	30.94	123.76	0.0864	4.46	5.21	+ 16½
	536					6.86	+ 34
	546					6.47	+ 27
	556					6.52	+ 28
NACA	1	29.65	19.8	0.0224	1.79 ¹⁾	0.98	— 45
	2	18.65		0.0261	2.23	1.50	— 33
	3	13.20		0.0363	2.69	2.54	— 6
	4	29.65		0.0448	2.54	1.90	— 25
	5	18.65	39.6	0.0522	3.22	2.96	— 8
	6	13.20		0.0726	4.01	3.62	— 10
	7	29.65		0.0672	3.23	2.54	— 21½
	8	18.65		0.0784	4.15	3.45	— 17
	9	13.20	59.4	0.109	5.30	5.65	+ 6½
	10	29.65		0.134	5.20	3.98	— 23½
	11	18.65		0.157	6.73	5.82	— 13½
	12	13.20		0.218	8.73	8.65	— 1

TABLE 6.2 (continued).

	No.	R/t	$10^3 R/L$	t_s/t	τ_u kg/mm ² formula	τ_u kg/mm ² test	percent difference
Ref. 3	0006	4.66 ²⁾	33.46	0.2488 ¹⁾	6.54	6.90	+ 5½
	0009	10.48	75.35	0.2488	8.38	7.10	— 15
	0015	29.10	209.40	0.2488	7.94	7.54	— 5
	16.012	8.30 ²⁾	59.60	0.2488	8.08	6.44	— 20
SAAB	10	75.0	811	0.45	9.10	10.25	+ 12
	11	75.0	1072	0.59	10.73	11.00	+ 2
	12	69.0	580	0.70	9.40	9.76	+ 4
	13	69.0	580	0.70	9.40	10.10	+ 7
	14	22.0	171	0.50	10.10	9.57	— 5
	15	22.5	168	0.50	10.05	10.70	+ 6
	16	22.5	126	0.376	8.25	8.40	+ 2
	17	70.0	870	0.48	9.97	10.00	0
	18	56.8	584	0.567	10.30	9.70	— 6
	19	49.1	584	0.483	10.82	9.40	— 12
	20	49.2	320	0.922	9.60	8.93	— 7
	21	10.6	76	0.227	8.15	8.00	— 2
	22	10.6	76	0.272	8.66	9.00	+ 4
	25	100	345	0.175	4.00	3.78	— 6
	26	67	296	0.277	5.78	5.83	+ 1

¹⁾ The width of the ribflange has been estimated 1/4.

²⁾ For values of $R/t < 9.5$ τ_s has been taken 28 kg/mm² (fig. 6.2).

7 An empirical formula for the ultimate shear strength, covering the NLL-specimens, and analysis of test results, leading to a design chart covering all data available.

As mentioned in sec. 2.1 a specimen of the type considered is fully determined, apart from the ribs and the spar, by five of its dimensions, e.g. R , L , C , a and t . Then it is also determined by one of its dimensions and four properly chosen dimensionless parameters. As size effects may be neglected, the ultimate shear strength of D-tubes, with the same relative rib and spar dimensions as the NLL-specimens, must be a function of these dimensionless parameters. The parameters should be chosen such that the least interaction possible exists between the influences, which each of them has on the ultimate stress.

The parameter L/c was held constant in the test programme ($L/c = 0.2$). A suitable choice for the remaining parameters was found to be

$$R/L, a/c, R/t, \quad (7.1)$$

where R/t is primarily concerned with the buckling resistance of the nose (compare ref. 2). The ultimate stresses of table 5.1 could be covered by the formula

$$\tau_u = 0.137 \lambda E (R/L) (t/R)^{0.9} \quad (7.2)$$

where $\lambda = 1.10$ if $a/c = 0.15$;

$\lambda = 1.02$ if $a/c = 0.20$;

$\lambda = 1.00$ if $a/c = 0.25$.

An interpolation graph for λ is being proposed in

fig. 7.1. For convenience, $(t/R)^{0.9}$ is represented as a function of t/R in fig. 7.5.

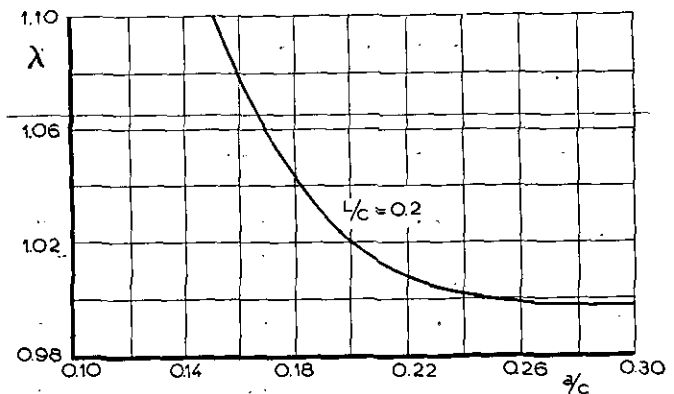


Fig. 7.1. Interpolation graph for the factor λ , occurring in formula (7.2), determining the influence of the closing web position on the ultimate stress.

Augmenting the value of a/c at a constant value of L/c will make it possible, that more than one wrinkle is originated in one skin panel. Failure of a specimen, caused by collapse of the strongly curved nose portion, will primarily be affected by wrinkles developing near the nose. It may be expected that the influence of a second wrinkle will be small because only one of the wrinkles extends into the nose region, the other being confined to the less curved portion of the skin adjacent to the closing web. The development of a third wrinkle will affect the ultimate stress even less. The graph

of fig. 7.1, intended for a value of $L/c = 0.2$, is drawn in accordance with this conception. Above $a/c = 0.25$, where all specimens but two did

show two wrinkles in one skin panel at failure (table 5.1), it gives only a very small variation of the ultimate strength with a/c .

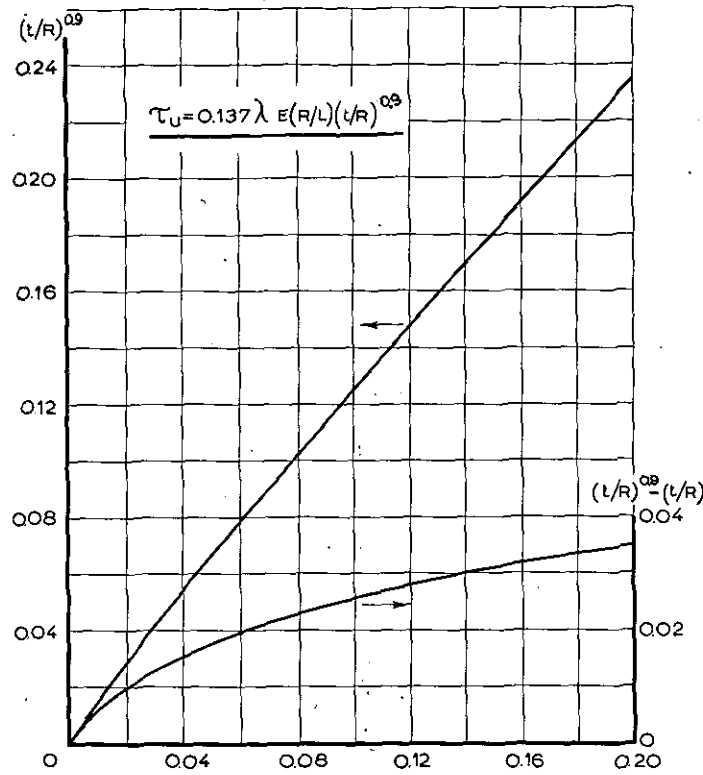


Fig. 7.5. Diagram for the determination of $(t/R)^{0.9}$.

TABLE 7.1.

Comparison between experimental values of the ultimate stress and the results of the NLL formula (7.2).

No.	τ_u kg/mm ² formula	τ_u kg/mm ² test	percent difference	No.	τ_u kg/mm ² formula	τ_u kg/mm ² test	percent difference
333	3.34	3.27	— 2	453	3.22	3.59	+ 11.5
334	4.32	4.02	— 7	454	4.17	4.32	+ 3.5
335	5.29	5.16	— 2.5	455	5.09	4.99	— 2
336	6.23	5.91	— 5	456	6.00	6.24	+ 4
343	3.10	2.88	— 7	533	3.68	3.51	— 4.5
344	4.00	4.43	+ 10.5	534	4.78	5.50	+ 15
345	4.90	4.78	— 2.5	535	5.85	6.07	+ 3.5
346	5.77	5.50	— 4.5	536	6.90	6.86	— 0.5
353	3.04	2.67	— 12	543	3.42	3.09	— 10
354	3.92	4.21	+ 7	544	4.44	4.44	0
355	4.81	4.57	— 5	545	5.42	5.23	— 3.5
356	5.66	5.44	— 4	546	6.40	6.47	+ 1
433	3.54	3.83	+ 8	553	3.35	3.30	— 1.5
434	4.59	4.98	+ 8.5	554	4.35	4.31	— 1
435	5.60	5.73	+ 2	555	5.32	5.21	— 2
436	6.60	6.29	— 5	556	6.27	6.52	+ 4
443	3.29	3.28	— 0.5				
444	4.26	4.38	+ 3				
445	5.20	5.83	+ 12				
446	6.12	6.58	+ 7.5				

A comparison between experimental stresses and stresses calculated from formula (7.2), is given in table 7.1. No systematic errors are present anymore and the overall correlation is within the limits of the scatter to be expected in the experimental data.

Formula (7.2) with the given values for λ does not cover the experimental results of ref. 1 and ref. 3, as is being shown in figs. 7.2 and 7.3, where $\frac{\tau_u(R/t)^{0.9}}{E}$ has been plotted versus R/L . If again the ultimate stress is expressed by a formula

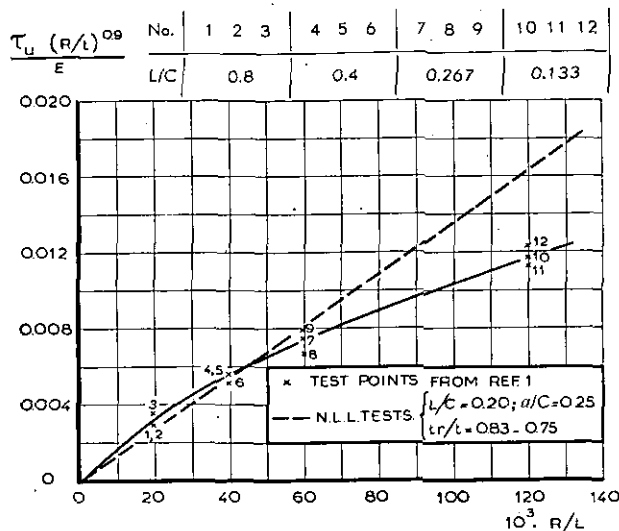


Fig. 7.2. Comparison between the NLL-test results and the data from ref. 1. ($a/c = 0.30$, $t_r/t = 0.89 - 0.78$).

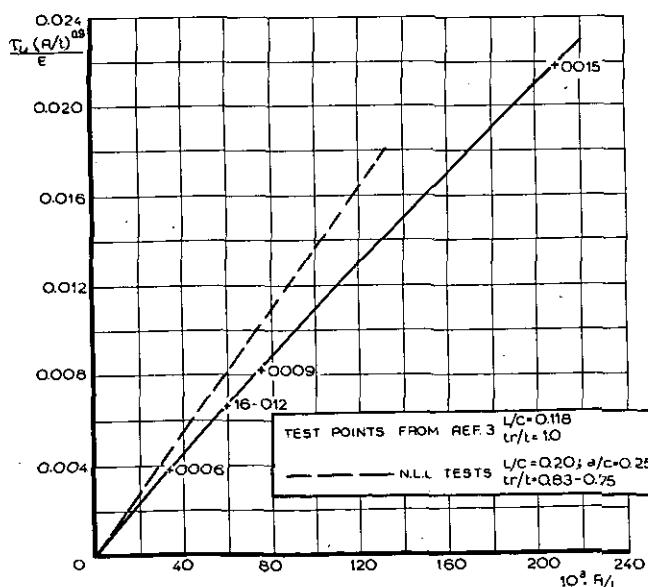


Fig. 7.3. Comparison between the NLL-test results and the data from ref. 1.

like (7.2), then it is clear from fig. 7.2 that λ is not a constant anymore for a given value of a/c . The values of the parameters R/L and R/t , used in ref. 1, ref. 3 and in the present investigation lie within the same range. In ref. 1 and ref. 3

$a/c = 0.30$, except for one specimen of ref. 3, where $a/c = 0.50$.

As was pointed out above for values of $a/c > 0.25$ only a very small variation of the ultimate stress with a/c may be expected, when the ratio L/c is held constant at $L/c = 0.2$. For values of $L/c > 0.2$ the influence of a/c may extend further than that, as the appearance of a second and a third wrinkle, due to augmenting the value of a/c , will be delayed by increasing the ratio L/c , while the buckling resistance of a skin panel is diminished. However, the deviations from formula (7.2) occur just for small values of L/c , so that the poor correlation between the results of ref. 1 and ref. 3 and the NLL formula (7.2), being illustrated in figs. 7.2 and 7.3, can hardly be explained by a possible influence of the parameter a/c .

In ref. 1 nor in ref. 3 a serious distortion of the sparflanges is reported. Therefore the divergence, found between the results of ref. 1 and ref. 3 and of the present investigation, must be mainly due to the fact, that the value of L/c was not held constant in the programme of ref. 1, while the ribs of the specimens of both ref. 1 and ref. 3 were weakened by lightening holes. From figs. 7.2 and 7.3 may be concluded, that the slope of $\frac{\tau_u(R/t)^{0.9}}{E}$ versus R/L is diminished by taking

lower values of L/c , this effect becoming more serious in general if a smaller relative rib thickness is chosen and if the ribs are weakened by lightening holes. This means that the weakening effect of taking lower values of R/c or h/c is not compensated by the relatively smaller rib distance, if at given values of R/L and R/t the value of L/c is diminished. Taking a smaller value of L/c at given values of R/c and R/t leads to a higher ultimate strength, the value of R/L being then increased simultaneously. However, the amount of the experimental data available does not allow the establishment of reliable design charts.

The analysis of the data of ref. 2 is seriously hampered by the fact, that the dimensions of the specimens are supplied incompletely. No information has been included on the values of c and a , while from the rib dimensions in most cases nothing is known except the values of t_s/t . A factor k , depending on the ratio t_s/t like in formula (6.4) of ref. 2, proves to be of no value for explaining the divergence between the test results of ref. 1, ref. 3 and the present investigation. A possible influence of the parameter t_s/t does not even show up. It is to be expected that both for full ribs and for ribs with lightening holes t_s/t will have a marked influence upon the ultimate stress only when it is very small, but that its influence will be practically negligible for most practical cases such as those covered by the present tests. The rather large variation of k with t_s/t in fig. 6.1 must be attributed to the fact that the test specimens from ref. 2 had only chordwise stiffeners instead of ribs.

Though the closing-web position of the specimens of ref. 2 is not known, it is expected to lie between 25 and 30 percent of the chord. So the data of ref. 2 have been put into one diagram (fig. 7.4)

with all data from ref. 1, ref. 3 and the present investigation, concerning closing-web positions between $a/c=0.25$ and $a/c=0.30$. Fig. 7.4 may be used as a design chart, giving the ultimate

SAAB specimens								
No.	10	11	12	13	14	15	16	17
R in cm	9.0	9.0	5.8	5.8	1.8	1.8	1.8	8.7
L in cm	11.1	8.4	10.0	10.0	10.5	10.7	14.3	10.0
t in mm	1.20	1.20	0.84	0.84	0.82	0.80	0.80	1.24
t_s/t	0.45	0.59	0.70	0.70	0.50	0.50	0.376	0.48
No.	18	19	20	21	22	25	26	
R in cm	5.9	5.9	3.2	1.9	1.9	5.0	4.0	
L in cm	10.1	10.1	10.0	25.0	25.0	14.5	13.5	
t in mm	1.04	1.20	0.65	1.80	1.80	0.5	0.6	
t_s/t	0.567	0.483	0.922	0.227	0.872	0.175	0.277	

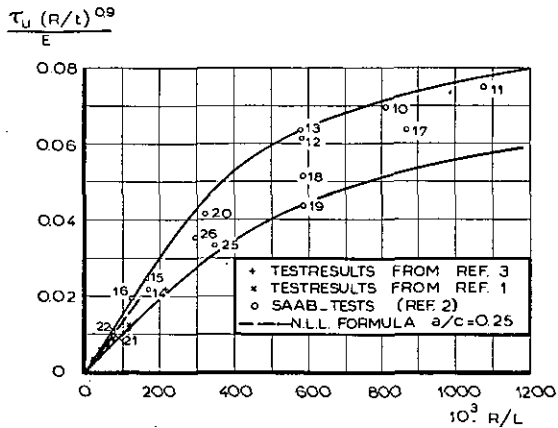


Fig. 7.4. Outline map of all data available on the ultimate shear strength of D-tubes, stiffened in chordwise direction only and having $0.25 < a/c < 0.30$.

shear strength of D-tubes, stiffened in chordwise direction only. By making a careful comparison between the dimensions of the specimens and the dimensions of an actual design it should be possible to estimate the ultimate stress with a greater amount of accuracy than would follow from the difference between the upper and lower boundaries for the ultimate stress, drawn in fig. 7.4. For values of $a/c < 0.25$ the ultimate stress, estimated from fig. 7.4, may possibly always be multiplied by the factor λ , given in fig. 7.1. Further it should be mentioned that the test points of ref. 2 refer to specimens with chordwise stiffeners in-

stead of ribs. For D-tubes with rubber pressed ribs, having a full web, the ultimate strength may be underestimated by using the diagram of fig. 7.4 in the range $10^3 R/L > 150$ approx.

8 Concluding remarks.

For the range of parameters covered by the 36 specimens, tested at the NLL (table 2.1), an empirical formula, (7.2), has been derived for the ultimate shear strength of D-tubes, stiffened in chordwise direction by ribs having a full web. The precision of the formula (7.2) is within the limits of the scatter, to be expected in the actual strength (table 7.1). Also a semi-empirical formula, (5.4), has been given, which yields an approximation to the buckling stress.

The experimental prebuckling stiffness has been compared with the stiffness after the Batho-Bredt theory for a single cell below the buckling limit. Substantial agreement was found between theory and experiment (sec. 5.1).

The tests have been performed such, that also valuable information was obtained concerning the postbuckling stiffness and the development of wrinkles and permanent distortion. These data, not yet included in this paper, may form the basis for a further study (sec. 5.3).

The results of the present investigation have been compared with the empirical formulae for the ultimate shear strength of D-tubes, given in ref. 1 and ref. 2 (sec. 6). The formula of ref. 1 is not dimensionless. Therefore it must lead to erroneous results for all specimens, which are not of equal size as the specimens of ref. 1. After being transposed into a non-dimensional form the formula of ref. 1, (6.3), yielded reasonable values for the ultimate stresses, though some systematic errors could be observed (table 6.1). The stresses according to the formula of ref. 2 in many cases differed considerably from the experimental values of the present investigation (table 6.2). This could be expected, the range of parameters of the NLL-specimens not being covered by the range for which the formula in ref. 2 was derived. However, in an analysis of all test results available this proved to be an insufficient explanation for the divergence.

TABLE 8.1.

Range of parameters, for which experimental data are available concerning the ultimate shear strength of D-tubes, chordwise reinforced by ribs.

	Ref. 1	Ref. 2	Ref. 3	NLL-tests
R/t	13.20—18.65	10.6—75	4.66—29.10	9.28—51.57
$10^3 R/L$	19.8—118.8	76—1072	33.46—209.40	44.56—123.76
L/c	0.8—0.133	?	0.118	0.2
a/c	0.30	?	0.30; 0.50	0.15; 0.20; 0.25
h/c	0.12	?	0.06—0.015	0.09; 0.12; 0.15
Type of ribs	Rubber pressed ribs with lightening holes	Stiffeners, bent from sheet metal	Rubber pressed ribs with lightening holes	Rubber pressed ribs with a full web
t_r/t	0.78—0.89	—	1.0	0.83—0.75
t_s/t	0.0224—0.218	0.175—0.922	0.2488	0.075—0.100

The main reason for the observed discrepancy is that test specimens with full ribs, such as in the present tests, or with ribs having lightening holes, such as in the tests from ref. 1 and 3 can not be compared, strictly speaking, with the specimens from ref. 2 which had only chordwise stiffeners instead of ribs. As a consequence, the influence of the rib dimensions included in the formula from ref. 2 does not apply to the specimens of refs. 1 and 3 and of the present investigation. In addition the influence of other parameters was neglected.

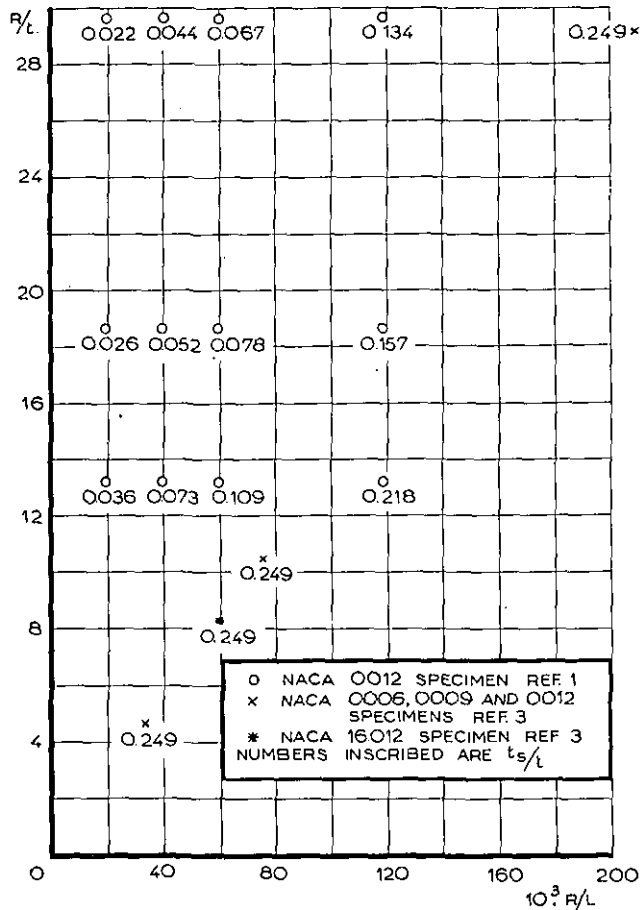


Fig. 8.1. Range of parameters covered by the tests from refs. 1 and 3.

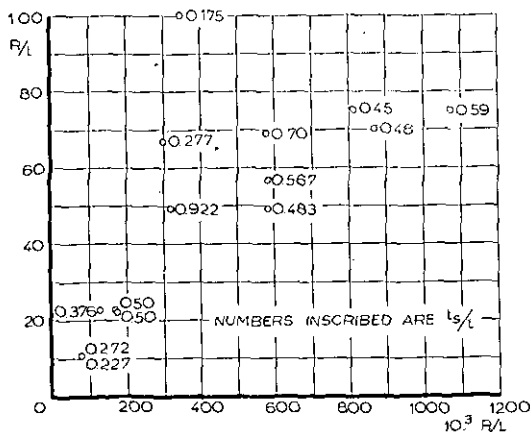
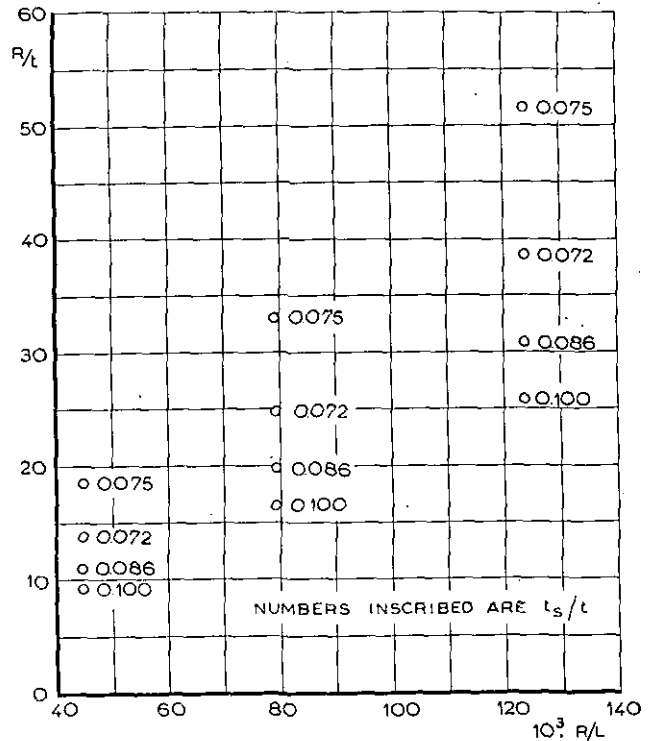


Fig. 8.2. Range of parameters covered by the tests from ref. 2.

An analysis of the data of ref. 2 was greatly hampered by the fact, that no information was supplied concerning the closing web position and the chord of the specimens.

All data available have been put into one diagram, fig. 7.4, which can be used as a design chart, determining the ultimate shear stress of D-tubes stiffened in chordwise direction only. It should be noted, however, that for D-tubes with normal ribs,



From 8.3. Range of parameters covered by the present tests.

the diagram may be conservative in the range $10^3 R/L > 150$ approx., where it is based on the data of ref. 2.

In case an actual design lies within the range of parameters, covered by the NACA-specimens, the use of formula (7.2) is recommended however. The data of ref. 1 and ref. 3, included in this paper, reveal the trend of the ultimate strength when changing the ribspacing or weakening the ribs (figs. 7.2, 7.3). For more detailed information on this matter some additional tests will be necessary.

The range of parameters, covered by the tests, described in ref. 1, ref. 2, ref. 3 and the present paper, is given in table 8.1. For the most important parameters the range covered in these tests is shown in a more convenient way in figs. 8.1 to 8.3 incl.

9 Notations.

- A Cross-sectional area of a specimen.
- A_r Cross-sectional area of one typical chordwise stiffener or effective ribflange (sec. 6).
- B Factor, occurring in the formula for the buckling stress.
- E Modulus of elasticity.
- G Modulus of rigidity.

- L Distance between ribs.
 R Minimum radius of the nose of a specimen.
 S_1 Actual length of a skin panel in chordwise direction (fig. 2.1).
 S_2 Height of the sparweb (fig. 2.1).
 T Applied torsional moment.
 a Distance from nose to web.
 c Chord of the airofoil section.
 d Diameter of a circular tube.
 h Height of the airofoil section.
 k Factor, occurring in the formula (6.4) of ref. 2 for the ultimate stress.
 t Thickness of skin.
 t_r Thickness of ribs.
 t_s Rib dimension parameter, used in ref. 2;
 $t_s = A_r/L$.
 t_w Thickness of web.
 λ Factor, occurring in the formula (7.2) of the present investigation for the ultimate stress.
 ν Poisson ratio..
 τ Shear stress in a skin panel.

- τ_2 Typical stress, occurring in the formula of ref. 2 for the ultimate stress.
 τ_u Ultimate shear stress.
 τ_{cr} Buckling shear stress.
 θ Unit twist, rad/cm.

10 References.

1. KAVANAUGH, E. S. and DRINKWATER, W. D. Torsional Strength of Stiffened D-Tubes, NACA-TN 2362, May 1951.
2. TURNER, F. An empirical formula for the ultimate shear strength of wing leading edges, SAAB-TN. 5, Sweden, December 1951.
3. KAVANAUGH, E. S. Torsional Strength of Stiffened D-Tubes, Part II, University of Notre Dame, Notre Dame, Ind., 1948.
4. TIMOSHENKO, S. Theory of Elasticity, Mc. Graw-Hill Book Co., Inc., 1934.
5. DONNELL, L. H. Stability of Thin-Walled Tubes under Torsion, NACA-TR 479, 1933.
6. PLANTEMA, F. J. Collapsing Stresses of Circular Cylinders and Round Tubes. Report S.280, Nationaal Luchtvaartlaboratorium, Amsterdam, 1946.

Completed June 1953.

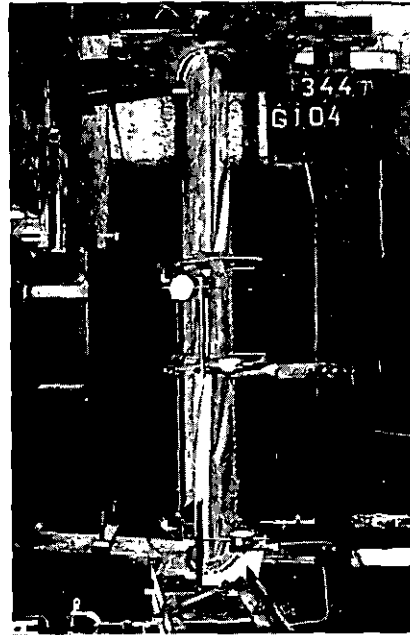


Fig. 3.1. General view of testing apparatus.

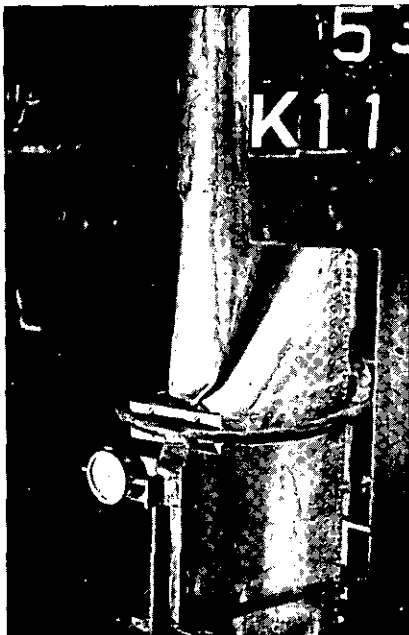


Fig. 5.7. Buckle crossing over the nose. Failure of type a_1 .

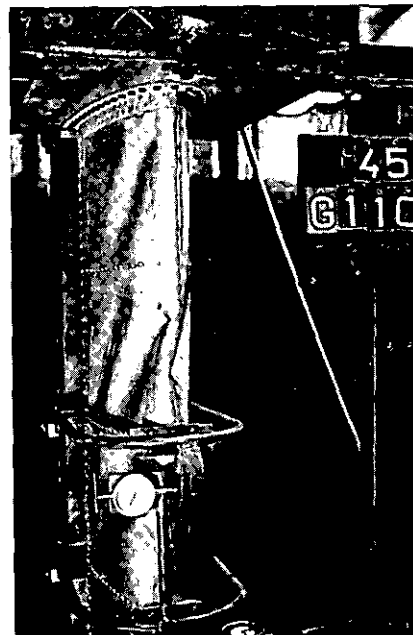


Fig. 5.8. Buckle rapidly extending into the nose. Failure of type a_2 .

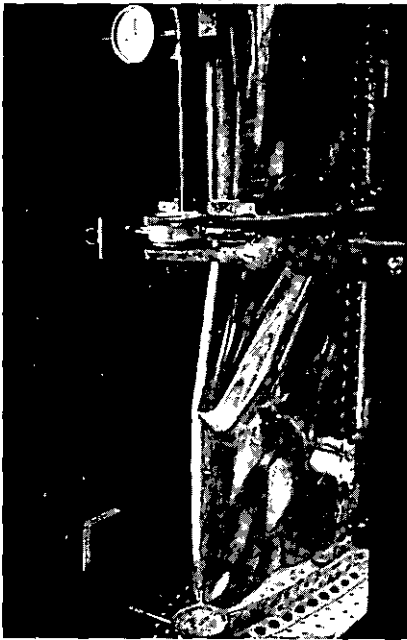


Fig. 5.9. Bending failure of the nose. Failure of type b.

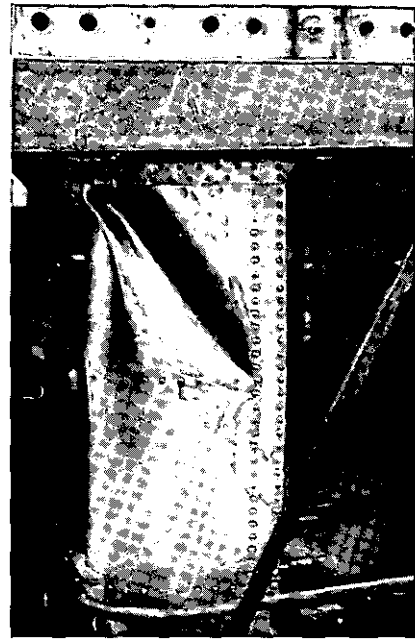


Fig. 5.10. Failure in end panel.

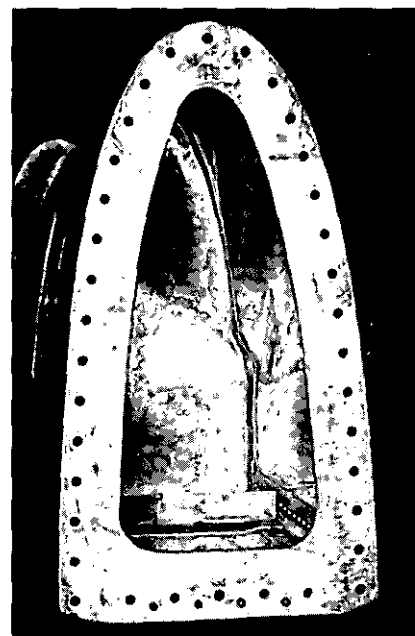
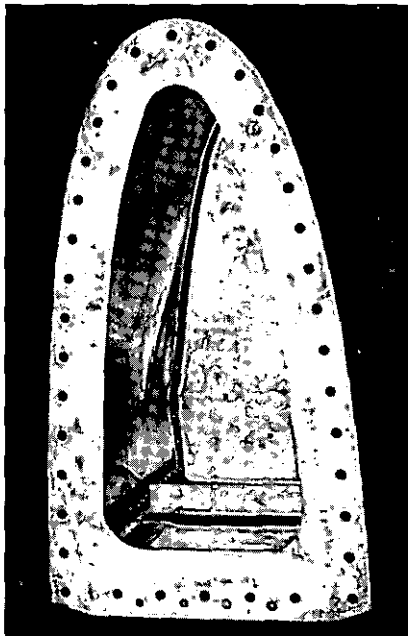


Fig. 5.11. Damage done to the rib.

REPORT V. 1648

The Effect of the Compressibility of the Air on the Dynamic Longitudinal Stability of an Aeroplane in Gliding Flight

by

C. M. KALKMAN and J. BUHRMAN.

Summary.

The trends of frequency and damping of the disturbed motions with the variation of Mach number in the sub-critical region are investigated. Approximate expressions for these quantities are derived from the equations of motion in which the speed dependence of the aerodynamic coefficients is taken into account. A numerical evaluation of the results for a typical high speed aeroplane is carried out.

Contents.

1.	Introduction.
2.	Equations of the disturbed motion.
3.	The coefficients of the characteristic quartic.
4.	The short period oscillation.
5.	The long period oscillation or phugoid motion.
5.1.	General.
5.2.	Forward c. g. position.
5.3.	Rearward c. g. position.
5.4.	Intermediate c. g. positions.
6.	Summary and conclusions.
7.	List of symbols.
8.	References.
9.	Tables in text.
9.	Figures.

This investigation has been performed by order of the Netherlands Aircraft Development Board (N.I.V.).

1 Introduction.

As a continuation of ref. 1 this report deals with the effect of the compressibility of the air on the dynamic longitudinal stability of an aeroplane in gliding flight. When the speed dependence of the aerodynamic coefficients is taken into account the stability derivatives as appearing in low speed theory (see for instance ref. 2) take a more complex form. In ref. 3 similar results are given, but the present report contains a more detailed numerical evaluation of the formulae derived. It will be presumed that during the disturbed motion the density or pressure of the air remains constant. This assumption is left out of consideration in ref. 4, which shows that in this case an equation of the fifth degree takes the place of the

usual stability quartic. Since the effect of height variations during the motion is considerable in the transonic and supersonic speed range but less important in the sub-critical speed range to be considered in this report, this height effect will be disregarded. For illustrating purposes the changes in damping and period of the disturbances of the longitudinal motion with Mach number are numerically given for an aeroplane, for which a few parameters (wing profile camber, c. g. position) are varied.

2 Equations of the disturbed motion.

The system of axes to which the equations are referred is fixed in the aeroplane the origin being at the c. g. and the positive X-axis pointing forwards in the direction of the speed in the undisturbed flight condition. The positive Z-axis is pointing downwards. Pitching moments are defined to be positive when tailheavy. According to the incompressible case the aerodynamic forces and moments are assumed to be linearly dependent on the increments in the velocity components along the axes u and w and the pitching velocity q . (See ref. 2).

$$X = X_0 + \frac{\partial X}{\partial u} u + \frac{\partial X}{\partial w} w + \frac{\partial X}{\partial q} q. \quad (2.1)$$

The equation for the pitching moments includes moreover an acceleration term $\frac{\partial M}{\partial \dot{w}} \dot{w}$. If according to usual practice the aerodynamic

time τ (expressed in $\tau = G/g\rho V^2$ seconds as a unit; see e. g. ref. 2) is introduced the equations of motion can be written (see sect. 7 for list of symbols)

$$\left. \begin{aligned} \left(\frac{d}{d\tau} - x_u \right) \frac{u}{V} - x_w \frac{w}{V} - \left(\frac{x_q d}{u d\tau} - \frac{1}{2} c_a \right) \theta &= 0 \\ - z_u \frac{u}{V} + \left(\frac{d}{d\tau} - z_w \right) \frac{w}{V} - \left\{ \left(1 + \frac{z_q}{\mu} \right) \frac{d}{d\tau} - \frac{1}{2} c_a \operatorname{tg} \varphi \right\} \theta &= 0 \\ - \frac{\mu}{i_B} m_u \frac{u}{V} - \left(\frac{\mu m_w}{i_B} \frac{d}{d\tau} + \frac{\mu m_w}{i_B} \right) \frac{w}{V} + \left(\frac{d^2}{d\tau^2} - \frac{m_q}{i_B} \frac{d}{d\tau} \right) \theta &= 0 \end{aligned} \right\} \quad (2.2)$$

whilst

$$\dot{\theta} = q.$$

When a solution of these equations is tried by substitution of

$$\frac{u}{V} = c_1 e^{\lambda \tau}, \text{ etc.}$$

it is found that λ has to satisfy the well-known stability quartic, the roots of which show the character of the disturbed motion:

$$\lambda^4 + B\lambda^3 + C\lambda^2 + D\lambda + E = 0 \quad (2.3)$$

where, neglecting the unimportant derivative z_q ,

$$\begin{aligned} B &= -x_u - z_w - \frac{m_q}{i_B} - \frac{\mu}{i_B} m_w \\ C &= x_u z_w - x_w z_u - \frac{\mu}{i_B} m_w + \\ &+ (x_u + z_w) \frac{m_q}{i_B} + \frac{\mu m_w}{i_B} (x_u + \frac{1}{2} c_a \operatorname{tg} \varphi) \\ D &= \frac{\mu}{i_B} m_w (x_u + \frac{1}{2} c_a \operatorname{tg} \varphi) + \\ &+ \frac{\mu}{i_B} m_w (\frac{1}{2} c_a - x_w) - \\ &- \frac{m_q}{i_B} (x_u z_w - x_w z_u) + \\ &+ \frac{\mu}{2 i_B} m_w c_a (z_u - x_u \operatorname{tg} \varphi) \\ E &= \frac{\mu c_a}{2 i_B} \{ (m_w z_u - m_u z_w) - \\ &- (m_w x_u - m_u x_w) \operatorname{tg} \varphi \}. \end{aligned} \quad (2.4)$$

3 The coefficients of the characteristic quartic.

In order to investigate the effect of the compressibility the influence of speed on the derivatives x_u , z_w , etc. must be taken into account.

As an example the derivation of the coefficient B is given in detail, for the other coefficients only the ultimate results are given.

In the expression for B (eq. 2.4) the derivatives x_u , z_w etc. have to be written in terms of the aerodynamic coefficients.

The component of the aerodynamic forces along the X-axis in disturbed flight can be written in the form

$$X = \frac{1}{2} \rho (V_0 + u)^2 \left[c_a \frac{w}{V_0} - \frac{\partial c_w}{\partial \alpha} \left(\alpha_0 + \frac{w}{V_0} \right) \right]. \quad (3.1)$$

Differentiation of this expression with respect to u or V ($= V_0 + u$) yields:

$$\begin{aligned} X_u &= \rho F' (V_0 + u) \left[c_a \frac{w}{V_0} - \frac{\partial c_w}{\partial \alpha} \left(\alpha_0 + \frac{w}{V_0} \right) \right] + \\ &+ \frac{1}{2} \rho F' (V_0 + u)^2 \left[\frac{\partial c_a}{\partial V} \frac{w}{V_0} - \frac{\partial}{\partial V} \frac{\partial c_w}{\partial \alpha} \left(\alpha_0 + \frac{w}{V_0} \right) \right] \end{aligned}$$

or after neglecting small quantities:

$$X_u = \rho F' V \left[-c_w - \frac{1}{2} V \frac{\partial c_w}{\partial V} \right]. \quad (3.2)$$

So the corresponding dimensionless coefficient $x_u = \frac{X_u}{\rho F' V}$ can be written:

$$x_u = -c_w - \frac{1}{2} V \frac{\partial c_w}{\partial V}. \quad (3.3)$$

In a similar way the expression for the derivative z_w can be derived.

The component of the aerodynamic forces along the axis of Z is

$$Z = \frac{1}{2} \rho F' (V_0 + u)^2 \left[-\frac{\partial c_a}{\partial \alpha} \left(\alpha_0 + \frac{w}{V_0} \right) - c_w \frac{w}{V_0} \right]. \quad (3.4)$$

Differentiation with respect to w gives:

$$Z_w = \frac{1}{2} \rho F' (V_0 + u)^2 \left[-\frac{1}{V_0} \frac{\partial c_a}{\partial \alpha} - \frac{c_w}{V_0} \right] \quad (3.5)$$

and for the dimensionless coefficient z_w :

$$z_w = -\frac{1}{2} \left[\frac{\partial c_a}{\partial \alpha} + c_w \right]. \quad (3.6)$$

This expression for z_w is identical with the one found in the incompressible case; in the compressible case, however, $\frac{\partial c_a}{\partial \alpha}$ and c_w are functions of speed.

It appears that only the derivatives with respect to V or u , give expressions which differ from those in the incompressible case.

So it follows that according to the incompressible theory

$$m_{q_{TAIL}} = -\frac{A_1}{2 \Gamma} \frac{F_H}{F} \quad (3.7)$$

and

$$\mu m_w = -\frac{A_1}{2 \Gamma} \frac{F_H}{F} \frac{d\varepsilon}{d\alpha} \quad (3.8)$$

where

$$\Gamma = 1 + \frac{F_H}{F} \frac{A_1}{A} \left(1 - \frac{d\varepsilon}{d\alpha} \right).$$

Substitution of x_u , z_w , m_q and m_w in equation (2.4) for the coefficient B and putting $m_q = 1.1 m_{q_{TAIL}}$ yields:

$$B = \frac{3}{2} c_w + \frac{M}{2} \frac{\partial c_w}{\partial M} + \frac{1}{2} \frac{\partial c_a}{\partial \alpha} + \frac{F_H A_1}{2 i_B F_T} \left(1.1 + \frac{d\varepsilon}{d\alpha} \right). \quad (3.9)$$

It is easily seen that B increases with Mach number since all four terms in (3.9) increase with speed. In the sub-critical speed range the first two terms are small and can be neglected.

The coefficient C can be dealt with in a similar manner. Expressing the derivatives x_u , x_w , etc. in terms of c_a , c_w , c_m and their derivatives with respect to speed yields:

$$C = \left(\frac{1}{2} c_a + \frac{M}{4} \frac{\partial c_a}{\partial M} \right) \left(c_a - \frac{\partial c_w}{\partial \alpha} \right) + \frac{1}{2} c_w \frac{\partial c_a}{\partial \alpha} + \frac{M}{4} \frac{\partial c_w}{\partial M} \frac{\partial c_a}{\partial \alpha} + c_w \left(\frac{1}{2} c_w + \frac{M}{4} \frac{\partial c_w}{\partial M} \right) - \frac{\mu t}{2 i_B l} \frac{\partial c_M}{\partial \alpha} + 1.1 \frac{F_H A_1}{4 i_B F_T} \frac{dc_a}{d\alpha} + \frac{A_1 F_H}{2 i_B F_T} \left(\frac{3}{2} c_w + \frac{M}{2} \frac{\partial c_w}{\partial M} \right) \left(1.1 + \frac{d\varepsilon}{d\alpha} \right)$$

which can be approximated with a sufficient degree of accuracy by

$$C = \frac{A_1}{4 i_B} \left(1.1 \frac{A_1 F_H}{F} - 2 \frac{\mu t}{l} \frac{\partial c_M}{\partial \alpha} \right). \quad (3.10)$$

The effect of speed on C , which is proportional to the manoeuvre margin is not very large at forward c.g. positions. For rearward c.g. positions, however, the changes in C with M can be considerable. More details will be given in the next section.

The coefficient D appears in the following form:

$$D = -\frac{3 c_w \mu t}{4 i_B l} \frac{\partial c_M}{\partial \alpha} + \frac{F_H A_1}{4 i_B F_T} \left(c_r^2 + \frac{M}{4} \frac{\partial c_r^2}{\partial M} \right) \left(1.1 + \frac{d\varepsilon}{d\alpha} \right) + \frac{\mu t M}{4 i_B l} \frac{\partial c_w}{\partial \alpha} \frac{\partial c_M}{\partial M} - 1.1 \frac{F_H A_1 c_a^2}{4 i_B F_T} \frac{\partial}{\partial \alpha} \left(\frac{c_w}{c_a} \right).$$

At high speeds (small c_a -values; see ref. 3) this formula can be simplified further to

$$D = \frac{\mu t}{4 i_B l} \frac{\partial c_a}{\partial \alpha} \left(-3 c_w \frac{\partial c_M}{\partial c_a} + \frac{\partial c_w}{\partial c_a} M \frac{\partial c_M}{\partial M} \right) + 1.1 \frac{A_1 A F_H}{4 i_B F} c_w. \quad (3.11)$$

The trend in the changes in D with Mach number are not immediately clear since formula (3.11) contains the derivatives $\frac{\partial c_M}{\partial M}$ and $\frac{\partial c_M}{\partial c_a}$, which are dependent on wing profile camber and c.g. position. In order to get a better insight in the possible variations of D and the character of the disturbed motion a few numerical elucidations will be given in the next section.

Finally the evaluation of the coefficient E leads to:

$$E = -\frac{c_a^2 \mu t}{4 i_B l} \frac{\partial c_a}{\partial \alpha} \left(\frac{\partial c_M}{\partial c_a} - \frac{\partial c_M}{\partial M} \frac{M}{2 c_a} \right) \quad (3.12)$$

which is proportional to the static stability margin. So changes in E are proportional to the changes in this margin as they are dealt with in ref. 1.

4. The short period oscillation.

The character of the disturbed motion of the aeroplane is given by the roots of the equation (2.3). According to Bairstow this equation can be factorized giving as a result two quadratics in an approximated form. In most cases both quadratics show a pair of conjugate complex roots corresponding to two oscillations: a short period heavily damped one and a long-period slightly damped or unstable one. The roots of the quadratic characterising the short period oscillation can be approximated by

$$\lambda_{1,2} = -\frac{B}{2} \pm \sqrt{\frac{B^2}{4} - C} \quad (4.1)$$

in which $-\frac{B}{2}$ stands for the damping and

$\frac{1}{2\pi} \sqrt{C - \frac{B^2}{4}}$ defines the frequency both expressed in aerodynamic time.

As an illustrating example, the variation of B with Mach number for a particular single-engined high speed aeroplane is given in table 1 (see ref. 1 for the required data of this aeroplane; the quantity i_B not mentioned in ref. 1 = 0.087).

TABLE 1.

M	0.4	0.6	0.7	0.8
B	6.42	7.12	7.75	8.82

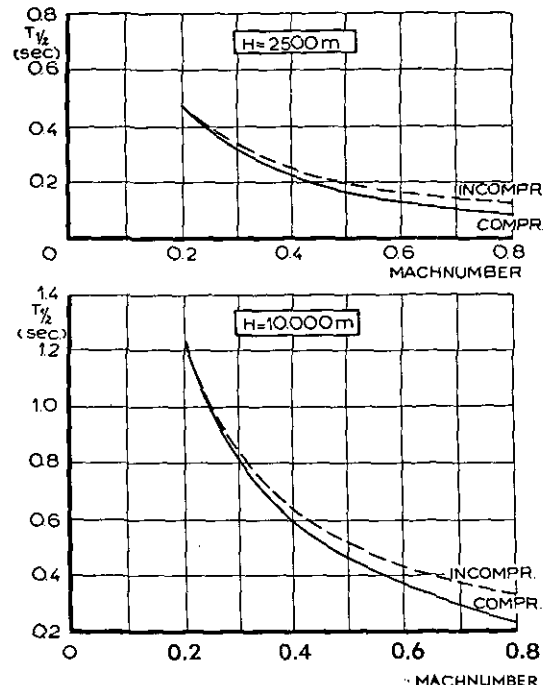


Fig. 1. Short period damping as a function of Mach number.

It follows from this table that the damping of the short-period oscillation increases with M as long as the motion remains periodic ($\frac{B^2}{4} - C$ remains negative). It may be remarked that neither altitude nor c.g. position affects B .

The time $T_{\frac{1}{2}}$ to damp the oscillation to half amplitude is given in fig. 1, in which curves for the compressible and incompressible case are plotted.

The frequency of the oscillations depends also on the coefficient C , the variation of which can be seen from table 2 for two different altitudes and four c.g. positions. The most rearward c.g. ($h - h_0 = 0.07$) is located at a point 2% MAC in front of the neutral point at low speed.

Only for the most rearward c.g. position at high altitude the changes in C appear to be considerable. In fig. 2 the period of the oscillation is plotted against Mach number for three c.g. positions and two altitudes. The dotted lines refer to the in-

TABLE 2.

The coefficient C as a function of M .

H (m)	$h - h_0$ (% MAC)	M			
		0.4	0.6	0.7	0.8
2500	-0.05	43.5	46.5	47.9	51.6
	0	30.3	32.0	32.4	34.2
	0.05	17.3	17.5	16.9	17.0
	0.07	12.0	11.7	10.7	10.0
10000	-0.05	91.7	96.4	98.3	103.8
	0	61.3	62.9	62.4	63.7
	0.05	30.7	29.4	26.5	23.5
	0.07	18.5	16.0	13.2	7.4

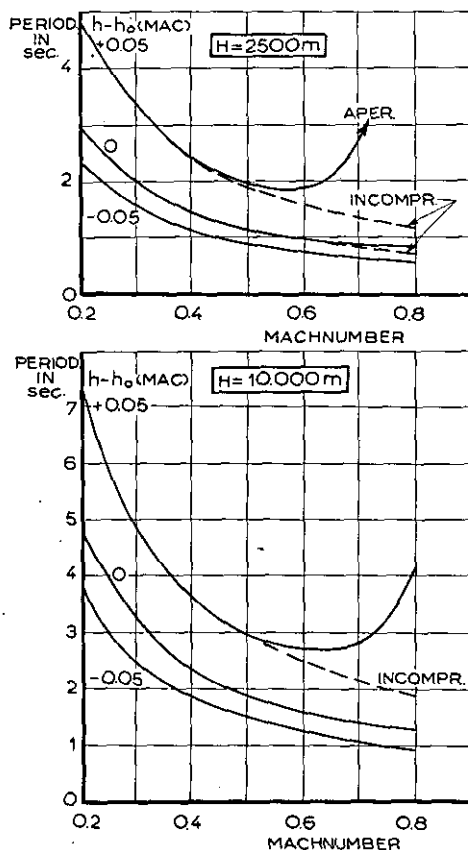


Fig. 2. Period of rapid oscillation as a function of Mach number for different c.g. positions.

compressible case. It is seen that the compressibility effect is noticeable only for the rearward c.g. position.

So it can be concluded that at forward c.g. positions (large values of C or manoeuvre margins) the character of the short period oscillation is almost unaffected by an increase in Mach number up to the critical Mach number, but that if the manoeuvre margin is small (C small) the periodic motion can pass into a damped and at still higher Mach numbers into an unstable aperiodic motion ($C < 0$).

5 The long period oscillation or phugoid motion.

5.1 General.

The roots of the second quadratic originating from the factorizing of the stability quartic according to Bairstow determine the character of the so called phugoid motion and can be written in the form

$$\lambda_{3,4} = -\frac{1}{2} \frac{CD - BE}{C^2} \pm \sqrt{\left(\frac{CD - BE}{2C^2}\right)^2 - \frac{E}{C}} \quad (5.1)$$

It is seen from this expression that these roots are also dependent on the coefficients D and E , which in turn are strongly affected by the varia-

tion of the derivatives $\frac{\partial c_M}{\partial c_a}$ and $\frac{\partial c_M}{\partial M}$ with Mach number.

The expression for $\frac{\partial c_M}{\partial M}$ is derived in ref. 1 and reads

$$\begin{aligned} \frac{\partial c_M}{\partial M} = & \frac{M}{V\sqrt{1-M^2}} \frac{1}{\Gamma} \left[\frac{c_{m_0}}{1-M^2} \left\{ \frac{A_1}{\pi\lambda_H} + \right. \right. \\ & + \frac{F_H}{F} \frac{A_1}{A} \left(1 - \frac{d\varepsilon}{d\alpha} \right) \left. \right\} - \left\{ \frac{A\alpha}{a_0} + \frac{A_1 c_a}{A a_{1c}} \right\} c'_{m_{fus}} - \\ & - \frac{A_1}{a_{10}} (h - h_0) c_a - \bar{V} A_1 A \alpha \left. \right\} - \frac{1}{a_0} + \\ & + \frac{\sqrt{1-M^2}}{2\pi\lambda} \frac{s^2}{l^2} \frac{1}{\sqrt{1 + (1-M^2) \left(\frac{\pi s}{4l} \right)^2}} \left. \right] \quad (5.2) \end{aligned}$$

The dominant term in this formula is the one with c_{m_0} , which is almost entirely dependent on the wing camber. The quantity c_{m_0} is positive for negative and negative for normal positive cambers.

So $\frac{\partial c_M}{\partial M}$ will increase with M for negative and decrease for positive cambered wings.

The variation of the coefficients D and E with Mach number for the above-mentioned high-speed aircraft is given in the following tables.

TABLE 3.

The coefficient D as a function of Mach number.

$H(m)$	$h - h_0 = -0.05 \text{ MAC}$				$h - h_0 = +0.07 \text{ MAC}$		
	M	$c_{m_0} = -0.04$	-0.02	$+0.01$	-0.04	-0.02	$+0.01$
2500	0.4	1.305	1.309	1.314	0.302	0.306	0.311
	0.6	1.317	1.323	1.333	0.256	0.262	0.272
	0.7	1.334	1.345	1.360	0.209	0.219	0.235
	0.8	1.395	1.417	1.449	0.144	0.166	0.198
10000	0.4	4.095	4.118	4.154	0.736	0.760	0.795
	0.6	3.088	3.126	3.182	0.403	0.441	0.497
	0.7	2.991	3.058	3.159	0.207	0.274	0.376
	0.8	2.838	2.976	3.183	-0.192	-0.054	0.153

TABLE 4.

The coefficient E as a function of Mach number.

$H(m)$	$h - h_0 = -0.05 \text{ MAC}$				$h - h_0 = +0.07 \text{ MAC}$		
	M	$c_{m_0} = -0.04$	-0.02	$+0.01$	-0.04	-0.02	$+0.01$
2500	0.4	0.370	0.385	0.408	0.035	0.050	0.073
	0.6	0.046	0.073	0.114	-0.034	-0.007	0.033
	0.7	-0.019	0.024	0.088	-0.070	-0.027	0.038
	0.8	-0.118	-0.031	0.101	-0.157	-0.069	0.063
10000	0.4	7.301	7.400	7.549	1.019	1.114	1.264
	0.6	1.474	1.651	1.916	-0.024	0.153	0.419
	0.7	0.621	0.900	1.322	-0.317	-0.036	0.384
	0.8	-0.160	0.418	1.285	-0.879	-0.301	0.566

It appears from table 3 that the effect of profile camber or c_{m_0} on the coefficient D is relatively smaller for forward c. g. positions than for rearward ones and from comparing table 3 and 4 it follows that the influence of camber is considerably larger on E than on D .

As the c. g. position plays an important part on the character of the phugoid motion differentiation will be made between forward and rearward c. g. positions. For each of these extreme cases approximative formulae can be derived for frequency and damping, from which an insight can be gained into the trends for the intermediate locations of the c. g. The data for the graphs and tables given in this report are, however, derived from the formulae, as they follow from the stability quartic according to Bairstow without any further approximation. It will be seen that the general conclusions, which can be drawn from the approximative formulae, derived in the next paragraphs are in good agreement with the numerical results of these more accurate formulae.

5.2 Forward c. g. position.

In the case of forward c. g. positions the expressions for frequency and damping can be approximated as follows.

As at a forward position of the centre of gravity the second term in the formula (3.10) for the coefficient C is relatively large the expression for C can be approximated by (putting $\Gamma=1$)

$$C = -\frac{1}{2} \frac{A}{i_B} \pi \frac{t}{l} \frac{\partial c_M}{\partial c_a} \quad (5.3)$$

The damping term $\delta = \left(\frac{D}{C} - \frac{BE}{C^2} \right) \frac{1}{2t}$ (sec 5.1) can now be written in the form (C being large the term with C^2 can be neglected):

$$\delta = \frac{1}{4t} \left[3c_w - \frac{\partial c_w}{\partial c_a} M \frac{\partial c_M / \partial M}{\partial c_M / \partial c_a} - \frac{\bar{V} A_1}{\mu} \frac{c_w}{\partial c_M / \partial c_a} \right] \quad (5.4)$$

With the same assumptions the corresponding expression for the frequency becomes:

$$\omega = \frac{c_a}{4\pi t} \sqrt{2 - \frac{M}{c_a} \frac{\partial c_M / \partial M}{\partial c_M / \partial c_a}} \quad (5.5)$$

As it appears from equation (5.4), the damping is almost unaffected by compressibility as the term with $\frac{\partial c_M}{\partial M}$ is only small in comparison with the others. So, as long as the motion remains periodic, it will be a damped one. For ease of comparison numerical values of damping times to half amplitude are given in the following table for the above-mentioned example of a high speed aeroplane for both the compressible and incompressible case.

TABLE 5.

Time to damp to half amplitude as a function of Mach number in seconds (forward c. g. position).

$$h - h_0 = -0.05 \text{ MAC.}$$

M	H = 2500 m			H = 10000 m		
	Incompr.	Compressible		Incompr.	Compressible	
		$c_{m_0} = -0.02$	$c_{m_0} = +0.01$		$c_{m_0} = -0.02$	$c_{m_0} = +0.01$
0.4	49.2	49.9	49.9	95.7	93.9	93.3
0.6	33.2	34.0	33.8	79.6	79.0	78.0
0.7	28.7	29.4	29.3	69.0	69.4	67.8
0.8	25.1	— *)	25.9	61.5	65.1	62.2

*) motion is aperiodic.

As $\frac{\partial c_M}{\partial c_a}$ does not vary much with M for the c. g. positions considered here it appears from (5.5) that the frequency of the disturbed motion will relative to the incompressible case increase with increasing Mach number for negative and decrease for positive cambered wings. For large positive camber the derivative $\frac{\partial c_M}{\partial M}$ is negative and decreases rapidly with M . As a consequence the expression under the radical sign will change sign, the motion becoming aperiodic.

An illustration of these facts is given in fig. 3 for two altitudes (2500 m and 10000 m). The

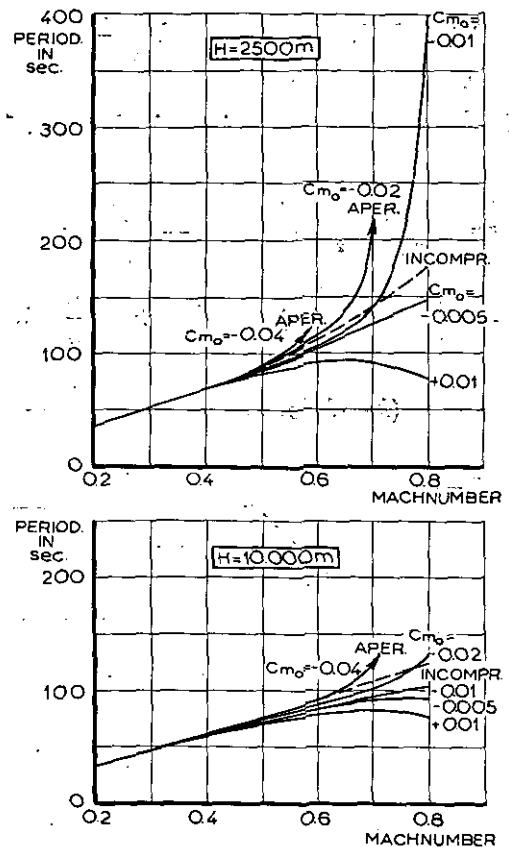


Fig. 3. Period of phugoid motion as a function of Mach number for different values of c_{m_0} (forward c. g. position; $h - h_0 = -0.05 \text{ MAC}$).

period (in sec) is plotted as a function of Mach number for different values of c_{m_0} or wing camber. The graph shows that for negative or even small positive cambers the period decreases relative to the incompressible case with increasing Mach number, but that for positive values the period is becoming larger and in particular at an altitude of 2500 m the motion converts into an aperiodic one for a normal positive cambered wing ($c_{m_0} = -0.02$) when the speed increases above $M = 0.7$.

Aperiodicity occurs according to formula (5.5) when:

$$\frac{M}{c_a} \frac{\partial c_M / \partial M}{\partial c_M / \partial c_a} > 2. \quad (5.6)$$

With increasing Mach number the periodic motion will at first split up in two subsidences, one of which will almost immediately change into a divergence, as the damping term $\frac{1}{2} \frac{CD - BE}{C^2}$ of equation (5.1) is only small. Thus it is clear that the velocity boundaries between which the motion is damped aperiodic are very close to each other.

Summarizing it can be concluded that at forward c. g. positions the effect of compressibility on the damping can be neglected as long as the disturbed motion remains periodic, that the frequency for negative cambered wings increases (decreasing period) with Mach number and that a divergence can occur for positive cambered wings the sooner the larger the camber is.

5.3 Rearward c. g. position.

In the case of a rearward c. g. position the effect of compressibility on the derivative $\frac{\partial c_M}{\partial c_a}$ is relatively large, but the quantity itself is small and can be neglected in the approximated expressions for frequency and damping. With this assumption the formula for the damping can after some reduction be written in the following form:

$$\delta = -\frac{1}{2t} \left[\frac{\mu}{A_1} \bar{V} M \frac{\partial c_M}{\partial M} \left\{ \frac{\partial c_w}{\partial c_a} - c_a \left(\frac{F}{F_H} \frac{i_B}{A_1} + \frac{1 + \frac{d\varepsilon}{d\alpha}}{A'} \right) \right\} + c_w \right]. \quad (5.7)$$

Writing for c_w

$$c_w = c_{w_0} + \frac{1}{\pi\lambda} c_a^2 \quad (5.8)$$

it follows that

$$\frac{\partial c_w}{\partial c_a} = \frac{2}{\pi\lambda} c_a. \quad (5.9)$$

Substituting this expression in (5.7) gives:

$$\delta = -\frac{1}{2t} \left[\frac{\mu}{A_1} \bar{V} M \frac{\partial c_M}{\partial M} c_a \left\{ \frac{2}{\pi\lambda} - \frac{F}{F_H} \frac{i_B}{A_1} - \frac{1 + \frac{d\varepsilon}{d\alpha}}{A} \right\} + c_w \right]. \quad (5.10)$$

The corresponding formula for the frequency reads:

$$\omega = \frac{c_a}{2\pi t} \sqrt{\frac{\mu}{A_1} \bar{V} \frac{M}{2c_a} \frac{\partial c_M}{\partial M}}. \quad (5.11)$$

The damping term δ decreases for negative cambered wings $\left(\frac{\partial c_M}{\partial M} \text{ increases with } M \right)$ with increasing Mach number. This follows from the

fact that the negative terms between the braces in (5.10) dominate the term $\frac{2}{\pi\lambda}$. The quantitative relations may even be so that an unstable oscillation will occur.

The trends in the variation of the damping with Mach number are illustrated on fig. 4 and fig. 5 (the incompressible case is plotted as a dotted line) for the single-engined high speed aeroplane mentioned before. On fig. 4 the c. g. is in a rear-

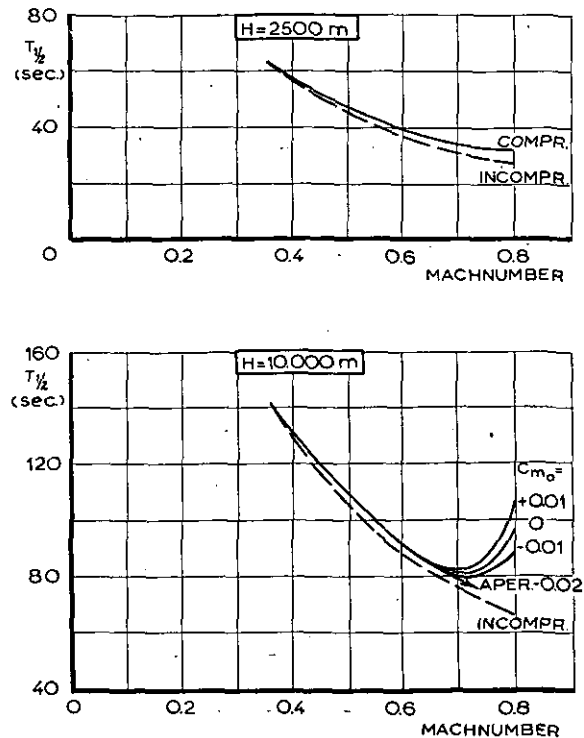


Fig. 4. Damping of phugoid motion as a function of Mach number for different values of c (rearward c. g. position; $h - h_0 = 0.05$ MAC).

ward position defined by $h - h_0 = 0.05$ MAC. The damping given as the time required to halve the amplitude is plotted against Mach number for different values of c_{m_0} at two altitudes (2500 m and 10000 m). It is seen from this graph that at an altitude of 2500 m, the influence of compressibility is small and that there is no practical difference between the curves for various cambers. At an altitude of 10000 m, however, the negative cambered wing shows a distinct decrease in damping.

For a 2% MAC more rearward located c. g., the variation of damping with Mach number, as plotted in fig. 5, shows that for negative and even small positive cambered wings the stable oscillation passes into an unstable one by increasing speed above $M = 0.7$ at an altitude of 10000 m. The unstable oscillation does not occur at $H = 2500$ m for the chosen example; so it will be more likely to encounter this phenomenon at high altitudes. At the same time according to formula (5.11) the corresponding frequency will increase with M caused by the increase of $\frac{\partial c_M}{\partial M}$. As the static margin is in the same way influenced by this

derivative, the instability will be accompanied by heavy stick forces, which can cause serious difficulties in handling the aeroplane.

When on the other hand $\frac{\partial c_M}{\partial M}$ decreases with M , as in the case of positive cambered wings, it fol-

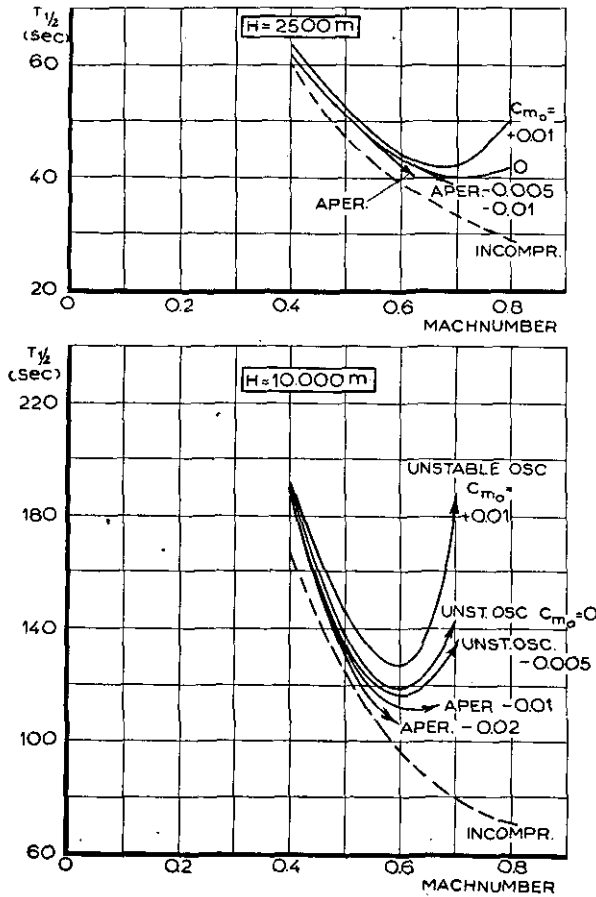


Fig. 5. Damping of phugoid motion as a function of Mach number for different values of c_{m0} (rearward c.g. position; $h - h_0 = 0.07$ MAC).

lows from (5.11) that the frequency will decrease much more rapidly (cf. eq. (5.5)) and divergence will occur at smaller values of M and camber than for forward located c.g. positions. Similar to the case of the forward c.g. positions the range of velocities where the motion is damped aperiodic is only small and by increasing speed the stable oscillation will almost immediately pass into a divergence.

The variation of the frequency with change of speed is illustrated in fig. 6 and 7 for the same values of the variables as for the damping. Comparing the two figures shows that shifting the c.g. 2% MAC in a rearward direction aggravates the above-mentioned tendencies. The character of the divergence for positive cambered wings is shown in fig. 8, where the time required to double the amplitude is plotted against M for four c.g. positions at two altitudes. It appears that the most rapid divergence occurs at rearward c.g. positions and for positively cambered wings.

5.4 Intermediate c.g. position.

Having treated the extreme c.g. positions separately, conclusions can now be drawn for the effect of shifting the c.g. from extreme forward to extreme rearward positions.

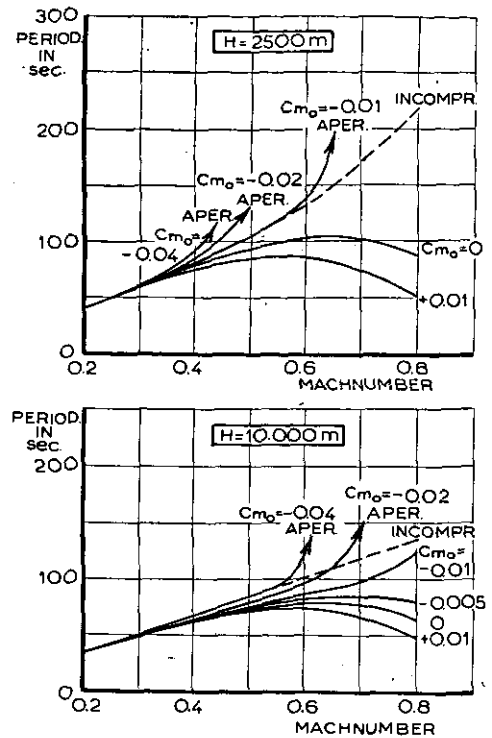


Fig. 6. Period of phugoid motion as a function of Mach number for different values of c_{m0} (rearward c.g. position; $h - h_0 = 0.05$ MAC).

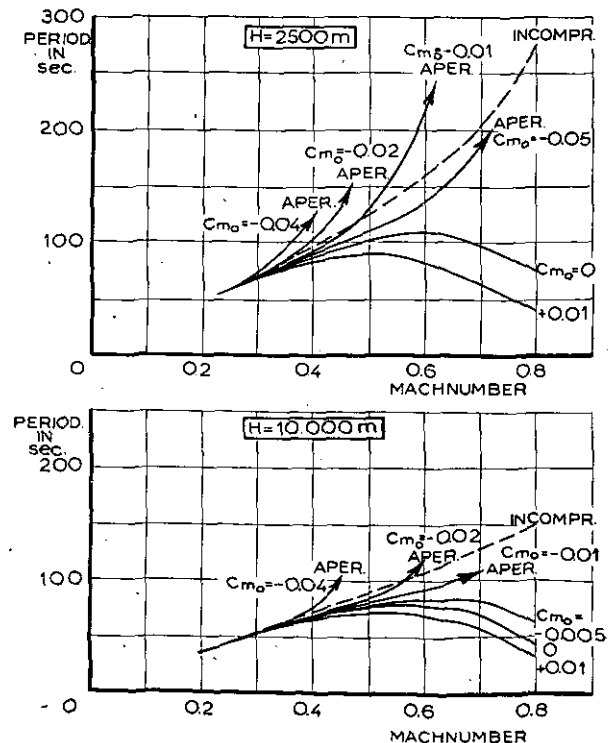


Fig. 7. Period of phugoid motion as a function of Mach number for different values of c_{m0} (rearward c.g. position; $h - h_0 = 0.07$ MAC).

The decrease of the damping of the phugoid due to increasing Mach number will increase by shifting the c. g. in a rearward direction and will finally result in an unstable oscillation, at first for

negative cambered wings and next for small positive cambered ones too (fig. 4 and 5). So it seems that in applying negative cambered wings the greatest care must be exercised because of the heavy stick forces accompanying the instability mentioned in the preceding section. For the most rearward c. g. position ($h - h_0 = 0.07$ MAC, that is about 2% MAC in front of the neutral point at low speed) for which the phugoid motion has been calculated the time to double the amplitude at an altitude of 10000 m amounts at $M = 0.8$ for the wing cambers defined by $c_{m0} = +0.01$, 0 and -0.005 to resp. 26.5; 56.0 and 126.7 sec. These values can become more unfavourable by shifting the c. g. still more rearward.

From a comparison of the two expressions derived for the frequency at forward and aft c. g. positions it can be concluded that the change in the period due to increasing Mach number will increase by rearward shifting of the c. g. As the c. g. is located more rearward, divergence will occur at lower values of M and begin at less positive values of wing camber. This is clearly demonstrated by the figures 3, 9, 6 and 7, where fig. 9 and 6 give the relations for the interjacent c. g. positions ($h - h_0 = 0$ resp. $+0.05$ MAC). The divergence time to double the amplitude for the different parameters is plotted on fig. 8.

6 Summary and conclusions.

An investigation was made of the influence of the air compressibility on the dynamic longitudinal stability of an aeroplane below the critical Mach number.

The following conclusions can be drawn from the formulae derived and the calculations performed:

- 1 The damping of the rapid oscillation with regard to the incompressible case increases with increasing Mach number and is independent of c. g. position (fig. 1).
- 2 The period of the rapid oscillation experiences hardly any influence of compressibility for forward c. g. positions. At more rearward located c. g. positions the period increases with Mach number (fig. 2) and for extreme aft positions the motion becomes aperiodic, at first damped and finally divergent. The period is independent of wing camber (fig. 2).
- 3 For forward c. g. positions the damping of the phugoid motion is nearly unaffected by compressibility. As long as the motion remains periodic it will be damped.
- 4 For aft c. g. positions the damping of the phugoid motion will decrease with respect to the incompressible case with increasing Mach number for symmetric and negatively cambered wings (fig. 4 and 5). Rearward shifting of the c. g. results in an increase of the compressibility effects. At aft positions the motion changes into an unstable oscillation (fig. 5).
- 5 For forward c. g. positions the period of the phugoid will decrease with regard to the incompressible case with increasing Mach number

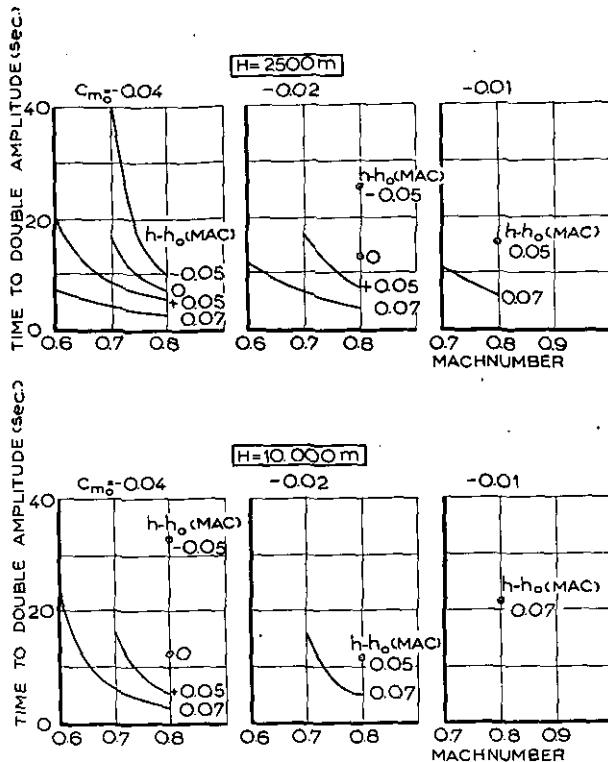


Fig. 8. Time required to double amplitudes of aperiodic modes of phugoid motion.

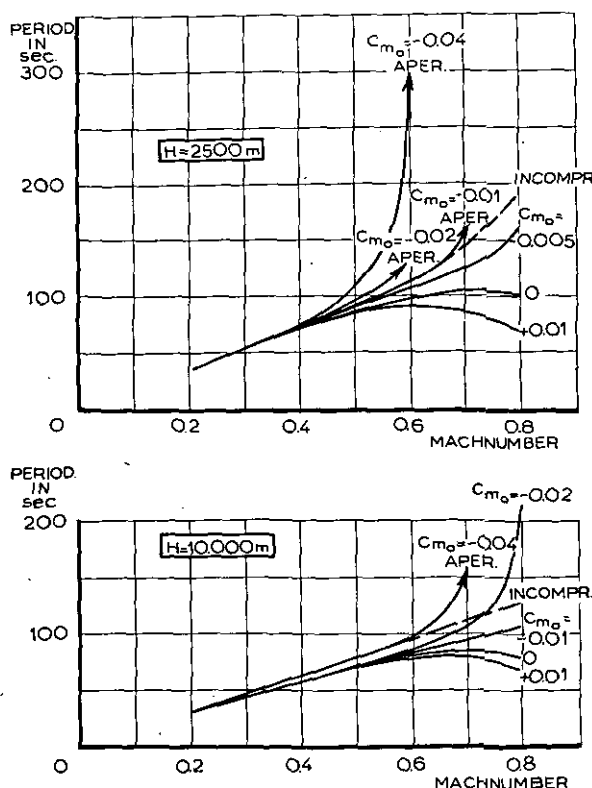


Fig. 9. Period of phugoid motion as a function of Mach number for different values of c_{m0} (intermediate c. g. position; $h - h_0 = 0$).

for small positive and negative camber. With normal positively cambered wings the period increases with increasing Mach number and for high positively cambered wings the motion changes into an aperiodic one, almost immediately divergent (fig. 3).

- 6 For aft e. g. positions the period of the phugoid decreases with M for negative and small positive wing cambers with respect to the incompressible case, the decrement being larger than for forward e. g. locations.

For positively cambered wings the period increases with M and divergence occurs at lower Mach numbers and sets in at less positive wing cambers than at forward e. g. locations (fig. 6 to 8).

- 7 Finally it can be concluded that although in most cases no serious difficulties are to be expected in the dynamic longitudinal behaviour of the aeroplane up to the critical Mach number, troubles can be encountered at high subcritical Mach numbers in the case of an aeroplane with a rearward located c. g. and a negatively cambered wing, since the phugoidal oscillation may become unstable, whilst the frequency may become high. The large positive static margins occurring in this condition involving heavy stick forces can give rise to unfavourable handling qualities of the aircraft. Moreover the rapid oscillation passes into a divergence when the manoeuvre margin is small at low speeds, which also is the case for rearward e. g. positions.

7 List of symbols.

A	$= \frac{\partial c_a}{\partial \alpha}$ of aeroplane without tail.
A_1	$= \frac{\partial c_{aH}}{\partial \alpha_H}$
a, a_1	$=$ low speed values of A, A_1 .
a_0, a_{10}	$=$ values of a, a_1 for infinite aspect ratio.
B	$=$ coefficient of λ^3 in the stability quartic.
C	$=$ coefficient of λ^2 in the stability quartic.
c_a	$=$ liftcoefficient of complete aeroplane.
c_{aH}	$=$ liftcoefficient of horizontal tail surfaces.
c_M	$=$ pitching moment coefficient (positive when tail heavy).
c_{M0}	$= c_{M \text{ wing}}$ when lift is zero.
c_w	$=$ drag coefficient of complete aeroplane.
c_m	$=$ low speed value of c_M .
c_{m0}	$=$ low speed value of c_{M0} .
$c_{m \text{ fus}}$	$=$ fuselage pitching moment coefficient.
$c_{m' \text{ fus}}$	$= \frac{\partial c_{m \text{ fus}}}{\partial \alpha}$
C_r	$=$ coefficient of resultant aerodynamic force on complete aeroplane.
D	$=$ coefficient of λ in the stability quartic.
E	$=$ constant in the stability quartic.
F	$=$ wing area.
F_H	$=$ area of horizontal tail surfaces.
G	$=$ aeroplane weight.
g	$=$ acceleration due to gravity.

H	$=$ altitude.
ht	$=$ distance of centre of gravity aft of leading edge of mean aerodynamic chord.
h_0t	$=$ distance of aerodynamic centre of aeroplane without tail aft of leading edge of mean aerodynamic chord.
$i_B ml^2$	$=$ moment of inertia of aeroplane about Y-axis.
l	$=$ distance of aerodynamic centre of tail aft of aerodynamic centre of aeroplane without tail.
M	$=$ pitching moment of the complete aeroplane.
M	$=$ Machnumber.
m	$= G/g =$ aeroplane mass.
m_u	$= \frac{Vt}{2l} \frac{\partial c_M}{\partial V}$
m_w	$= \frac{t}{2l} \frac{\partial c_M}{\partial \alpha}$
$m_{\dot{w}}$	$= \frac{V^2 t}{2 \mu l^2} \frac{\partial c_M}{\partial \dot{w}}$
m_q	$= \frac{Vt}{2l^2} \frac{\partial c_M}{\partial q}$
q	$=$ angular velocity about lateral axis.
s	$=$ semispan of wing.
t	$=$ mean aerodynamic chord (MAC).
\hat{t}	$=$ unit of aerodynamic time ($= G/\rho g F V$ sec).
u	$=$ increment in V in disturbed flight.
V	$=$ forward speed.
\bar{V}	$= \frac{F_H l}{F t}$, tailvolume.
w	$=$ velocity component along Z-axis in disturbed flight.
\dot{w}	$= \frac{dw}{dt}$
X	$=$ aerodynamic force along X-axis.
X_0	$=$ aerodynamic force along X-axis in equilibrium condition.
x_u	$= (\partial X / \partial V) / \rho F V$.
x_w	$= (\partial X / \partial \alpha) / \rho F V^2$.
Z	$=$ aerodynamic force along Z-axis.
z_u	$= (\partial Z / \partial V) / \rho F V$.
z_w	$= (\partial Z / \partial \alpha) / \rho F V^2$.
z_q	$= (\partial Z / \partial q) / \rho F V^2 l$.
α	$=$ angle of incidence of zero lift line of aeroplane without tail.
α_H	$=$ angle of incidence of horizontal tailplane.
δ	$=$ damping term (positive when damped) sec^{-1} .
φ	$=$ angle of inclination of the flight path to the horizontal in equilibrium condition in straight flight (positive in the climb).
ϵ	$=$ angle of downwash at the horizontal tail.
Γ	$= 1 + \frac{F_H A_1}{F A} \left(1 - \frac{d\epsilon}{d\alpha} \right)$.
θ	$=$ angle of rotation of X-axis from equilibrium condition.
λ	$=$ root of stability quartic (eq. (2.3)).
λ	$=$ aspect ratio of wing.
λ_H	$=$ aspect ratio of horizontal tailplane.

- $\mu = \frac{G}{\rho g Fl}$, relative density of aeroplane.
 ρ = air density.
 τ = time in aerodynamic units.
 ω = frequency (oscillations/sec).

8 References.

1. BUHRMAN, J. and KALKMAN, C. M. The Static Longitudinal Stability and Control of an Aeroplane as Affected by the Compressibility of the Air. Report V.1625, National Aeronautical Research Institute.
2. LYON, H. M., TRUSCOTT, P. M., AUTERSON, E. I. and WHATHAM, J. A Theoretical Analysis of Longitudinal Dynamic Stability in Gliding Flight, R and M No. 2075.
3. BADER, W. Ueber den Einfluss hoher Fluggeschwindigkeiten auf die Flugzeug-Längsbewegung, Institut für Flugmechanik der DVL. PB Report 36118.
4. NEUMARK, S. Longitudinal Stability, Speed and Height. *Airer. Eng.* Vol. 22 (1950) p. 323.
5. GATES, S. B. and LYON, H. M. A Continuation of Longitudinal Stability and Control Analysis. R and M No. 2027.

Completed February 1953.

REPORT V. 1535

Airflow through Helicopter Rotors in Vertical Flight

by

J. MEIJER DREES, L. R. LUCASSEN and W. P. HENDAL.

Summary.

In this report an attempt is made to describe the field of flow through a helicopter rotor, in various working conditions in vertical flight. The limitations of the momentum theory are discussed. The spread of the slipstream explains the existence of an airbody around the rotor, working in the vortex ring state. By considering the properties of this airbody, the working conditions and the rough behaviour of helicopters at moderate rates of descent can be understood more clearly.

Contents.

- 1 Introduction.
 - 2 List of symbols.
 - 3 Graphical presentation of the working conditions.
 - 4 Momentum equation.
 - 5 Deviations from momentum theory.
 - 5.1 Vortex ring state.
 - 5.1.1 Velocity distribution along rotor axis.
 - 5.1.2 Low rates of descent.
 - 5.1.3 Region of roughness.
 - 5.1.4 Spread of the slipstream.
 - 5.1.5 Higher rates of descent.
 - 5.2 Windmill brake state.
 - 6 References.
- Appendix: The field of flow from windtunnel smoke tests.
- 11 Figures.

1 Introduction.

At low rates of descent in vertical flight, the air passes downwards through a helicopter rotor, i. e. in the same direction as in the case of an ascending rotor. The sign of the relative velocity changes at increasing rate of descent. This implies the existence of various rotor working conditions.

The corresponding fields of flow have been studied by many investigators. A comparison of their results with the results obtained with the momentum theory shows that a fair approximation of the actual field of flow for the propeller state and for a part of the windmill brake state can be obtained.

This theory does not hold in the vortex ring state condition. In this report an attempt is made to describe the flow through rotors in these inter-jacent conditions with the object of elucidating the

characteristic behaviour of a helicopter in vertical flight.

2 List of symbols.

α	ratio of frontal area of airbody to rotor disc area.
α	actual spreading angle of the slipstream.
β	angle describing the spread of the slipstream generally.
c_D	drag coefficient.
f	Glauert's rate of climb factor.
f_a	Hafner's rate of climb factor.
F	Glauert's rate of axial flow factor.
k	ratio between the actual and ideal induced velocity.
κ	rate of climb coefficient.
$\bar{\lambda}$	rate of axial flow coefficient.
$\bar{\lambda}_{corr}$	corrected rate of axial flow coefficient.
R	rotor radius.
R_z	radius of the slipstream cross-section at a distance z below the rotor.
R_{z_0}	radius of the slipstream cross-section at a distance z_0 below the rotor.
ρ	air density.
u	axial flow velocity.
u_{corr}	corrected axial flow velocity.
u_z	axial velocity at a distance z behind the rotor.
v_i	induced velocity.
w	rate of climb.
W	weight of the helicopter.
z	distance along the rotoraxis under the disc.
z_0	distance of the stagnation point under the disc.

3 Graphical presentation of the working conditions.

Results of former investigations are usually plotted in a graph, showing $1/f$ against $1/F$, these coefficients being defined by

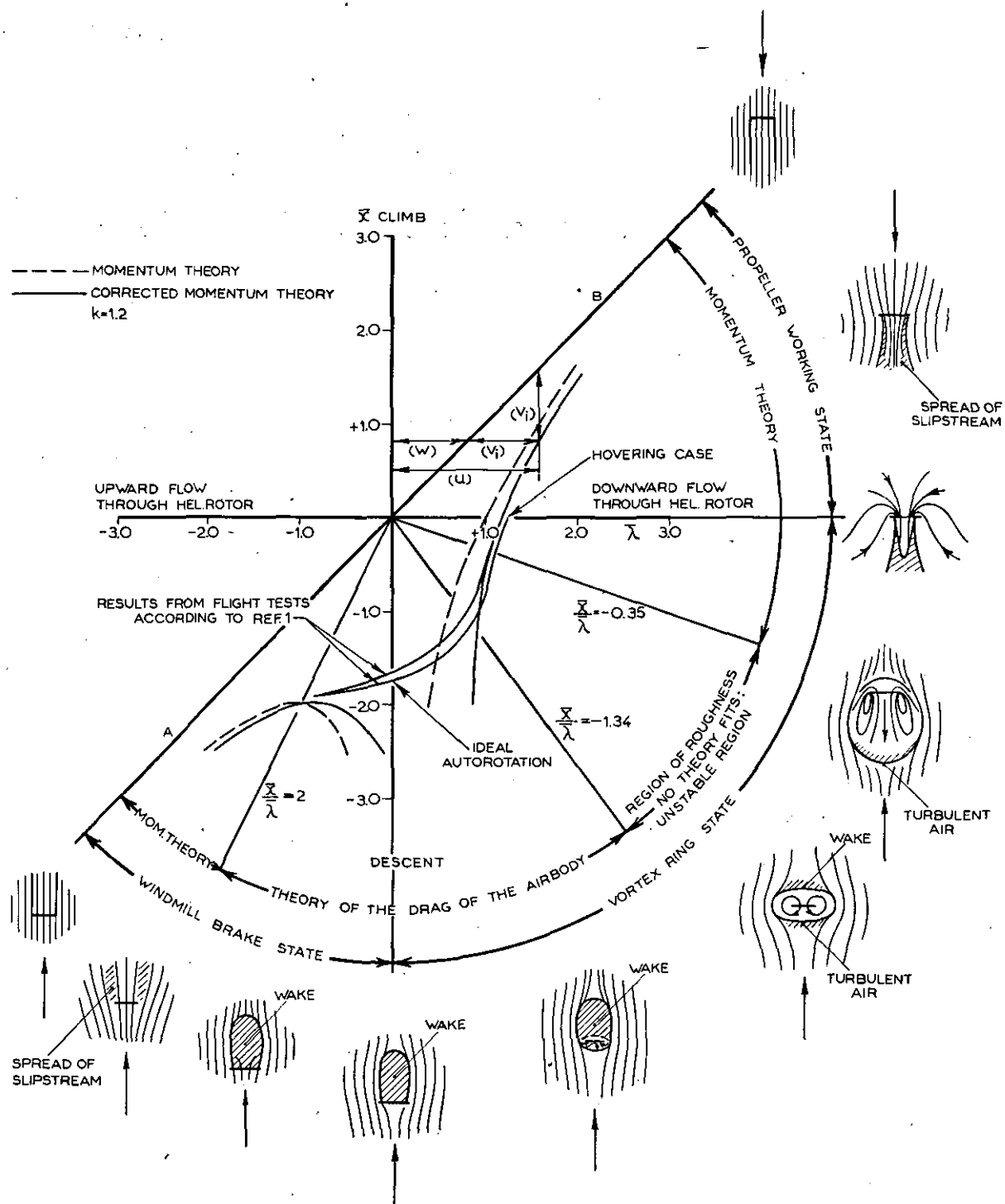


Fig. 1. Relationship between axial flow coefficient λ and rate of climb coefficient κ .

$$\frac{1}{f} = w^2 \cdot 2\rho \cdot \frac{\pi R^2}{W}, \quad (3.1)$$

$$\frac{1}{F} = u^2 \cdot 2\rho \cdot \frac{\pi R^2}{W}. \quad (3.2)$$

Hence, the non-dimensional coefficients are based on the squares of the axial velocity (rate of climb) w of the airscrew and the mean axial velocity u through the rotordisc, respectively.

In this report, use has been made of

$$\kappa = w \sqrt{2\rho \frac{\pi R^2}{W}}, \quad (*) \quad (3.3)$$

$$\lambda = u \sqrt{2\rho \frac{\pi R^2}{W}}, \quad (3.4)$$

these coefficients being based on the first powers of w and u . The parameter κ is essentially the same as Hafner's $1/\sqrt{f_a}$ (ref. 1).

Fig. 1 presents two curves obtained from helicopter flight tests (ref. 1) and two calculated

*) The symbols κ and λ without overlining are reserved for the climb- and airflow ratios w/v_t and u/v_t , with v_t = tip speed.

curves (see Sect. 4 and 5), showing the relationship between $\bar{\lambda}$ and $\bar{\kappa}$.

The mean line through these experimental and theoretical curves is divided by the $\bar{\kappa}$ and $\bar{\lambda}$ axes into three distinct parts, each belonging to one of the main working conditions: propeller working state, vortex ring state and windmill brake state.

The rotor is working in the *propeller state* if its thrust is acting along the direction of motion relative to the undisturbed flow. This case, which prevails if a helicopter climbs vertically, includes two extreme conditions, namely very fast climb and hovering. The air moves downward through the rotordisc. Its relative speed always exceeds the rate of climb, as shown by the straight line AB through the origin under 45 degrees. The difference is called the induced velocity v_i :

$$v_i = u - w. \quad (3.5)$$

Obviously v_i is represented in fig. 1 by the horizontal (or vertical) distance of point $(\bar{\lambda}; \bar{\kappa})$ to AB.

The second working condition, i.e. the *vortex ring state*, is limited by the hovering and the ideal autorotation conditions. In this region the air passes through the disc in the same direction as in the propeller working state, but the helicopter descends vertically.

Beyond the region of ideal autorotation the rotor enters into the *windmill brake state*. In this case the flow through the disc is directed upwards.

4 Momentum equation.

The familiar relationship between thrust or weight W of the helicopter, the mass flow through the disc and the induced velocity $2v_i$ at infinity in the slipstream is

$$W = \rho \pi R^2 |u| 2v_i. \quad (4.1)$$

From this equation, making use of eqs. (3.3), (3.4) and (3.5), the following relation between the coefficients $\bar{\kappa}$ and $\bar{\lambda}$ is obtained.

$$\bar{\kappa} - \bar{\lambda} + \frac{1}{|\bar{\lambda}|} = 0. \quad (4.2)$$

A representation of this equation is shown by the dotted line in fig. 1. It is obvious that the results obtained in this way, will only hold if the velocity of the flow through the rotordisc differs considerably from zero. Large deviations are to be expected at low and moderate rates of descent.

5 Deviations from momentum theory.

A better agreement between the results from eq. (4.2) and those from flight tests, may be obtained by introducing a correction factor k , which accounts for the deviations of the flow through the rotordisc from the ideal flow of momentum theory (the radial and tangential velocities at the disc). Let kv_i be the true induced velocity. Then it follows that

$$kv_i = u_{corr} - w, \quad (5.1)$$

and after eliminating v_i with eq. (3.5)

$$\bar{\lambda}_{corr} = k\bar{\lambda} - (k-1)\bar{\kappa}. \quad (5.2)$$

From results of flight and tunnel tests follows that k is about 1.2 or 1.3.

With this value of k and making use of eqs. (4.2) and (5.2) the theoretical curve has been recalculated and is shown by the drawn line in fig. 1.

As can be seen from this figure, a reasonable agreement between experimental and calculated results is obtained for the propeller state and for the windmill brake state at large negative values of the axial flow coefficient $\bar{\lambda}$.

Due to several basic assumptions, the momentum theory breaks down in the interjacent working states. The remarkable behaviour of helicopters under these conditions and the lack of an explanation for the difference between the experimental results and the curve obtained by the momentum theory, justify the following investigation into the corresponding airflow patterns.

5.1 Vortex ring state.

5.1.1 Velocity distribution along rotor axis.

The momentum theory considers a slipstream of infinite length (i.e. without stagnation points), in which the induced velocity at infinity equals twice its value at the disc. The continuous acceleration of the air implies a contraction of the slipstream.

Actually the induced velocity along the axis in the vortex ring state increases from zero far above the rotor to a value at the disc which exceeds the rate of descent (see fig. 2). This means the existence of a stagnation point above the rotor (A in fig. 2). A similar point should also occur below the rotor as the induced velocity of the slipstream decreases and again becomes equal to the rate of descent (B in fig. 2). This retardation of the flow is due to an exchange of energy by friction and mixing between slipstream and surrounding air. It is accompanied by a *spreading of the slipstream*. Fig. 3 shows the corresponding flow pattern and explains the name "vortex ring state". Thus the helicopter rotor is probably surrounded by an *air-body* the dimensions of which are comparable with the rotordiameter.

5.1.2 Low rates of descent.

As the lower stagnation point will occur at low rates of descent, i.e. at high downward velocities through the rotordisc, at a rather large distance below the rotor, the airbody has an elongated shape in axial direction. A large boundary-area between this body and the surrounding air is available for energy exchange. Moreover, small horizontal disturbing velocities may alter the flow direction of the slow moving slipstream air in the lower part of the airbody. Hence, only a small proportion of the original slipstream air will be redrawn through the disc. These considerations explain the fact that, as shown by fig. 1, the results of the momentum theory still give a reasonable approximation of the actual circumstances.

5.1.3 Region of roughness.

The working condition of a helicopter between certain limits of moderate rates of descent is called the region of roughness, because the behaviour may then be very rough, in attitude as well as in control, and unexpected loss of altitude, and/or large nose-down pitching moments may occur. These phenomena may be explained as follows.

When the rate of descent is higher than in the case treated in Section 5.1.2, the lower stagnation point approaches the disc; then the airbody will more or less resemble a sphere. Due to its relatively small surface area, it is impossible to impart suf-

down in the region of roughness, due to the absence of a large tailboom with anti-torque rotor.

A rough behaviour occurs between 500 and 1500 ft/min R.O.D., as has been measured with the Sikorsky R. 4 (ref. 3). A reduction with $W = 1200$ kg; $R = 5.8$ m; $\rho = 0.125$ kg sec²/m⁴, to $\bar{\kappa}$ and $\bar{\lambda}$ leads with fig. 1 to

$$\text{upper limit } \bar{\kappa} = -0.38 \quad \bar{\lambda} = 1.1 \quad \bar{\kappa}/\bar{\lambda} = -0.35$$

$$\text{lower limit } \bar{\kappa} = -1.14 \quad \bar{\lambda} = 0.85 \quad \bar{\kappa}/\bar{\lambda} = -1.34$$

These values are shown in fig. 1.

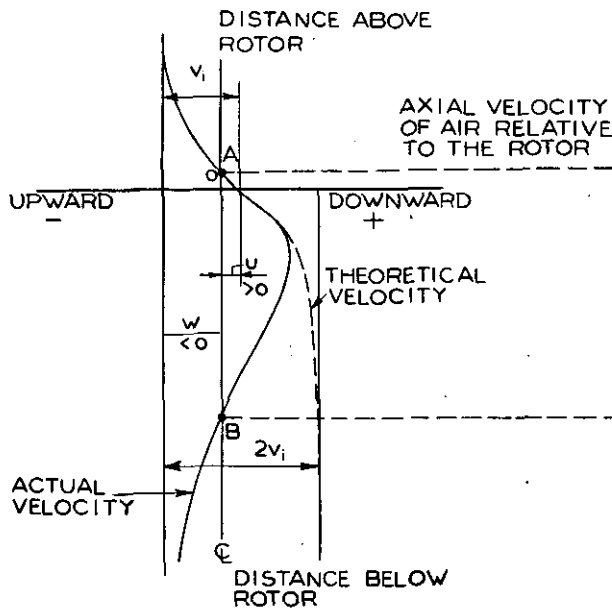


Fig. 2. Average axial velocity near a rotor in the vortex ring state (moderate rate of descent).

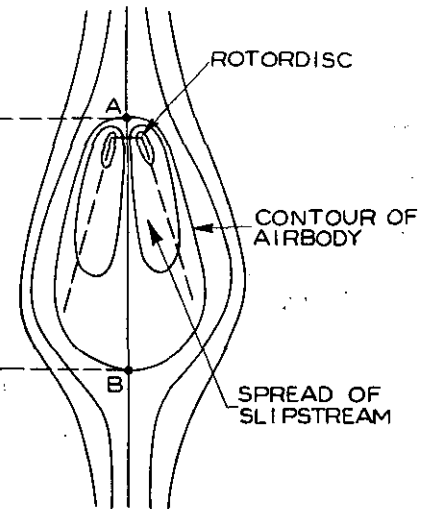


Fig. 3. Airflow pattern near a rotor in the vortex ring state (moderate rate of descent). See also fig. 2.

ficient kinetic energy to the surrounding air. The air in the closed circuit will therefore to a certain degree be speeded up. An unstable increase of collective pitch and/or power supply is necessary to maintain the relative position of the helicopter, in spite of the accelerating flow through the rotor. Thus, the distance between the lower stagnation point and the disc increases again and better possibilities for energy exchange arise.

The probable cause of the *nose-down pitching moment* is indicated by fig. 4. The central part of the fuselage, being in the downwash of the rotor, is rather symmetrical with respect to the C. G. and cannot give any serious contribution to the pitching moment. The tailboom, however, is placed in an upflow of rather high velocity, giving a nose-down pitching moment, in particular if this boom is not streamlined.

A horizontal tailplane, installed on some types of helicopters to improve their high speed stability characteristics, may for the same reason show an even more unfavourable effect on the pitching moment in the region of roughness.

It would be interesting to study the behaviour of helicopters with coaxial rotors in this respect. This type should not show any tendency to nose-

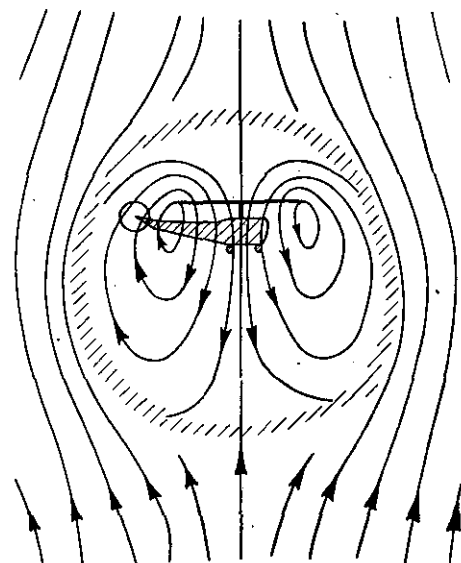


Fig. 4. A helicopter in the region of roughness.

5.1.4 Spread of the slipstream.

This paragraph presents a coarse theoretical confirmation of the fact, that the momentum theory, which for a part of the vortex ring state still may give acceptable results, may not be used for values of κ/λ below about -0.5 .

Consider the spread of a slipstream (fig. 5) as

the ratio between the principal axes of the airbody is found to be

$$\frac{z_0}{2R_{z_0}} = \frac{\sqrt{1 - \frac{u}{w}} - 1}{2\beta \left(1 - \frac{w}{u}\right) \sqrt{1 - \frac{u}{w}}} \quad (5.6)$$

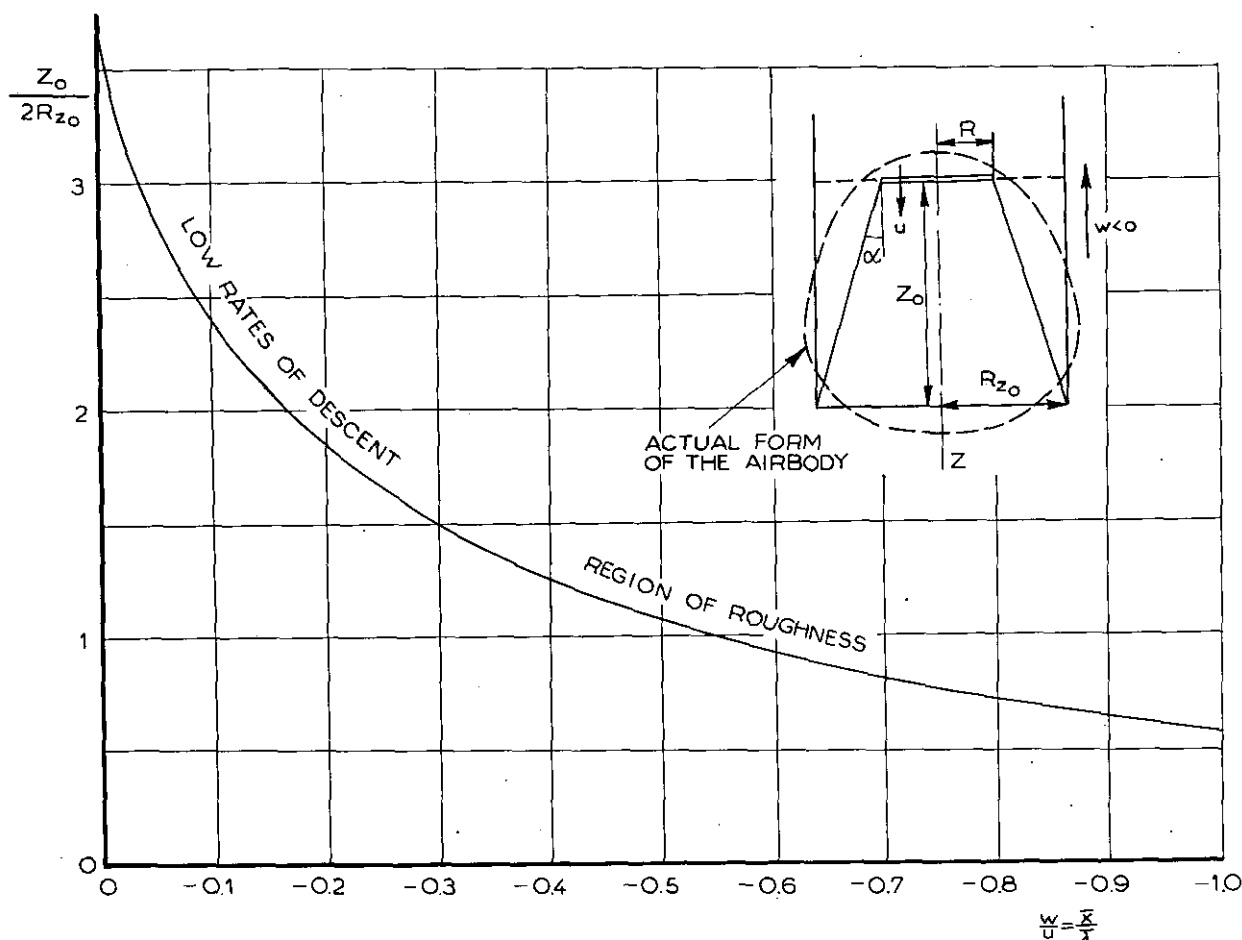


Fig. 5. Rough theoretical approximation of the principal axes z_0 and R_{z_0} of the airbody, calculated with $\beta = 0.135$.

produced by the intermixing of air at its boundary. Let the velocities at the disc and at a distance z downstream be u and u_z , and the corresponding radii of the slipstream R and R_z respectively. To find z_0 for the stagnation point below the disc and the radius R_{z_0} , suppose that the air which is blown down through the rotor, turns upwards after reaching the stagnation level. Further suppose that it passes the disc level through an annulus with an inner radius R and an outer radius R_{z_0} . This is expressed by

$$R^2 u + (R_{z_0}^2 - R^2) w = 0. \quad (5.3)$$

The spreading of the slipstream may be obtained according to ref. 4 by making use of the relation:

$$\alpha = \beta \frac{u - w}{v_d}. \quad (5.4)$$

With

$$R_{z_0} = R + \alpha z_0 \quad (5.5)$$

After plotting $z_0/2R_{z_0}$ against w/u for $\beta = 0.135$ (according to the results of windtunnel experiments, see below), it is found (fig. 5) that the airbody is about spherical for $w/v_d = \kappa/\lambda \approx -0.5$. This value gives a rough estimate for the limit of validity for the momentum theory, because the length of the slipstream in this case becomes comparable with its diameter. The agreement with the value of κ/λ , as found during flight tests for the upper limit of the region of roughness (Sect. 5.1.3) is satisfactory.

An experiment has been carried out to investigate the spread of the slipstream and to estimate the form of the airbody around the rotor. A tube, which was connected to a smoke generator, was mounted in an open jet windtunnel. The open end of the tube, representing the helicopter rotor, faced the airstream. Fig. 6 clearly illustrates the spread of the slipstream when the tunnel windspeed equals zero. In the next photograph (fig. 7) the airbody

has an elongated shape, corresponding to the air-flow pattern as described in item 5.1.2. The airbody is very unsteady and waves periodically. A good mixing of fresh air is possible. Fig. 8 gives an example of the flow if the ratio κ/λ is about -0.4 , this being a condition comparable with the flow pattern in the region of roughness. The axial dimension of the slipstream is smaller; the airbody is nearly spherical. The form of the body is more stable but a waving of its lower end could be observed. This last phenomenon may in this case result in an additional effect in relation to the rough behaviour of the helicopter rotor.

5.1.5 Higher rates of descent.

At higher rates of descent, the axial dimension of the airbody becomes small compared with the rotor radius. In that case the situation resembles that of a flat solid body moving through the air and having a drag equal to the gross weight of the helicopter. A wake exists downstream of the airbody, enabling the air inside and outside to mix sufficiently to exchange the energy delivered by the rotor. Thus, the rate of descent depends on the drag of the airbody. Supposing a ratio a between the areas of the horizontal cross section of the body and the rotor radius, we find

$$W = \frac{1}{2} \rho w^2 \cdot \pi R^2 \cdot a \cdot c_D, \quad (5.7)$$

and after transformation with eq. (3.3):

$$\frac{\kappa^2}{4} \cdot a \cdot c_D = 1. \quad (5.8)$$

In the extreme case of *ideal autorotation*, there is no axial flow through the rotor and it may then be supposed that the rotor can be replaced by a solid disc with the same diameter, the factor a being equal to unity. From fig. 1 it can be deduced that in this case ($\lambda = 0$) the rate of climb coefficient κ equals -1.7 , so that with $a = 1$, c_D becomes $c_D = 1.38$.

In the vortex ring state, the factor a will have a value slightly higher than unity, because the air, moving downwards through the disc will be forced to return outside the disc radius. The dragcoefficient c_D depends on the form and surface condition of the airbody. As this body will be very flat, c_D may be roughly equal to the value 1.38 as mentioned above. From this may be concluded that for a condition ($\lambda = 0.5$) well into the vortex ring state, the factor a will have a value of about $a = 1.3$.

5.2 Windmill brake state.

From fig. 1 follows, that the momentum theory gives a rather good prediction of the flow conditions in the windmill brake state at very high rates of descent. It fails, however, near the ideal autorotation condition. This can be understood by considering the development of the slipstream above the rotor. A figure resembling to fig. 2 was prepared, giving the axial velocity along the centre

line of the rotor axis (see fig. 9). Far below the rotor, the airspeed is equal to the rate of descent; near the rotor, the upward flowing air is decelerated to a value $u = w + v_i$ in the plane of rotation. Downstream, the relative airspeed is further decreased to an extreme value of about $u_z = w + 2v_i$.

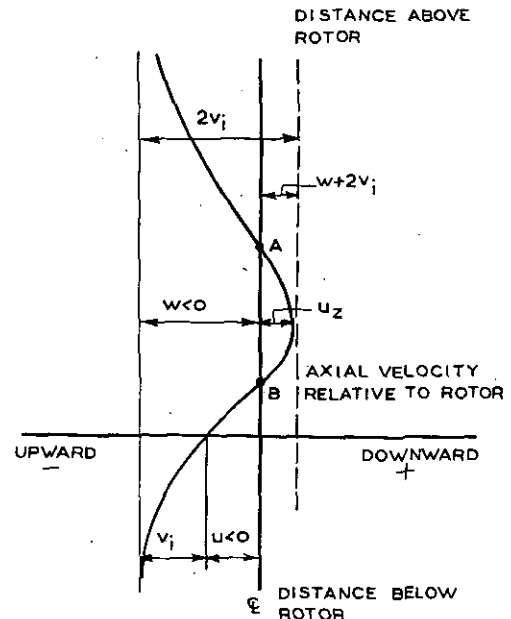


Fig. 9. Average axial velocity near a rotor in the windmill brake state.

The air then accelerates again, resuming the rate of descent far above the rotor.

No stagnation points (A and B) will exist if $u_z < 0$. The condition for a well developed slipstream in the windmill brake state is therefore:

$$\frac{w}{u} = \frac{\kappa}{\lambda} < 2. \quad (5.9)$$

This condition has been plotted also in fig. 1. The momentum theory may only be employed if condition (5.9) is fulfilled. If on the other hand $w/u > 2$, the rotor can be considered as a porous disc, having a drag equal to the weight of the helicopter. Its wake enables the exchange of energy. Eqs. (5.7) and (5.8) will also apply to this case. Again the dragcoefficient c_D will be nearly equal to that of a solid disc, but the factor a will now have a value slightly less than unity, because the effective area of a porous disc is smaller than the area of a solid one. From fig. 1 can be calculated, that $a = 0.83$ for $c_D = 1.38$ and $\lambda = -0.5$.

The conditions on both sides of the ideal autorotation state are treated separately in items 5.1.5 and 5.2. It is realised, however, that this range of flow conditions may be treated as a whole by considering the velocity distribution along the rotor radius.

6 References.

1. STEWART, W. Flight Testing of Helicopters. J. Roy. Aero. Soc. 52 (1948) no. 449, p. 261.

2. CASTLES, W. A Direct Method of Estimating the Performance of a Helicopter in Powered Flight. *J. Aero. Sci. Oct. 1945*, p. 477.
3. REEDER, J. P., GUSTAFSON, F. B. On the Flying Qualities of Helicopters. NACA T.N. 1799, Jan. 1949.
4. WEING, F. *Aerodynamik der Luftschraube*. Julius Springer, 1940, p. 424.
5. GLAUERT, H. The Analysis of Experimental Results in the Windmill Brake and Vortex Ring States of an Airscrew. R. and M. No. 1026, February 1926.
6. LOCK, C. N. H., BATEMAN, H., TOWNEND, H. C. H. An Extension of the Vortex Theory of Airscrews with Application to Airscrews of Small Pitch, Including Experimental Results. R. and M. No. 1014, June 1926.
7. PRANDTL, L. *Aerodynamic Theory*, Durand, W. F., vol. III, Division G, section 25. Julius Springer, 1935.

APPENDIX.

The field of flow from windtunnel smoke tests.

Although with the aid of the calculations described a more or less comprehensible picture of the field of flow through a helicopter rotor can be obtained, its value will remain questionable as long as no experimental data exist to confirm the hypothesis developed in the foregoing sections. For this reason an investigation was carried out, in the free jet windtunnel of the N.L.L. whereby the field of flow through a simplified rotor with "see-saw" blades was made visible with the aid of smoke-threads, produced by a number of hot-wire smoke generators. For a complete description of the test-method, the apparatus and the results obtained, reference is made to N.L.L. Report A.1205.

The various pictures concerning the vertical flight conditions are shown in figs. A.1 and A.2.

In order to get a clear picture of the field of flow, two test series were made.

The first with a rotor of small diameter, the second with a rotor of about twice the diameter of the first. With this rotor only half of the field

of flow was made visible, thus enabling a more detailed study.

Fig. A.1 a, b, c show the wellknown pattern for a rotor or propeller in the windmill brake state. The air passes upwards through the disc. The streamlines show the divergence due to the loss of momentum. Fig. A.1b was obtained by placing the smoke generators downstream of the rotor and gives a clear picture of the airbody as predicted in section 4.2 for this condition.

By increasing the rotor tip-speed, the working condition changes from the windmill state into the autorotation (see figs. A.1-c and d and A.2-b). The "wake" of the rotor already shows the tendency to close, while the "stagnation point" as mentioned in sect. 5.1.4 lies in the plane of the rotordisc. The method of treating the rotordisc in the case of autorotation as a round flat plate is confirmed by fig. A.1-d where the smoke generators are placed behind the rotor plane and no smoke passes through the disc.

By again increasing the tip-speed, the rotor enters into the various conditions of the vortex ring state.

As can be seen from figs. A.1-e to j and A.2-c to g the form of the airbody around the rotor resembles more and more the spherical, the stagnation point moves still further downward till at last the flow becomes unstable (see fig. A.1-i and f and A.2-e, f, g) and the region of roughness is reached.

In this condition no clear picture of the field of flow could be obtained. One point, however, is made clear, namely that the flow through the rotordisc has a periodically changing character. While at one side of the disc a vortex is building up, at the opposite side it reaches, while moving upstream, its ultimate unstable condition and detaches itself from the rotor. It could be observed that in the region of roughness the rotor performs a slow periodical tumbling motion.

By making the tunnel windspeed zero the hovering condition is obtained (see fig. A.2-h) and from this condition by turning on the windspeed the rotor enters into the propeller working state (fig. A.2-i). Both pictures obtained show the wellknown flow conditions.

Completed: December 1949.

A. 2
i



Vertical climb

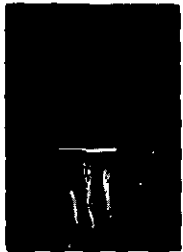
Fig. A. 2

A. 2
h



Hovering

A. 1
i



A. 1
j



A. 2
f



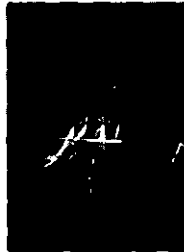
A. 2
g



A. 1
g



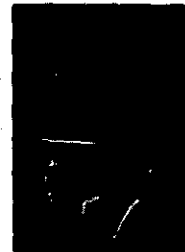
A. 1
h



A. 2
e



A. 2
d



Vortex ring state

A. 1
e



A. 1
f



A. 2
c



Fig. A 1

A. 1
c



A. 1
d



A. 2
b



Ideal autorotation

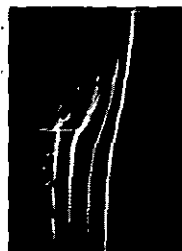
A. 1
a



A. 1
b



A. 2
a



Windmill
brake state

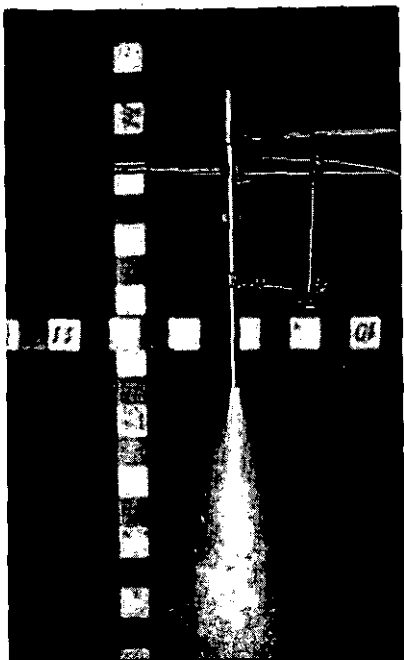


Fig. 6. Tunnel speed 0 m/sec
mean jet veloc. 1.5 m/sec



Fig. 7. Tunnel speed 1.3 m/sec
mean jet veloc. 14.9 m/sec

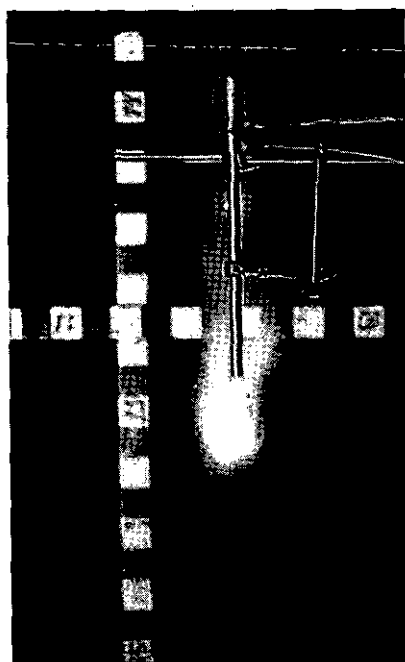


Fig. 8. Tunnel speed 2.0 m/sec
mean jet veloc. 5.0 m/sec

